



# MID-AMERICA TRANSPORTATION CENTER

Report # MATC-UNL: 004-34

Final Report

WBS: 27-1121-0005-004-34



## Protecting Critical Civil Infrastructure Against Impact from Commercial Vehicles - Phase III, A System Based Approach Including Fire

**Daniel G. Linzell, PhD, PE, F.ASCE, F.SEI**

Associate Dean for Graduate and International Programs  
Department of Civil and Environmental Engineering  
University of Nebraska-Lincoln

**Qusai Abdulkarim Alomari, PhD, EIT**

Postdoctoral Research Associate  
Midwest Roadside Safety Facility  
University of Nebraska-Lincoln



2024

A Cooperative Research Project sponsored by  
U.S. Department of Transportation- Office of the Assistant  
Secretary for Research and Technology

The contents of this report reflect the views of the authors, who are responsible for the facts and the accuracy of the information presented herein. This document is disseminated in the interest of information exchange. The report is funded, partially or entirely, by a grant from the U.S. Department of Transportation's University Transportation Centers Program. However, the U.S. Government assumes no liability for the contents or use thereof.

MATC

Protecting Critical Civil Infrastructure Against Impact from Commercial Vehicles – Phase III, A  
System Based Approach Including Fire

Daniel G. Linzell, Ph.D., P.E., F.ASCE, F.SEI  
Associate Dean for Graduate and International Programs  
College of Engineering  
Leslie D. Martin Professor  
Department of Civil and Environmental Engineering  
University of Nebraska-Lincoln

Qusai Abdulkarim Alomari, Ph.D., E.I.T  
Postdoctoral Research Associate  
Midwest Roadside Safety Facility (MwRSF)  
University of Nebraska-Lincoln

A Report on Research Sponsored by

Mid-America Transportation Center  
University of Nebraska–Lincoln

September 2024

## Technical Report Documentation Page

1. Report No. 25-1121-0005-004-34	2. Government Accession No.	3. Recipient's Catalog No.	
4. Title and Subtitle Protecting Critical Civil Infrastructure Against Impact from Commercial Vehicles - Phase III, A System Based Approach Including Fire		5. Report Date September 2024	
		6. Performing Organization Code	
7. Author(s) Daniel G. Linzell <a href="https://orcid.org/0000-0002-7158-1776">https://orcid.org/0000-0002-7158-1776</a> Qusai Abdulkarim Alomari <a href="https://orcid.org/0000-0002-9994-9704">https://orcid.org/0000-0002-9994-9704</a>		8. Performing Organization Report No. 25-1121-0005-004-34	
9. Performing Organization Name and Address Mid-America Transportation Center Prem S. Paul Research Center at Whittier School 2200 Vine St. Lincoln, NE 68583-0851		10. Work Unit No. (TRAIS)	
		11. Contract or Grant No. 69A3551747107	
12. Sponsoring Agency Name and Address Office of the Assistant Secretary for Research and Technology 1200 New Jersey Ave., SE Washington, D.C. 20590		13. Type of Report and Period Covered November 2021-June 2024	
		14. Sponsoring Agency Code MATC TRB RiP No. 91994-103	
15. Supplementary Notes			
16. Abstract Bridges and bridge piers are vulnerable to multi-hazard events triggered by vehicle collisions coupled with correlated and cascading events, such as explosions and fires. Despite recent catastrophic incidents that have highlighted the profound consequences of these extreme demands, including substantial damage, adverse economic impact, and loss of life, there has been a notable lack of research investigating the performance of bridges and bridge structural components under the aforementioned multi-hazards. Furthermore, current bridge design codes do not address these events assuming that, after these destructive events, replacement of the pier columns or entire bridge will occur. As a result, more comprehensive studies are justified to investigate bridge resiliency under these multi-hazards to determine if, in certain situations, effective retrofitting schemes could be developed and deployed in lieu of replacement. Consequently, LS-DYNA was utilized to simulate the behavior of prototype isolated, round, reinforced concrete columns and multi-column piers, and an existing bridge in Sidney, NE, under coupled vehicle collision and air blast before or after fire. A unique and advanced multi-step modeling approach that incorporates uncoupled implicit heat transfer analyses and explicit structural analyses was developed and validated against published test results. The study also examined the feasibility of various in-situ retrofitting schemes, including fiber reinforced polymers and soil infills, to improve bridge resiliency under combinations of vehicle collision, air blast, and fire. Furthermore, an empirically-based, simplified, equivalent static force predictive equation, that can be used to conservatively represent substructure impact forces and used for analysis and design, and a companion assessment framework were proposed. The outcomes of this study significantly contributed to the existing knowledge base, providing valuable insights, and improving bridge analysis and design methods that can be adopted by relevant codes and specifications.			
17. Key Words Bridge; Reinforced Concrete; Column; Collision; Blast; Fire; LS-DYNA		18. Distribution Statement	
19. Security Classif. (of this report) Unclassified	20. Security Classif. (of this page) Unclassified	21. No. of Pages 308	22. Price

## Table of Contents

Acknowledgments.....	xi
Disclaimer.....	xii
Abstract.....	xiii
Chapter 1 Introduction and Background.....	1
1.1 Background.....	1
1.2 Problem Statement.....	3
1.3 Objectives.....	3
1.4 Scope.....	4
Chapter 2 Literature Review.....	6
2.1 Introduction.....	6
2.2 Material Behavior and Structural Response under Fire, Impact, and Blast.....	8
2.2.1 Material behavior under impact and blast.....	8
2.2.2 Material properties under fire and elevated temperatures.....	10
2.3 Highway Bridge Vehicle Collisions.....	15
2.3.1 Vehicle collisions with bridge elements - examples.....	15
2.3.2 Vehicle collisions with bridge elements - research.....	17
2.4 Highway Bridges Air Blasts.....	20
2.4.1 Highway bridge blasts - examples.....	20
2.4.2 Highway bridge blasts - research.....	23
2.5 Highway Bridge Fires.....	29
2.5.1 Bridge fires - examples.....	29
2.5.2 Bridge fires - research.....	37
2.6 Combined fire, impact, and blast - examples.....	42
2.7 Combined fire, impact, and blast - research.....	44
2.8 Retrofitting RC structural elements using Fiber Reinforced Polymers (FRP).....	48
2.8.1 FRP strengthening of structural elements subjected to blast and impact.....	48
2.8.2 FRP repair of fire or heat damaged columns.....	51
2.9 Summary.....	54
Chapter 3 Finite Element Model Development.....	56
3.1 Introduction.....	56
3.2 Prototype RC Pier Column.....	56
3.3 Vehicle Collision.....	58
3.4 Air Blast.....	60
3.5 Fire.....	61
3.6 Material Models.....	64
3.6.1 Concrete.....	64
3.6.2 Steel reinforcement.....	66
3.6.3 Soil.....	67
3.6.4 Air and explosive.....	68
3.6.5 Thermal material models.....	70
3.7 Model Coupling and Boundary Conditions.....	72
3.8 Time and Mass Scaling.....	74
3.9 FE Modeling Approach.....	75
3.10 Summary.....	77

Chapter 4 Validation Study.....	79
4.1 Introduction.....	79
4.2 RC Column, Fire Exposure.....	80
4.3 RC Slab under Fire and Impact.....	83
4.4 RC Beam under Fire and Blast .....	86
4.5 Summary .....	89
Chapter 5 Critical Fire, Impact, Blast, Load Sequencing.....	91
5.1 Introduction.....	91
5.2 Selected Load Sequences.....	91
5.2.1 Analytical procedure.....	92
5.3 Thermal Analysis – <i>F-I-B, I-B-F</i> .....	94
5.3.1 Fire, impact, blast – F-I-B.....	94
5.3.2 Impact, blast, fire – I-B-F.....	96
5.4 Isolated Column Response– <i>F-I-B, I-B-F</i> .....	97
5.4.1 Damage propagation .....	97
5.4.2 Effect of column diameter.....	100
5.4.3 Residual capacity .....	103
5.5 Summary and Conclusions .....	104
Chapter 6 Isolated Column Performance Evaluation, F-I-B.....	106
6.1 Introduction.....	106
6.2 Bridge Column Damage Levels.....	106
6.3 Fire Damaged Isolated Bridge Column Performance under Impact and Blast.....	111
6.3.1 Damage propagation .....	111
6.3.2 Final damage states, concrete spalling volume, permanent sets .....	117
6.3.3 Residual axial load carrying capacity .....	121
6.3.4 Shear resistance.....	123
6.4 Summary and Conclusions .....	125
Chapter 7 Effectiveness of In-Situ Repair Techniques of Fire Damaged Bridge Columns Subjected to Impact and Blast.....	130
7.1 Introduction.....	130
7.2 Numerical Modeling .....	130
7.2.1 Retrofit schemes.....	130
7.2.2 CFRP wrapping.....	132
7.2.3 Epoxy adhesive .....	133
7.2.4 CFRP reinforcement .....	134
7.2.5 Model development.....	135
7.3 Validation.....	136
7.3.1 CFRP wrapped pier column under impact.....	136
7.3.2 GFRP strengthened RC panel under blast.....	139
7.4 Numerical Studies.....	141
7.4.1 Fire damaged column.....	141
7.4.2 Retrofit design.....	143
7.4.3 Study matrix.....	144
7.5 Results.....	145
7.5.1 Scheme 1 .....	145
7.5.2 Scheme 2 .....	154

7.6 Effect of Bridge Column Diameter .....	158
7.7 Summary and Conclusions .....	164
Chapter 8 Multi-Column Piers Subjected to Fire, Vehicle Collision, and Air Blast .....	168
8.1 Introduction .....	168
8.2 Finite Element Models .....	168
8.2.1 Prototype RC multi-column piers .....	168
8.2.2 Material models.....	171
8.2.3 Boundary conditions .....	171
8.3 Response of Multi-column Piers.....	172
8.3.1 Fire response and damage propagation, F90.....	173
8.3.2 Post-fire impact and blast response, damage propagation, F90-I-B .....	175
8.3.3 Final damage states, permanent sets, deflections.....	181
8.4 Multi-column Pier CFRP Retrofitting, <i>F-I-B</i> .....	184
8.4.1 Retrofitting scheme details.....	184
8.4.2 Response, damage propagation, permanent sets .....	185
8.5 Summary and Conclusions .....	189
Chapter 9 Full Bridge Performance under Fire, Impact, and Air Blast .....	191
9.1 Introduction.....	191
9.2 Prototype Bridge Model.....	191
9.3 Finite Element Modeling .....	193
9.3.1 Element formulation and material models .....	194
9.3.2 Model coupling, contact, and boundary conditions .....	196
9.3.3 Load application.....	198
9.4 FE Model Validation.....	199
9.5 Bridge System Response to Fire, Impact, and Blast.....	202
9.5.1 Vehicle collision (I) .....	202
9.5.2 Air blast (B) .....	205
9.5.3 Coupled vehicle collision and air blast (I-B) .....	207
9.5.4 Fire, vehicle collision, and air blast (F90-I-B).....	210
9.6 Resiliency Enhancement using Soil Infill.....	217
9.6.1 FE model development .....	217
9.6.2 Simulation results.....	218
9.6.3 Bogie Crash Tests .....	221
9.7 Summary and Conclusions .....	223
Chapter 10 Advanced Analysis of Intact, Fire-Damaged, and CFRP Retrofitted Bridge Pier Columns under Vehicle Collisions: Empirical Equivalent Static Force Equation and Framework .....	226
10.1 Introduction.....	226
10.2 Background .....	227
10.3 Finite Element Model .....	231
10.4 Parametric Study .....	231
10.4.1 Study matrix.....	232
10.5 Parametric Study Results .....	235
10.5.1 Effect of column diameter (D).....	235
10.5.2 Effect of column height (H).....	238
10.5.3 Effect of unconfined compressive strength ( $f_c'$ ).....	239

10.5.4 Effect of longitudinal steel reinforcement ratio ( $\rho$ ) .....	240
10.5.5 Effect of fire exposure and fire duration ( $FD$ ) .....	241
10.5.6 Effect of CFRP wrap thickness ( $t_{CFRP}$ ) .....	243
10.5.7 Effect of CFRP wrapping configuration (Conf) .....	244
10.5.8 Effect of vehicle mass ( $M$ ) .....	246
10.5.9 Effect of impact speed ( $V$ ) .....	247
10.6 Impact Force Estimation and ESF assessment .....	248
10.7 Proposed ESF Equation, Derivation and Validation .....	252
10.7.1 ESF equation development .....	252
10.7.2 ESF equation validation .....	254
10.8 ESF assessment framework .....	256
10.9 Axial Load Capacity Calculation .....	258
10.9.1 Capacity of intact (undamaged) RC columns .....	259
10.9.2 Capacity of bare fire-damaged RC columns .....	259
10.9.3 Capacity of CFRP wrapped RC columns .....	262
10.10 Summary and Conclusions .....	264
Chapter 11 Conclusions and Future Work .....	266
11.1 Summary .....	266
11.2 Conclusions .....	267
11.2.1 Isolated bridge columns .....	267
11.2.2 Multi-column piers .....	270
11.2.3 Full bridge system .....	270
11.2.4 Retrofitting schemes .....	272
11.2.5 ESF predictive equation and advised assessment framework .....	275
11.3 Recommendations for Future Work .....	277
References .....	280
Appendix A .....	294

## List of Figures

Figure 2.1 Relationship between concrete strength and strain rate (Malvar and Crawford 1998) ..	9
Figure 2.2 Relationship between steel strength and strain rate (Malvar 1998) .....	10
Figure 2.3 Relative compressive strength and elastic modulus of concrete as a function of temperature (reproduced from Eurocode 2, part 1-2) .....	12
Figure 2.4 Relative yielding strength and elastic modulus of steel as a function of temperature (reproduced from Eurocode 2, part 1-2) .....	12
Figure 2.5 Thermal material properties: (a) concrete; (b) steel reinforcement (reproduced from Eurocode 2, part 1-2) .....	13
Figure 2.6 Reduction of dynamic increase factor (DIF) for concrete at various temperatures (Su, Xu, and Ren 2014) .....	14
Figure 2.7 Tanker truck pier collision, I-37, Corpus Christi, TX (Buth et al. 2010).....	16
Figure 2.8 Tractor-trailer pier collision, I-35, Red Oak, TX (Buth et al. 2010).....	16
Figure 2.9 Truck collision, I-80, Big Springs, NE (Wehbe et al., 2017).....	17
Figure 2.10 Truck tanker explosion and bridge collapse I-80, Emeryville, CA (Bay City News, 2007) .....	21
Figure 2.11 Truck tanker explosion, I-65, Franklin, TN (The Tennessean News, 2014).....	22
Figure 2.12 Truck carrying fireworks explosion, China (Stochino and Tattoni 2013).....	23
Figure 2.13 Shock wave parameters for TNT explosions (Department of Defense 2008).....	24
Figure 2.14 Idealized pressure-time history of an explosive in free air (Williams 2009) .....	25
Figure 2.15 Effect of angle of incidence on reflected pressure coefficient (Williamson 2010)....	26
Figure 2.16 Blast-loading categories (Williamson 2010) .....	27
Figure 2.17 Pressure design ranges (Department of Defense 2008).....	27
Figure 2.18 Highway bridge collapse as a result of fire, Oakland, CA (Bulwa and Fimrite 2007) .....	31
Figure 2.19 Hazel Park bridge overpass collapse as a result of fire, Detroit, MI (Guthrie, Goodwill, and Hicks 2009).....	32
Figure 2-2.20 Tanker truck fire under Paramount Boulevard bridge in Montebello, Los Angeles, CA (Giuliani, Crosti, and Gentili 2012).....	33
Figure 2.21 Post fire damage to I-85 bridge, Atlanta, GA (Venkatesh Kodur and Naser 2021)....	34
Figure 2.22 Tanker truck accident on the Wiehlthal Bridge, Rhine-Westphalia, Germany (photo by C. Buschorn, 26 Aug. 2004, public domain image).....	35
Figure 2.23 The most common standard fire curves.....	38
Figure 2.24 Collapse of a part of I-95 highway after a multi-hazard incident, Philadelphia, Pennsylvania (Tebor and Sottile 2023).....	43
Figure 2.25 Damage in I-65 bridge overpass caused by multi-hazards, in Brimingham, Alabama, 2002 (Cardone, 2023) .....	44
Figure 3.1 FHWA multi-column pier (unit: mm) (Wassef et al. 2003).....	57
Figure 3.2 Isolated column and foundation system (Fang et al. 2021).....	57
Figure 3.3 Column cross sections (units: mm) .....	58
Figure 3.4 Ford F800 Single Unit Truck (SUT), LS-DYNA model.....	59
Figure 3.5 ISO-834 (ISO 1999) .....	63
Figure 3.6 Full and half surface area fire exposure schemes .....	63
Figure 3.7 Modeled pier column air, soil volume, and SUT .....	74
Figure 4.1 Fire and residual capacity test setup (Kodur et al., 2017) .....	80

Figure 4.2 FEM: (a) RC column under fire; (b) temperature profile and corresponding column layers .....	81
Figure 4.3 FEM and test temperature time histories .....	82
Figure 4.4 Simulated and test load-displacement curves .....	83
Figure 4.5 RC slab dimensions and reinforcement (Parmar et al. 2014) .....	84
Figure 4.6 FEM of fire damaged RC slab .....	84
Figure 4.7 Failure pattern (a) simulated, (b) experimental .....	85
Figure 4.8 Mid-span displacement time-history .....	86
Figure 4.9 Impact force time history .....	86
Figure 4.10 Developed LS-DYNA FE model: (a) fire-damaged RC beam subjected to air blast; (b) steel reinforcement; (c) fire exposure scheme .....	87
Figure 4.11 RC beam heat transfer analysis results: (a) beam cross section and instrument locations (Zhai et al., 2016); (b) temperature time-histories at thermocouple locations .....	88
Figure 4.12 Experimental and modeled mid-span displacement time histories .....	89
Figure 5.1 Demand sequences and analyses flow chart .....	92
Figure 5.2 Studied Demand Sequences .....	93
Figure 5.3 Temperature contours and corresponding column layers: (a) F90; (b) H90 .....	95
Figure 5.4 Effective thermal stress distribution and crack propagation: (a) FEM, 750 mm diameter, F90-I-B; (b) Experiment (Chinthapalli et al. 2019) .....	95
Figure 5.5 Fire damaged column: (a) concrete layers, (b) reinforcement layers .....	96
Figure 5.6 Effective thermal stress distribution, and crack propagation 1050 mm diameter, I-B-F90 .....	97
Figure 5.7 Applied load and mid-height lateral displacement time histories, 750 mm diameter, F90-I-B, I-B-F90 .....	98
Figure 5.8 750 mm diameter column damage, F90-I-B and I-B-F90:(a) effective plastic strains, damage propagation; (b) reinforcement fracture, buckling .....	99
Figure 5.9 Column lateral displacements, all study cases: (a) 750-mm diameter; (b) 1050-mm diameter; (c) 1350-mm diameter .....	101
Figure 5.10 Final damage states, studied column diameters and loading scenarios .....	102
Figure 5.11 Residual axial capacities for studied column diameters and load sequences .....	104
Figure 6.1 Surface crack propagation - M1 .....	109
Figure 6.2 Concrete cover spalling - M2 .....	109
Figure 6.3 Plastic hinge formulation - M3 .....	109
Figure 6.4 Direct shear failure - M4 .....	110
Figure 6.5 Reinforcement failure – M5 .....	110
Figure 6.6 Column core breach - M6 .....	110
Figure 6.7 Effective thermal stress distribution and crack propagation, F90 .....	111
Figure 6.8 F90-I-B 750 mm diameter impact and blast demand progression, and resulting damage: (a) impact and blast time steps progression; (b) column effective plastic strains and damage propagation; (c) reinforcement response and damage propagation .....	113
Figure 6.9 Applied load, and mid-height lateral displacement time histories, 750 mm diameter, F90-I-B .....	113
Figure 6.10 F90-I-B 1050 mm diameter impact and blast demand progression, and resulting damage: (a) impact and blast time steps progression; (b) column effective plastic strains and damage propagation; (c) reinforcement response and damage propagation .....	114

Figure 6.11 Applied load, and mid-height lateral displacement time histories, 1050 mm diameter, F90-I-B.....	114
Figure 6.12 F90-I-B 1350 mm diameter impact and blast demand progression, and resulting damage: (a) impact and blast time steps progression; (b) column effective plastic strains and damage propagation; (c) reinforcement response and damage propagation.....	115
Figure 6.13 Applied load, and mid-height lateral displacement time histories, 1350 mm diameter, F90-I-B.....	115
Figure 6.14 Final damage states for studied column diameters and demand scenarios .....	119
Figure 6.15 Column lateral displacements: (a)750 mm diameter; (b) 1050 mm diameter; (c) 1350 mm diameter; (d) all diameters. ....	120
Figure 6.16 Spalled concrete volume fraction, 750 mm diameter .....	120
Figure 6.17 Load-mid height displacement curve, 1050 mm diameter, F60-I-B .....	121
Figure 6.18 Residual axial capacities for all column diameters and loading scenarios.....	122
Figure 6.19 Column shear diagrams: (a) F60-I-B; (b) F90-I-B; (c) H60-I-B; (d) H90-I-B.....	124
Figure 6.20 Shear demand to capacity ratios .....	124
Figure 7.1 Studied retrofitting schemes: (a) Scheme 1, CFRP wrap; (b) Scheme 2, hybrid system .....	132
Figure 7.2 Pendulum setup and FE model (Sha and Hao 2015).....	138
Figure 7.3 Experimental, modeled final damage states (Sha and Hao 2015).....	138
Figure 7.4 Experimental, numerical impact force and reinforcement strain time histories (Sha and Hao 2015).....	139
Figure 7.5 Blast test, FE model (Razaqpur et al. 2007).....	140
Figure 7.6 Experimental, numerical: (a) displacement time history; (b) reflected pressure time history. ....	141
Figure 7.7 Fully CFRP wrapped isolated pier column .....	142
Figure 7.8 Load-axial displacement curve, 750 mm column, F90 .....	143
Figure 7.9 Residual axial load carrying capacity, 750 mm wrapped columns, F90.....	144
Figure 7.10 Crack propagation, bare and CFRP-wrapped columns .....	146
Figure 7.11 Final damage states and spalled concrete volumes, bare and CFRP-wrapped columns .....	147
Figure 7.12 Displacements and kinetic energies, bare and CFRP-wrapped columns .....	148
Figure 7.13 Residual axial load carrying capacities, bare and CFRP-wrapped columns .....	149
Figure 7.14 Partially CFRP wrapped columns: (a) HH-9L; (b) I1000-9L; (c) I500-9L.....	150
Figure 7.15 Crack propagation; fully and partially CFRP-wrapped columns .....	151
Figure 7.16 Final damage states and spalled concrete volumes; fully and partially CFRP-wrapped columns .....	152
Figure 7.17 Displacements and kinetic energies; fully and partially CFRP-wrapped columns ..	153
Figure 7.18 Residual axial load carrying capacities; fully and partially CFRP-wrapped columns .....	154
Figure 7.19 Crack propagation, bare and hybrid retrofitted columns.....	155
Figure 7.20 Final damage states, bare and hybrid retrofitted columns.....	156
Figure 7.21 Displacements and kinetic energies, bare and hybrid retrofitted columns.....	157
Figure 7.22 Residual axial load carrying capacities, bare and hybrid retrofitted columns.....	158
Figure 7.23 Concrete crack propagations for different retrofitting schemes and column diameters .....	159
Figure 7.24 Final damage states, selected retrofitting schemes.....	161

Figure 7.25 Comparison of lateral displacement in bare and retrofitted columns (a) D1050 mm; (b) D1350 mm.....	162
Figure 7.26 Comparison of kinetic energies in bare and retrofitted columns.....	163
Figure 7.27 Residual axial load carrying capacity for studied column diameters and retrofitting schemes.....	164
Figure 8.1 Four-column pier finite element model and geometry.....	169
Figure 8.2 Two- and three-column piers finite element models and geometry.....	170
Figure 8.3 Representative two-column pier FE model depicting, air and soil volumes and impact and blast loads.....	172
Figure 8.4 Effective thermal stress distribution and crack propagation: (a) two-column pier; (b) three-column pier; (c) four-column pier.....	174
Figure 8.5 Applied load and mid-height lateral displacement time histories, all piers, F90-I-B.....	175
Figure 8.6 Two-column pier: impact and blast load propagation; damage propagation, I-B and F90-I-B.....	178
Figure 8.7 Three-column pier: impact and blast load propagation; damage propagation, I-B and F90-I-B.....	179
Figure 8.8 Four-column pier: impact and blast load propagation; damage propagation, I-B and F90-I-B.....	180
Figure 8.9 Final damage states for studied piers under I-B and F90-I-B.....	181
Figure 8.10 Permanent sets of impacted columns in two-, three-, and four-column pier.....	182
Figure 8.11 Pier cap deflection: (a) two-column pier (b) three-column pier (c) four-column pier.....	183
Figure 8.12 Studied retrofitting schemes.....	185
Figure 8.13 Crack propagation, bare and retrofitted columns.....	186
Figure 8.14 Final damage states and spalled concrete volumes, bare and retrofitted columns.....	187
Figure 8.15 Permanent sets: (a) column lateral displacement (b) pier cap deflection.....	188
Figure 9.1 Bridge elevation.....	192
Figure 9.2 Pier elevation and details.....	192
Figure 9.3 Superstructure cross section.....	193
Figure 9.4 Superstructure details.....	193
Figure 9.5 Bridge FE model.....	197
Figure 9.6 Studied loading sequences.....	199
Figure 9.7 Effective Width.....	201
Figure 9.8 Deflections in the middle bridge girder.....	202
Figure 9.9 Damage propagation under SUT collision: (a) full bridge (b) slab (c) girders (d) pier.....	204
Figure 9.10 Final damage state of bridge and pier, SUT collision.....	205
Figure 9.11 Damage propagation under air blast: (a) full bridge (b) slab (c) girders (d) pier.....	206
Figure 9.12 Final damage state of bridge and pier, air blast.....	207
Figure 9.13 Damage propagation under I-B: (a) full bridge (b) slab (c) girders (d) pier.....	209
Figure 9.14 Final damage state of bridge and pier, I-B.....	210
Figure 9.15 Fire damaged structural elements, F90.....	211
Figure 9.16 Thermal stress distribution, F90: (a) bridge (b) slab (c) girders and (d) pier.....	212
Figure 9.17 Damage propagation under F90-I-B: (a) full bridge (b) slab (c) girders (d) pier.....	214
Figure 9.18 Failure modes of bridge girders.....	215
Figure 9.19 Final damage state of bridge and pier, F90-I-B.....	216

Figure 9.20 Separation between the bridge girders and the elastomeric bearings (Lin et al., 2020)	216
.....	
Figure 9.21 Proposed retrofitting scheme	218
Figure 9.22 Damage propagation under I-B: (a) original pier (b) retrofitted pier	220
Figure 9.23 Final damage state of bridge and pier, I-B: (a) original pier (b) retrofitted pier	221
Figure 9.24 MATC-1 Bogie test	223
Figure 9.25 MATC-2 Bogie Test	223
Figure 10.1 Finite Element Model: (a) structural system and (b) full domain and soil volume	232
Figure 10.2 Vehicle FE models	235
Figure 10.3 Effect of column diameter on impact performance	238
Figure 10.4 Effect of column height on impact performance	239
Figure 10.5 Effect of unconfined compressive strength on impact performance	240
Figure 10.6 Effect of longitudinal steel reinforcement ratio on impact performance	241
Figure 10.7 Effect of ISO-834 fire exposure on impact performance	242
Figure 10.8 Effect of fire exposure duration on impact performance	243
Figure 10.9 Effect of CFRP wrap thickness on impact performance	244
Figure 10.10 CFRP partial wrapping configurations	245
Figure 10.11 Effect of CFRP wrapping configuration on impact performance	246
Figure 10.12 Effect of vehicle mass on impact performance	247
Figure 10.13 Effect of vehicle speed on impact performance	248
Figure 10.14 Representative PDFs and their corresponding ESFs; Cases <b>C0 – C4</b>	249
Figure 10.15 Predicted ESFs, all studied cases	250
Figure 10.16 Developed ESF equation, FE model comparison	254
Figure 10.17 Developed ESF equation, FE results, published study results	256
Figure 10.18 Proposed ESF Framework	258

## List of Tables

Table 2.1 Catastrophic bridge fires .....	36
Table 3.1 Thermal study cases.....	64
Table 3.2 CSCM (MAT-159) material properties and model parameters .....	66
Table 3.3 Piecewise Linear Plasticity (MAT-24) material properties and model parameters.....	67
Table 3.4 FHWA Soil (MAT-147) material properties and model parameters.....	68
Table 3.5 Null (MAT-009) material properties and EOS parameters .....	69
Table 3.6 High Explosive Burn (MAT-008) material properties and EOS parameters.....	70
Table 3.7 Concrete and steel thermal material properties.....	72
Table 3.8 Concrete and steel strength reduction factors (Eurocode 2, 2004).....	77
Table 6.1 Bridge column damage categories .....	108
Table 6.2 Response of 750 mm, 1050 mm, and 1350 mm diameter columns, F90-I-B.....	116
Table 6.3 Pier column performance summary .....	126
Table 7.1 SikaWrap -301C Material Properties.....	133
Table 7.2 Sika CarbDur Rods Material Properties .....	135
Table 7.3 Material properties of the pier column (Sha and Hao, 2015) .....	137
Table 7.4 Material properties (Razaqpur et al. 2007).....	140
Table 7.5 Retrofitting Schemes Cases .....	145
Table 7.6 Retrofitted pier column performance summary.....	165
Table 8.1 Material Models.....	171
Table 8.2 Response of two-, three-, and four-column piers, F90-I-B.....	177
Table 9.1 Material properties of the bridge overpass .....	195
Table 10.1 Selected study parameters.....	234
Table 10.2 Study cases.....	236
Table 10.3 Normalized ESFs, all studied cases .....	250
Table 10.4 Summary of FE models used in validation.....	255
Table 11.1 Damage states and corresponding damage categories.....	267
Table 11.2 Isolated columns, post-fire impact and blast performance summary .....	269
Table 11.3 Performance of CFRP retrofitted columns, F90-I-B .....	273

## Acknowledgments

The authors would like to acknowledge the financial support of Mid-America Transportation Center (MATC) via a grant from the USDOT's University Transportation Centers Program (UTC). The authors would also like to express his gratitude to the University of Nebraska's Holland Computing Center (HCC) for providing computational resources needed to accomplish this study.

## Disclaimer

The contents of this report reflect the views of the authors, who are responsible for the facts and the accuracy of the information presented herein. This document is disseminated in the interest of information exchange. The report is funded, partially or entirely, by a grant from the U.S. Department of Transportation's University Transportation Centers Program. However, the U.S. Government assumes no liability for the contents or use thereof.

## Abstract

Given their close proximity to traffic and improper employment of protective systems, bridges and bridge piers are vulnerable to multi-hazard events triggered by vehicle collisions coupled with correlated and cascading events, such as explosions and fires. Despite recent catastrophic incidents that have highlighted the profound consequences of these extreme demands, including substantial damage, adverse economic impact, and loss of life, there has been a notable lack of research investigating the performance of bridges and bridge structural components under the aforementioned multi-hazards. Furthermore, current bridge design codes do not address these destructive events, instead assuming replacement of the pier columns or entire bridge will occur. Consequently, the performance of bridges under the combined effects of these extreme demands remains largely unidentified. As a result, more comprehensive studies are justified to study bridge resiliency under these multi-hazards to determine if, in certain situations, effective retrofitting schemes could be developed and deployed in lieu of replacement.

Consequently, LS-DYNA was utilized to simulate the behavior of prototype isolated, round, reinforced concrete columns and multi-column piers, and an existing bridge in Sidney, NE, under coupled vehicle collision and air blast before or after fire. A unique and advanced multi-step modeling approach that incorporates uncoupled implicit heat transfer analyses and explicit structural analyses was developed and validated against published test results. The study also examined the feasibility of various in-situ retrofitting schemes, including fiber reinforced polymers and soil infills, to improve bridge resiliency under combinations of vehicle collision, air blast, and fire. Furthermore, this study proposed an empirically-based, simplified, equivalent static force predictive equation can be used to conservatively represent substructure impact forces, for analysis and design, and as a companion assessment framework. The outcomes of this

study significantly contributed to the existing knowledge base, providing valuable insights, and improving bridge analysis and design methods that can be adopted by relevant codes and specifications.

## Chapter 1 Introduction and Background

### 1.1 Background

Highway bridges are commonly supported by substructure units consisting of reinforced concrete (RC) bridge piers with round columns. These units are often located adjacent to roads that pass beneath the structures they support. Historically, it has been demonstrated that bridge multi-hazard scenarios are commonly caused by vehicle collisions into bridge elements (e.g., piers), and correlated, cascading events, such as blasts and fires (T. Roy & Matsagar, 2021; Tilloy et al., 2019). The combined effect of these demands may produce severe damage, rapid loss of stiffness and strength, and potentially collapse, which may cause lengthy closures, economic impacts, and, most importantly, injury and loss of life.

Current bridge design codes, such as the *American Association of State Highway and Transportation Officials (AASHTO) Load and Resistance Factor Design (LRFD) Bridge Design Specifications (AASHTO 2020)*, do not address multi-hazards given their infrequent occurrence and because it is generally assumed that, after these events, replacement of components or the entire bridge will occur (Fang et al., 2021a; T. Roy & Matsagar, 2021). Bridge design codes ignore the effects of fire in their codified analysis and design procedures due to uncertainties associated with characterization and potential causes (Michael et al., 2013). In the absence of any guidance and given uncertainties that can include fire intensity, heating phase duration, source and location, flame height, heat release rate, and wind and other environmental conditions, effects of fire on bridge support elements have not been addressed and have received limited research attention.

As expected, pier support columns are inadequately designed for extreme demands resulting from vehicle collisions, blasts, and fires. However, it has been demonstrated that in many instances, bridges are more resilient to these extreme events than expected, and repair may

be possible (Buth et al., 2010; Giuliani et al., 2012; V. Kodur & Naser, 2021). As a result, more comprehensive research is justified investigating behavior of bridge elements under multi-hazard scenarios to better understand their resilience and see if effective retrofitting schemes could be developed and employed in lieu of replacement.

Many research studies have indicated that the response of RC structural elements to the combined effects of extreme temperatures and high strain rates must be considered. It was shown that at elevated temperatures, micro-cracks distribution coupled with concrete material degradation significantly influenced dynamic strength under high loading rates (Ruta, 2018a). In particular, it has been found that extreme temperatures from a fire mitigate concrete strength gains caused by high strain rates (L. Chen et al., 2015; Ruta, 2018a). This information indicates that if a bridge survives a fire, its dynamic response should be reassessed (W. Chen et al., 2016; Guo et al., 2017; Ruan et al., 2015). The response of columns subjected to fire before or after dynamic loads resulting from vehicle impact and air blast was investigated in this research study. Since vehicle collisions, air blasts, and fire could be concentrated around supporting units, studying pier column performance under these combined demands is warranted (Naser & Kodur, 2015).

A previous study in association with this research effort examined the response of single columns and multi-column piers under vehicle collision and air blast and identified that the critical demand sequence was when impact occurred prior to blast (Fang et al., 2021a). Accordingly, research presented herein focused on two multi-hazard sequences, namely, fire prior to and after an impact and blast event on isolated bridge columns, multi-column piers, and a representative bridge.

## 1.2 Problem Statement

In the absence of guidelines, specifications, and proven assessment tools, and given the limited research that addresses multi-hazards, research that better understands response and strived to improve highway bridge resiliency to cascading events, such as vehicle collisions, blasts, and fire, is needed. As a result, comprehensive studies are justified to understand the performance of bridge and bridge structural elements and potentially recommend feasible analysis tools, design procedures, and retrofitting techniques to improve their resiliency to these multi-hazards to avoid severe consequences that may cause extensive damage, collapse, closures, adverse economic impact, and, most importantly, potential injury and loss of life.

## 1.3 Objectives

The goal of this research study was to explore the performance of bridges and bridge components subject to multi-hazards and to investigate feasible retrofitting schemes and, if needed, recommend viable analysis and design procedures. Three-dimensional Finite Element (FE) models were created using LS-DYNA to simulate the response of prototype isolated pier columns and multi-column piers, and an existing bridge system in Sidney, NE under the combined effects of fire, vehicle collisions, and air blasts. Given the study encompassed multi-time scale problems involving fire, impact, and blast, a unique and advanced multi-step modeling approach, that incorporates uncoupled implicit heat transfer analyses and explicit structural analyses, was developed and validated against published test results. A detailed parametric study that involved various design parameters and loading scenarios was completed to better understand the performance of bridges and bridge structural components under the combined effects of the aforementioned extreme events. The study also examined the feasibility of various in-situ retrofitting schemes, including fiber reinforced polymers and soil infills, to improve

bridge resiliency under combinations of vehicle collision, air blast, and fire. Furthermore, an empirically-based, simplified, equivalent static force predictive equation, that can be used for analysis and design and to conservatively represent substructure impact forces, and a companion assessment framework were proposed. The outcomes of this study significantly contributed to the existing knowledge base, provided valuable insights, and improved bridge analysis and design methods that can be adopted by relevant codes, specifications, and real-world practical implementations.

#### 1.4 Scope

These objectives were addressed by:

- 1) Performing a detailed literature review of studies that investigated:
  - Reported bridge incidents associated with fire, vehicle collisions, and air blasts;
  - Material behavior and response of bridge components and other reinforced concrete structural elements subjected to multi-hazards that included fire, impact, and blast;
  - Available retrofitting techniques for improving resiliency of fire damaged bridge columns and substructure units when also subjected to impact and air blast; and
  - Existing design requirements of RC bridge columns under vehicle collisions and available Equivalent Static Force prediction models.
- 2) Developing and validating finite element modeling techniques for three-dimensional models of isolated, round, RC, bridge columns, multi-column piers, and a representative bridge.
- 3) Utilizing the validated FE models to simulate round column response to standard fire prior to or following simulated single unit truck (SUT) impacts and air blast, where studied parameters were selected based on findings from a previous study (Fang, 2020):

- a. Column diameters: 750 mm, 1050 mm, and 1350 mm.
  - b. SUT impact speed of 120 km/h.
  - c. Blast scaled distance,  $Z = 0.25 \text{ kg/m}^{1/3}$ .
- 4) Performing parametric studies that examined effects of various fire scenarios including full and half surface area fire exposures, and 60- and 90-minute fire durations, SUT impact speeds, air blast scaled distances, and significant design parameters on pier column response.
  - 5) Evaluating the performance of bridge components under post and pre-fire impact and blast by comparing damage propagation, final damage states, permanent sets, concrete spalling severity, residual axial capacities, and shear resistance for all demand scenarios and column diameters.
  - 6) Investigating the effectiveness of various retrofitting techniques to improve resistance of bridge columns subjected to fire, impact and blast.
  - 7) Assessing the feasibility of the equivalent static force (ESF) recommended by AASHTO-LRFD bridge design specifications to design bridge columns under vehicular impacts for the case where columns are exposed to fire prior to impact.
  - 8) Deriving an empirically-based and simplified equation that estimates ESF over a wide range of vehicle collision scenarios that involved intact and CFRP repaired fire-damaged bridge columns.
  - 9) A complementary ESF assessment framework was devised to facilitate realistic implementation of the derived equation. This framework serves as a powerful tool for practitioners and engineers to rapidly, and more accurately, determine if pier columns or varying conditions are susceptible to impact.

## Chapter 2 Literature Review

### 2.1 Introduction

Highway bridges are often supported by substructure units consisting of reinforced concrete (RC) bridge piers and round columns. These support units are usually located adjacent to roads that pass beneath the structures they support and, as a result, they could be subjected to extreme loading conditions resulting from natural hazards such as earthquakes, tornados, floods, and wildfires or manmade hazards such as vehicle collisions, blasts, and accidental or purposeful fires. These extreme demands can have severe consequences that may produce extensive damage, pronounced loss of strength and stiffness, and potential collapse. Highway bridge performance under the effects of earthquakes, vehicle collisions, and air blasts has been widely studied while limited attention has been given to fire even when reported incidents demonstrated that bridge fires have severe consequence (Chung et al., 2008; Timilsina et al., 2021). A survey conducted by Lee et al. that examined 1062 bridge failures in the U.S between 1980 and 2012 revealed that failures resulting from bridge fires exceeded those resulting from earthquakes and design defects (Lee et al., 2013). Another survey carried by the New York Department of Transportation (NYDOT) in 2008 reported that bridges are more likely to fail due to fire than earthquakes (V. Kodur et al., 2010; Wright et al., 2013). However, limited details on bridge fire safety and design requirements are available in current codes and provisions compared to what is provided for the analysis and design of bridges subject to earthquakes and vehicular impacts (Garlock et al., 2012; V. Kodur et al., 2010).

Reported bridge multi-hazard scenarios are attributed to vehicle collisions and correlated, cascading events, such as blasts and fires (T. Roy & Matsagar, 2021; Tilloy et al., 2019). Current bridge design codes, such as the *American Association of State Highway and Transportation Officials (AASHTO) Load and Resistance Factor Design (LRFD) Bridge Design Specifications*

(AASHTO 2020), do not address these multi-hazards given their infrequent occurrence and that, after these events, replacement of the support units or entire bridges often occurs (Fang et al., 2021a; T. Roy & Matsagar, 2021). As expected, support columns are under-designed for extreme demands resulting from vehicle collisions, blasts, and fires. However, it has been demonstrated that in many instances, bridges are more resilient to these extreme events than is widely assumed, in which no complete failure occurs, and repair may be possible (Buth et al., 2010; Giuliani et al., 2012; V. Kodur & Naser, 2021).

While response of bridge columns to the independent or combined effects from vehicle impact and air blast have been widely investigated, the consequences of fire in conjunction with these loads has not been widely studied. Detailed studies are needed to better understand performance of bridge columns subject to these multi-hazards and to develop techniques that could potentially improve column resiliency to these demands, which may mitigate costly and lengthy closures, traffic detouring and, most importantly, injury and loss of life.

The goal of this study is to investigate the performance of isolated bridge columns, multi-column piers and a complete bridge under combined effects of fire, vehicle impact, and air blast. The study also intends to explore and, if needed, develop, and recommend viable retrofit and repair techniques and investigate, develop, and recommend feasible analysis and design procedures. As a result, a comprehensive literature review that focused on studies that examined behavior and analysis of reinforced concrete materials and structural elements subjected to impact, blast, and fire, independently or in combination, current bridge design provisions and specifications, and innovative in-situ retrofitting schemes was completed.

## 2.2 Material Behavior and Structural Response under Fire, Impact, and Blast

### *2.2.1 Material behavior under impact and blast*

Loading rate has been shown to have a significant impact on response of RC structural elements subjected to dynamic loads, such as vehicle collision and air blast (Grote et al., 2001). As concrete crack development is relatively slow under static or quasistatic loads, high loading rate demands could restrain their formulation and, as a result, make concrete tends more resilient to higher loading rates. Under high loading rates, concrete confinement and inertial effects have been shown to improve its strength (Sudeep & Rao, 2019). Figure 2.1 illustrates how concrete strength varies with strain rate in both tension and compression. As demonstrated in this figure, concrete experiences considerable increase in strength at a given strain rate which is known as the “strain rate threshold”. This threshold is about  $3 \text{ s}^{-1}$  for concrete in tension and  $25 \text{ s}^{-1}$  for concrete in compression (Malvar & Crawford, 1998).

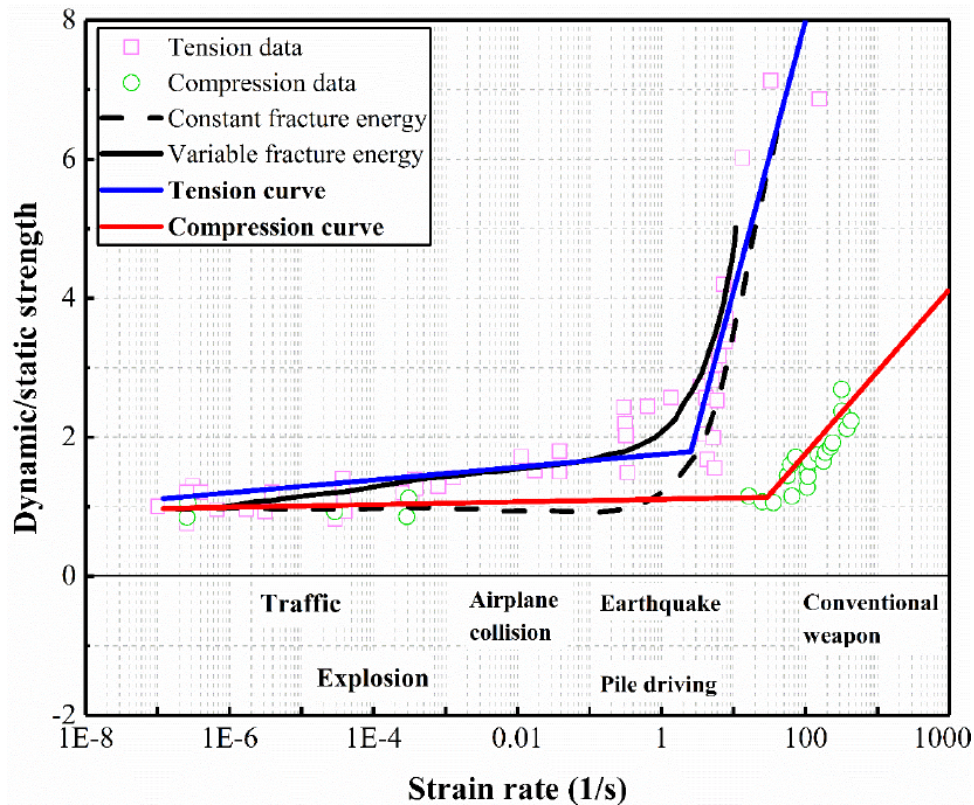


Figure 2.1 Relationship between concrete strength and strain rate (Malvar and Crawford 1998)

Similarly, steel reinforcement strength, which typically represents its yield and ultimate capacities, is highly influenced by variation in loading rate (Malvar, 1998). However, it has been demonstrated that the modulus of elasticity remains constant under various strain rates (Malvar, 1998). As depicted in Figure 2.2, both steel yield and ultimate strengths increase linearly with increasing strain rates. Yield strength is more sensitive to loading rate compared to ultimate strength, which indicates that steel reinforcement experiences considerable ductility reduction at higher load rates. This reduction in ductility is commonly referred to “high-velocity brittleness” (Malvar, 1998).

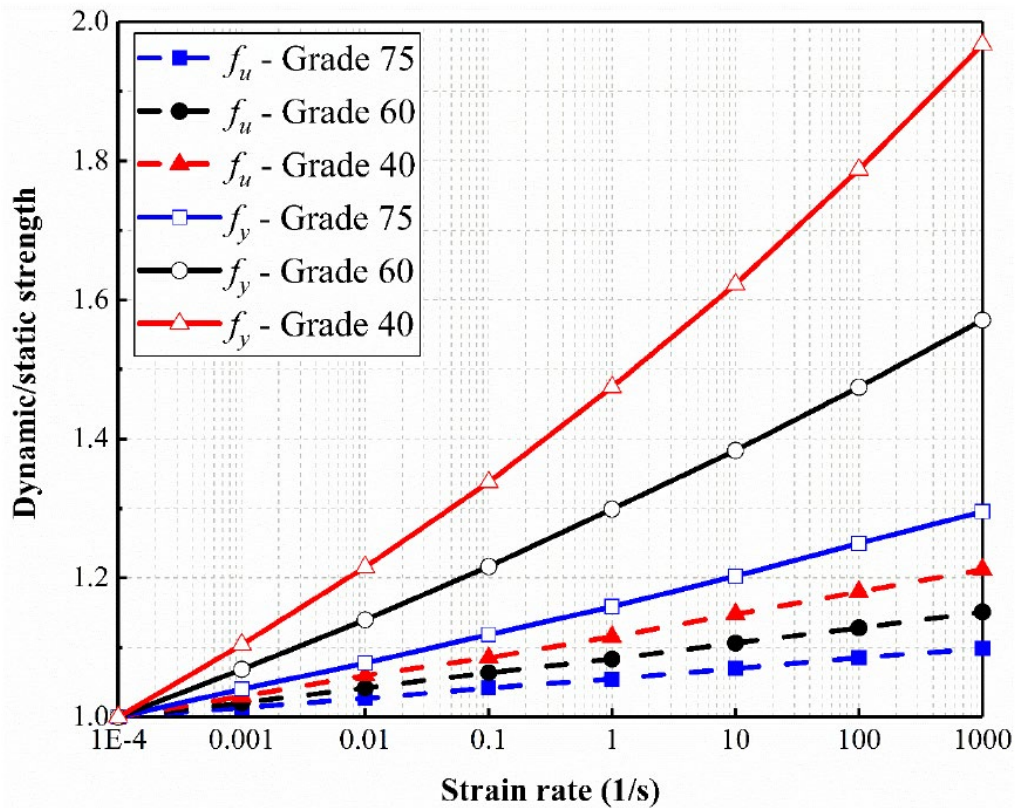


Figure 2.2 Relationship between steel strength and strain rate (Malvar 1998)

### 2.2.2 Material properties under fire and elevated temperatures

Although reinforced concrete structures perform well under fire exposure, they can also experience significant property changes due to high temperatures exposure (Fletcher et al., 2007). One of the most common effects of fire is compressive strength degradation over time. Reinforced concrete commonly is a combination of cement paste, aggregate, and steel reinforcement. As each of these materials have different properties and react differently to temperature variations, spalling (forcible removal of material from a member's surface), and surface cracking are important factors that can affect structural performance (Fletcher et al., 2007; Khoury, 2000).

Performance of reinforced concrete structures under effects of extreme temperatures is influenced by concrete and steel reinforcement mechanical and thermal properties (V. Kodur, 2014). As a result, variation of concrete and steel mechanical properties subjected under extreme temperatures has been extensively investigated in the literature (Khaliq & Kodur, 2012; V. Kodur, 2014; V. K. R. Kodur et al., 2012). Temperature dependent material properties are provided in many design codes, such as Eurocode 2, *Design of Concrete Structures, Part 1-2 General Rules, Structural Fire Design* (Eurocode 2, 2004), and American Society of Civil Engineers (ASCE), *Structural Fire Protection* (ASCE, 1992).

In the current study, concrete and steel reinforcement temperature dependent material properties were selected in accordance with Eurocode 2, Part 1-2. Figure 2.3 and Figure 2.4 illustrate relative variation in concrete and steel strength and moduli of elasticity under temperatures between 20° C and 1200° C. As shown in Figure 2.3, concrete experiences gradual reduction in compressive strength and modulus of elasticity with increasing temperature. Figure 2.4 indicates that steel reinforcement preserves its yielding strength at temperatures below 400° C and experience linear decrease in its elastic modulus when temperature exceeds 100° C.

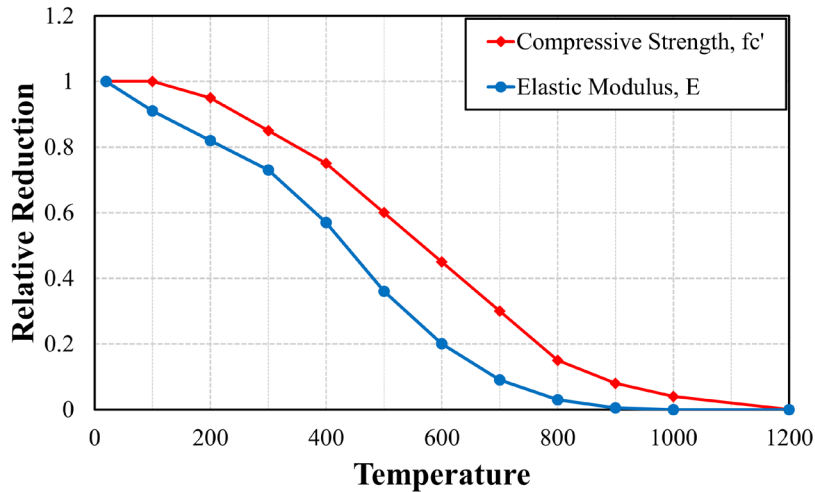


Figure 2.3 Relative compressive strength and elastic modulus of concrete as a function of temperature (reproduced from Eurocode 2, part 1-2)

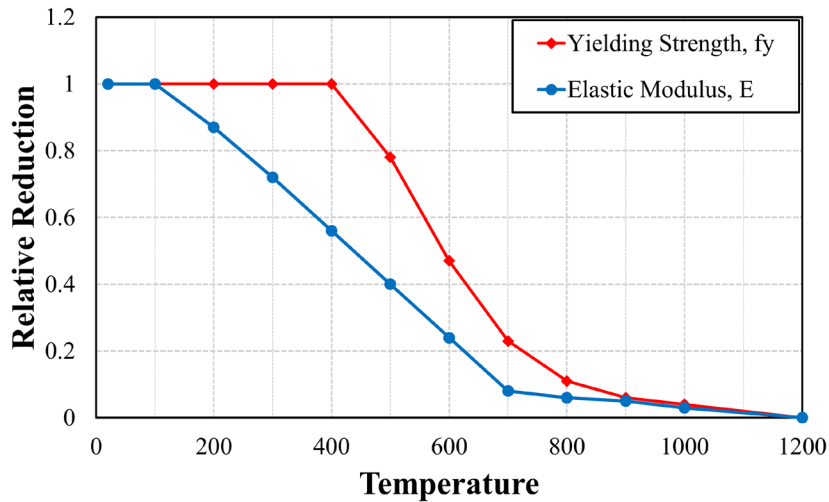


Figure 2.4 Relative yielding strength and elastic modulus of steel as a function of temperature (reproduced from Eurocode 2, part 1-2)

Variations in reinforced concrete element thermal properties are depicted in Figure 2.6, which indicates that concrete has low thermal conductivity and relatively high specific heat, which enhances its fire resistance (V. Kodur, 2014). As a result, providing adequate concrete cover is necessary for structural fire design to protect embedded steel reinforcement and maintain structural integrity (Fletcher et al., 2007). Concrete cover requirements are explicitly

provided by several design codes, such as Eurocode 2 (Buchanan & Abu, 2017; Eurocode 2, 2004).

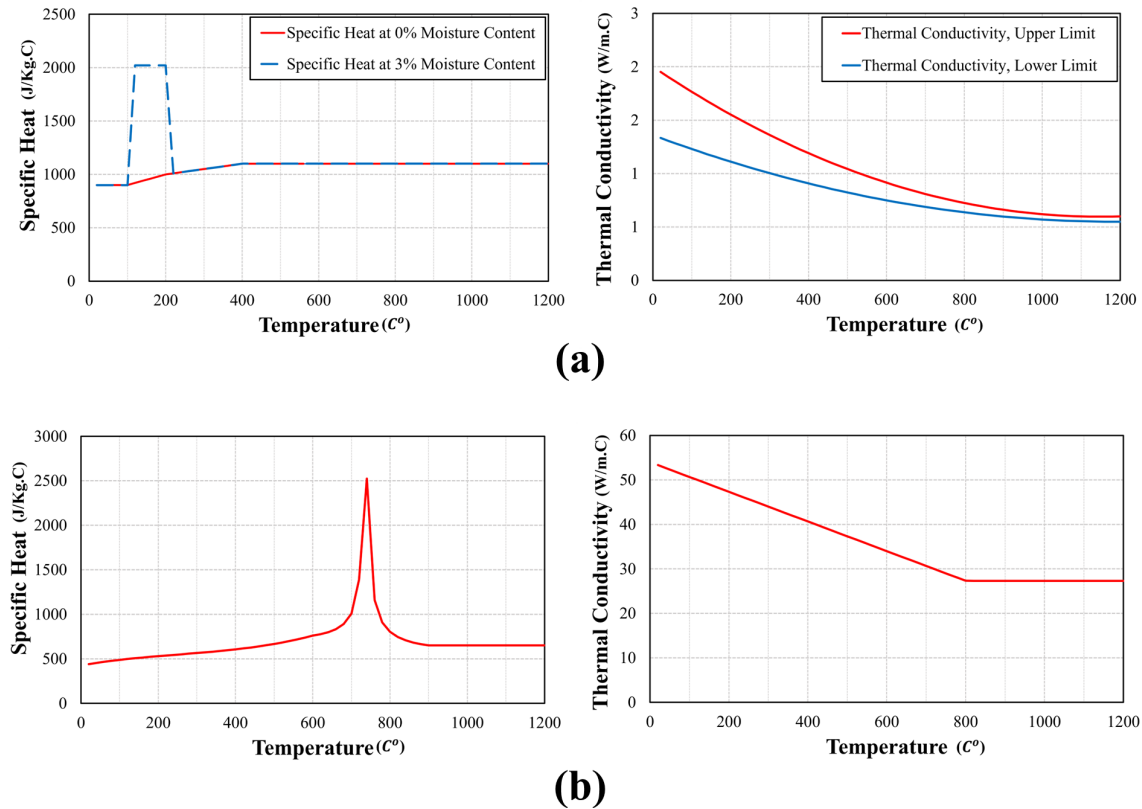


Figure 2.5 Thermal material properties: (a) concrete; (b) steel reinforcement (reproduced from Eurocode 2, part 1-2)

Studies of RC structural elements at elevated temperatures indicated that the distribution of micro-cracks coupled with concrete material degradation significantly influenced their dynamic strength of under high loading rates (Ruta, 2018a). In particular, it was found that extreme temperatures from a fire mitigated strength gains from high strain rates (L. Chen et al., 2015; Ruta, 2018a). A number of recent studies considered performance of concrete under the combined effects of extreme temperatures and high load rates (L. Chen et al., 2015; Echevarria et

al., 2016; Ruan et al., 2015; Ruta, 2018a). These studies indicated that concrete strength decreases significantly at high temperatures prior to increasing slightly under high load rates.

An experimental study carried out by Su et al. (2014) examined the effects of elevated temperature on concrete dynamic compressive mechanical properties (Su et al., 2014). In accordance with previous studies mentioned, the research revealed that concrete dynamic strength decreases with temperature, as illustrated in Figure 2.6, with more reduction of the dynamic increase factor (DIF), which is the apparent increase in strength under high loading rates, at 200° C due to pressure gradients developing from excess water evaporation.

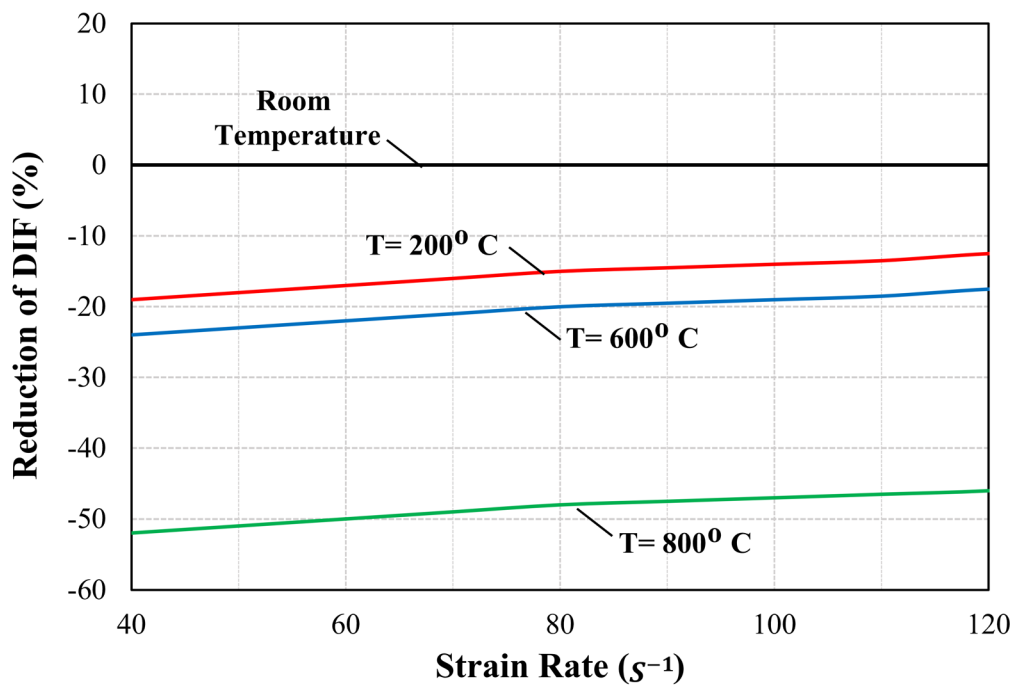


Figure 2.6 Reduction of dynamic increase factor (DIF) for concrete at various temperatures (Su, Xu, and Ren 2014)

## 2.3 Highway Bridge Vehicle Collisions

### *2.3.1 Vehicle collisions with bridge elements - examples*

Even though vehicular impacts with bridge components could lead to severe damage and bridge collapse, current design codes and specifications treat vehicular collision as a rare event when designing pier columns (Buth et al., 2010). In Corpus Christi, Texas in 2004 a tanker truck moving at a speed of 88.5 km/h collided with the outermost column in a three-column pier supporting a reinforced concrete bridge passing over I-37 (Figure 2.7) (Buth et al., 2010). The 750 mm pier column failed due to severe spalling near its ends accompanied by longitudinal reinforcement buckling and fracturing. As shown in the figure, the bridge did not collapse.

In 2005, a bridge pier passing over I-35 in Red Oak, Texas was impacted by a tractor-trailer moving at 97 km/h, as shown in Figure 2.8 (Buth et al., 2010). The 750 mm diameter pier column exhibited concrete surface cracking that propagated to the non-impact column face and extensive shear cracking with longitudinal steel reinforcement buckling observed at its top. Again, the bridge did not collapse.

Another incident happened in Big Springs, Nebraska, where bridge collapse did occur after a semitrailer truck collided with a reinforced concrete bridge overpass and a second truck traveling in the opposite direction impacted one of the pier columns, as shown in Figure 2.9 (Wehbe et al., 2017). Other representative incidents that involved vehicle collisions with bridge structural elements resulting in unsafe conditions, loss of integrity, and collapse are provided in the literature (Gomez, 2014; Maghiar et al., 2017; Sharma et al., 2012).



Figure 2.7 Tanker truck pier collision, I-37, Corpus Christi, TX (Buth et al. 2010)



**(a) Tractor-trailer truck collision**



**(b) Failure mode**

Figure 2.8 Tractor-trailer pier collision, I-35, Red Oak, TX (Buth et al. 2010)



**(a) Bridge collapse**



**(b) Truck collision**

Figure 2.9 Truck collision, I-80, Big Springs, NE (Wehbe et al., 2017)

These representative events reveal that vehicular collisions could induce severe damage, failure, and potentially collapse of structural elements or the entire bridge system. These consequences may lead to lengthy closures, costly repair or replacement, and loss of life and property.

### *2.3.2 Vehicle collisions with bridge elements - research*

Several research studies and surveys have indicated that vehicle collisions are one of the main causes of bridge failures in the U.S. A survey conducted by Lee et al. that examined 1062 U.S bridge failures between 1980 and 2012 revealed that the majority were caused by floods and vehicle collisions (Lee et al., 2013). Additional research carried out by Wardhana and

Hadipriono investigated the causes of 503 bridge failures in the U.S between 1989 to 2000. This study indicated that floods, scouring, and vehicular collisions were the leading causes of bridge failures, with about 12% of bridges failing due to vehicle collision (Wardhana & Hadipriono, 2003).

Typically, U.S. highway bridges are designed following AASHTO LRFD bridge design specifications and state Department of Transportation (DOT) guidelines. Vehicle collision is addressed in pier column design by introducing an equivalent transverse static load applied at a certain distance from the column base. According to the 9<sup>th</sup> edition of *American Association of State Highway and Transportation Officials (AASHTO) Load and Resistance Factor Design (LRFD) Bridge Design Specifications*, RC pier columns should be designed for an equivalent static force (ESF) of 600 Kips (2,670 kN) located 5 ft (1.52 m) above the ground, with an impact angle varying between 0 and 15 degrees with respect to the edge of the pavement (AASHTO 2020). This equivalent static load was identified based on full-scale tests of 910-mm diameter rigid columns impacted by a 36,300-kg tractor-trailer moving at 80.5 km/h (Buth et al., 2010, 2011).

Response of bridge columns to vehicle impact has been widely investigated. Sharma et al. utilized LS-DYNA to examine response of RC bridge pier columns to vehicle collisions (Sharma et al., 2015). A performance-based framework that involved analysis and design of bridge columns subjected to vehicle collisions was developed and three performance levels identified. Performance levels were then calibrated using probabilistic models initially developed to estimate column demands and shear capacities corresponding to vehicular impact. Demand and resistance factors were proposed to achieve a desired level of performance.

El-Tawil et al. used LS-DYNA numerically investigated RC bridge pier performance under truck impacts (El-Tawil et al., 2005). Two vehicle models, a 14 kN Chevy C-2500 pickup truck and a 66-kN Ford F800 single unit truck (SUT), were used to apply the impact loads. A parametric study that examined various impact speeds and pier geometries was completed to investigate the feasibility of the ESF provided in the 2002 *American Association of State Highway and Transportation Officials (AASHTO) Load and Resistance Factor Design (LRFD) Bridge Design Specifications* for columns under vehicle impacts. Simulation results indicated that the ESF underestimated actual effects (AASHTO 2020).

Agrawal et al. analytically examined dynamic response of RC bridge piers impacted by a SUT (Agrawal et al., 2013). Three dimensional numerical models of a three-span bridge supported by three-column piers and pile foundations were created in LS-DYNA. A parametric study examined the effects of various impact speeds, impact angles, and pier column diameters. Pier column performance was assessed based on damage extent, mode of failure, and a damage ratio that corresponded to the ratio of the peak impact load to the column's shear capacity.

Gomez and Alipour also utilized LS-DYNA to study performance of RC bridge piers subject to vehicular collisions (Gomez & Alipour, 2014). A parametric study was conducted that examined the effects of impact speed, number of pier columns, column diameter, reinforcement detailing, and pile cap thickness on bridge column response to vehicle collisions. Study results indicated that the number of columns and their diameter had a pronounced effect on response and failure modes. Lower displacements and larger shear resistance was observed for larger diameter columns and two-column piers.

Abdelkarim and ElGawady carried out an extensive parametric study using LS-DYNA to examine ESF and peak dynamic force (PDF) effectiveness for bridge column design under

vehicle collisions (Abdelkarim & ElGawady, 2017). Several parameters were involved in this study and included concrete compressive strength, steel reinforcement ratio, shear reinforcement spacing, column diameter, boundary conditions, axial load, strain rate, and vehicle velocity. Three approaches were used to examine ESF effectiveness. In the first approach, the ESF was estimated so that it produced the same displacement caused by a vehicle collision at the point of impact. The second approach calculated the ESL in accordance with Eurocode 1: *Actions on structures – Part 1–1: General actions – Densities, self-weight, imposed loads for buildings* (E. 1991-1-1 Eurocode 1, 2002). The third approach defined the ESF as the Peak of the Twenty-five Milli-Second Moving Average (PTMSA). Estimated ESFs were compared to the 600 kips force from the AASHTO-LRFD (AASHTO 2020) and results demonstrated that the 600 kip static force was sufficient for design of columns under heavy vehicle and/or high-speed impacts and was conservative for light vehicle and/or low-speed impacts.

## 2.4 Highway Bridges Air Blasts

### *2.4.1 Highway bridge blasts - examples*

The 2001 terrorist attack on the World Trade Center highlighted the susceptibility of critical structural systems, which includes bridges, to blasts, making them accessible targets whose damage or destruction may impact human lives and the economy (Yi et al., 2014b, 2014a). However, limited details on analysis and design of bridge structural elements subjected to blast loads are available in current design codes (Yi et al., 2014a). As a result, bridge structural units could be under-designed for these extreme demands that may produce extensive damage, pronounced loss of strength and stiffness, and potential collapse.

In 2007, Bay Bridge spans in Emeryville, California, collapsed after a tanker truck explosion (Bay City News, 2007). As shown in Figure 2.10, the explosion caused the upper deck

of the ramp connecting highway 580 to I-80 to collapse onto the lower deck. In 2014, a tanker truck traveling on I-65 near the Peytonsville bridge overpass in Franklin, Tennessee collided with a pier column and exploded, as shown in Figure 2.11 (The Tennessean News, 2014). According to the Tennessee Department of Transportation, the explosion resulted in serious structural damage and extended roadway closures.

In 2013, at least eleven people were killed after a truck carrying fireworks exploded beneath an expressway bridge in China (Stochino & Tattoni, 2013). As shown in Figure 2.12, more than 80 m of the bridge collapsed and most of the substructure units were severely damaged. This extreme event significantly impacted traveling traffic.



(a)



(b)

Figure 2.10 Truck tanker explosion and bridge collapse I-80, Emeryville, CA (Bay City News, 2007)



(a)



(b)

Figure 2.11 Truck tanker explosion, I-65, Franklin, TN (The Tennessean News, 2014)



(a)



(b)

Figure 2.12 Truck carrying fireworks explosion, China (Stochino and Tattoni 2013)

## 2.4.2 Highway bridge blasts - research

### 2.4.2.1 Blast loads

Blast load intensity is proportional to the TNT equivalent explosive charge weight ( $W_{TNT}$ ) and distance between the charge center and the target ( $R$ ). According to the Hopkinson or the Cube-root scaling approach, these two variables are usually represented using a single quantity known as the scaled distance ( $Z$ ), as expressed in Equation 1 (Castellano et al., 1982; Sudeep & Rao, 2019). Research and testing have indicated that this law is valid only for scaled distances greater than  $0.16 \text{ m/kg}^{1/3}$  (Department of Defense, 2008).

$$Z = \frac{R}{\sqrt[3]{W_{TNT}}} \quad \text{Equation. 1}$$

As shown in Figure 2.13, the scaled distance can be used to determine shock wave parameters that characterize blast loads. In addition, reflected and incident pressures resulting from both hemispherical and spherical blasts can be approximated.

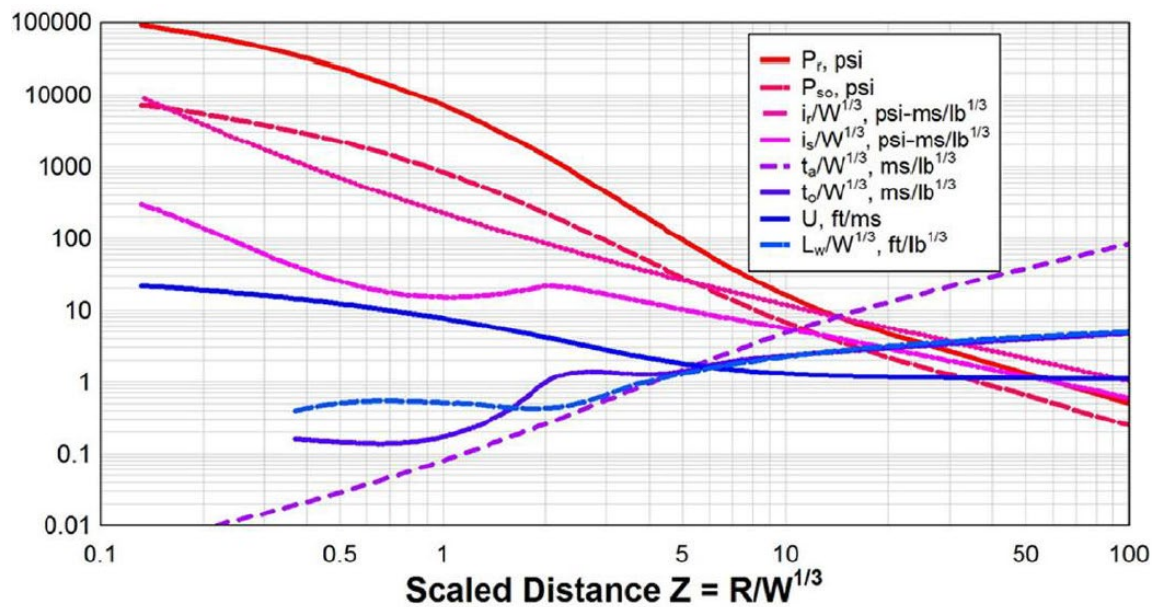


Figure 2.13 Shock wave parameters for TNT explosions (Department of Defense 2008)

Detonation is due to a rapid chemical reaction that suddenly releases enormous energy and shock waves traveling at high speed through the surrounding air domain. Consequently, an intensive pressure higher than the ambient air pressure, called the “overpressure,” is produced. Typically, a shock wave overpressure-time history consists of positive and negative phases, as shown in Figure 2.14. The positive phase ( $P_{so}$ ) overpressure “pushes” on the structure while the

overpressure created by the negative phase “pulls” on the structure ( $P_{so-}$ ) (Department of Defense, 2008).

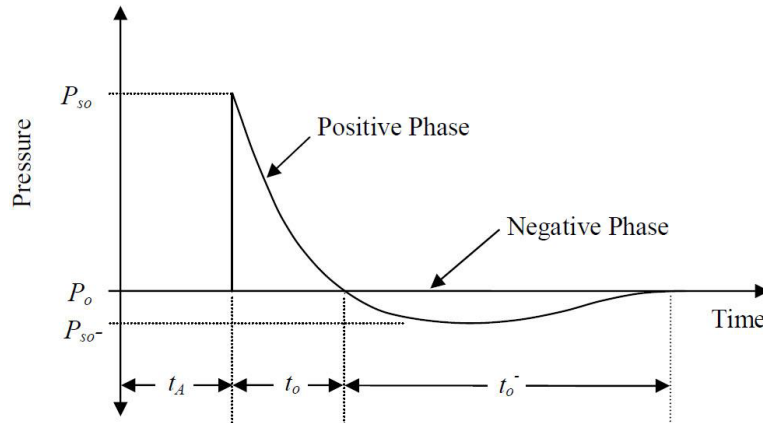


Figure 2.14 Idealized pressure-time history of an explosive in free air (Williams 2009)

Shock waves produced by an explosion are usually classified into incident and reflective waves. The incident wave is produced when an explosive charge detonates in open air. The reflective wave is created when an incident wave hits a surface of a structure or an obstacle and reflected off the surfaces (Department of Defense, 2008). Reflected and incident waves pressure can be correlated based on the angle of reflection ( $\alpha$ ), as illustrated in Figure 2.15 (Williamson, 2010). In this figure,  $C_{r\alpha}$  corresponds to the ratio between peak reflected and incident pressures.

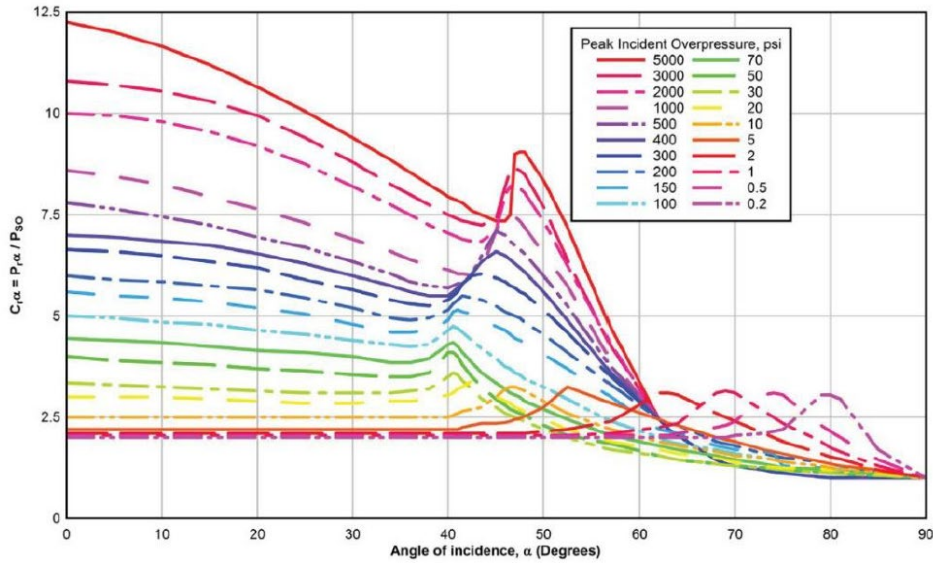


Figure 2.15 Effect of angle of incidence on reflected pressure coefficient (Williamson 2010)

Blast resistant structural design air blasts are classified as: (i) contact blasts; (ii) close-in blasts; and (iii) planar-wave blasts, as shown in Figure 2.16 (Williamson, 2010). For contact blasts, the target structure undergoes a highly intensive impulsive load. Close-in blasts generate non-uniform hemispherical or spherical shock waves while planar-wave blasts are generated when the standoff distance is relatively large, which produces less intensive, uniformly distributed loads. Based on these loading categories, three demand ranges are commonly utilized to design structures under blast loads, as shown in Figure 2.17, where the selection of a range is controlled by the ratio between the natural period of the structure ( $t_m$ ) to the explosion duration ( $t_o$ ) (Department of Defense, 2008; Williamson, 2010). Accordingly, close-in blasts with high intensity impulsive load are utilized when their affects are considered in bridge design (Williamson, 2010).

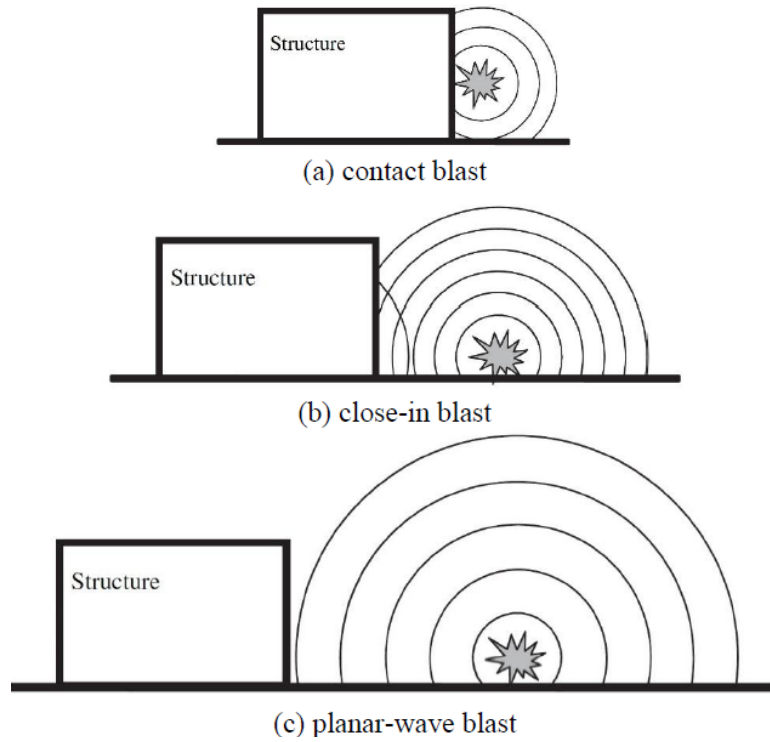


Figure 2.16 Blast-loading categories (Williamson 2010)

<b>Pressure design range</b>	High	Low	Very Low
<b>Design load</b>	Impulse	Dynamic (Pressure-time)	Quasi-static (Pressure)
<b>Incident pressure</b>	$\gg 100$ psi	$< 100$ psi	$< 10$ psi
<b>Pressure duration</b>	Short	Intermediate	Long
<b>Response time</b>	Long	Intermediate	Short
<b>Relationship of <math>t_m/t_0</math></b>	$t_m/t_0 > 3$	$3 > t_m/t_0 > 0.1$	$t_m/t_0 < 0.1$

Figure 2.17 Pressure design ranges (Department of Defense 2008)

#### 2.4.2.2 Effects of blast loads on bridges and bridge elements

Highway bridges are infrequently designed to directly resist air blast demands using bridge design codes and specification criteria. Instead, seismic design and detailing procedures are recommended to address blast loads by several researchers (Williamson, 2010; Winget, 2003). It has been shown, however, that blast-resistant structural design processes could be utilized to design bridges under air blast (Department of Defense, 2008).

A comprehensive study was conducted for the National Cooperative Highway Research Program (NCHRP) to investigate bridge blast load analysis and design (Williamson, 2010). This detailed study served as a precursor for future research studies that focused on air blasts on bridges by providing a general overview of the response of bridge columns to blast loads and establishing broad guidelines for blast-resistant design. The study classified the design approach into three categories based on the scaled standoff distance ( $Z$ ). The first category corresponded to  $Z$  larger than  $1.19 \text{ m/kg}^{1/3}$  which did not require special design considerations. The second category recommended using seismic design procedures and detailing for  $Z$  between 0.6 and  $1.19 \text{ m/kg}^{1/3}$ . The final category was for air blasts with  $Z$  less than  $0.6 \text{ m/kg}^{1/3}$ , which corresponded to the most severe threats and required single-degree-of-freedom (SDOF) analyses of bridge columns to ensure appropriate ductility and support rotational freedom.

Williams investigated response of RC bridge columns to air blast through a series of reduced scale experimental work and finite element analyses (Williams, 2009). The experimental study focused on identifying failure modes by varying blast load intensity. LS-DYNA was utilized to model bridge column response. Research findings demonstrated that for a given scaled distance, square bridge columns were more susceptible to blast loads than round columns. A

simplified approach was proposed to identify failure bridge column mechanisms under the effects of air blast.

Yi et al. (2013) used LS-DYNA to numerically examine performance of a three-span highway bridge subjected to air blast (Yi et al., 2014b, 2014a). A Hybrid Blast Load (HBL) modeling approach was utilized to simulate the blast and was validated against experimental results. Simulation results indicated that localized damage in bridge structural elements resulting from blast loads could lead to complete collapse of an entire bridge system.

Tang and Hao (2010) investigated the response of a cable-stayed bridge subjected to air blast (Tang & Hao, 2010). Damage and failure modes resulting from a TNT charge weighing 1000 kg and placed 1 m above the bridge deck were examined using LS-DYNA. Results indicated that a scaled distance ( $Z$ ) of  $1.2 \text{ m/kg}^{1/3}$  severely damaged the bridge deck but did not result in bridge collapse.

Fujikura et al. (2008) experimentally studied the performance of concrete-filled, steel tube (CFST) bridge columns under air blast (Fujikura et al., 2008). Reduced scale multi-pier columns were tested to examine the capability of CFST columns to resist blast loads. Results indicated that prototype pier columns exhibited more ductile response and enhanced resistance compared to the conventional RC columns.

## 2.5 Highway Bridge Fires

### *2.5.1 Bridge fires - examples*

Although fires are less frequent than vehicle collisions into bridge elements, they can have serious consequences. It has been revealed by several research studies that the number of reported bridge fires significantly increased recently (V. Kodur & Bhatt, 2016; V. Kodur & Naser, 2021). A database documenting 1746 cases of bridge collapse between 1960 and 2013

was created by the New York Department of Transportation (NYDOT) (Woodworth, 2013) and collapse due to fire exceeded other causes of common concern, such as construction and design deficiencies, earthquakes, and geotechnical reasons. While several bridge collapse events occurred in urban areas, most collapse events were reported for small rural bridges. The survey also indicated that fire sources were not well identified, with 76% of reported causes being unknown. A study conducted by Peris-Sayol et al. examined causes of 154 bridge fires in the U.S between 1998 and 2015 (Peris-Sayol et al., 2017). The study categorized causes as follows:

1. Vehicles including cars, trucks, and tankers: corresponded to fire resulting from vehicle crashes in the vicinity of bridges, overturned vehicles, collisions with a bridge component, and the ignition of carried goods.
2. Electrical problems.
3. Stored materials.
4. Forest or natural fires.
5. Arson.
6. Others, which included causes that did not fit in the other categories, such as formwork fires.

Another database established by the National Highway Traffic Safety Administration (NHTSA) and the Fatal Accident Reporting Service (FARS) reported fatal bridge collisions occurring between 1994 and 2008 (Michael et al., 2013). The database indicated that 10% of collisions with bridge structural components produced a fire.

In 2007, a fatal fire incident occurred in Oakland, California, when a tanker carrying more than 32 m<sup>3</sup> of fuel overturned in the vicinity of a bridge interchange connecting I-80 and I-880 (Bulwa & Fimrite, 2007). It was estimated that the steel bridge girders and bolted

connections were suddenly exposed to temperatures of 1100° C, which resulted in the collapse of two spans of the bridge onto the highway underneath within 22 minutes (Figure 2.18). The incident resulted in significant traffic detours and closures for weeks and the replacement cost was estimated to be \$10 million.

In July, 2009, a large fire was produced when a tanker transporting 50 m<sup>3</sup> of crashed into a car and exploded under the Hazel Park bridge on I-75 near Detroit, Michigan (Guthrie et al., 2009). As shown in Figure 2.19, the overpass collapsed onto the freeway, with the collapse happening within 30 minutes of the accident due to intense fire exposure. Preliminary inspections indicated that the entire nine-mile bridge should be reconstructed, and the freeway required major repairs before reopening.



Figure 2.18 Highway bridge collapse as a result of fire, Oakland, CA (Bulwa and Fimrite 2007)



Figure 2.19 Hazel Park bridge overpass collapse as a result of fire, Detroit, MI (Guthrie, Goodwill, and Hicks 2009)

In 2011, a tanker truck carrying 34 m<sup>3</sup> of gasoline caught fire under the Paramount Boulevard bridge in Montebello, Los Angeles, CA, as illustrated in Figure 2.20 (Giuliani et al., 2012). It was reported that the fire lasted for several hours and resulted in significant damage to the reinforced concrete bridge deck. Post-fire evaluations indicated that both the eastbound and westbound overpass bridges should be replaced, and that substructure needed some levels of repair.



Figure 2.20 Tanker truck fire under Paramount Boulevard bridge in Montebello, Los Angeles, CA (Giuliani, Crosti, and Gentili 2012)

In 2017, a large fire initiated underneath a bridge on I-85 near Atlanta, GA when large PVC pipes stored under ignited (V. Kodur & Naser, 2021). As reported by the Georgia Department of Transportation, the bridge was exposed to a peak temperature of 1100° C, which resulted in a collapse of 30 m long span and significant damage to adjacent span prestressed concrete girders and reinforced concrete piers, as shown in Figure 2.21. Post-fire inspections revealed that major repairs were required, and losses were estimated to be \$10 million.



Figure 2.21 Post fire damage to I-85 bridge, Atlanta, GA (Venkatesh Kodur and Naser 2021)

In 2004, a car crashed into a tanker truck transporting more than 32 m<sup>3</sup> of diesel fuel, which resulted in an explosion and severe fire 10 m underneath the Wiehltal highway bridge in Rhine-Westphalia, Germany, as shown in Figure 2.22 (Giuliani et al., 2012). It was believed that fire temperatures reached 1200° C and, although the bridge did not collapse, 60 m of the deck exhibited significant deformation.



Figure 2.22 Tanker truck accident on the Wiehltal Bridge, Rhine-Westphalia, Germany (photo by C. Buschorn, 26 Aug. 2004, public domain image)

Other bridge fire incidents reported in the literature are summarized in Table 2.1 (Garlock et al., 2012; V. Kodur et al., 2010; V. Kodur & Naser, 2021; Peris-Sayol et al., 2017).

Table 2.1 Catastrophic bridge fires

Location	Year	Cause	Damage
Big Four Bridge, Louisville, Ky, USA	2008	<i>Electrical problem in the lighting system</i>	<i>Minor structural damage</i>
Bill Williams River Bridge, AZ, USA	2006	<i>Tanker carrying gasoline overturned</i>	<i>Minor structural damage</i>
I-95 Howard Avenue Overpass in Bridgeport, CT, USA	2003	<i>Car crashed into a tanker transporting heating oil</i>	<i>Complete collapse of the southbound and partial collapse of northbound</i>
I-80W–I-580E ramp in Emeryville, CA, USA	1995	<i>Gasoline tanker crashed</i>	<i>Moderate structural damage</i>
I-375 bridge, MI, USA	2015	<i>Gasoline tanker crashed</i>	<i>Significant damage in the concrete deck</i>
I-15 at Cajon, CA, USA	2014	<i>Framework caught fire</i>	<i>Bridge collapse</i>
Bridge over freeway 60, Los Angeles, CA, USA	2011	<i>Tanker carrying gasoline caught fire under the bridge</i>	<i>Significant damage resulted in bridge replacement</i>
Zhuoshui Fengyu Bridge, China	2013	<i>Unknown</i>	<i>Wooden bridge collapse</i>
Rio–Antirrio bridge, Greece	2005	<i>Lightning strike</i>	<i>Unknown</i>
Stop Thirty Road, State Route 386 Nashville, TN, USA	2007	<i>Fuel tanker caught fire under the bridge</i>	<i>Minor structural damage</i>
Belle Isle Bridge in NW Expressway, Oklahoma City, OK, USA	2006	<i>A truck collided the bridge</i>	<i>Minor structural damage</i>
Bridge over the Norwalk River near Ridgefield CT, USA	2005	<i>Gasoline tanker caught fire and burned out on the bridge</i>	<i>Bridge deck was replaced</i>
I-20/I-59/I-65 interchange in Birmingham, AL, USA	2002	<i>Gasoline tanker crashed</i>	<i>Main span was replaced</i>
Mezcala Bridge, Mexico	2007	<i>A truck collided with two school buses and produced fire</i>	<i>Failure in one stay cable</i>
Highway 57, Dormagen, Germany	2012	<i>Plastic stored under the bridge caught fire</i>	<i>Bridge was replaced</i>
Pont Mathilde, Rouen, France	2012	<i>A tanker overturned and caught fire under the bridge</i>	<i>Bridge was partially replaced</i>
Ed Koch Queensboro Bridge, NY, USA	2013	<i>Tractor trailer caught fire</i>	<i>Severe damage in two stringers</i>
Overpass in El Cairo, Egypt	2014	<i>Gas cylinders stored under the bridge exploded</i>	<i>Three sections of the bridge collapsed</i>
I-65/Peytonsville Road, Franklin, TN, USA	2014	<i>A gasoline tanker impacted the bridge pier and exploded</i>	<i>Severe damage</i>
I270/I-70 Ramp, Ohio, USA	2015	<i>A tanker carrying ethanol caught fire</i>	<i>Significant concrete spalling</i>
Interchange I-85/route 23-322, Harrisburg, PA, USA	2013	<i>A diesel tanker crashed</i>	<i>Bridge was replaced</i>

### 2.5.2 Bridge fires - research

Information provided in Section 2.5.1 indicates that bridge fires have various sources. Each type of fire is characterized by a unique heat release rate, with extreme temperatures attained over different time durations. Irrespective of the source, standard fire curves established based on real fires provide temperature-time relations (Khoury, 2000). These curves are commonly used for fire testing, design, and analysis, including numerical simulations, to replicate actual fire scenarios (Buchanan & Abu, 2017; Hurley et al., 2015).

The most common fire curves for thermal analyses are the Hydrocarbon, RWS, RABT-ZTV, ASTM E119, and ISO-834 curves. Hydrocarbon curves are characterized by high temperature change rates in American and European standards (Eurocode 2, 2004, p. 1; Hurley et al., 2015; NFPA, 2017). In these curves, temperatures exceed 1000 °C in less than 10 minutes and continue to increase for the duration of the fire (V. Kodur et al., 2010). This approach might not be realistic for gasoline fires, a common situation for bridges, since the fuel source will eventually be consumed (V. Kodur et al., 2010). The RWS and RABT-ZTV curves are commonly used to characterize tunnel fires, which occur under different conditions from bridge fires with both fire curves mimicking a rapid temperature rise with a sustained, extremely high, temperature plateau (Y. Z. Li & Ingason, 2010; NFPA, 2017). The RWS curve simulates fire caused by tankers carrying gasoline in tunnels and extends for two hours. The RABT-ZTV fire curve represents a less severe tunnel fire and accounts for fire decay (Khoury, 2000). The most widely used fire curves are ISO 834 and ASTM E119, which were derived from full and reduce scale fire tests under supervision of international technical committees (ASTM, 2007; Buchanan & Abu, 2017; Hurley et al., 2015; ISO, 1999; Y. Z. Li & Ingason, 2010). Unlike other fire curves, ISO 834, and ASTM E119 curves have slower temperature rise rates as they characterize

fires resulting from burning materials other than chemicals and petroleum products, such as construction materials and building components. Figure 2.23 compares the five standard curves discussed herein.

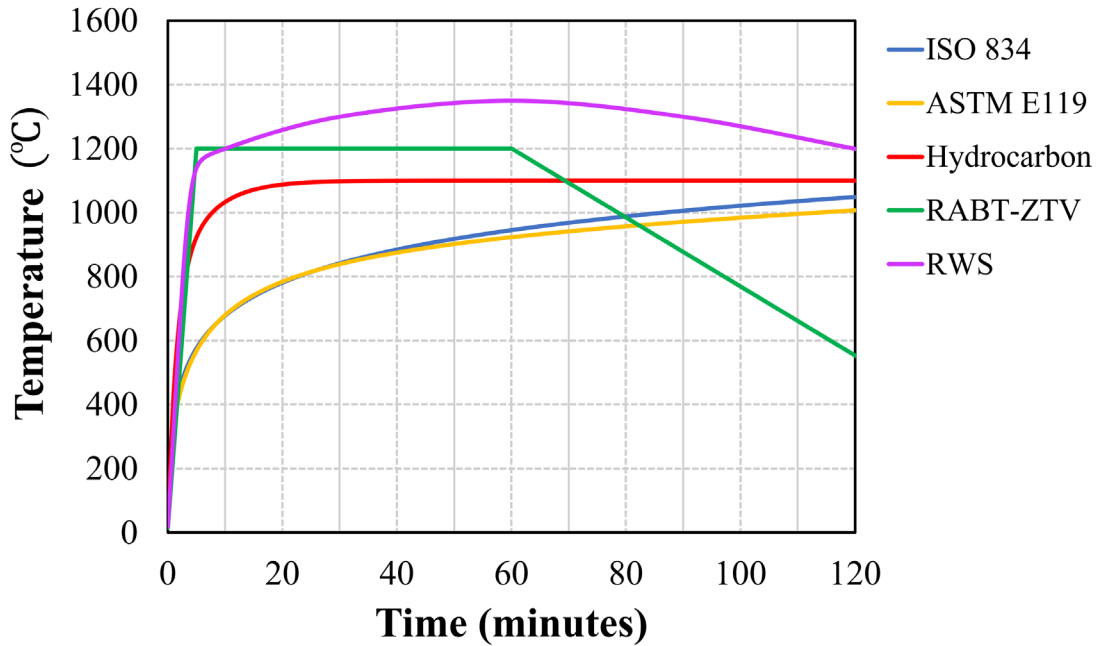


Figure 2.23 The most common standard fire curves

In comparison to standard fire curves, real fires can produce higher temperatures, though they are rarely sustained due to source consumption and fluctuations in intensities (Khoury, 2000). Therefore, standard fire curves could represent a severe fire but not the most critical fire scenario. As there is no specific guidance concerning how fire curves should be selected for modeling bridge fires, and given uncertainties associated with incorporating key fire characteristics in numerical analyses, researchers often adopt their own approaches (Garlock et al., 2012; V. Kodur et al., 2010; Y. Z. Li & Ingason, 2010). Given that the intention of the current study was to examine the effects of fires that could result from events beneath the bridge

other than a vehicle collision, the ISO-834 curve was selected as it has been consistently adopted in previous numerical and experimental studies (W. Chen et al., 2019; Hurley et al., 2015; ISO, 1999; Jin et al., 2021; Kakogiannis et al., 2013; Ožbolt et al., 2019; Ruan et al., 2015; Ruta, 2018b).

While bridge design codes such as *American Association of State Highway and Transportation Officials (AASHTO) Load and Resistance Factor Design (LRFD) Bridge Design Specifications* ignore the effects of fire, it is a major design consideration for buildings and tunnels (AASHTO 2020; Guillem Peris-Sayol et al. 2017). Eurocode 2, *Design of Concrete Structures, Part 1-2 General Rules, Structural Fire Design*, provides details for building structural fire design (Eurocode 2, 2004; Garlock et al., 2012). Detailed procedures for tunnel fire design are available in the *National Fire Protection Association: Standard for Road Tunnels, Bridges, and Other Limited Access Highways (NFPA 502)* (NFPA, 2017). The publication contains some broad guidelines for bridges over 300 m but does not explain how those bridges should be analyzed or protected. According to Giuliani et al., bridge design codes do not address fire design due to uncertainties associated with characterizing fires and potential causes (Michael et al., 2013). In the absence of any guidance and given uncertainties that define fire intensity, such as the duration of the heating phase, source and location, flame height, heat release rate, and wind and other environmental conditions, fire effects on bridge structural elements are largely ignored.

Nasser and Kodur (2015) developed a simplified statistical approach to categorize bridges based on vulnerability to fire hazards using data obtained from fire events (Naser & Kodur, 2015). A fire-based importance factor was derived and used to identify expected bridge fire risk. Five key characteristics that affect bridge performance under fire, including geometric

configuration, material properties, fire likelihood, traffic demand, economic impact, and anticipated fire losses, were used to derive an importance factor. Study results indicated that the proposed factor can be used as a practical tool to quantify fire risk in existing and new bridges.

Nahid examined the response of a steel girder, concrete deck bridge under fire exposure using a series of uncoupled fire and structural numerical analyses (Nahid, 2015). A parametric study was carried out to investigate the effect of various fire intensities and girder geometries on fire performance. Simulation results demonstrated that hydrocarbon fires, which correspond to tanker trucks and heavy good vehicle fires, caused more severe damage compared to standard fires. Box girders were shown to be more resilient to fire compared to other girder geometries.

Timilsina et al. investigated post event performance of a reinforced concrete bridge in Texas that was exposed to fire from a tanker through a set of numerical simulations and in situ tests (Timilsina et al., 2021). A three-step finite element modeling technique was utilized to simulate bridge response to fire. In the first step, a computational fire model was developed using Pyrosim software to simulate the actual fire scenario. The fire model was then incorporated into a three-dimensional heat transfer analysis using ABAQUS to determine bridge girders and deck temperature distributions. Concrete compressive strength and moduli of elasticity were then modified based on nodal temperatures from the heat transfer analyses. The final step modeled the fire-damaged bridge under static loads from two fully loaded dump trucks used for field testing. Results indicated that thermal profiles and corresponding material properties generated by the FE model matched those obtained from on-site inspections. Furthermore, the calibrated bridge model could accurately predict actual strains and displacements obtained from the static load test.

Quiel et al. examined the performance of steel bridges exposed to a hydrocarbon fire from an overturned tanker truck and subsequent fuel spill (Quiel et al., 2015). Semi-empirical and physics-based models were utilized to quantify damage caused by the open pool hydrocarbon fire. A design framework was proposed to evaluate the response of the bridge. The framework: (1) determined fire key characteristics; (2) estimated the amount of heat transferred to the structural components; (3) and calculated material and structural response to the fire. The proposed approach was shown to be efficient for evaluation and rehabilitation design of simple bridges subject to fire when strength reduction is the only considered failure criterion. However, the approach was unable to predict more complex fire induced load distributions and damage.

Alos-Moya et al. numerically investigated the response of an I-65 overpass in Alabama, USA, which was exposed to fire resulting from a tanker truck crash into one a support piers (Alos-Moya et al., 2014). Computational fluid dynamics analyses were initially performed to develop a representative fire model using Fire Dynamic Simulator (FDS) software. Two-step uncoupled thermal and mechanical analyses were then performed using ABAQUS. In the first step, the developed fire model was used in the heat transfer analyses so that resultant temperature distributions could be used to estimate strength degradation. For the second step, dead loads corresponding to the self-weight of the steel girders and concrete deck and the superimposed wearing surface were applied to the fire-damaged bridge. Results demonstrated that the model adequately simulated bridge response under fire. It was also shown that using standard fire curves did not accurately represent real bridge response to the fire event.

Peris-Sayol et al. investigated the response of a bridge superstructure exposed to a simulated fire caused by a tanker truck (Peris-Sayol et al., 2015). The bridge consisted of five steel girders that supported a reinforced concrete slab. Similar to the previously cited studies, a

multi-step modeling approach was utilized. In the first step, FDS was used to develop a hypothetical fire model. ABAQUS was then utilized to carry out heat transfer analyses using temperature variations from FDS. Resultant nodal temperatures were then used to impose strength reduction in steel and concrete. Finally, the response of the fire-damaged superstructure under self-weight and the weight of the pavement was determined. A parametric study was conducted to examine the effects of various bridge configurations and wind speeds on response. Simulation results demonstrated that the bridge exhibited the most critical damage when the tanker fire was close to the single span bridge abutments. It was also shown that damage was reduced by increasing the vertical clearance and in the presence of wind.

Woodworth computationally examined response of bridge superstructure to fire (Woodworth, 2013). Fire models obtained from FDS were incorporated to ABAQUS to study response to various fire scenarios of differing intensity and location with respect to the bridge. Studied parameters were initially selected based on statistics related to bridge fire incidents in the U.S for the past three decades, with the survey indicating that accidents resulted in an average of 175 fire incidents per year, with at least one fire event caused by a tanker truck. Results also indicated that tanker fires were anticipated to cause more severe damage while effects of smaller vehicle fire, such as from single unit trucks and buses, were minimal.

## 2.6 Combined fire, impact, and blast - examples

As indicated earlier, current U.S. bridge design codes, such as the *American Association of State Highway and Transportation Officials (AASHTO) Load and Resistance Factor Design (LRFD) Bridge Design Specifications* (AASHTO LRFD, 2020), do not address these multi-hazards given their perceived infrequent occurrence. However, the significance of investigating the performance of these substructure units has been highlighted by several multi-hazard

incidents. One recent incident occurred on June 11, 2023, when a truck tanker carrying gasoline crashed and caught fire, causing an elevated portion of Interstate 95 in Philadelphia, Pennsylvania, to collapse, as shown in Figure 2.24 (Tebor & Sottile, 2023). Transportation and fire department officials declared that, in conjunction with the intense fire, the collapse was also attributed to explosions of underground mains caused by fuel runoff. In response to this urgent situation, the FHWA promptly disbursed a \$3 million emergency relief fund to the Pennsylvania Department of Transportation (PennDOT) to alleviate the financial burden of repairing the damaged section and restoring traffic flow on I-95.



Figure 2.24 Collapse of a part of I-95 highway after a multi-hazard incident, Philadelphia, Pennsylvania (Tebor and Sottile 2023)

A similar event took place in 2002 when a tanker transporting gasoline crashed into a bridge overpass and exploded on a busy highway junction of interstates 65, 20, and 59 in Birmingham, Alabama and produced a huge fire (Cardone, 2023). As illustrated in This multi-hazard incident resulted in significant damage to the bridge substructure and required complete replacement of the bridge overpass. According to the Alabama Department of Transportation (ALDPT), the projected cost for the replacement of the bridge overpass amounted to \$2.1 million.

These representative events demonstrate the catastrophic consequences of multi-hazards and the urgent need for comprehensive studies that investigate bridge performance under their effects.



Figure 2.25 Damage in I-65 bridge overpass caused by multi-hazards, in Birmingham, Alabama, 2002 (Cardone, 2023)

### 2.7 Combined fire, impact, and blast - research

Extensive research has examined the behavior of RC structural elements subject to the combined effects of elevated temperatures and high loading rates resulting from impact or blast, as they often occur sequentially. While numerous research studies have been carried out to examine the performance of RC structural elements under the combined effects of fire and individual impact or blast, none of these studies examined bridges and bridge structural components to coupled impact and blast in conjunction with fire. Representative studies on the influence of fire when coupled with one other dynamic event are presented in this section.

The performance of RC structural elements subjected to combined fire and blast loads has been extensively investigated. Zhai et al. investigated the post-fire blast response of RC beams experimentally and numerically (Zhai et al., 2016). RC beams were initially heated in a furnace following ISO-834 standard fire curve and a series of blast tests were then performed.

Finite element models were developed to simulate fire-damaged beam response to blast loads. A two-step modeling approach was implemented using ABAQUS and involved implicit heat transfer and explicit structural analyses, with FE models being calibrated against test results. Study results indicated that longer fire durations resulted in more severe crack propagation and larger mid-span deflections.

Kakogiannis et al. utilized LS-DYNA to numerically examine the performance of a RC hollow core slab subjected to a blast load after being exposed to fire (Kakogiannis et al., 2013). Again, heat transfer and structural analyses were performed in two separate modeling stages. Developed models ignored stresses, strains, and geometric imperfections resulting from the fire, while strength reduction was considered by dividing the slab into layers, each with a reduced compressive strength and modulus of elasticity depending on the temperature distribution. The layers were localized to a region where displacement response was measured. Findings indicated that dynamic deflections increased dramatically when slabs were exposed to fire prior to blast.

Ruan et al. investigated response of RC columns subjected to coupled fire and blast (Ruan et al., 2015). A nonlinear concrete material model was initially developed in ABAQUS using data obtained from a set of experiments that examined combined effects of high temperatures and high loading rates on concrete behavior. Three-dimensional FE models were then created using the developed concrete nonlinear material model, with uncoupled implicit heat transfer and explicit structural analyses being completed. The ISO-834 standard fire curve was used for the heat transfer analysis to define the variation of temperature with time, with temperature dependent material properties selected based on resulting nodal temperatures. Four conditions involving symmetrical and unsymmetrical fire exposures were investigated. Fire damaged columns were then examined under blast loads. The proposed modeling approach was

shown to be efficient to predict key structural column response characteristics when compared to test results. More pronounced damage was observed for symmetrical fire exposure when the entire surface of the column was exposed to fire.

Chen et al. utilized ANSYS to investigate blast resistance of concrete-filled steel tubular (CFST) columns after fire exposure (W. Chen et al., 2016). Heat transfer analyses were initially carried out to simulate temperature distributions through the cross section using ISO-834 standard fire curve. Weighted average based on resultant temperature profiles was utilized to approximate concrete and reinforcing steel strength reductions. Blast response was then examined using several scaled distances. Results indicated that fire duration was the most critical factor influencing column blast resistance. Blast intensity influenced failure modes, which changed from flexural to shear flexural when charge weight increased.

The influence of fire exposure on impact response of RC structural components was also addressed by a number of researchers. Ožbolt et al. and Jin et al. numerically examined behavior of fire-damaged RC slabs subjected to an impact load (Jin et al., 2021; Ožbolt et al., 2019). Both studies utilized the same two-step modeling approach, where heat transfer analyses were initially performed with output results used in the subsequent impact analyses. Various fire exposure durations and impactor drop heights were examined. Simulation results were compared with results obtained from tests carried out and showed an acceptable agreement. Study findings showed that fire duration was an essential contributor to both permanent deformations and failure modes, and dynamic resistance was considerably reduced for slabs subjected to fire prior to impact.

Pahlaviani et al. also employed FEM to examine effects of high temperatures and impact on performance of CFST columns (Pahlaviani et al., 2020). Temperature dependent material

properties provided in Eurocode 2: Part 1-2 were used to impose strength reductions at selected temperatures without conducting heat transfer analyses. A parametric study was then completed to investigate impact response of CFST columns under four impact hammer velocities and two concrete confinement ratios. Results showed that increasing confinement would enhance ductile response to impact loading, and higher temperatures resulted in more critical damage.

Petrini et al. numerically investigated the response of multi-span bridge subjected to vehicle impact load followed by fire (Petrini et al., 2020). STRAND7 was used to model the bridge with shell and beam elements representing the steel girders, RC slab, and pier columns. Vehicle impact was modeled as an impulsive load applied 1.25 m above the column base. Fire loads were then applied to the superstructure utilizing hydrocarbon fire curves. It was indicated that bridge collapse occurred prior to fire when impulsive loads corresponding to 90 km/h and 110 km/h impact speeds were applied. It was also demonstrated that the bridge deck was the most vulnerable structural element to fire.

A single study by Choi et al. examined the response of RC and prestressed concrete (PSC) contaminant vessel and storage tanks wall panels subject to combinations of fire paired with impact or blast. In that study LS-DYNA and MIDAS were utilized to conduct multi-step finite element analyses that assessed performance subjected to impact or blast applied before fire exposure (Choi et al., 2017). An element erosion algorithm was developed that coupled the explicit structural and implicit heat transfer analyses. In this algorithm, elements were eliminated before applying fire when their maximum strains exceeded 0.003. FE models were validated against a set of impact and blast fire tests and demonstrated acceptable agreement. Permanent sets, impact and blast load time histories, and fire damage depths, defined as the depth where concrete experienced a temperature of 380° C, were compared for RC and PSC panels. Results

revealed that more severe damage was observed in PSC panels due to effects from the prestressing forces.

## 2.8 Retrofitting RC structural elements using Fiber Reinforced Polymers (FRP)

Fiber Reinforced Polymers (FRP), which have high strength and lightweight, have emerged as an effective method to enhance structural performance under extreme demands such as impact, blast, and fire (Hollaway & Teng, 2008). Several techniques are used to implement FRP composite materials in retrofitting. One method is to adhesively bond thin rigid FRP strips, ropes, or round bars to the surface of the structural element, which is called near surface mounting (NSM). The other method, known as hand layup or externally bonded (EB) composites, attaches premanufactured FRP fabrics or sheets of widths between 150 to 1500 mm to the surface of the structural element. More recently, hybrid retrofitting techniques that use combinations of FRP composites such as sheets, strips, plates, and rods are being used. A common hybrid retrofitting example is the use NSM strips, ropes, or bars with EB fabrics. The selection of retrofitting scheme depends mainly on structural element and extent of retrofitting needed. For instance, NSM, FRP strips/EB, and FRP sheets are commonly bonded to beam tensile and slab tensile faces to improve flexural resistance. Columns axial capacities and shear resistances are typically enhanced by wrapping FRP fabrics around the entire column periphery to provide additional confinement (Bank, 2006).

### *2.8.1 FRP strengthening of structural elements subjected to blast and impact*

The effectiveness with which various FRP retrofitting schemes improve structural resiliency subjected to blast and impact loads has been extensively examined. Baylot et al. experimentally investigated effectiveness of using glass fiber reinforced polymer (GFRP) to strengthen masonry wall panels subjected to blast loads (Baylot et al., 2005), with a 1 mm GFRP

sheet being attached to the wall surface using epoxy. Results demonstrated that the strengthening technique effectively mitigated wall panel damage level and prevented concrete fragments from being ejected due to the blast.

Ross et al. examined response of carbon fiber reinforce polymer (CFRP) strengthened beams under blast loads using a series of experiments (Ross et al., 1997). Three RC beams were strengthened using EB, CFRP sheets attached to their sides and bottom surfaces, with 110 kg ANFO charges placed 4.5 m above the beam at mid-span generating the blast loads. Impulsive loads and residual displacements were recorded and compared to results obtained from testing non-retrofitted beams. Test results indicated that CFRP strengthened beams experienced lower displacements and did not fail under blast, while non-strengthened beams exhibited direct shear failure.

Muszynski and Purcell experimentally studied response of CFRP strengthened RC wall panels to four high explosive detonations (Muszynski & Purcell, 2003). Explosive charges were placed at a standoff distance of 14.5 m so that complete failure did not occur. Peak displacements of the CFRP strengthened panels were significantly reduced compared to bare, control, walls and non-strengthened wall panels experienced severe spalling while no spalling was observed in the strengthened panels.

Kadhon studied the effectiveness of various CFRP strengthening schemes for improving performance of RC columns subjected to blast (Kadhon, 2016). Experimental investigations of full scale, seismically detailed, bare and CFRP wrapped RC columns were initially carried out to examine response to blast loads of varying intensity. RC-BLAST software was then employed to analytically examine effects of various design parameters and retrofitting schemes on RC response. Results indicated that wrapping the columns with CFRP laminates containing a

combination of unidirectional and  $\pm 45^\circ$  oriented fibers was shown to have the most beneficial effects on column performance, with more pronounced enhancement observed for seismically detailed, retrofitted columns.

Li et al. used LS-DYNA to examine performance of CFRP wrapped RC columns under blast (Z.-X. Li et al., 2021). Four columns, including one bare column and three columns wrapped using 2, 4, and 6 CFRP layers were modeled. The model was validated against published test results and demonstrated good accuracy. Simulation results showed that CFRP wrapped columns experienced lower displacements compared to as-built columns, with more noticeable reductions observed when six layers CFRP sheets were used.

Xu et al. evaluated the effectiveness with which CFRP wrapped, RC bridge pier columns improved performance under low speed vehicle collisions (Xu et al., 2020). Impact tests were completed on reduced scale cantilever columns with various reinforcement details and under two impact velocities. CFRP wrap was applied to the bottom half of the column height and two wrap thicknesses were investigated. Results demonstrated that retrofitted columns experienced flexural failure while shear failure dominated the bare columns. Thicker CFRP wraps contributed to more energy dissipation and damage mitigation.

Pham et al. experimentally investigated the response of reduced scale, rubberized, concrete columns wrapped using CFRP sheets to lateral pendulum impacts (Pham et al., 2018). Concrete mix designs with various rubber contents were studied. One layer of unidirectional, 0.131 mm thick, CFRP fabrics was used to wrap the rubberized columns. Test results demonstrated that wrapped columns containing 15% to 30% of crumb rubber outperformed bare columns with the same rubber content with respect to damage mitigation, energy dissipation, and ductility.

Sha and Hao examined response of reduced scale, CFRP wrapped, RC, round, pier columns under barge impact through a series of experimental tests and numerical simulations (Sha & Hao, 2015). The effects of several retrofitting parameters, such as wrap thickness and strength, on column performance were examined. Wrapped column response was compared to similar, non-strengthened columns. Results indicated that CFRP wrapped columns experienced less damage and enhanced resistance to impact loads. Also, it was shown that increasing CFRP thickness had more predominant effects on reducing column response compared to increasing CFRP strength.

Pham and Hao experimentally investigated the impact response of CFRP strengthened RC beams by testing thirteen beams under various impact loads (Pham & Hao, 2016). The effectiveness of using 45°-angled, U-shaped, and fully wrapped CFRP strengthening schemes was examined. Results showed that the 45°-angle wraps enhanced beam shear capacity, while improved damage mitigation and displacement reduction was observed for fully wrapped beams.

### *2.8.2 FRP repair of fire or heat damaged columns*

Repairing of fire or heat damaged RC columns using FRP composites has been widely studied. While fire damage usually corresponds to utilizing standard fire curves to define temperature variations in tested specimens, heat damage is imposed by gradually increasing temperature to 400° C – 600° C and maintaining that temperature for a specific time period. Usually, heat damage specimens have uniform strength degradation and are commonly used to examine structural system collapse (Eurocode 2, 2004; Qin et al., 2021).

Al-Nimry and Ghanem experimentally investigated effectiveness of wrapping heat damaged columns using CFRP and GFRP sheets to improve axial load capacity (H. S. Al-Nimry & Ghanem, 2017). A parametric study was conducted to examine the effects of heat duration and

FRP sheet thickness and strength on performance. Test results demonstrated that the number of FRP layers required to restore columns capacity should be correlated to heat duration.

A similar experimental study was conducted by Yaqub and Bailey, where residual axial load capacities of glass or carbon FRP wrapped, fire damaged, round, RC columns were determined (Yaqub & Bailey, 2011). Tested columns were classified as: (1) bare and undamaged; (2) bare and damaged; (3) damaged and FRP wrapped; and (4) damaged and repaired using mortar. Column axial strength, ductility, and stiffness were determined using a series of uniaxial compression tests. Results demonstrated that wrapping fire damaged columns with unidirectional glass or carbon FRP fabrics has notable effects on axial load capacity and ductility. However, no significant enhancement in axial stiffness was observed when FRP wrapping was utilized.

Al-Kamaki et al. examined the effectiveness of using CFRP fabrics for repairing fire damaged RC columns through a series of experimental tests and numerical simulations (Al-Kamaki et al., 2015). Twenty RC columns having various fire exposures and CFRP fabric thicknesses were initially tested under axial load. FE models were then developed and calibrated against test results to study other additional parameters, such as boundary conditions and loading frequency. Results indicated that repaired columns experienced enhanced strength and ductility compared to bare fire damaged columns. It was shown that increasing the number of CFRP layers contributed more pronounced improvement.

Utilizing hybrid retrofitting techniques to repair fire or heat damaged RC columns has also been examined by multiple researchers. Chinthapalli et al. evaluated effectiveness of a FRP hybrid retrofitting method that used a combination of NSM CFRP round, bars and EB CFRP fabrics to repair severely fire damaged RC columns (Chinthapalli et al., 2019). Fire damage was

initially imposed by heating the columns in a furnace for 2- and 3-hours using ISO 834 fire curves. Repaired, unrepaired, and undamaged columns were axially loaded until failure to estimate axial load capacities. Results revealed that repaired columns retained 80% to 116% of their original capacity, with more capacity retention corresponding to lower fire exposure duration.

Ashteyat et al. studied the performance of hybrid repaired, heat damaged, circular, RC columns. Six reduced scale RC columns were exposed to temperatures of 400° C to 600° C for three hours (Ashteyat et al., 2021). Intermittent CFRP cords were adhesively bonded in the circumferential direction to heat damaged columns. The columns were then wrapped using a single unidirectional layer of CFRP fabric. Columns were axially loaded to failure and complementary three-dimensional FE models were developed and calibrated against test results to examine behavior under various fire exposures. Results demonstrated that hybrid retrofitting enhanced column axial capacity, with repaired column capacities exceeded original, undamaged column, design capacities.

Al-Nimry et al. examined effectiveness of hybrid retrofitting 1/3<sup>rd</sup> scale, heat damaged, RC columns (H. Al-Nimry et al., 2013). Columns were exposed to a temperature of 500° C for three hours before being repaired using a combination of CFRP plates and wrapped sheets. A parametric study was completed to examine the effects of full and partial CFRP wrapping, the number of wrapped layers, and CFRP plate cross-sectional area on restoring column axial capacity and stiffness. Results showed that repaired column axial capacity and stiffness were significantly improved compared to unrepaired columns, but with no pronounced improvement being observed for partial wrapping. Moreover, a combination of externally bonded CFRP plates

and at least two CFRP layers confining the entire height of the column was recommended to restore the bridge to its original design capacity.

## 2.9 Summary

This chapter summarized research in areas related to bridge column performance under multiple hazards involving fire, vehicular impacts, and air blast. The literature review included the following topics:

1. Material behavior under extreme temperatures caused by fire and high loading rates corresponding to impact and blast;
2. Examples of reported bridge catastrophic incidents resulting from individual or a chain of hazards involving fire, vehicular collisions, and blasts;
3. Studies that examined response of RC structural elements under fire, impact, and blast, with an emphasis on bridge structural units;
4. Current analysis and design requirements for bridges and bridge components under extreme demands; and
5. Available techniques, design procedures, and innovative materials used to improve resiliency and performance of RC structural systems when subjected to extreme demands.

Even though the majority of bridge fires and other correlated extreme events are concentrated around supporting columns and can substantially damage bridge structures, none of the cited investigations examined the response of bridges and their structural elements under coupled impact and blast in conjunction with fire. As a result, the study presented herein fills a clear knowledge gap. Understanding how bridge structural components perform under the

combined effects of these extreme demands would offer insights into improving bridge resiliency, minimizing closures, and most importantly, preventing injuries and loss of life.

## Chapter 3 Finite Element Model Development

### 3.1 Introduction

Prior to examining the performance of multi-column piers and a representative bridge, isolated reinforced concrete bridge pier columns were initially considered to establish a basis for the analytical work. In this chapter, the numerical modeling approach utilized to model response of isolated bridge columns subjected to simulated standard fire, vehicle impact, and air blast is presented. The computational work was completed using LS-DYNA. Bridge column proportions and reinforcement details were obtained from a Federal Highway Administration (FHWA) design example and modeled to match the isolated column examined previously (Wassef et al. 2003; Fang et al. 2021). Additionally, techniques used to represent properties of the concrete and steel reinforcement, the soil and air domains, and the explosive were selected based on available literature.

### 3.2 Prototype RC Pier Column

Following a previously reported, validated modeling approach (Fang et al. 2021), LS-DYNA was used to model isolated, RC, circular pier columns, their pile foundation systems, and the surrounding air and soil volumes. Structural elements were proportioned according to an FHWA design example (Wassef et al., 2003). The design example is shown in Figure 3.1 and the numerical model in Figure 3.2. An isolated column was modeled prior to examining the performance of multi-column piers and piers supporting a bridge system to provide initial and computationally cost-effective insight into the effects of multi hazards on pier column behavior.

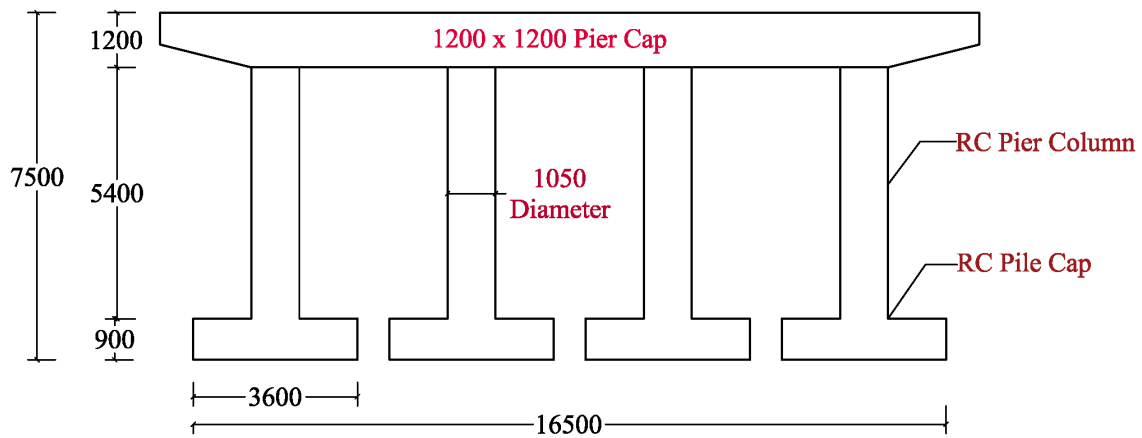


Figure 3.1 FHWA multi-column pier (unit: mm) (Wassef et al. 2003)

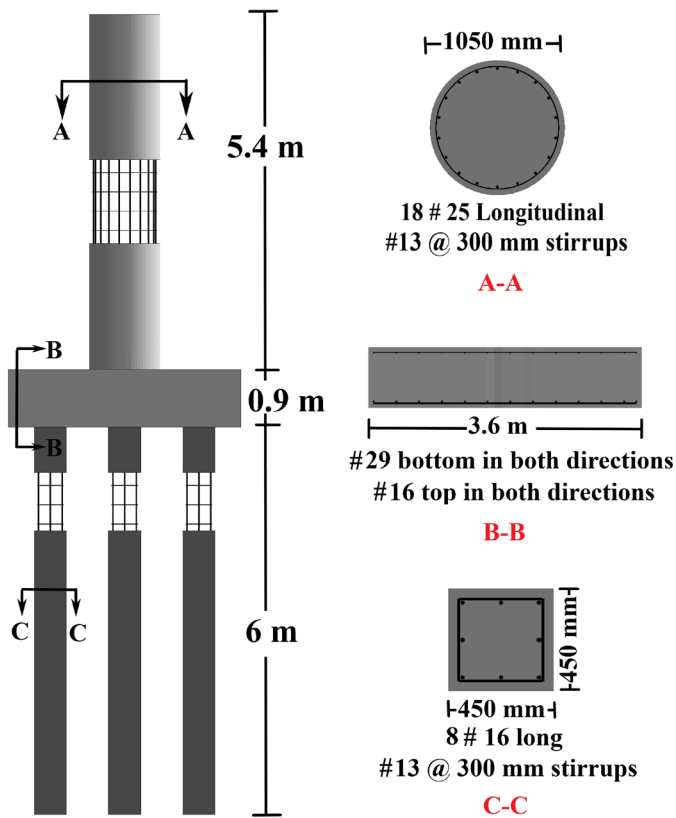


Figure 3.2 Isolated column and foundation system (Fang et al. 2021)

The round column is 1050 mm in diameter and 5400 mm long when measured from the spread footing. The foundation system consists of a 900 mm thick, 3600 mm square isolated footing supported by eight 450 mm square piles extending 6000 mm into the soil. The column was reinforced using 18 #25 longitudinal bars tied using #10 stirrups spaced at 300 mm to satisfy requirements spelled out in the AASHTO-LRFD Bridge Design Specifications (AASHTO 2020). Spread footing and pile reinforcement details are illustrated in Figure 3.2.

As recommended by a state DOT survey reported in NCHRP Report 645, *Blast-Resistant Highway Bridges: Design and Detailing Guidelines*, 750 mm and 1350 mm diameter pier columns were also considered as they are frequently used in highway bridges. The reinforcement ratio was set to 1% for all column diameters and resulting reinforcement for the three examined diameters is detailed in Figure 3.3 (Wassef et al., 2003; Williamson, 2010).

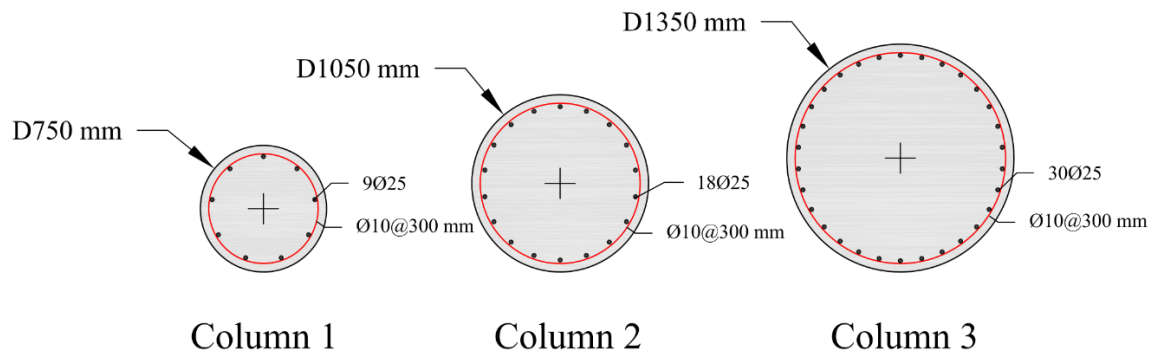


Figure 3.3 Column cross sections (units: mm)

### 3.3 Vehicle Collision

A modified version of the Ford F800 Single Unit Truck (SUT) finite element model developed by the National Crash Analysis Center (Mohan et al., 2007) was utilized to simulate impact into the pier columns (Figure 3.4). The modeled SUT was validated against test results

and many modifications have been completed to improve its robustness and stability at high strain rates (Miele et al., 2005). According to the Fatality Analysis Reporting System (FARS) and the National Center for Statistics and Analysis (U.S Department of Transportation, 2013), SUT's are commonly involved in critical accidents that cause serious injuries and property damage. SUT's are frequently used to transport various goods, which may increase the risk of fire initiation accompanying any accidents (Carrigan & Ray, 2017). Previous studies (Fang et al., 2021b) used impact speeds of 65 km/h (40 mph), 95 km/h (60 mph), and 120 km/h (75 mph) to mimic rural highway speed limits in the U.S. Since, as expected, the examined maximum speed limit (i.e., 120 km/h) was found to be the worst-case scenario, it was selected for the current study.

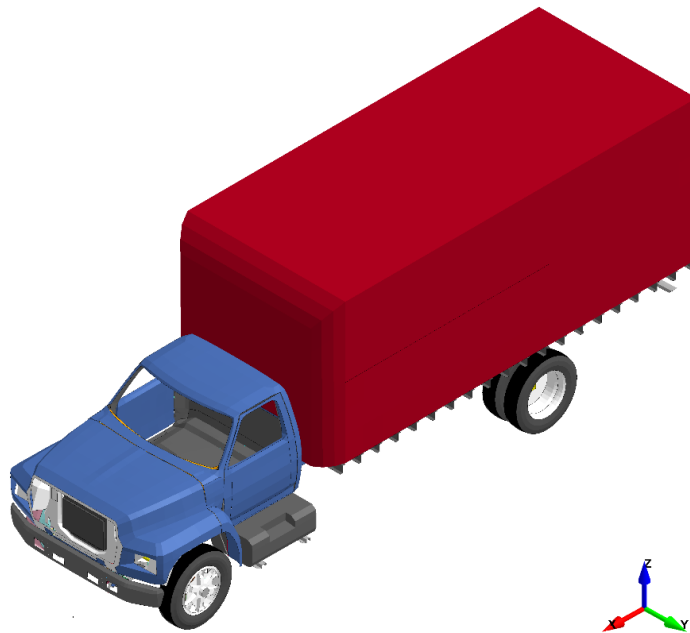


Figure 3.4 Ford F800 Single Unit Truck (SUT), LS-DYNA model

### 3.4 Air Blast

Blast load intensity is proportional to charge weight and distance between the charge center and the target. These two variables are usually represented using a single quantity known as the scaled distance ( $Z$ ). As recommended by NCHRP Report 645 (Williamson, 2010), response of bridge columns to air blast should be examined for blast loads at which  $Z \leq 0.6$  m/kg<sup>1/3</sup>, with the charge weight being measured using a TNT equivalence. Based on estimated TNT equivalencies for structures under terrorist attacks reported by the Federal Emergency Management Agency (FEMA) (Chipley, 2003), a scaled distance of 0.25 m/kg<sup>1/3</sup> was selected for the current study.

To accurately simulate blast wave propagation through the air and soil domains, LS-DYNA's *Multi-Material Arbitrary Lagrangian Eulerian (MM-ALE)* approach was implemented (Hallquist, 2014). This algorithm is commonly utilized to model near field explosions where severe mesh distortions could lead to explicit solver instabilities (Day, 2009). MM-ALE air blast simulation encompasses three stages: i) blast detonation, ii) blast wave propagation, and iii) interaction between fluid (i.e., air) and the structural system; known as Fluid-Structure Interaction (FSI).

The air, soil, and explosive were modeled using ALE meshes defined within LS-DYNA's *Multi-Material Group* with the air and explosive coupled together using the *Set Multi-Material Group List* command to represent the fluid (Hallquist, 2014). The *Lagrangian in Solid* penalty-based contact algorithm was utilized to simulate interaction between the Lagrangian structural system, and the ALE explosive, air, and soil meshes.

### 3.5 Fire

A substantial portion of the current study focused on developing an effective approach to incorporate fire effects into LS-DYNA analyses. Most computational tools utilize static solvers for structural fire analysis due to the quasi-static nature of fire loads. Despite their capability to accurately model highly nonlinear problems, explicit solvers such as those available in LS-DYNA are infrequently used for fire analysis (Rackauskaite et al., 2019). Many recent studies have attempted to validate LS-DYNA static solvers against experimental data for structural fire analyses and for heat transfer analyses of steel and reinforced concrete structural members (Kwaśniewski et al., 2013; Rackauskaite et al., 2017, 2019; Šelešovský & Krupka, 2007). These studies indicated that LS-DYNA could effectively model highly non-linear structural fire problems. As a result, the present study focused on developing an effective technique to integrate fire effects into impact and blast finite element analyses using LS-DYNA.

Based on research summarized in Section 2.5, the current study adopted the ISO-834 standard fire curve (ISO, 1999), also known as Cellulosic curve, as it is commonly used in fire tests, for building fire design, and for guiding fire resistance tests in North America (Hurley et al., 2015). Due to the capability of ISO-834 to simulate fires resulting from a wide range of ignitable materials and products, it has been utilized in many fire induced blast and impact tests and analyses (L. Chen et al., 2015; W. Chen et al., 2016, 2018, 2019; Ding et al., 2013; Guo et al., 2017; Jin et al., 2021; Kakogiannis et al., 2013; Ožbolt et al., 2019; Ruan et al., 2015). Given the intention to study performance of pier columns under combined impact, blast, and fire, a more intense fire may lead to partial or complete collapse of the RC column prior to vehicle impact and air blast. Therefore, the author felt utilization of the ISO-834 curve was appropriate.

The relationship between time and temperature is given in Equation 2 and plotted as shown in Figure 3.5, where  $T_o$  is the ambient temperature, and  $t$  is the time in minutes.

$$T = T_o + 345 \log (8t + 1) \quad \text{Equation. 2}$$

As recommended in the literature, thermal loads were treated as boundary conditions and defined as a combination of radiation and convection heat transfer (Kim et al., 2013). LS-DYNA's *INITIAL TEMPERATURE SET* and *BOUNDARY TEMPERATURE SET* keywords were used to define column and footing initial temperatures and to apply fire loads to the column using nodal temperature changes (Hallquist, 2014). It is widely reported that major bridge fires may last for one to three hours (Garlock et al., 2012; V. Kodur et al., 2010; X. Wu et al., 2020). As a result, columns were exposed for 60 or 90 minutes with selected fire durations based on reported RC structural-fire analyses (W. Chen et al., 2016; Guo et al., 2017; Zhai et al., 2016). Possible exposure scenarios were examined by subjecting either the full column circumference or half the circumference to fire, as shown in Figure 3.6. Research indicated that non-uniform fire exposure conditions, such as exposure of half the surface area, should be considered in fire analysis as they affect column axial load response (X. Li et al., 2021; Meng et al., 2020; Yang, Liu, & Gardner, 2013; Yang, Liu, Zhang, et al., 2013). Under non-uniform fire conditions the column centroid shifts towards the nonexposed surface, which causes applied axial load eccentricities that produce second order effects that could further reduce capacity (X. Li et al., 2021). As a result, four thermal analyses were carried out for each column diameter, as illustrated in Table 3.1, where  $F$  and  $H$  refer to either full or half surface fire exposure.

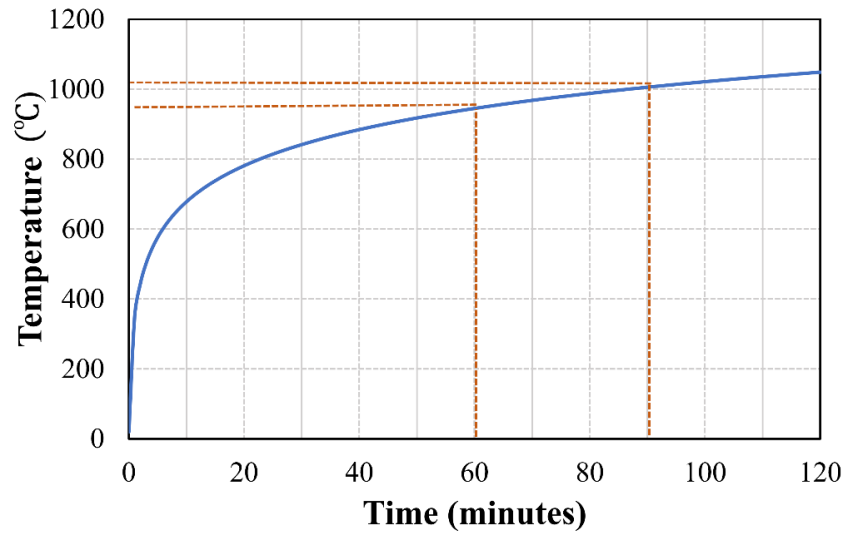


Figure 3.5 ISO-834 (ISO 1999)



Figure 3.6 Full and half surface area fire exposure schemes

Table 3.1 Thermal study cases

Surface Area Exposure	Fire Duration (min)	Nomenclature
Full	90	F-90
Full	60	F-60
Half	90	H-90
Half	60	H-60

### 3.6 Material Models

#### 3.6.1 Concrete

LS-DYNA's nonlinear *Continuous Surface Cap Concrete* material (CSCM) model (*MAT-159*) was used to model the concrete (Hallquist, 2014). This model was initially developed by FHWA to simulate the concrete behavior under high strain rates resulting from vehicle impact (Murray, 2004; Murray et al., 2007). The model was validated against a series of tests of RC structural elements subjected to impact and blast and demonstrated good agreement (AuYeung & Alipour, 2016; Coughlin et al., 2010; Murray et al., 2007; Sharma et al., 2012).

The CSCM model effectively reproduces the mechanical behavior of concrete when its unconfined compressive strength ( $f_c'$ ), maximum aggregate size (*DAGG*), and density ( $\rho_c$ ) are the only known parameters. A scalar damage parameter,  $d$ , is used to define damage accumulation based on two concrete damage scenarios, brittle and ductile, where brittle damage is tension and ductile damage is compression. The brittle and ductile damage parameters are expressed in Equation 3 and Equation 4 (Hallquist, 2014; Murray, 2007)

$$\text{Brittle concrete damage} \quad d(\tau_t) = \frac{0.999}{D} \left[ \frac{1 + D}{1 + D \exp^{-C(\tau_t - \tau_{ot})}} - 1 \right] \quad \text{Equation. 3}$$

Ductile concrete damage

$$d(\tau_c) = \frac{d_{max}}{B} \left[ \frac{1 + B}{1 + B \exp^{-A(\tau_c - \tau_{oc})}} - 1 \right] \quad \text{Equation. 4}$$

where:  $A$ ,  $B$ ,  $C$ , and  $D$ , are softening curve shape parameters;  $\tau_t$  is a tensile energy term based on the maximum principle strain;  $\tau_{ot}$  is an initial tensile damage threshold;  $\tau_c$  is a compressive energy term;  $\tau_{oc}$  is an initial compressive damage threshold; and  $d_{max}$ , is the maximum damage level.  $d_{max}$  equals one for concrete under tensile stresses and low confining pressures, and is typically 0.999 to avoid computational instabilities when moderate confining pressures are applied (Hallquist, 2014).  $d$  ranges between 0 and 1, with crack formulation corresponding to  $d = 1$  and crack free conditions to  $d = 0$ .

Concrete spalling is simulated in the CSCM model by defining an erosion coefficient (*EROD*) to delete highly strained elements. Element erosion occurs when  $d > 0.999$  and the maximum principal strain is greater than 1.0. As recommended in the literature, element erosion was controlled by setting the coefficient to  $EROD = 1.10$ , which corresponds to 10% maximum principle strain, to prevent computational difficulties (Hallquist, 2014; Murray et al., 2007; O'Hare, 2011). To account for apparent increase in strength due to high loading rates, LS-DYNA's *IRATE* coefficient was set to one. Concrete material properties and CSCM parameters selected for the current study are summarized in Table 3.2.

Constant stress hexahedral solid elements were utilized to model the concrete column and foundation system. Zero energy deformation modes, which represented distortion of elements that are strain free, were controlled using Type 5 hourglass control with an hourglass coefficient of 0.10 (Fang et al., 2021a; Hallquist, 2014; Islam & Singh, 2019; Murray, 2007).

Table 3.2 CSCM (MAT-159) material properties and model parameters

Property	Value
Mass Density (kg/m <sup>3</sup> )	2380.00
Unconfined Compressive Strength (MPa)	28.00
Maximum Aggregate Size (mm)	19.00
Erosion Parameter	1.10
Hourglass Coefficient (Type-5)	0.10

### 3.6.2 Steel reinforcement

Steel reinforcement was modeled using a *Piecewise Linear Plasticity* model in LS-DYNA (*MAT-24*) and Hughes-Liu, two node, round beam elements. The model accounts for strain rate dependency by utilizing Cowper and Symonds strain rate parameters, as expressed in Equation 5 (Cowper & Symonds, 1957; Hallquist, 2014). In this equation,  $f_d$  is the dynamic stress,  $f_y$  the static yield stress,  $\dot{\epsilon}$  the strain rate; and  $C$  and  $P$ , are the Cowper and Symonds parameters. Based on previous research,  $C$  and  $P$  were set to 40 and 5, respectively (Fang et al. 2021; Murray 2007; O'Hare 2011). Selected steel properties are summarized in Table 3.3.

$$f_d = f_y + f_y \left( \frac{\dot{\epsilon}}{C} \right)^{1/p} \quad \text{Equation. 5}$$

Table 3.3 Piecewise Linear Plasticity (MAT-24) material properties and model parameters

Property	Value
Mass Density (kg/m <sup>3</sup> )	7850.00
Yielding Stress (MPa)	475.00
Elastic Modulus (GPa)	200.00
Tangential Modulus (MPa)	2110.00
Ultimate Strain (Failure Strain) (%)	12.00
Poisson's Ratio	0.30

### 3.6.3 Soil

Based on previous research (Fang et al., 2021a; Hallquist, 2014), LS-DYNA's ALE multi-material solid element ( $ELFORM = 11$ ) was used to model the soil domain in conjunction with the *FHWA Soil (MAT-147)* material model. This model was initially developed by the FHWA with a smooth hyperbolic yield surface and a first order Mohr-Coulomb failure mode in which failure occurs when combined shear and effective normal stresses exceed the failure envelope (Fang et al. 2021; Lewis 2004). Model parameters utilized in the current study were determined from the literature and the LS-DYNA user manual and are listed in Table 3.4 (Reid et al. 2004; Lewis 2004; Hallquist 2014; Fang et al. 2021).

Table 3.4 FHWA Soil (MAT-147) material properties and model parameters

Property	Value
Mass Density (kg/m <sup>3</sup> )	1600
Specific Gravity	2.65
Bulk Modulus (MPa)	146.00
Shear Modulus (MPa)	56.00
Friction Angle (degrees)	35.00
Cohesion Coefficient (Pa)	5.00

### 3.6.4 Air and explosive

Based on previous research (Fang et al. 2021), LS-DYNA's ALE multi-material solid element (*ELFORM = 11*) was also used to model the air volume. The air domain was modeled using the *NULL (MAT-009)* material model. Standard LS-DYNA viscous hourglass control (Type 5) with  $1 \times 10^{-6}$  coefficient was used to mitigate hourglass energy. A linear polynomial Equation of State (EOS) expressed in Equation 6 and Equation 7 was adopted to control ideal gas behavior (Hallquist, 2014; Williams, 2009):

$$P_{air} = C_0 + C_1\mu + C_2\mu^2 + C_3\mu^3 + (C_4 + C_5\mu + C_6\mu^2)E_{o,air} \quad \text{Equation. 6}$$

$$\mu = \frac{\rho_{air}}{\rho_{o,air}} - 1 \quad \text{Equation. 7}$$

where:  $C_0$ ,  $C_1$ ,  $C_2$ ,  $C_3$ ,  $C_4$ ,  $C_5$  and  $C_6$  are polynomial equation coefficients;  $E_{o,air}$  is the initial internal energy per unit reference volume; and  $\mu$  is a volumetric parameter in which  $\rho_{air}$  and  $\rho_{o,air}$  are current and reference densities, respectively. Air density and polynomial EOS constants were

selected based on previous research to define the pressure-volume behavior of the TNT detonation products (Williams, 2009) and are presented in Table 3.5.

Table 3.5 Null (MAT-009) material properties and EOS parameters

Property	Value
Mass Density (kg/m <sup>3</sup> )	1.29×10 <sup>-9</sup>
E <sub>o,air</sub> (MPa)	0.25
C <sub>0</sub>	0.00
C <sub>1</sub>	0.00
C <sub>2</sub>	0.00
C <sub>3</sub>	0.00
C <sub>4</sub>	0.40
C <sub>5</sub>	0.40
C <sub>6</sub>	0.00

The *High Explosive Burn* material model (MAT-008) was selected to model the explosive (Hallquist, 2014). The Jones-Wilkins-Lee (JWL) EOS was used to define the relationship between detonation pressure, volume, and internal energy, as expressed in Equation 8.

$$P_d = A \left( 1 - \frac{\omega}{R_1 V} \right) e^{-R_1 V} + B \left( 1 - \frac{\omega}{R_2 V} \right) e^{-R_2 V} + \left( \frac{\omega E_{o,v}}{V} \right) \quad \text{Equation. 8}$$

where,  $P_d$  is the detonation pressure;  $A$ ,  $B$ ,  $R_1$ ,  $R_2$  and  $\omega$  are explosive type dependent constants;  $V$  is the detonation product specific volume; and  $E_{o,v}$  is the produced detonation energy per unit

volume. Material properties for the TNT explosive and associated EOS constants are provided in Table 3.6.

To optimize computational cost, LS-DYNA's *Initial Volume Fraction Geometry* keyword was used to define an initial spherical shaped air volume occupied by the explosive charge (Hallquist, 2014). The *Initial Detonation* option was used to specify detonation coordinates (Hallquist, 2014). A one-point ALE multi-material solid element formulation (*ELFORM = 11*) was used to define the explosive.

Table 3.6 High Explosive Burn (MAT-008) material properties and EOS parameters

Property	Value
Mass Density (kg/m <sup>3</sup> )	1.64×10 <sup>-6</sup>
Detonation Speed (m/s)	6930.00
Chapman-Jouget pressure (GPa)	21.00
<i>A</i> (GPa)	371.20
<i>B</i> (GPa)	3.23
<i>R</i> <sub>1</sub>	4.15
<i>R</i> <sub>2</sub>	0.95
<i>ω</i>	0.30
Detonation Energy per unit volume (GPa)	7.00
Initial Relative Volume	1.00

### 3.6.5 Thermal material models

European and American standards are commonly used to select concrete and steel reinforcement temperature dependent material properties. Unlike American specifications, thermal material properties provided in the Eurocode are applicable to a wide range of concrete

types, such as normal and high strength concrete and siliceous or calcareous aggregates (Eurocode 2, 2004; V. Kodur, 2014).

In this study, the thermal conductivity and specific heat of concrete and steel reinforcement were determined in accordance with Part 1-2: *General Rules – Structural Fire Design* of Eurocode 2, *Design of Concrete Structures* and Eurocode 3, *Design of Steel Structures*. For the present study, coefficients of thermal expansion were selected as proposed by the Society of Fire Protection Engineers (SFPE) *Handbook of Fire Protection Engineering* and Lie and Denham (Hurley et al., 2015; Lie, T.T. & Denham, E.M.A., 1993). Thermal properties are expressed over a range of temperatures, as provided in Table 3.7, where  $\lambda$  is the thermal conductivity;  $C$  is the specific heat; and  $\alpha$  is the coefficient of thermal expansion.

According to the literature, temperature change in concrete and steel can be modeled utilizing isotropic thermal properties (de Borst & Peeters, 1989; Mazars, 1987; Saetta et al., 1995; Ulm et al., 1999). As a result, LS-DYNA's *Thermal Isotropic TD (MAT\_T03)* material model was used (Hallquist, 2014). This material model was selected because temperature dependent properties can be defined by the user. Variation of the thermal coefficient of expansion with respect to temperature was also determined using a user-defined curve and was an input to LS-DYNA's *Add Thermal Expansion (MAT\_000)* material model (Hallquist, 2014).

Table 3.7 Concrete and steel thermal material properties

Temperature (C°)	Concrete			Steel		
	$\alpha_c$ (1/C°)	$\lambda_c$ (W/m.k)	$C_c$ (J/kg.k)	$\alpha_s$ (1/C°)	$\lambda_s$ (W/mk)	$C_s$ (J/kg.k)
20	$6.2 \times 10^{-6}$	1.330	900	$12.1 \times 10^{-6}$	53.33	439.80
100	$6.8 \times 10^{-6}$	1.230	900	$12.4 \times 10^{-6}$	50.67	487.62
200	$7.6 \times 10^{-6}$	1.110	1000	$12.8 \times 10^{-6}$	47.34	529.76
400	$9.2 \times 10^{-6}$	0.907	1100	$13.6 \times 10^{-6}$	40.68	605.88
600	$10.8 \times 10^{-6}$	0.749	1100	$14.4 \times 10^{-6}$	34.02	760.22
800	$12.4 \times 10^{-6}$	0.637	1100	$15.2 \times 10^{-6}$	27.36	803.26

### 3.7 Model Coupling and Boundary Conditions

LS-DYNA's penalty-based *Lagrangian in Solid* algorithm was utilized to couple steel reinforcement to surrounding concrete following previous research (Fang et al. 2021; Hallquist 2014; Murray 2007). The same keyword was used to couple the structural system to its surrounding explosive, air, and soil ALE meshes. The coefficient of friction between the foundation system and the soil used in the coupling algorithm was defined based on critical friction angle to be 0.315 (Reese et al., 2014).

As recommended in previous studies, the segment-based, penalty-type, *Automatic Surface to Surface* algorithm was selected to model contact between the SUT and column with both static and dynamic friction coefficients set to 0.30 (Hallquist, 2014; Koneshwaran et al., 2015; Murray, 2004; Reese et al., 2014). The same algorithm represented contact between the foundation and the surrounding soil.

To limit the spatial extent of the air and soil meshes and to mitigate inaccurate blast wave reflections that may also cause solver instabilities, LS-DYNA's *Boundary Non-reflecting* option was applied to air and soil domain external surfaces (Hallquist, 2014). While the column's top end was restrained against translation, common nodes between the column and pile cap were merged to simulate a fixed connection. As a result, columns were modeled as being fixed-pinned. A dead load equal to 6% of a column's nominal axial capacity was applied prior to any explicit analyses, with the nominal axial capacity computed according to AASHTO-LRFD column design equation, as shown in Equation 9.

$$P_n = 0.85 f'_c (A_c - A_s) + f_y A_s \quad \text{Equation. 9}$$

where:  $P_n$  is the nominal axial capacity;  $f'_c$  is the unconfined concrete compressive strength;  $f_y$  is the steel yielding stress;  $A_c$  is the concrete column cross sectional area;  $A_s$  is the reinforcement bars cross sectional area.

The coupled thermal-structural solution procedure was controlled using LS-DYNA's *Control Solution* command. LS-DYNA's symmetric direct solver (*SOLVER = 11*) was utilized within the *Control Thermal Solver* keyword to perform nonlinear thermal analyses with material properties evaluated at an element's average temperature (*PTYP = 2*). The thermal speed-up factor (*TSF*) was set to 100 to ensure that thermal velocity terms were not affected by time scaling (Hallquist, 2014; Shapiro, 2005). The maximum temperature change for each thermal time step above which the time step would be shortened was set to five using the *Control Thermal Timestep* option (Hallquist, 2014). The full representative finite element model domain including the RC bridge column, SUT, soil, air, and charge is depicted in Figure 3.7.

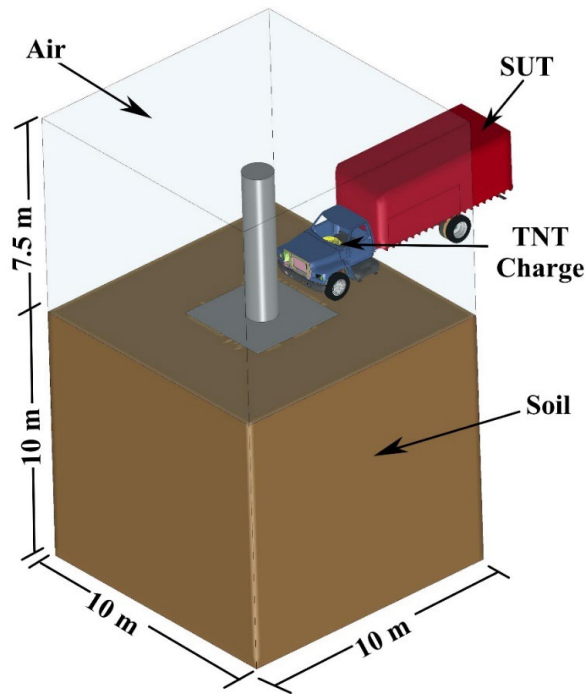


Figure 3.7 Modeled pier column air, soil volume, and SUT

### 3.8 Time and Mass Scaling

Time and mass scaling are implemented in FE analyses to minimize computational cost. Mass scaling adds non-physical mass to the system to increase an explicit time step and reduce simulation time (Shapiro, 2005). The length of a time step is controlled by the side length of the smallest element and its assigned material density (Surech & Regalla, 2014). When mass scaling is implemented, artificial mass added to the system should not exceed 5% of the total mass to avoid introducing significant inertia that may affect simulation results (Ma et al., 2019; Rackauskaite et al., 2017). For this study, the mass scaling factor was determined using trial and error, which focused on varying the scaling factor until acceptable mass was added to the system so that computational time was reduced without appreciably affecting kinetic energy. Consequently, scaling factors ranging between  $6.5$  and  $7.5 \times 10^{-6}$  were used for studied column diameters.

Time scaling is a technique in which analyzed event time is reduced. This technique is commonly used to simulate fire and in heat transfer analyses (Ma et al., 2019; Rackauskaite et al., 2017) since, as stated earlier, fires may last for hours. The time scaling factor was set to 100 based on previous research (Lu et al., 2012), which reduced analysis time for a 5400 second (90 minute) fire to 54 seconds. When both time and mass scaling techniques are employed, the ratio of kinetic to internal energies must be less than 1% for all time steps (Rackauskaite et al., 2017), and for the current study the maximum ratio was 0.076%.

### 3.9 FE Modeling Approach

Multi-step analyses can be implemented when examining the response of structural elements to multi-time scale problems resulting from a combination of dynamic and static or quasi-static loads (Choi et al., 2017; Garlock et al., 2012; Kim et al., 2013; Ma et al., 2019; Ruan et al., 2015; X. Wu et al., 2020; Zhai et al., 2016). A unique two-step approach was explored in LS-DYNA for the current study, one that involved implicit thermal analyses and explicit structural analyses to ensure accurate prediction of mechanical and physical properties changes due to fire prior to or after applying other demands. LS-DYNA's *Interface Springback* keyword was utilized so that results from the first analysis step served as the initial conditions for subsequential analyses (Hallquist, 2014).

Temperature dependent steel and concrete material properties are represented using *MAT202* and *MAT172* constitutive models in LS-DYNA (Hallquist, 2014). These material models were developed for beam elements following Eurocode 2 and 3 specifications (Eurocode 2, 2004; Eurocode 3, 2007) and can account for heat transfer and corresponding strength degradation in the same analysis stage. They were solely developed for beam elements and may not accurately predict crack propagation and failure mechanisms under other extreme demands

and with more advanced element types, such as the solid elements selected for the current study. Therefore, three-dimensional heat transfer analyses of representative bridge columns were conducted using solid elements to ascertain if essential structural response characteristics were accurately replicated. The *Interface Springback* LS-DYNA (Hallquist, 2014) keyword was employed so that resulting stresses, strains, erosion, nodal constraints, and geometric imperfections caused by fire exposure or impact and blast would be used as initial conditions for subsequent analyses.

As the strength of reinforced concrete structures is not recoverable after being exposed to elevated temperatures, the effect of cooling on concrete and steel reinforcement strength was disregarded (W. Chen et al., 2019; Eurocode 2, 2004; Yang et al., 2008). As a result, concrete and steel reduced strengths were defined based on maximum temperatures their elements experienced. Previous research indicated that using temperature distributions that divide a structural element into layers, with each layer comprised of elements having the same average temperature and material properties, showed good agreement with experimental results measuring strength reduction under extreme temperatures (W. Chen et al., 2016; Choi et al., 2017; Guo et al., 2017; Kakogiannis et al., 2013). The present study adopted this approach and concrete and steel reinforcement within an isolated column were divided into layers around the column periphery, each having a reduced strength determined as a function of mesh size and maximum temperature. Layering was completed before applying impact and blast for the cases where fire was applied first or before estimating column residual capacities when fire exposure occurred after impact and blast. Concrete and steel strength reduction factors are available in Eurocode 2, Part 1-2 and are reproduced in Table 3.8. Although not explicitly shown in the table, strength reductions for concrete temperatures below 120 °C were neglected.

Preliminary analysis showed that peak steel reinforcement temperature recorded during a fire was approximately 200 °C for the case in which fire was applied first, indicating negligible strength reduction. Previous research supported excluding reinforcement from thermal analyses to optimize computational cost as it did not appreciably affect temperature distributions within the concrete cross section (W. Chen et al., 2016; Guo et al., 2017; Lie & Erwin, 1993; Raut & Kodur, 2012; Zhai et al., 2016). Steel reinforcement was included in the thermal analyses when fire applied after impact and blast as it might be exposed due to extensive concrete spalling during SUT impact and the subsequent air blast.

Table 3.8 Concrete and steel strength reduction factors (Eurocode 2, 2004)

Temperature (C°)	Concrete	Steel Reinforcement	
	$(f'_{c,T}/f'_c)$	$(f_{y,T}/f_y)$	$(E_T/E)$
20	1.00	1.00	1.00
100	1.00	1.00	1.00
200	0.95	1.00	0.90
300	0.85	1.00	0.80
400	0.75	1.00	0.70
500	0.60	0.78	0.60
600	0.45	0.47	0.31

### 3.10 Summary

This chapter summarizes the modeling approach proposed to model response of round, RC, isolated bridge pier columns subjected to simulated standard fires, SUT impact, and air blast. A three-dimensional finite element model consisting of a single column, pile foundation system, the surrounding soil and air domains and exposed to SUT impact, and air blast was developed using LS-DYNA to match previous research (Fang et al. 2021). Consecutive material

models of the concrete, steel reinforcement, soil, and air were selected based on published literature.

A unique multi-step FE modeling technique was essentially developed to incorporate the combined effects of multi-time scale demands resulting from fire, impact, and blast. This modeling technique involved uncoupled implicit thermal analyses and explicit structural analyses to ensure physical and mechanical degradation due to fire are accurately predicted prior to or after applying other demands. LS-DYNA's *Interface Springback* keyword was utilized so that results from the first analysis step serve as initial conditions for the subsequent analyses. Strength degradation in concrete and steel reinforcement were determined based on temperature profiles obtained from thermal analyses. Thermal material models were used to define concrete and steel temperature dependent material properties. LS-DYNA's Multi-material Arbitrary Lagrangian Eulerian (*MM-ALE*) technique was utilized to accurately model air blast and resulting fluid structure interaction (*FSI*). Vehicle impact was simulated using a Ford F800 SUT moving at a prescribed speed.

## Chapter 4 Validation Study

### 4.1 Introduction

This chapter summarizes validation studies used to explore reliability and robustness of the proposed FE modeling approach. It should be noted that experimental research studying response of RC structural elements under the effects of coupled impact, blast, and fire could not be located in the literature. Research that predated this effort validated vehicle impact and air blast models against published results from separate experimental impact and blast tests (Fang et al. 2021). Results indicated that proposed modeling techniques could accurately predict key structural response characteristics.

For the current study, the previously validated FE modeling approach and the proposed multi-step approach, both of which were outlined in the previous chapter, were validated against three published structural element tests that included fire. The first validation test focused on estimating residual axial load carrying capacity of a square RC column after a 90-minute fire exposure (V. Kodur et al., 2017). The second test investigated dynamic response of a RC slab subjected to impact load after exposure to extreme temperatures that mimicked the ISO-834 fire curve (Jin et al., 2021; Ožbolt et al., 2019). The third test examined RC beam response to fire and air blast by subjecting specimens to extreme temperatures that, again, mimicked ISO-834 and then subjecting the beam to an air blast (Zhai et al., 2016).

## 4.2 RC Column, Fire Exposure

The first investigation of modeling approach effectiveness focused on residual axial capacity tests of a fire damage RC column (V. Kodur et al., 2017). A 200 x 200 mm column was exposed to 90-minute ASTM E118 fire along the middle third of its height, as shown in Figure 4.1. The column was subjected to 50% of its design axial load capacity during fire exposure. After cooling down, the applied axial load gradually increased until failure.

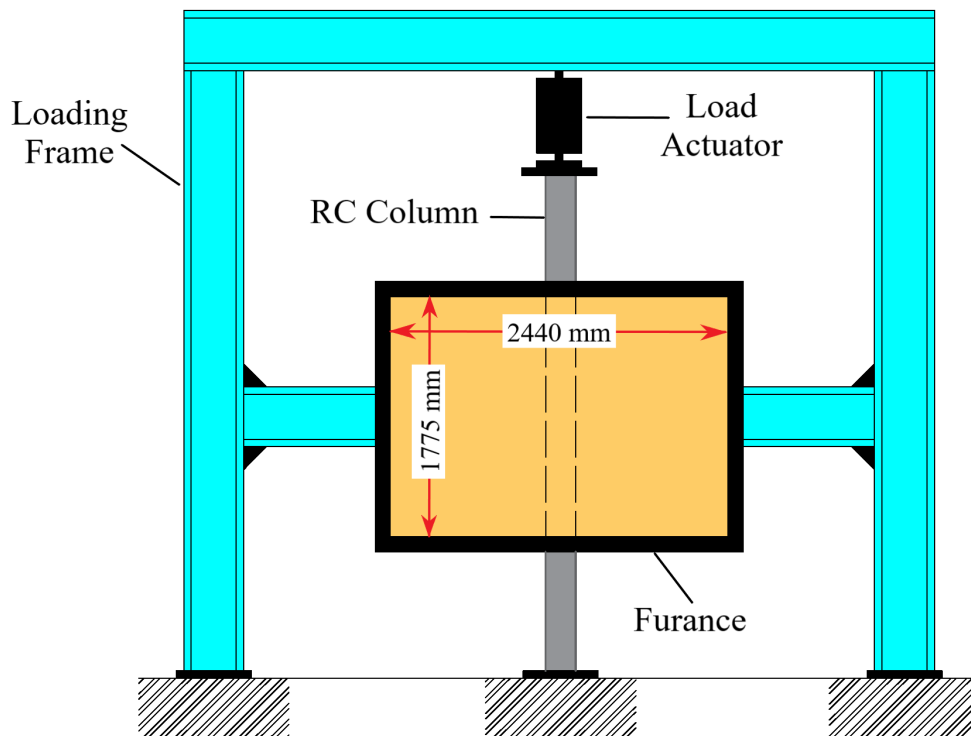


Figure 4.1 Fire and residual capacity test setup (Kodur et al., 2017)

An FE model was developed in LS-DYNA and analyzed following the two-step procedure presented in Section 3.9. The model is illustrated in Figure 4.2(a). In the first step, the modeled column was subjected to axial load and a simulated fire in the same region specified by the test. Average element temperature and the corresponding temperature contours were then obtained and used to divide the column into four layers with varying unconfined compressive strengths, as shown in Figure 4.2(b). Comparisons between simulated and experimental temperature variations at three locations within the cross section, the surface, location of reinforcing bars, and center are shown in Figure 4.3 and good agreement was achieved at the end of the exposure period.

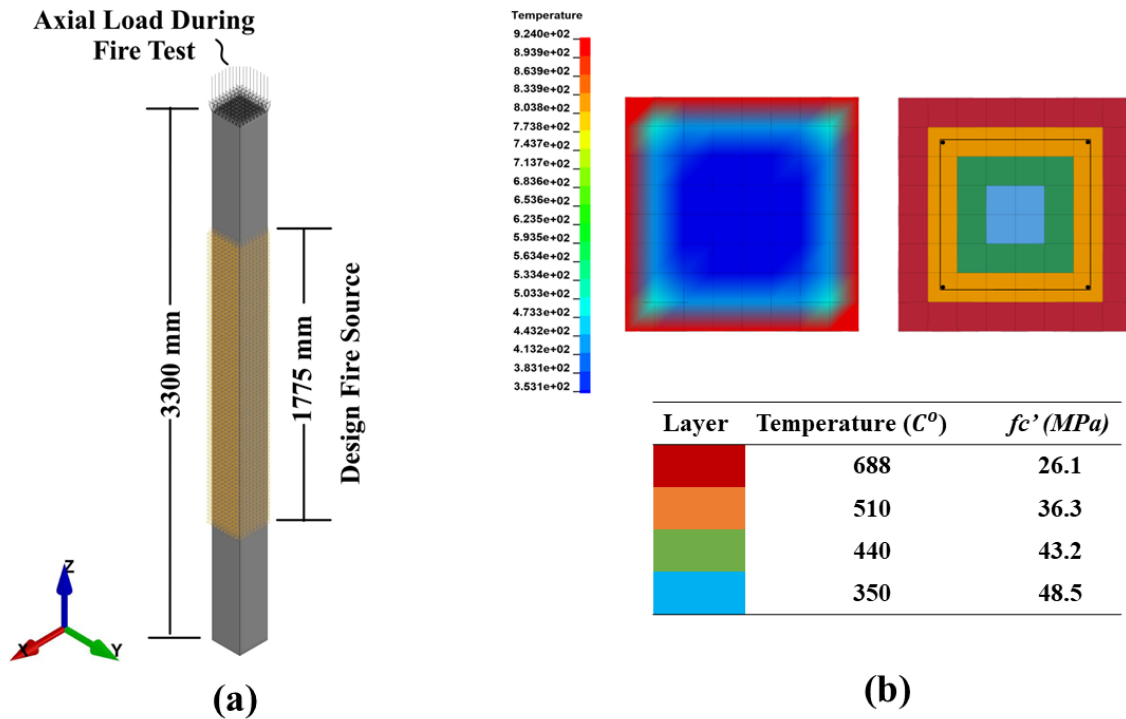


Figure 4.2 FEM: (a) RC column under fire; (b) temperature profile and corresponding column layers

The second simulation stage was a “push down” analysis where the applied axial load incrementally increased until failure, which was represented by a sudden decrease in loading capacity. As indicated in Figure 4.4, though residual deformation estimated by the FE model after fire exposure was greater than what was observed in the test, simulated and measured load-displacement curves showed a good agreement and acceptable prediction of the column’s capacity was achieved, where 7% larger capacity was estimated by the FE model. The discrepancy in residual deformations is justified as different coefficients of thermal expansion for concrete and steel reinforcement might be used in the test and FEM. As the coefficient were not explicitly specified in the test, values listed in Table 3.7 were utilized.

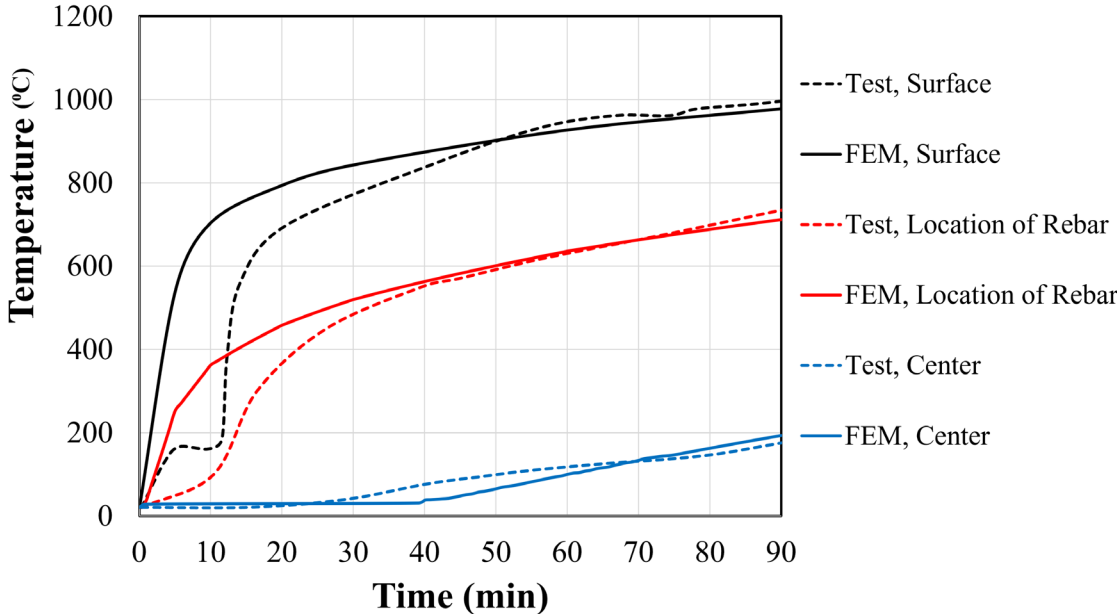


Figure 4.3 FEM and test temperature time histories

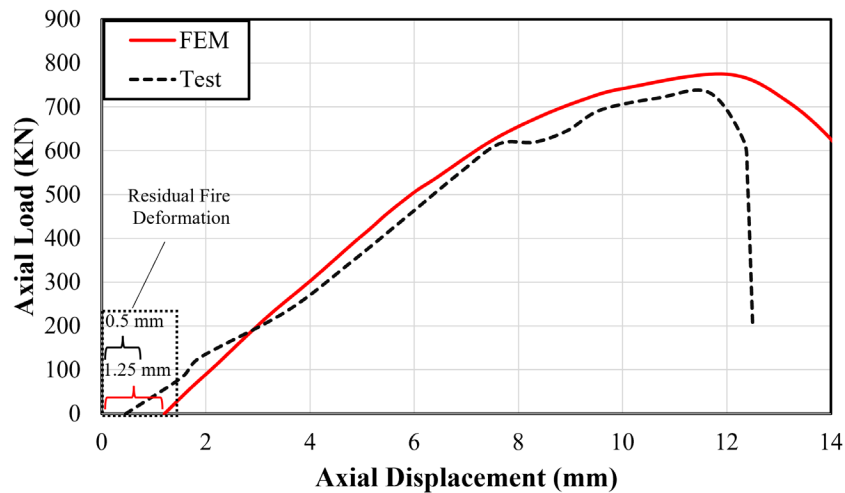


Figure 4.4 Simulated and test load-displacement curves

### 4.3 RC Slab under Fire and Impact

The second study experimentally studied the performance of three RC slabs heated according to ISO-834 and impacted by a 588 kg drop weight at mid span. Two drop heights were used, and the most critical case was selected for validation. This case involved heating the bottom surface of the slab and a drop height of 5 m. Selected slab dimensions and reinforcement details are shown in Figure 4.5. More details on the tests can be found elsewhere (Jin et al., 2021; Ožbolt et al., 2019).

A three-dimensional heat transfer analysis was completed in LS-DYNA to estimate temperature distributions, with the fire load being modeled following ISO-834 specifications (ISO, 1999). According to the developed modeling approach, the slab was divided into four layers based on temperature distributions observed from the heat transfer analysis, as shown in Figure 4.6. Four layers were selected so the 200 mm thickness could be divided into four, 50 mm hexahedral solid elements.

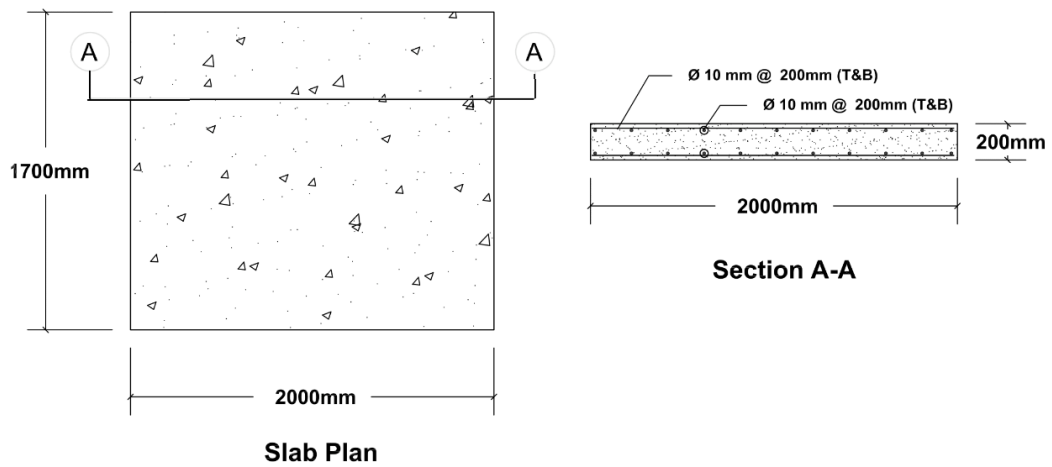


Figure 4.5 RC slab dimensions and reinforcement (Parmar et al. 2014)

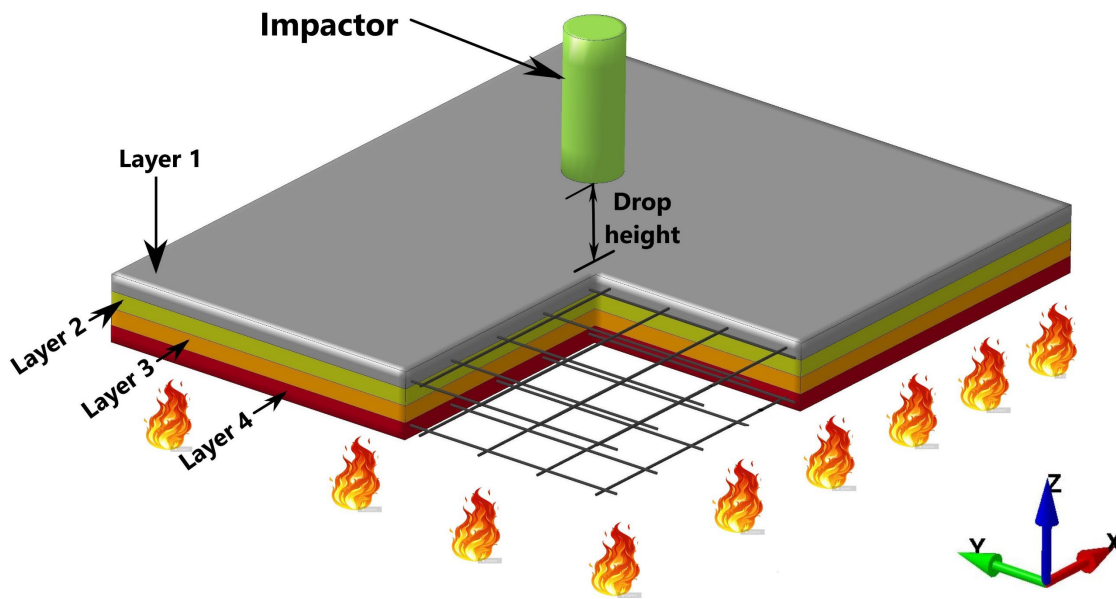
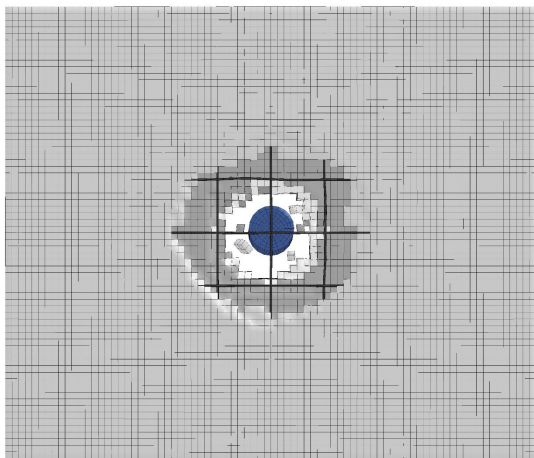


Figure 4.6 FEM of fire damaged RC slab

The top layer, Layer 1, represented the portion with no strength reduction. Layer 2 was for concrete whose average element temperature reached 200 °C, Layer 3 for average temperatures of 350 °C, and Layer 4 (i.e., the bottom layer) for averages of 650 °C. Each layer was assigned a unique compressive strength according to Eurocode 2 temperature-strength correlations provided in Table 3.8. LS-DYNA results showed good agreement between simulated and experimental damage at the end of the test, as shown in Figure 4.7. Mid-span displacement and impact force time-history comparisons also matched well, with simulated peak displacement and force being 9% and 11% higher, respectively, than measured values, as illustrated in Figure 4.8 and Figure 4.9. Differences were attributed to the model boundary conditions, which were fixed, as bolts used in the test and would not provide full fixation.



(a) FEM



(b) Experiment

Figure 4.7 Failure pattern (a) simulated, (b) experimental

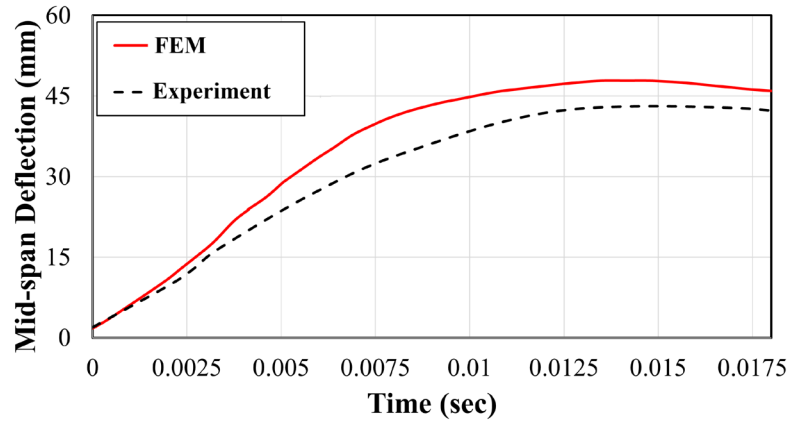


Figure 4.8 Mid-span displacement time-history

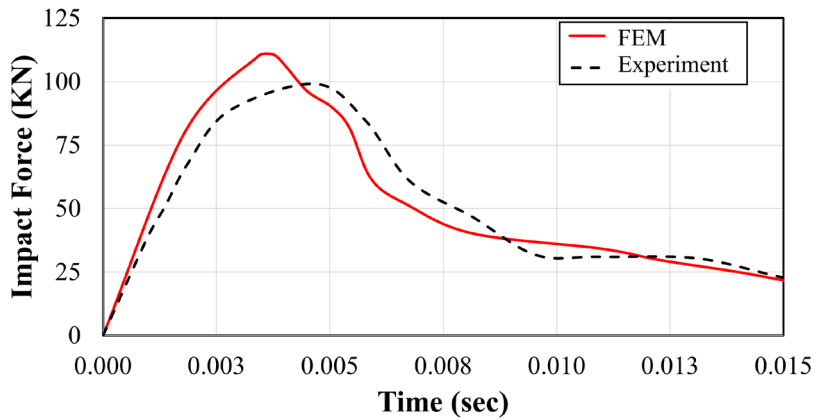


Figure 4.9 Impact force time history

#### 4.4 RC Beam under Fire and Blast

Combined fire and air blast model validation utilized tests of RC beams initially exposed to temperatures mimicking a 90-minute, ISO-834 standard fire followed by a rock emulsion explosion from a 7 kg size charge located 1500 mm above the beam top surface (ISO, 1999; Zhai et al., 2016). LS-DYNA models were again developed following the developed approach, as illustrated in Figure 4.10. As shown in this figure, both sides and the bottom surface of the beam were exposed to simulated fire since fire insulation was applied to the top surface and beam ends

during test setup. The fire-damaged beam depicted in Figure 4.10(a) refers to the beam with four layers each characterized with its unique compressive strength determined based on the average element temperature obtained from the thermal analysis stage. Again, the number of layers was determined based on the selected element size.

Experimental temperature variations were recorded during fire exposure using six thermocouples, as illustrated in (Zhai et al., 2016). Predicted temperature time histories were compared to experimental time histories as shown in Figure 4.11, with comparisons being made at four locations (i.e., C, L, S, and T). Predicted and measured temperature time histories were in good agreement, demonstrating a maximum error of 11%. Discrepancies were attributed to thermal material properties selected to model the behavior of the RC beam under fire, which were not provided in the test details and could have been selected based on specifications other than Eurocode 2, part 1-2 that were adopted in the current study.

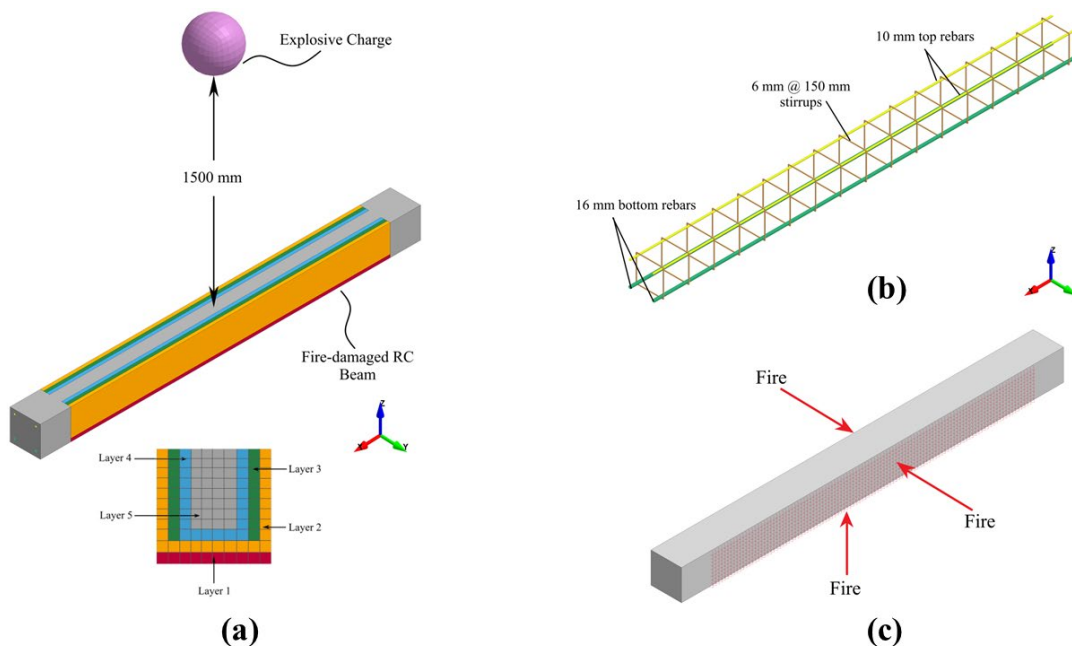


Figure 4.10 Developed LS-DYNA FE model: (a) fire-damaged RC beam subjected to air blast; (b) steel reinforcement; (c) fire exposure scheme

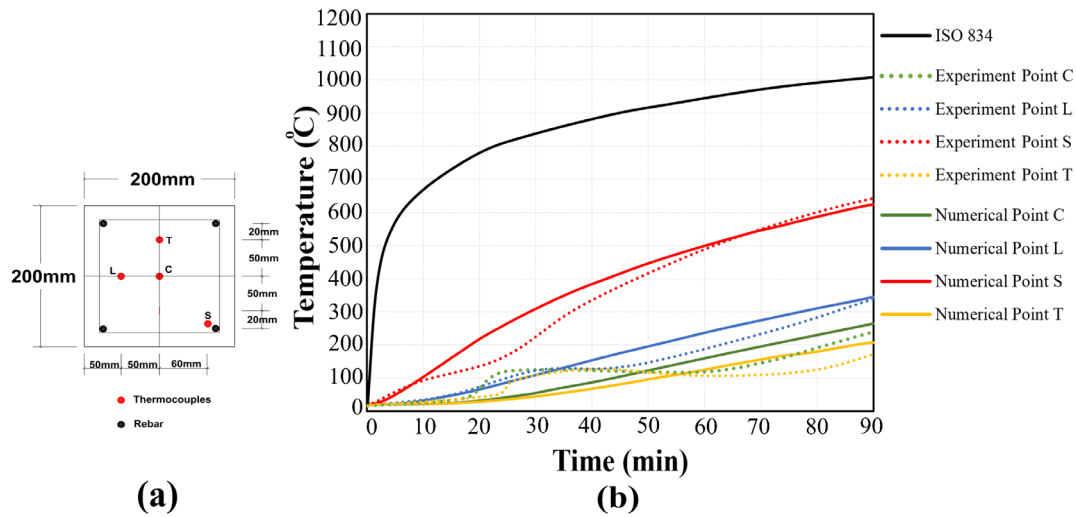


Figure 4.11 RC beam heat transfer analysis results: (a) beam cross section and instrument locations (Zhai et al., 2016); (b) temperature time-histories at thermocouple locations

Modeled and experimentally obtained mid-span displacement time histories were compared and demonstrated adequate agreement at the peak displacement, with 7% error existing, as shown in Figure 4.12. As indicated in the figure, displacement spring-back was not adequately predicted with differences being attributed to bolts used for the test not maintaining full fixation that existed in the model. Results were deemed acceptable, however, due to good agreement during the initial peak displacement phase because it is understood that first-peak response is generally used for blast resistant structural design (Sudeep & Rao, 2019).

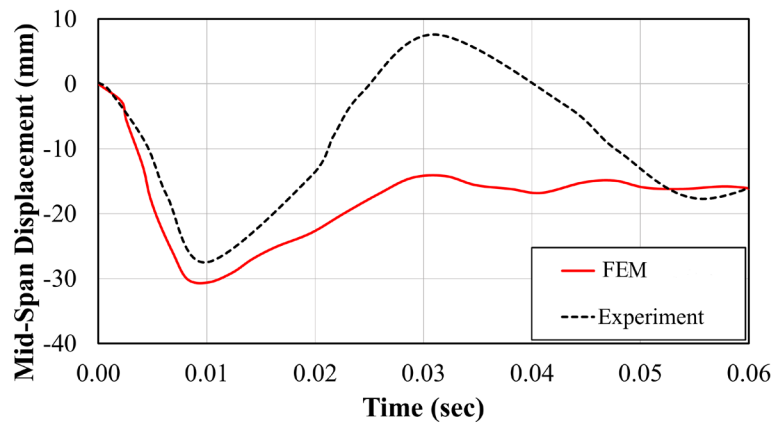


Figure 4.12 Experimental and modeled mid-span displacement time histories

#### 4.5 Summary

Extending validation work carried out during an earlier stage of research (Fang et al., 2021b), the feasibility of the developed FE modeling approach was validated by comparing simulation results to those obtained from three separate tests reported in the literature. The first validation test focused on estimating the residual axial load carrying capacity of a square RC column after a 90-minute fire exposure (V. Kodur et al., 2017). The second test investigated the dynamic response of a RC slab subjected to impact load after exposure to extreme temperatures that mimicked the ISO-834 fire curve (Jin et al., 2021; Ožbolt et al., 2019). The third test examined RC beam response to fire and air blast by subjecting specimens to extreme temperatures that, again, mimicked ISO-834 and then subjected the beam to an air blast (Zhai et al., 2016).

A unique two-step modeling approach was utilized in the analyses completed in this chapter. In this approach, concrete was divided into layers, where the number of layers determined based element dimensions which was initially selected after several trials to achieve sufficient balance between accuracy and computational cost. Layers were also selected based on

temperature profiles obtained from the thermal analysis stage so that each layer comprises of elements with the same average temperature. Consequently, each layer was assigned a unique compressive strength determined in accordance with Eurocode 2, part 1-2 temperature dependent strength listed in Table 3.7.

Results indicated that the proposed two-step modeling approach is sufficiently accurate and can be used to model the response of RC bridge columns under combined fire, impact, and blast. Discrepancies between FEM and test results mainly refer to the variation in thermal material properties and boundary conditions as no sufficient details were provided in any of the tests.

## Chapter 5 Critical Fire, Impact, Blast, Load Sequencing

### 5.1 Introduction

The validated multi-step modeling approach was used to establish a critical sequence for fire exposure, impact, and air blast. This was accomplished via a parametric study that examined the effects of various fire exposure conditions and column diameters when columns were impacted by a single unit truck at a prescribed speed and scaled distance was completed to identify the which produced maximum demand on studied columns. The critical sequence was identified by qualitatively examining resulting damage levels and final mid-height displacements and residual load capacities and comparing performance to columns subjected to just impact and blast.

### 5.2 Selected Load Sequences

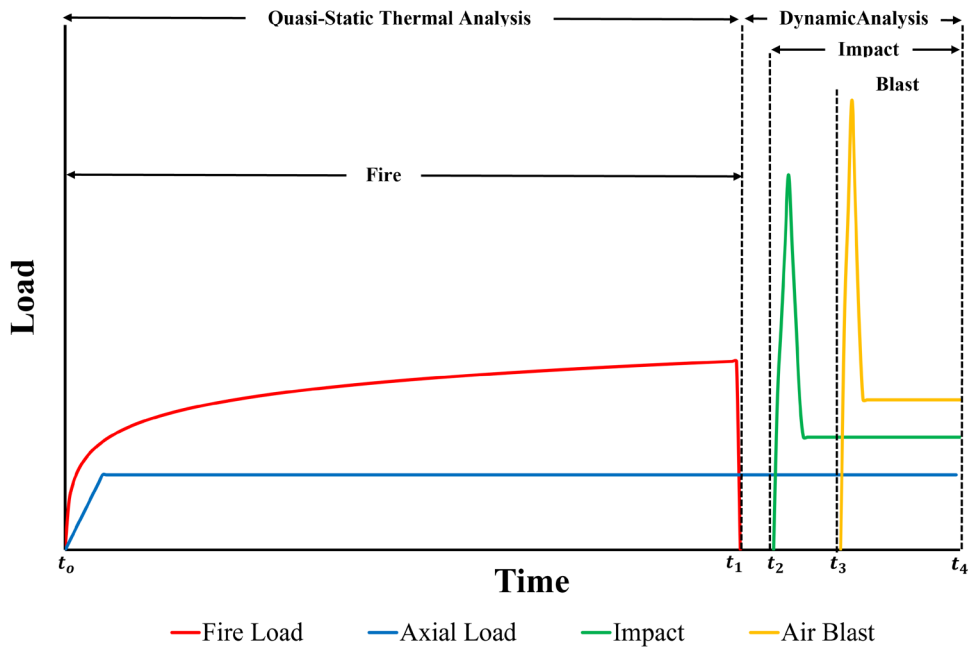
Previously completed research identified vehicle collision followed by air blast as the most severe sequence of those multi-hazards (Fang et al. 2021). In accordance with the labeling scheme from that study, models used to investigate effects of fire followed by impact and blast were identified as *F-I-B* and those investigating impact and blast followed by fire were identified as *I-B-F*. “*I*” referred to impact, “*B*” blast, and “*F*” fire. In thermal analysis, “*F*” corresponds to two exposure conditions “*FD*” and “*HD*”, where “*FD*” designated full surface area exposed to fire duration “*D*” and “*HD*” represents half periphery fire exposure scenarios with duration “*D*”, as discussed in Section 3.5.

### 5.2.1 Analytical procedure

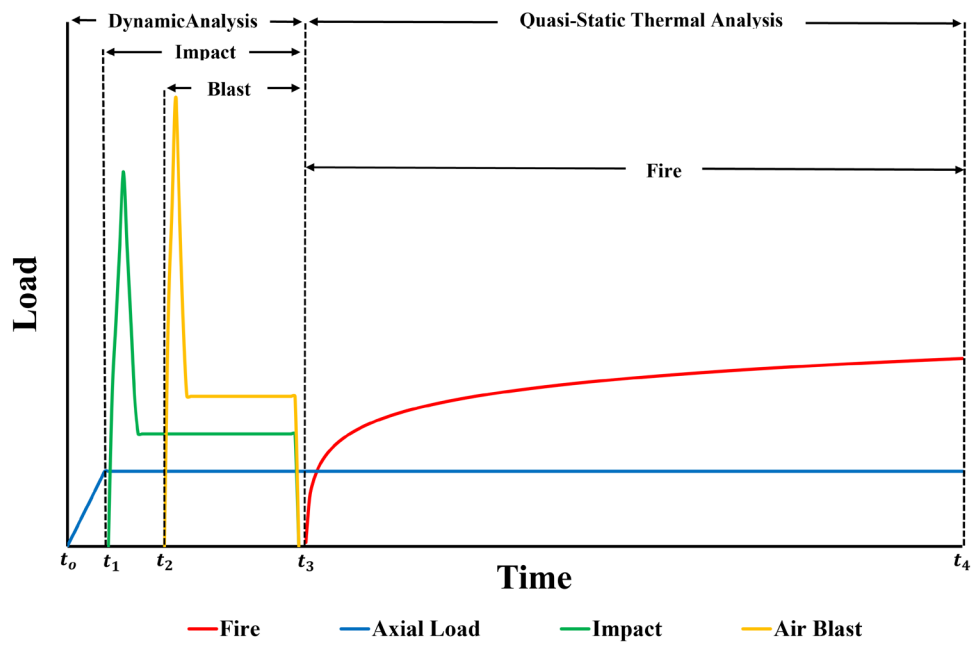
The procedure whereby demands were applied to isolated bridge columns for the studied load sequences is provided in the Figure 5.1 flow chart and further illustrated in Figure 5.2, which shows the sequences of fire, impact, blast, and axial load and main LS-DYNA commands used to implement each analysis.



Figure 5.1 Demand sequences and analyses flow chart



(a) F-I-B



(b) I-B-F

Figure 5.2 Studied Demand Sequences

### 5.3 Thermal Analysis – *F-I-B, I-B-F*

Four fire exposure cases were examined for each of the load sequences (Table 3.1). Bridge column diameters previously selected (i.e., 750 mm, 1050 mm, and 1350 mm) (see Figure 3.3) were studied for each fire scenario and load sequence.

#### *5.3.1 Fire, impact, blast – F-I-B*

For cases where fire was applied prior to impact and blast, stresses, strains, and deformed shapes resulting from the thermal implicit analyses were used as initial conditions for explicit structural analyses that followed. Prior to applying impact and blast loads, concrete strength degradation due to fire exposure was incorporated into the models using the procedure outlined in Section 3.9. Representative temperature contours and corresponding column layers are shown in Figure 5.3 for *F90* and *H90* fire exposures. As indicated in the figure, the *F90* column was divided into four layers, with layer 1 corresponding to a concrete temperature of 665 °C, layer 2 to 381 °C, and layer 3 to 204 °C. Layer 4, the column core, corresponded to no strength reduction since its temperatures were below 120 °C. The number of layers were initially selected based on temperature gradients and selected element size. In particular, elements having approximately the same average temperature were grouped in one layer. As temperatures were below 120 °C in the fourth element annulus and further decreased moving towards column core, four layers were sufficient to represent strength reduction due to temperature. A consistent procedure of layering was repeated for the rest of exposure conditions (i.e, *H90, F60, H60*).

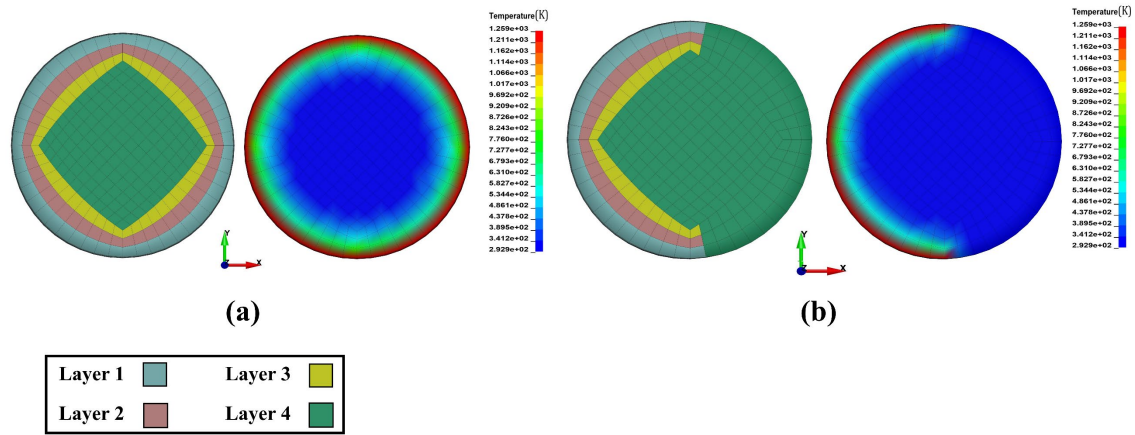


Figure 5.3 Temperature contours and corresponding column layers: (a) F90; (b) H90

The stress distribution from exposing a 750 mm diameter column to an *F90* fire is depicted in Figure 5.4. This figure illustrates that the column experienced coupled flexural-shear cracking through its middle third, which mimics reported test results (Chinthapalli et al., 2019).



Figure 5.4 Effective thermal stress distribution and crack propagation: (a) FEM, 750 mm diameter, F90-I-B; (b) Experiment (Chinthapalli et al. 2019)

### 5.3.2 Impact, blast, fire – I-B-F

For the second loading sequence concrete layers were not uniform along the column height due to damage caused by impact and blast in and around the SUT impact zone, as shown in Figure 5.5(a). As discussed previously, steel reinforcement was included in these thermal analyses and strength reductions from Table 3.8 were conservatively applied to reinforcement located in the bottom half of the column height based upon observed damage [Figure 5.5(b)]. A representative thermal stress distribution resulting from exposing the 1050 mm diameter column to a simulated *F90* fire scenario after impact and blast is illustrated in Figure 5.6. Compared to *F-I-B* case, this figure indicates that more severe thermal stresses distributed over the height of the column due to the damage caused by impact and blast prior to fire exposure.

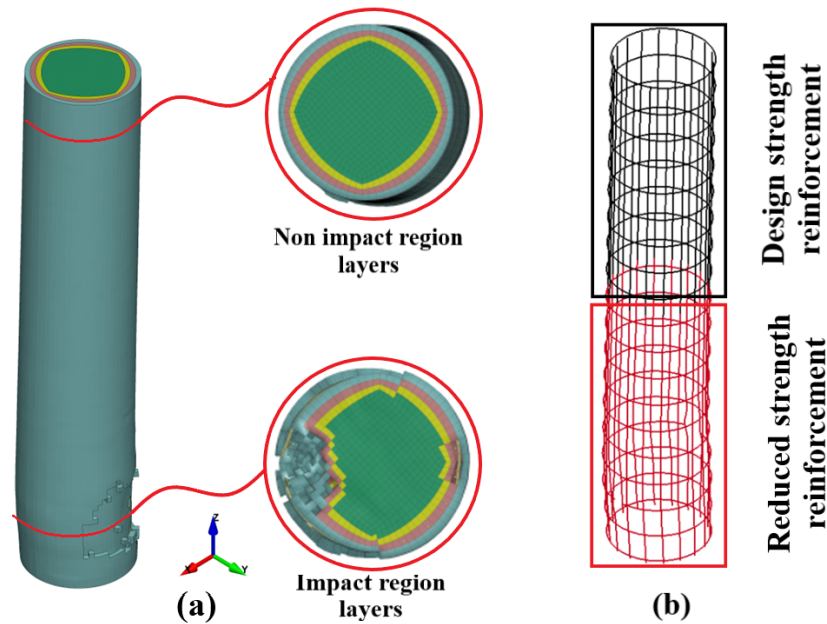


Figure 5.5 Fire damaged column: (a) concrete layers, (b) reinforcement layers

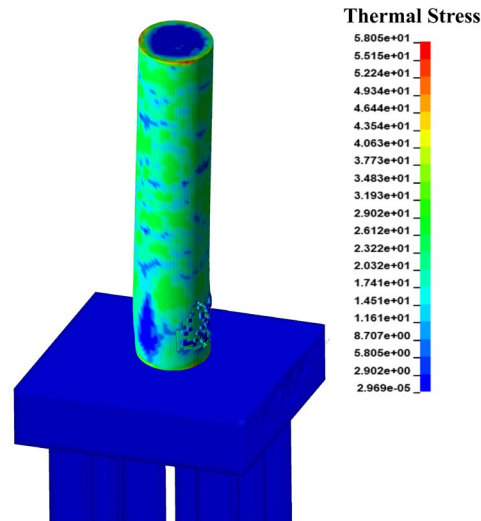


Figure 5.6 Effective thermal stress distribution, and crack propagation 1050 mm diameter, I-B-F90

#### 5.4 Isolated Column Response– *F-I-B, I-B-F*

Isolated column response was examined under selected fire exposures and extreme threats resulting from SUT impact at a speed of 120 km/h and air blast at a scaled distance of  $0.25 \text{ m/kg}^{1/3}$ , as specified previously (Fang et al. 2021). To investigate column performance under *F-I-B* and *I-B-F*, comparisons between final damage states, mid-height displacements, and residual capacities were made for all loading scenarios and column diameters. The critical loading scenario was ultimately identified by the sequence of demands that would most severely affect column performance.

##### *5.4.1 Damage propagation*

Representative results for 750-mm columns subjected to *F90-I-B* and *I-B-F90* loading sequences are presented. Figure 5.7 illustrates impact and blast load time histories and resulting mid-height displacement time histories for the two loading sequences. As shown in the figure, vehicle impact initiated approximately after 0.035 s, with peak impact load occurring when the engine hits the column at  $t = 0.055 \text{ s}$ . The explosive detonated at  $t = 0.060 \text{ s}$  and reached a

maximum pressure within 0.02 s. The figure shows that the peak impact force applied to the fire damaged column *F90-I-B* was lower than that applied to the undamaged column due to reduced flexural stiffness from fire exposure. The peak blast load also increased slightly for the *I-B-F90* since the column experienced less impact damage compared to the column that was initially fire damaged, which has a reduced strength and stiffness. The *F90-I-B* column permanently displaced 552 mm at mid-height while the *I-B-F90* displaced 579 mm at mid-height.

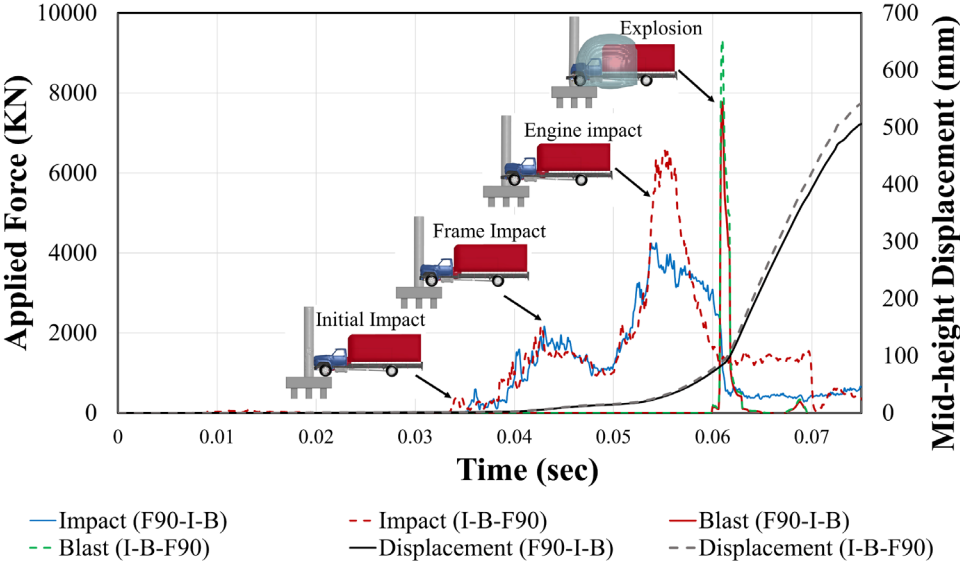


Figure 5.7 Applied load and mid-height lateral displacement time histories, 750 mm diameter, F90-I-B, I-B-F90

Final damage states experienced by the isolated column for both sequences are depicted in Figure 5.8. In this figure, the concrete damage index associated with *MAT-159* in LS-DYNA correlates with the effective plastic strain, with crack formulation corresponding to a damage index equal to 1 (i.e., red contours) and no damage corresponding to a damage index equal to 0 (i.e., blue contours). The erosion parameter defined the maximum plastic strain after which the

element would be deleted, with those elements representing spalled concrete in the simulations. The failure strain adopted for *MAT-24* equated to steel reinforcement fracture.

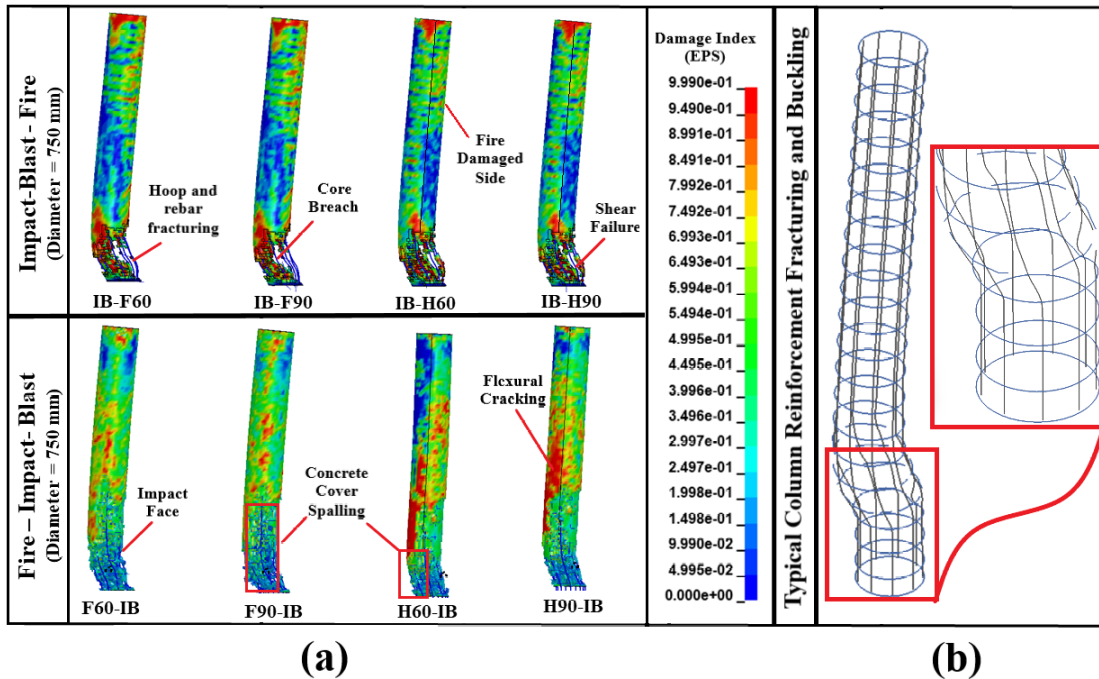


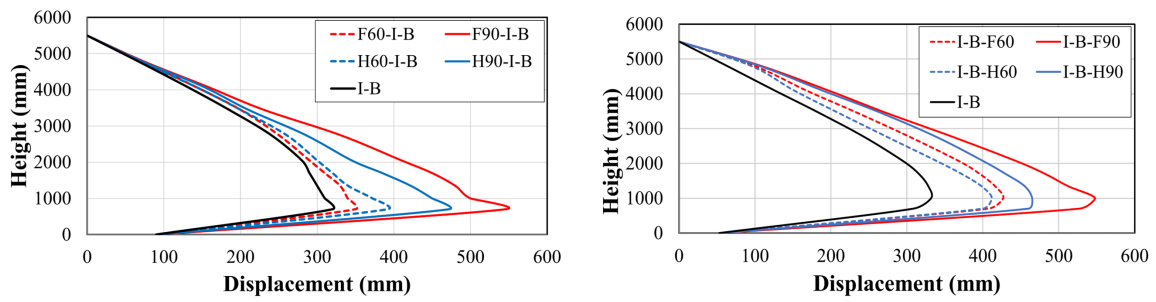
Figure 5.8 750 mm diameter column damage, F90-I-B and I-B-F90:(a) effective plastic strains, damage propagation; (b) reinforcement fracture, buckling

For both loading scenarios, the column experienced severe concrete spalling with the majority of longitudinal reinforcing bars buckled and fractured in the vicinity of the impact. More significant spalling was observed at the interface between thermally degraded concrete and concrete that retained its original design strength for half surface area fire exposure cases. Mid-height flexural cracks were evident on the non-impact side for cases where fire was applied prior to impact and blast as that concrete lost a significant portion of its strength. Shear failure at the column base occurred for both cases due to extensive concrete spalling and reinforcement

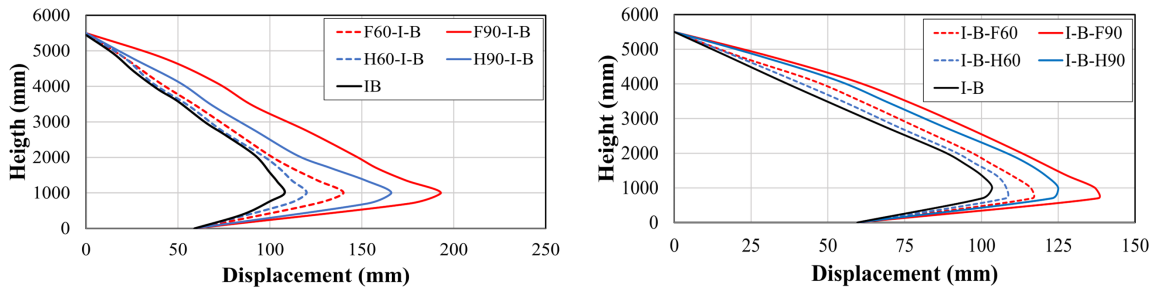
fractures. Although columns under both loading sequences largely behaved similarly, column core breaching was more severe for the impact, blast, fire cases.

#### 5.4.2 Effect of column diameter

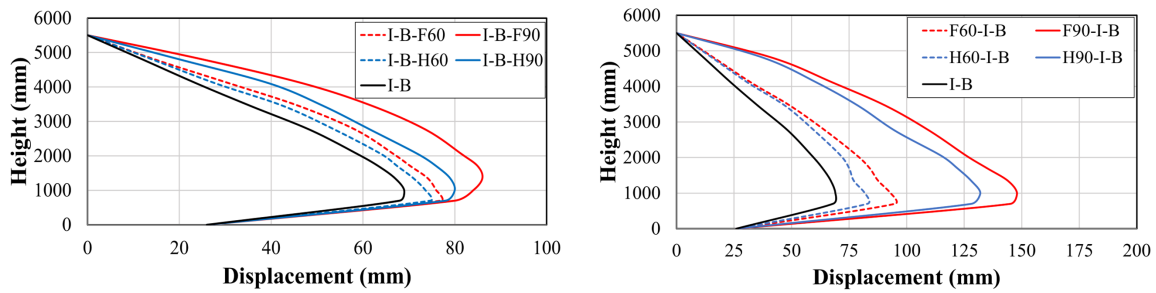
Figure 5.9 depicts lateral displacements under all exposure conditions for the two selected load sequences and compares those results to *I-B* cases. As expected, exposing columns to fire before or after impact and blast resulted in considerably larger displacements than those observed for similar columns not exposed to fire. Unsurprisingly, longer fire durations contributed to larger displacements for all column diameters under a given impact speed and blast intensity. Furthermore, larger displacements were observed in the smaller diameter columns. It is of interest to note that displacements corresponding to full surface area exposure for similar fire durations were slightly larger than those experienced when half the surface area was exposed. Based on previous observations, *F90-I-B* and *I-B-F90* were shown to be the most critical loading scenarios. Except for the 750 mm diameter column, displacements from exposure to fire prior to impact and blast were larger than those in which fire was applied after impact and blast. This is because the 750 mm diameter columns experienced more severe damage before applying fire (i.e., after *I-B*), as shown in Figure 5.10. Column core breaching was also observed in the 750 mm column for this sequence.



(a)



(b)



(c)

Figure 5.9 Column lateral displacements, all study cases: (a) 750-mm diameter; (b) 1050-mm diameter; (c) 1350-mm diameter

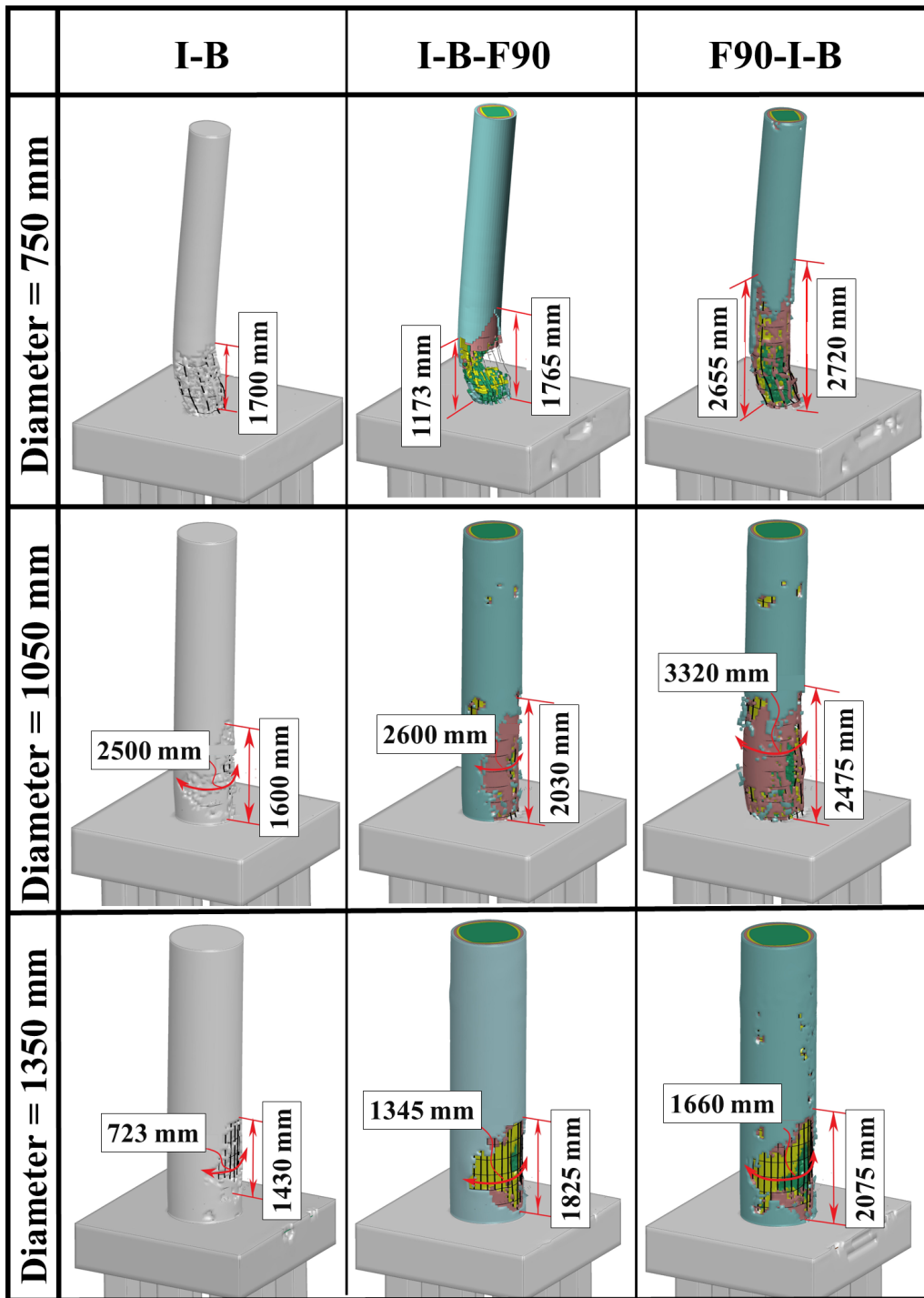


Figure 5.10 Final damage states, studied column diameters and loading scenarios

### 5.4.3 Residual capacity

In similar fashion to previous studies (Fang et al., 2021a, 2021c; V. Kodur et al., 2017), column residual capacities were determined using push down analyses. After applying each load sequence, the applied axial load was gradually increased until a maximum value was attained. The ratio of residual to nominal column capacities ( $\lambda_{res} = P_{res}/P_n$ ) was calculated for all column diameters and loading sequences, with nominal capacities calculated according to AASHTO-LRFD column design specifications (AASHTO 2020).

Figure 5.11 depicts  $\lambda_{res}$  estimates for all column diameters and loading sequences. Irrespective of loading sequence and column diameter, exposing RC columns to fire significantly reduced residual capacities when compared to cases involving impact and blast. For example,  $\lambda_{res}$  for the 1350 mm diameter column when subjected to *I-B*, *F90-I-B*, and *I-B-F90* equaled 39%, 28%, and 33%, respectively. This figure also indicates that exposure to fire prior to other events most severely reduced capacity for the 1050 mm and 1350 mm column diameters. On the other hand, 750 mm diameter columns contributed to lower residual capacities when exposed to fire after impact and blast which signifies that *I-B-F* would be the critical loading sequence in smaller column diameters.

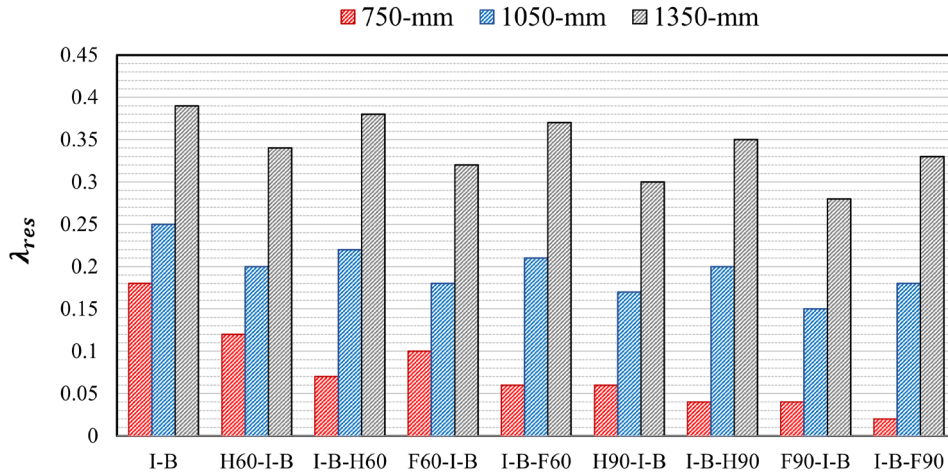


Figure 5.11 Residual axial capacities for studied column diameters and load sequences

### 5.5 Summary and Conclusions

In this chapter, the developed modeling approach was used to examine the response of isolated bridge columns subjected to various combinations of fire, impact, and blast demands. Simulation results were used to identify critical load sequence(s). For the columns and loading sequences examined, results indicated that:

- 1) During a multi-hazard event involving fire, impact, and blast, irrespective of loading sequence, bridge column damage encompassed:
  - (a) permanent deformation with concrete cover spalling.
  - (b) plastic hinge formation in the vicinity of impact region.
  - (c) flexural cracking extended to the non-impacted column face.
  - (d) shear failure and column core breaching for 750 mm diameter columns.
  - (e) longitudinal reinforcement and hoop buckling and fracture in collision region.
- 2) Exposing columns to fire in addition to impact and blast produced more severe damage compared to impact and blast without fire.

- 3) For a given impact speed and blast intensity, exposing columns to longer fire durations increased damage and reduced residual capacity.
- 4) Slightly larger permanent deformations and more damage were observed when the entire column periphery was exposed to fire.
- 5) Fire prior to impact and blast found was a more critical load sequence for the 1050 mm and 1350 mm columns. Although the 750 mm diameter columns experienced similar failure mode (i.e., core breach and shear failure) in both load sequences, more pronounced damage, larger displacements, and lower residual capacities were observed in post impact and blast fire exposure (i.e., *I-B-F*). Therefore, fire applied before impact and blast was assumed to be the worst-case scenario.
- 6) In both studied sequences, a 750 mm diameter column was liable to the coupled fire, impact, and blast compared to the two larger diameters. The resulting damage was potentially repairable for 1050 mm and 1350 mm diameter.
- 7) Establishing concrete bridge component repair feasibility commonly occurs after visual inspections and non-destructive tests, as discussed in the AASHTO *Manual for Condition Evaluation and LRFR of Highway Bridges* (AASHTO, 2003). Given that, for the 1050-mm 1350-mm diameter columns, analyses indicated that spalling was relatively localized with limited reinforcement buckling they could be deemed repairable. More extensive parametric studies are required to verify this conclusion and are part of ongoing research.

## Chapter 6 Isolated Column Performance Evaluation, F-I-B

### 6.1 Introduction

As simulation results demonstrated that the 750 mm diameter column failed after imposing the selected extreme demands and despite that these columns were more vulnerable to *I-B-F*, they experienced severe damage, large permanent set, and considerably low residual capacities under *F-I-B*. Therefore, column response to *F-I-B* is selected to be further investigated as it corresponds to the more critical sequence of loading for the 1050 mm and 1350 mm diameter columns. Consequently, this chapter summarizes computational work used to evaluate performance of isolated, RC, round bridge columns from *F-I-B* for a set range of fire exposures and column diameters. Damage parameters included observed severity, estimated concrete spalling volume, permanent set, residual axial load capacities, and shear demand to capacity ratios. Damage levels were classified into six categories based on previous research studies that examined the damage of RC columns subjected to vehicle impact and air blast (G. Liu, 2012; Sharma et al., 2012; Williamson et al., 2011; Yi et al., 2014b).

### 6.2 Bridge Column Damage Levels

Previous research indicates that fire exposure may lead to partial or complete structural collapse for cases in which intense, long duration, exposures occur (Garlock et al., 2012; Khoury, 2000; V. Kodur et al., 2010). In many other circumstances, fire damage might not be apparent and structures could maintain acceptable levels of serviceability (Moftah, 2008; Qin et al., 2021; Raut & Kodur, 2012). Visual assessment, such as examining concrete discoloration and thermal spalling could be used to help quantify damage levels (Qin et al., 2021). Post fire residual strengths can also be established using non-destructive techniques, such as the Schmidt hammer and ultrasonics, and destructive mechanical tests, such as coring (Qin et al., 2021).

Earlier research defined six damage categories to qualitatively evaluate column performance when subjected to coupled impact and blast (Fang et al. 2021). The categories were selected based on previous studies that examined the damage of RC columns subjected to vehicle impact and blast (G. Liu, 2012; Sharma et al., 2012; Williamson et al., 2011; Yi et al., 2014b). Sharma et al. (2012) categorized column damage caused by vehicle collision into: (i) minor concrete spalling; (ii) severe concrete cracking and longitudinal reinforcement buckling; and (iii) loss of columns capacity and reinforcement fracturing. Liu et al. (G. Liu, 2012) numerically studied the response of bridge columns to vehicle collisions and classified column damage into: (i) concrete surface spalling; (ii) breakage of pier; (iii) reinforcement fracturing; and (v) plastic hinge formulation. Williamson (2011) identified four damage levels of bridge column subjected to air blast: (i) surface crack propagation; (ii) concrete cover spalling; (iii) direct shear failure; and (iv) column core breaching. Yi et al. (2014) examined the performance of an RC highway bridge under blast loading and classified column damage into: (i) concrete cover spalling; (ii) shear cracking; (iii) reinforcement fracturing; and (iv) plastic hinge formulation. Six categories that match those in an earlier research (Fang et al., 2021b) were selected from the previously cited literature to better represent column damage. Damage categories are summarized in Table 6.1 and corresponding figures.

Table 6.1 Bridge column damage categories

Damage Category	Description	Representative Figure
Surface Crack Propagation (M1)	<ul style="list-style-type: none"> <li>• Concrete surface cracking.</li> <li>• Flexural cracks at the column's mid-height.</li> <li>• Diagonal shear cracks near the impact location and propagated to the non-impacted side of the column.</li> </ul>	Figure 6.1
Concrete Cover Spalling (M2)	<ul style="list-style-type: none"> <li>• Concrete spalling along column's height.</li> </ul>	Figure 6.2
Plastic Hinge Formulation (M3)	<ul style="list-style-type: none"> <li>• Plastic hinge in the vicinity of impact location.</li> <li>• Recognized when concrete cover spalling accompanies column core cracking, reinforcement yielding, and localized buckling.</li> </ul>	Figure 6.3
Direct Shear Failure (M4)	<ul style="list-style-type: none"> <li>• Occurs at the column base due to extensive concrete spalling, buckling and fracturing in longitudinal reinforcement, and hoops failure.</li> <li>• Applied lateral load exceeds column's capacity.</li> <li>• Results in significant reduction in structural integrity and potential collapse of the column or entire bridge system.</li> </ul>	Figure 6.4
Reinforcement Failure (M5)	<ul style="list-style-type: none"> <li>• Failure in both longitudinal reinforcements and ties.</li> </ul>	Figure 6.5
Column Core Breach (M6)	<ul style="list-style-type: none"> <li>• Observed in the vicinity of impact location in the columns that experienced direct shear failure.</li> <li>• Columns can no longer support axial loads and failure is unavoidable.</li> </ul>	Figure 6.6

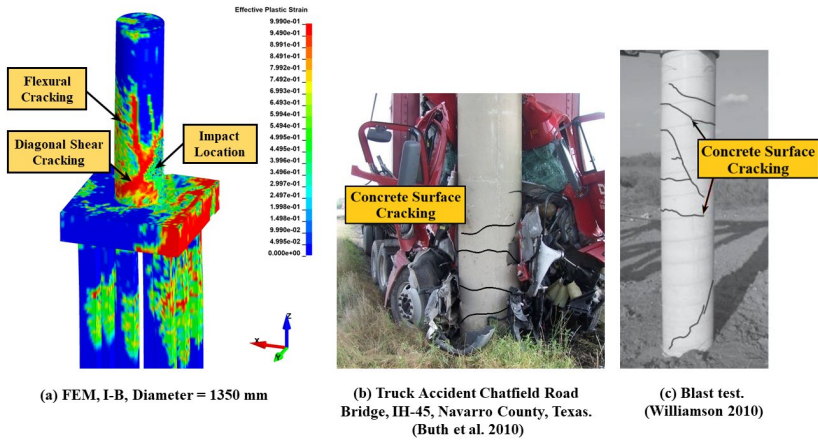


Figure 6.1 Surface crack propagation - M1

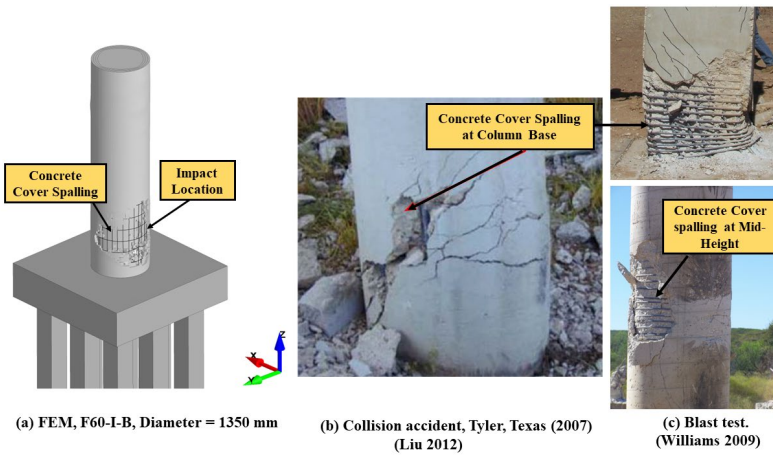


Figure 6.2 Concrete cover spalling - M2

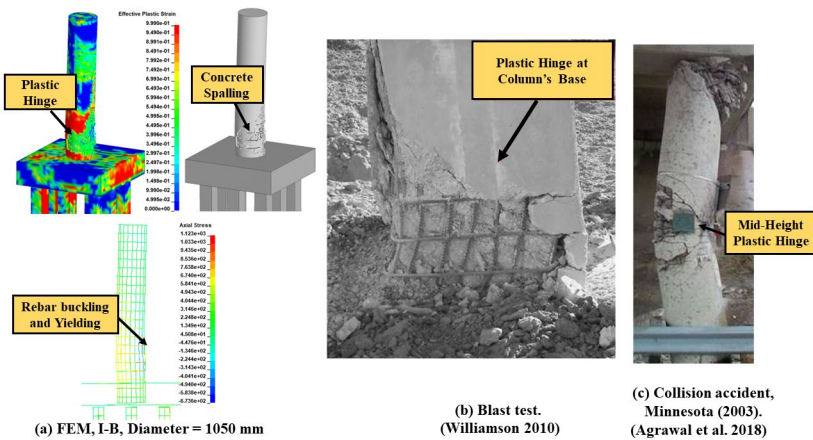


Figure 6.3 Plastic hinge formulation - M3

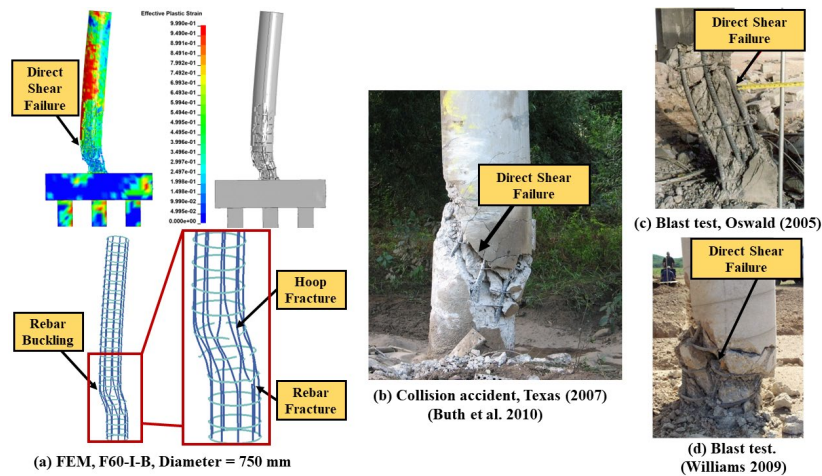


Figure 6.4 Direct shear failure - M4

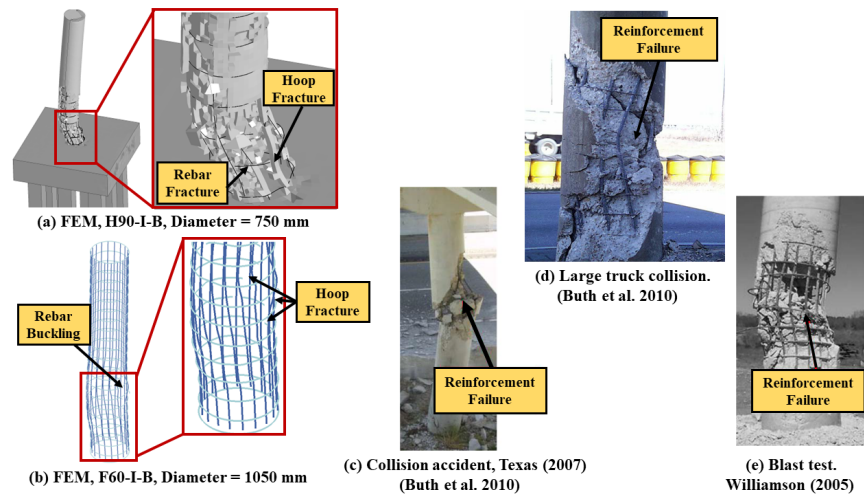


Figure 6.5 Reinforcement failure – M5

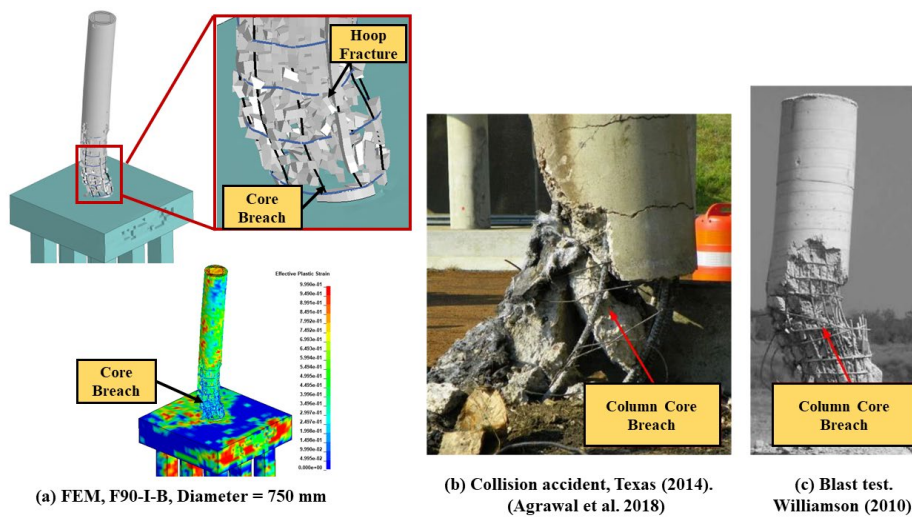


Figure 6.6 Column core breach - M6

### 6.3 Fire Damaged Isolated Bridge Column Performance under Impact and Blast

Isolated columns from Figure 3.3 were examined using the analysis procedure outlined in 3.9 under various fire conditions from Table 3.1 prior to a 120 km/h SUT collision and air blast at a scaled distance of  $0.25 \text{ m/kg}^{1/3}$ . Results were again compared to those from analyses of similar isolated columns subjected to impact and blast (Fang et al., 2021a).

#### 6.3.1 Damage propagation

Resultant effective stresses after exposing the columns to a simulated, *F90* are depicted in Figure 6.7. Resulting thermal stresses produced flexural-shear cracks over the column height, which matches reported test results, as discussed in Section 5.3.1 (Chinthapalli et al., 2019).

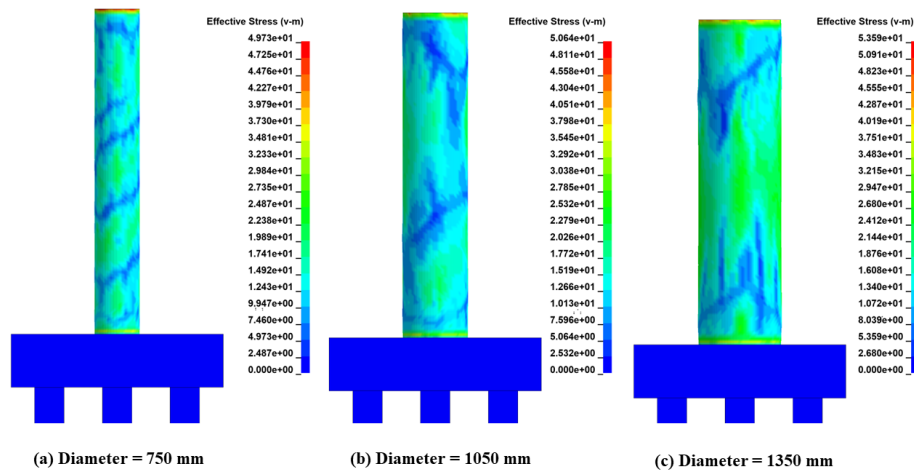


Figure 6.7 Effective thermal stress distribution and crack propagation, F90

Damage was examined incrementally so that propagation and resulting failure mechanisms could be clearly identified (Figure 6.8, Figure 6.10, and Figure 6.12). In addition to tracking damage and crack propagation, the ratio between buckled longitudinal reinforcement to the total number of longitudinal reinforcing bars ( $\gamma_{br}$ ) was estimated for all cases. Applied impact and blast loads and peak column displacements are shown in conjunction with applied

demand sequences in Figure 6.9, Figure 6.11, and Figure 6.13. It is of interest to mention that in these figures, measured impact and blast forces increased with increasing column diameter as larger columns are stiffer and have more contact with the applied loads. Major findings are summarized in Table 6.2.

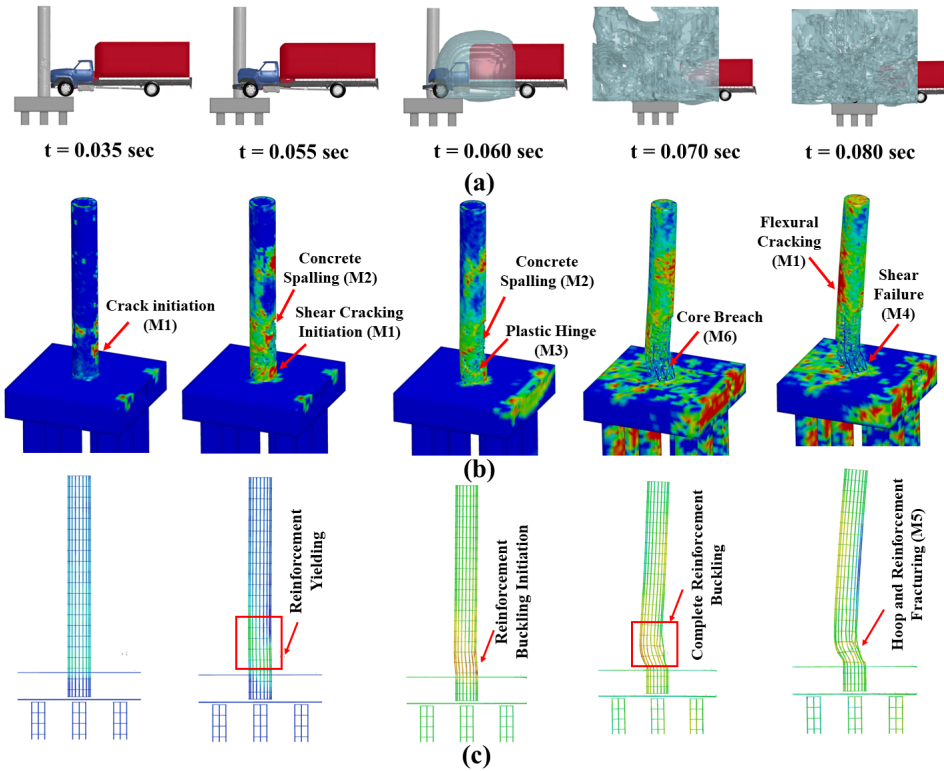


Figure 6.8 F90-I-B 750 mm diameter impact and blast demand progression, and resulting damage: (a) impact and blast time steps progression; (b) column effective plastic strains and damage propagation; (c) reinforcement response and damage propagation

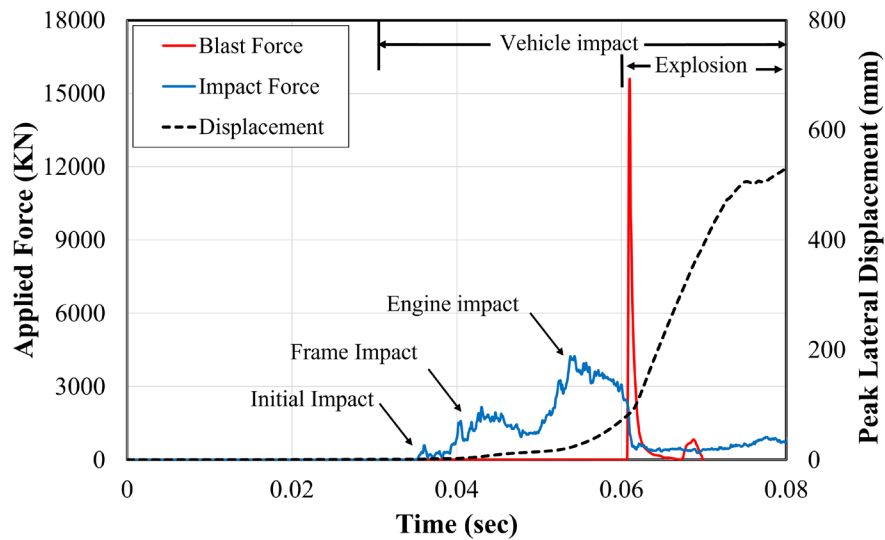


Figure 6.9 Applied load, and mid-height lateral displacement time histories, 750 mm diameter, F90-I-B

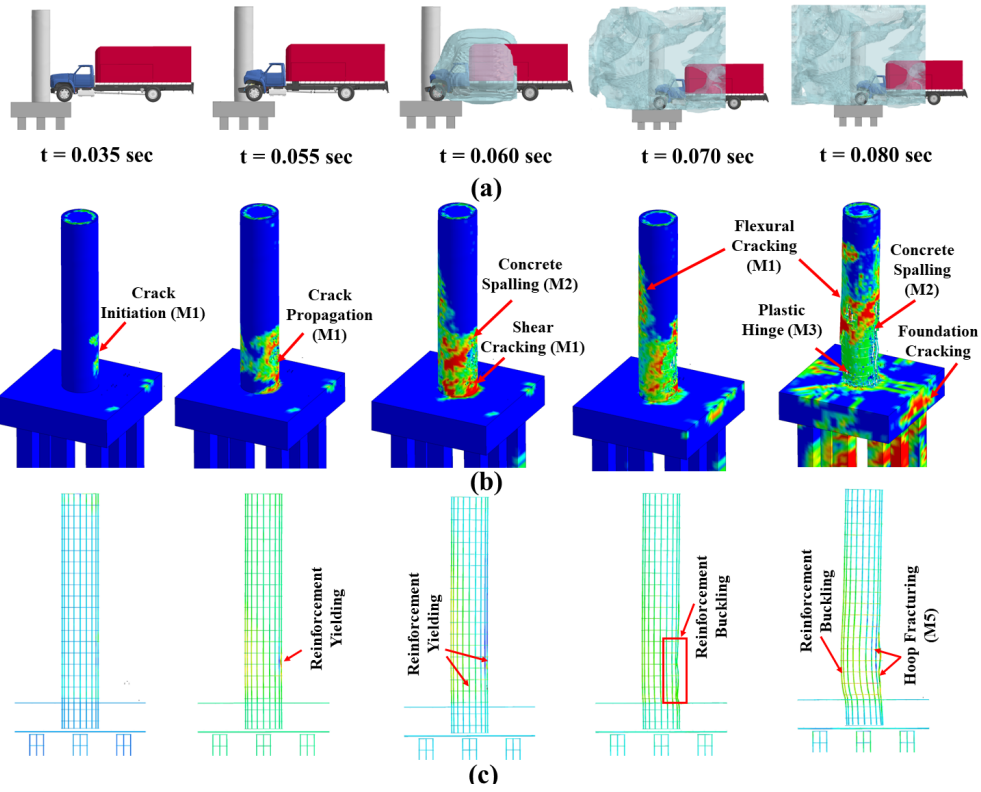


Figure 6.10 F90-I-B 1050 mm diameter impact and blast demand progression, and resulting damage: (a) impact and blast time steps progression; (b) column effective plastic strains and damage propagation; (c) reinforcement response and damage propagation

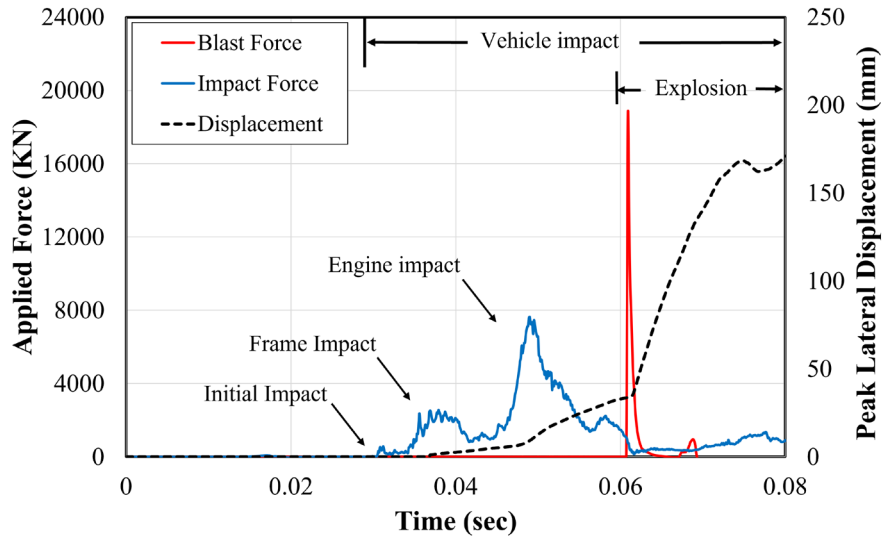


Figure 6.11 Applied load, and mid-height lateral displacement time histories, 1050 mm diameter, F90-I-B

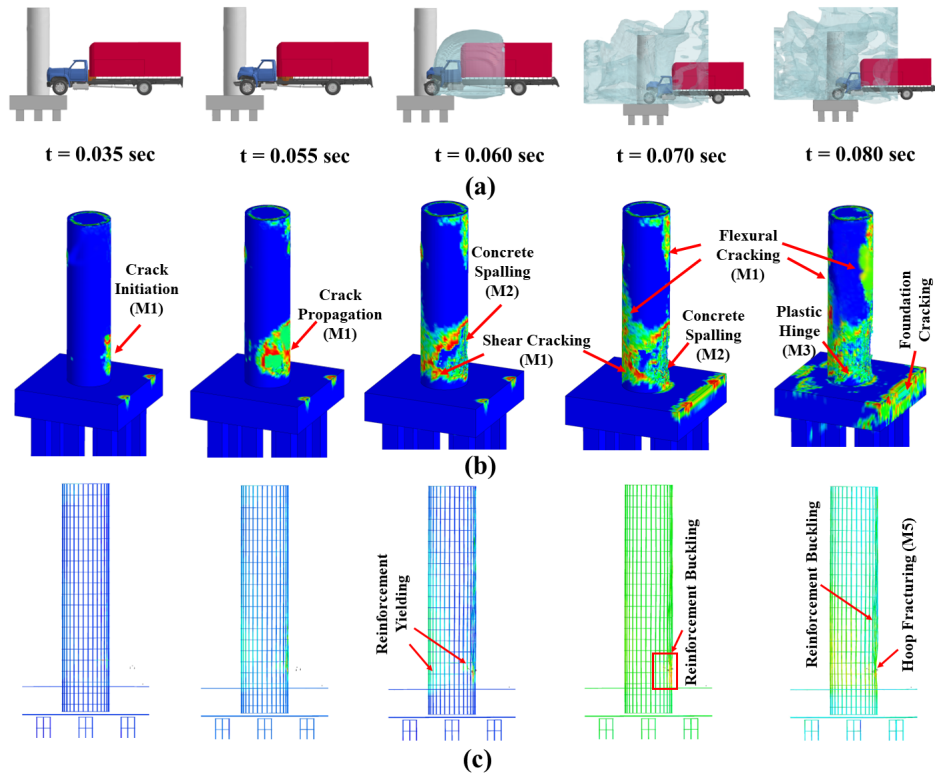


Figure 6.12 F90-I-B 1350 mm diameter impact and blast demand progression, and resulting damage: (a) impact and blast time steps progression; (b) column effective plastic strains and damage propagation; (c) reinforcement response and damage propagation

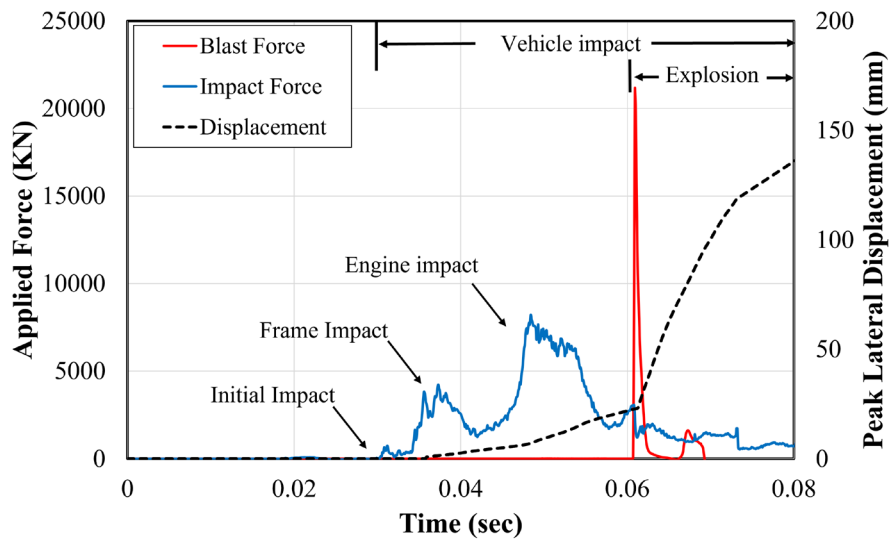


Figure 6.13 Applied load, and mid-height lateral displacement time histories, 1350 mm diameter, F90-I-B

Table 6.2 Response of 750 mm, 1050 mm, and 1350 mm diameter columns, F90-I-B

Time Step		t = 0.035 sec	t = 0.055 sec	t = 0.060 sec	t = 0.07 sec	t = 0.08 sec
Demand Progression		Initial SUT Collision	SUT Engine impact	Air Blast Detonation	Blast Wave Engulfment	Blast Wave Propagation
D (mm)	Response					
750	Damage	Cracks localized in impact region.	Cracking throughout height, on impact and non-impact faces; cover spalling at impact location; and shear cracks at base.	Extensive concrete spalling; shear cracks; mid-height flexural cracks; and Plastic hinge formed.	Extensive concrete spalling and core breaching initiated.	Shear failure at the base; concrete core completely breached; and cracks in foundation.
	Reinforcement	Normal	Two bars yielded at base	Seven bars buckled ( $\gamma_{br} = 77.8\%$ )	all bars buckled. ( $\gamma_{br} = 100\%$ )	Two bars and five hoops fractured.
	Displacement	0	61	193	439	552
1050	Damage	Cracks localized in impact region.	Cracks on impact and non-impact faces.	Shear cracks at base; and mid-height flexural cracks.	Cracks throughout height; concrete spalled in impact region.	Spalling in non-impact face; plastic hinge formed at the base; and cracks in foundation.
	Reinforcement	Normal	Two bars yielded at base	All longitudinal bars yielded at base	Five bars buckled. ( $\gamma_{br} = 28\%$ )	Two bars and four hoops fractured.
	Displacement	0	17	66	118	174
1350	Damage	Cracks localized in impact region.	Cracks on impact and non-impact faces.	Shear cracks at base; and mid-height flexural cracks	Cracks throughout height; and concrete spalled in impact region.	Widespread concrete cover spalling and cracking along the column's height; cracks in foundation.
	Reinforcement	Normal	Normal	All longitudinal bars yielded at base	three bars buckled. ( $\gamma_{br} = 10\%$ )	Four hoops fractured; six bars buckled.
	Displacement	0	11	53	102	147

### 6.3.2 Final damage states, concrete spalling volume, permanent sets

Figure 6.14 and Figure 6.15 depict final damage states of permanent sets under different fire exposures for given impact and blast demands. For all column diameters, damage states resulting from fire, impact, and blast were compared to the case in which columns were subjected to impact and blast.

As expected, for a given impact speed and standoff distance, longer fire duration contributed to more significant damage due to significant concrete strength reduction. Concrete spalling, significant loss of strength and stiffness, and reinforcement buckling were observed for all cases. Their severity increased with increasing fire duration and exposed surface area.

As expected, column performance was highly influenced by diameter, with larger permanent sets observed for smaller diameters, as illustrated in Figure 6.15. This is mainly due to both flexural stiffness and fire damage intensity, where smaller column diameters are less stiff and more vulnerable to fire damage compared to larger column diameters. In particular, the ratio of the volume of concrete with strength reduction to the volume of concrete that maintains its design strength ( $\lambda_{FV}$ ) increases with decreasing column diameter. For instance, when columns exposed to *F90*,  $\lambda_{FV}$  was 52%, 41%, and 29% for the 750 mm, 1050 mm, and 1350 mm column diameters, respectively.

Concrete spalling in the three column diameters under all loading scenarios was estimated using LS-DYNA's eroded volume time history plots. A representative plot for the 750 mm diameter column is shown in Figure 6.16. Compared to a similar column under impact and blast loads, fire damaged columns exhibit more spalling.

In relation to the potential column repairs, inspectors would need to evaluate the level of deterioration using visual inspection, nondestructive testing, and potential analyses in accordance with *AASHTO Manual for Condition Evaluation and LRF of Highway Bridges* and FHWA regulations to determine if repairs are feasible (AASHTO, 2003; FHWA, 1995; Tapan & Aboutaha, 2008). Except for the *F90-I-B* loading scenario, since damage experienced by the 1050 mm and 1350 mm diameter columns was localized to the area of impact, a zone having lower flexural demands, and since the ratio of spalled to original concrete volume was relatively small, it is believed that the damage could be repaired. More comprehensive research is certainly needed to validate this presumption.

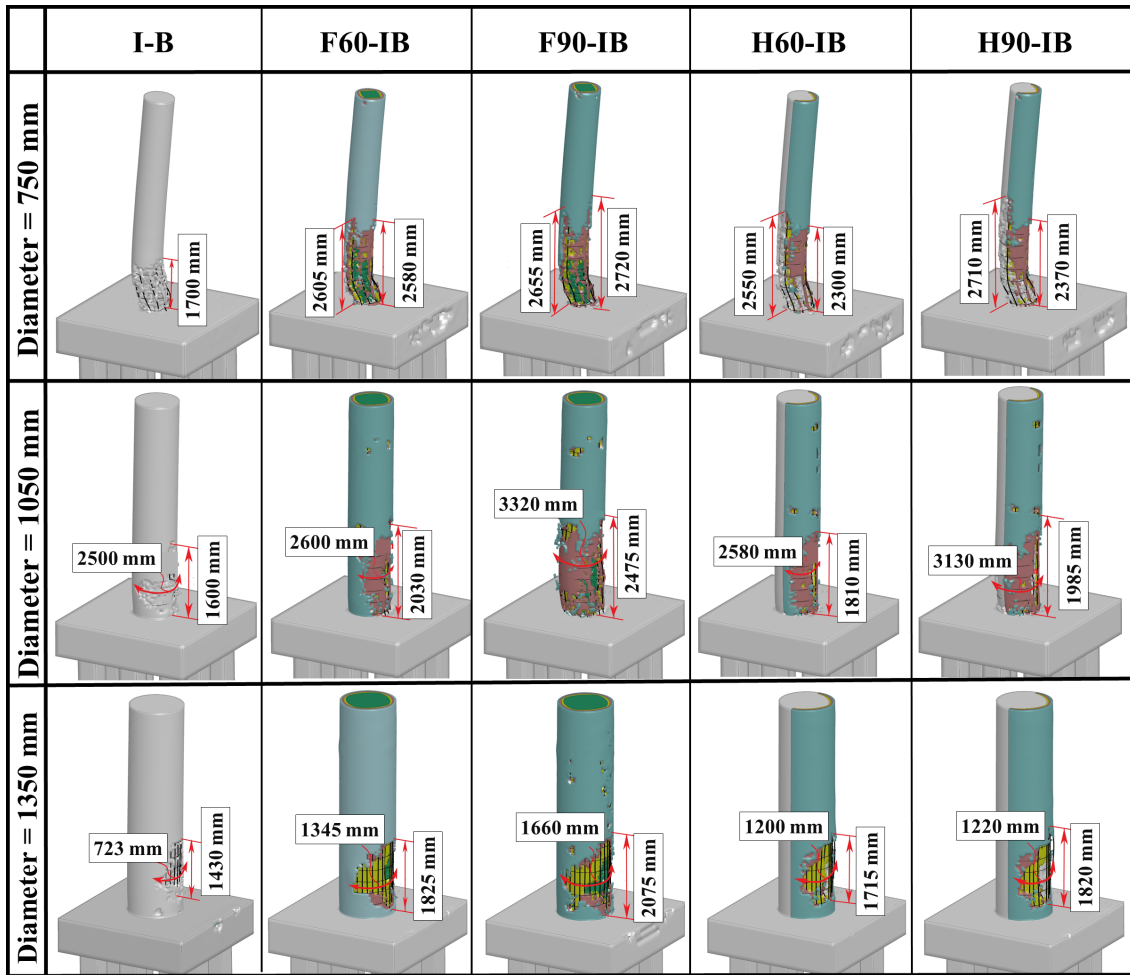


Figure 6.14 Final damage states for studied column diameters and demand scenarios

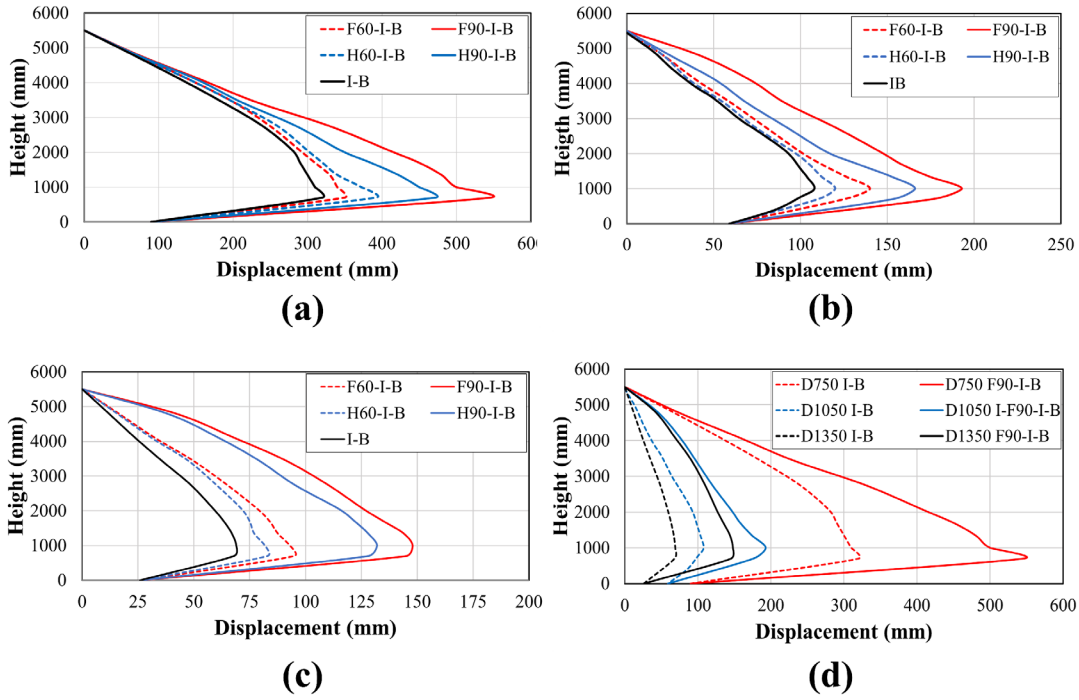


Figure 6.15 Column lateral displacements: (a) 750 mm diameter; (b) 1050 mm diameter; (c) 1350 mm diameter; (d) all diameters.

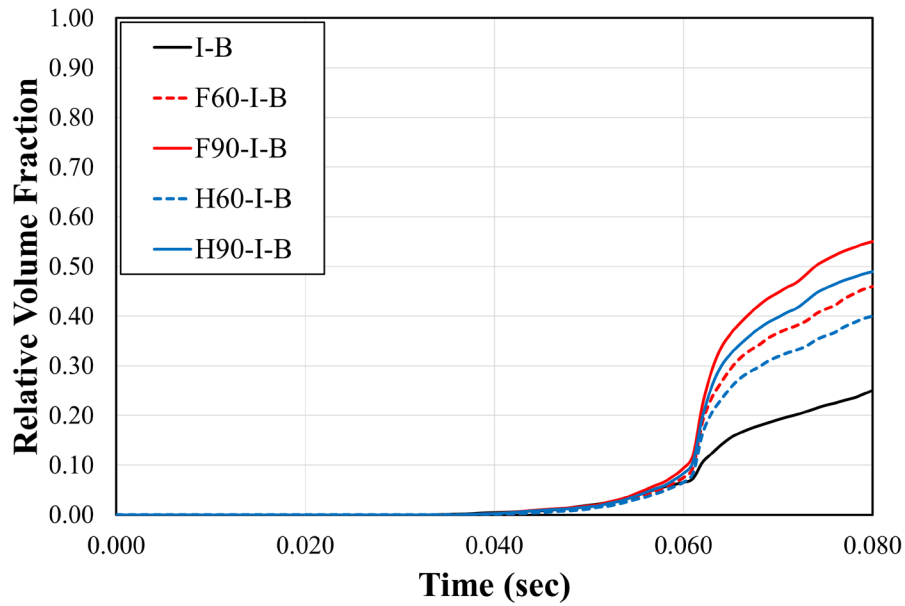


Figure 6.16 Spalled concrete volume fraction, 750 mm diameter

### 6.3.3 Residual axial load carrying capacity

A representative “push down” curve for a 1050 mm diameter column under the *F60-I-B* demands is shown in Figure 6.17. As in Fang et al. (2021c), fluctuation in axial load observed during impact and blast (i.e., the blue portion of the curve) was due to inertial effects associated with the dynamic load application (Bao & Li, 2010; K.-C. Wu et al., 2011).

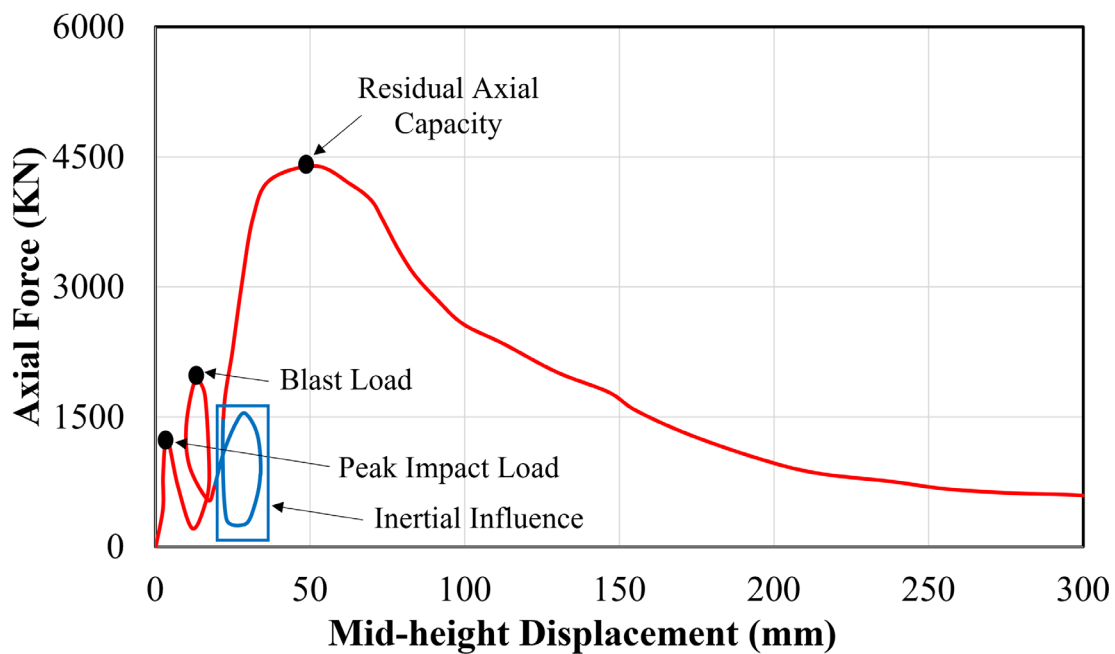


Figure 6.17 Load-mid height displacement curve, 1050 mm diameter, F60-I-B

Similar to the previous study (Fang et al. 2021), a ratio was calculated to evaluate performance involving column residual and nominal capacities ( $\lambda_{res}$ ) (Equation 10). The nominal capacity ( $P_n$ ) was calculated using Equation 11 in accordance with the AASHTO-LRFD RC column design specifications (AASHTO 2020):

$$\lambda_{res} = P_{res} / P_n, \quad \text{Equation. 10}$$

$$P_n = 0.85 f'_c (A_c - A_s) + f_y A_s, \quad \text{Equation. 11}$$

where:  $P_{res}$  is the residual capacity;  $P_n$  is the nominal capacity;  $f'_c$  is the unconfined concrete compressive strength;  $A_c$  is the cross-sectional area; and  $f_y$  and  $A_s$  are the yielding strength and cross-sectional area of longitudinal steel reinforcement, respectively.

Residual axial load capacities for all column diameters and loading scenarios are shown in Figure 6.18. Each bar corresponds to  $\lambda_{res}$  with corresponding percentages indicating reduction in capacity from that column's AASHTO design value. Irrespective of column diameter, applying fire before impact and blast reduced residual axial capacity, with longer fire exposure producing the greatest capacity reductions. Additionally, for any fire duration, columns exposed to fire around their entire periphery had lower residual capacities.

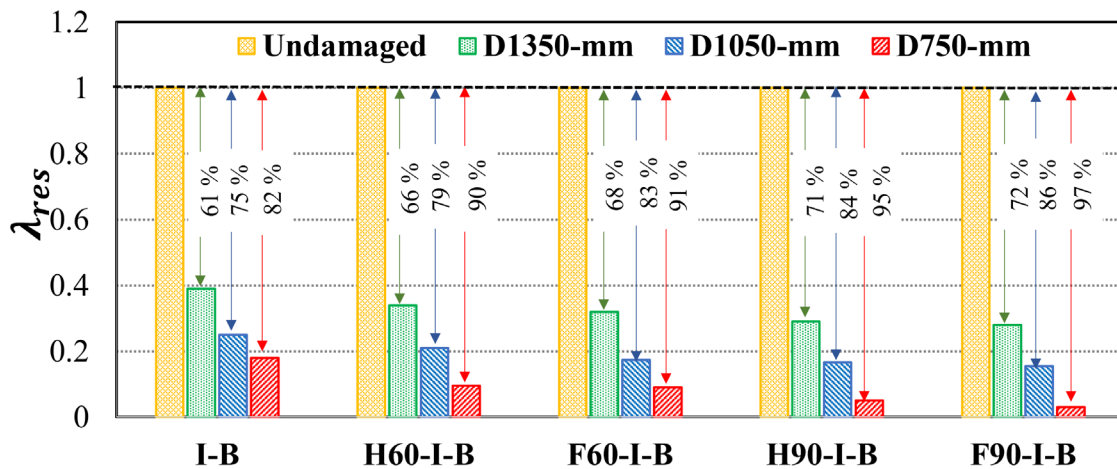


Figure 6.18 Residual axial capacities for all column diameters and loading scenarios

#### 6.3.4 Shear resistance

Shear failure at the column base was shown to be a critical damage state that significantly influenced performance. As a result, the ratio of shear demand ( $V_d$ ) to capacity ( $V_c$ ) which is designated by  $\lambda_{sh}$ , was calculated for all column diameters and studied loading scenarios.

LS-DYNA's *Cross Section Plane Database* option was utilized to calculate column shear demand. Maximum shear forces were calculated at twelve equally spaced cross sections along the height of the column. Representative shear diagrams for the three studied column diameters under various fire exposures are illustrated in Figure 6.19, with maximum shear demand found at the column base. Irrespective of loading scenario, shear demand increases with increasing column diameter as expected. Columns subjected to full surface area fire exposure experienced lower shear demands due to degradation of concrete strength prior to impact and blast.

Column shear capacity was estimated using a separate LS-DYNA simulation where an applied lateral load at the column base was gradually increased until failure. As expected, columns experiencing longer fire exposures had the lowest shear capacity. Shear demand to capacity ratios were compared cases involving solely impact and blast and are presented in Figure 6.20. Shear failure is expected when the ratio is greater than 1.0. Results indicate that exposing columns to fire prior to impact and blast contributed to larger demand to capacity ratios, which indicates lower shear resistance. Consequently, 750 mm diameter columns were expected to experience shear failure and 1050 mm columns maintained an acceptable shear capacity for all cases except *F90-I-B*. The 1350 mm columns maintained acceptable shear capacity.

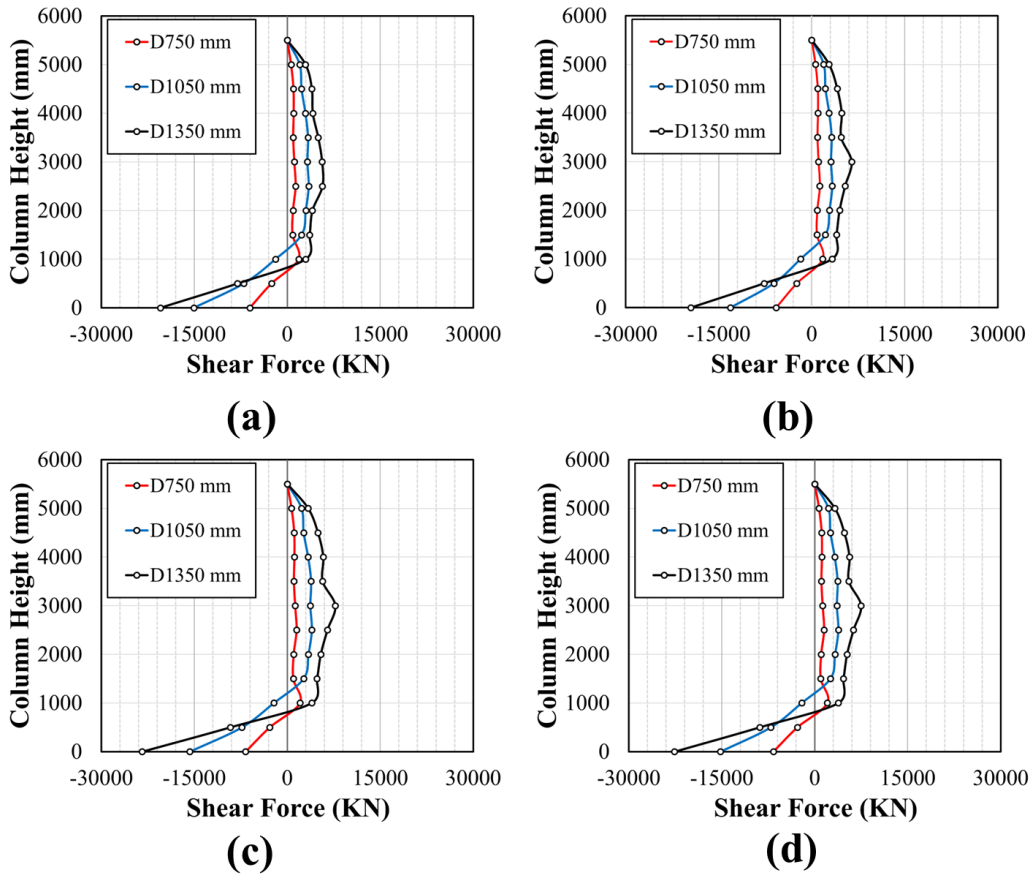


Figure 6.19 Column shear diagrams: (a) F60-I-B; (b) F90-I-B; (c) H60-I-B; (d) H90-I-B

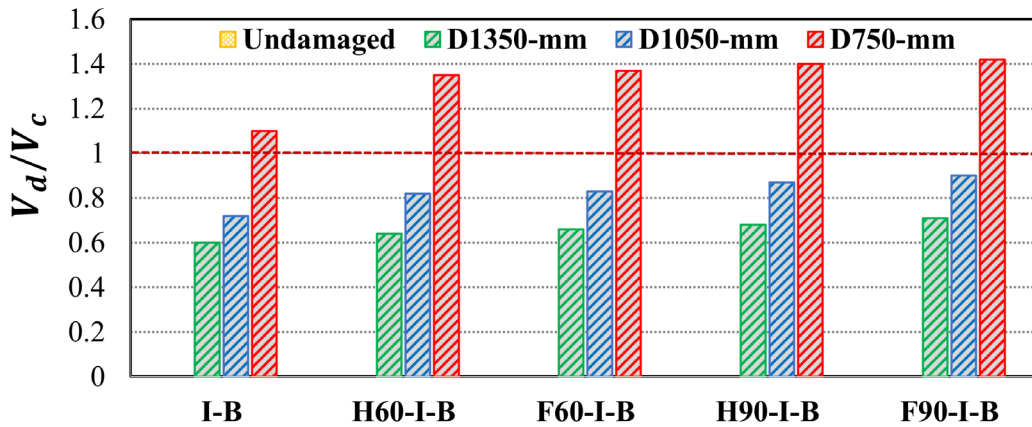


Figure 6.20 Shear demand to capacity ratios

## 6.4 Summary and Conclusions

This chapter summarized numerical simulations of fire-damaged RC bridge columns when subjected to vehicle collision and air blast. Four fire exposure conditions and three column diameters were studied for a particular single unit truck (SUT) speed and explosive scaled distance ( $Z$ ). Simulation results were used to assess isolated pier column performance under the combined effects of fire, impact, and blast. Quantitative performance assessments were completed based on damage propagation and severity, and volume of spalled concrete, permanent lateral displacements, residual axial load capacities, shear demand to capacity ratios, and qualitative damage levels categories. Simulation results and damage categories are presented in Table 6.3. Several design parameters were constant for these studies:

- 1% column reinforcement ratio ( $\rho_s$ ).
- 300 mm transverse reinforcement ( $S_t$ ) spacing.
- 5400 mm column height (H).
- Axial load ratio ( $\rho_a$ ), 6% of nominal capacity.
- 120 km/h SUT impact velocity.
- $0.25 \text{ kg/m}^{1/3}$  scaled distance.

Table 6.3 Pier column performance summary

<b>D (mm)</b>	<b>Load Scenario</b>	<b><math>\gamma_{cs}</math> (%)</b>	<b><math>\gamma_{br}</math> (%)</b>	<b><math>\gamma_{res}</math> (%)</b>	<b><math>\gamma_{sh}</math></b>	<b><math>D_{max}</math></b>	<b>Damage Categories</b>
750	I-B	22	89	18	1.06	317	M1, M2, M5, M6
	H60-I-B	31	100	10	1.38	353	M1, M2, M3, M4, M5, M6
	F60-I-B	34	100	9	1.39	391	M1, M2, M3, M4, M5, M6
	H90-I-B	36	100	5	1.40	478	M1, M2, M3, M4, M5, M6
	F90-I-B	41	100	3	1.41	547	M1, M2, M3, M4, M5, M6
1050	I-B	12	17	25	0.70	106	M1, M2
	H60-I-B	19	27.8	21	0.81	122	M1, M2, M3
	F60-I-B	22	27.8	17	0.83	136	M1, M2, M3, M5
	H90-I-B	26	27.8	16	0.85	165	M1, M2, M3, M5
	F90-I-B	36	33.3	14	0.89	189	M1, M2, M3, M5
1350	I-B	8	10	39	0.60	68	M1, M2
	H60-I-B	14	20	34	0.62	85	M1, M2, M5
	F60-I-B	17	20	32	0.65	94	M1, M2, M5
	H90-I-B	21	20	29	0.67	129	M1, M2, M3, M5
	F90-I-B	24	23	28	0.71	147	M1, M2, M3, M5

As summarized in Table 6.3, all columns exhibited concrete surface cracking (M1) along their height and concrete cover spalling (M2), with spalling varying in severity and propagating to the non-impact side for 750 mm and 1050 mm columns. As shown in the table, the volume of spalled concrete significantly increased for columns exposed to fire prior to impact and blast compared to cases involving impact and blast. Except for *F90-I-B* cases, similar volumes of spalled concrete were observed for a given column diameter. Plastic hinges (M3) formed at the bases of all columns except for 1350 mm columns under 60 minutes of fire exposure. Studied 750 mm columns were shown to be heavily damaged and would need to be replaced while the 1050- and 1350-mm columns could continue in operation after being repaired.

The analyses indicated that:

- 1) Based on the observed damage extent and in accordance with previous research (Fang et al. 2021), six damage categories were identified to assess bridge column performance: (a) surface crack propagation; (b) concrete cover spalling; (c) plastic hinge formulation; (d) direct shear failure; (e) reinforcement failure; and (f) column core breach.
- 2) Concrete core breaching (M6) and direct shear failure (M4) were concurrently observed for the 750 mm diameter column under all loading conditions, resulting in column failure.
- 3) Except for the 750 mm diameter columns, displacements corresponding to full surface area exposure for similar fire durations were slightly larger than those experienced when half the surface area was exposed, a finding that could be beneficial in many practical applications where protective tools and techniques could be utilized.

- 4) Exposing concrete to elevated temperatures prior to impact and blast resulted in more pronounced damage compared to cases in which studied columns were subjected to impact and blast only.
- 5) Simulation results demonstrated that fire duration and column diameter were key variables controlling single bridge column response and damage propagation when subjected to fire followed by impact and blast.
- 6) Larger lateral deformations and more damage were observed when the entire surface area of the column was exposed.
- 7) Column residual load carrying capacities increased with increasing diameter and with shorter fire exposure duration.
- 8) Based on the estimated shear demand to capacity ratios, 750 mm diameter columns were expected to experience shear failure, 1050 mm columns maintained an acceptable shear capacity in all cases except *F90-I-B* (where the ratio approached 1.0), and 1350 mm columns had adequate shear capacity under applied lateral forces.
- 9) Except for the longest fire duration prior to impact and blast, 1050 mm and 1350 mm diameter columns were shown to withstand superimposed gravity loads and could potentially remain in service in their final damage states.

Results presented herein provide enhanced understanding of single bridge column performance response to multi-hazards. A larger scale study, involving multi-column piers, and a representative bridge system will be completed to better assess substructure performance when subjected to examined hazards and assess the effectiveness of developed and studied repair techniques. The more detailed study will also look to develop and examine the efficacy of

modifications to current bridge design specifications and tools to better address studied multi-hazards.

## Chapter 7 Effectiveness of In-Situ Repair Techniques of Fire Damaged Bridge Columns Subjected to Impact and Blast

### 7.1 Introduction

In this chapter, the effectiveness of using two in-situ retrofitting schemes to rehabilitate isolated, fire-damaged, round, RC pier columns subjected to vehicular collision and air blast was investigated. The first scheme wrapped the columns using externally bonded carbon fiber reinforced polymer (CFRP) sheets. Three different wrapping approaches were examined: the entire column, a portion of the column height, and intermittently along the height. The second scheme implemented a hybrid technique from the literature that combined externally bonded CFRP wrap and near surface mounted (NSM) longitudinal FRP bars (Ashteyat et al., 2021; Chinthapalli et al., 2019). Scheme performance was examined using previously developed isolated bridge column LS-DYNA models modified to include the retrofits. Repaired column impact and blast performance was compared to fire-damaged columns not retrofitted and to intact columns for the three column diameters examined previously. Prior to completing the comparisons, the effectiveness of the modeling approach used to represent each retrofit scheme was validated against published impact and blast tests.

### 7.2 Numerical Modeling

#### *7.2.1 Retrofit schemes*

In the first retrofitting scheme, externally bonded CFRP laminates were attached to the column's periphery, as they tend to increase column confinement. As confining concrete apparently increases its compressive strength, FRP wrapping is frequently used to enhance column ductility and shear and axial load capacities (Bank, 2006). This apparent increase in strength is referred to a concrete confined compressive strength ( $f_{cc}'$ ). According to ACI 440.2-R17: *Guide for the Design and Construction of Externally Bonded FRP Systems for*

*Strengthening Concrete Structures*,  $f_{cc}'$  is directly proportional to the overall thickness of FRP wrap ( $t_{FRP}$ ) which is the number of FRP layers ( $n$ ) multiplied by the thickness of each layer ( $t$ ) (ACI 440.2R-17, 2017). This identifies that for a given FRP laminates, the number of layers should be preliminary specified prior to analyzing column performance.

Typically, repair of the structural element is not explicitly driven by the desire to increase element strength, but rather, it is compelled by the extent of damage and susceptibility of the structural element to be repaired (Bank, 2006). On the other hand, strengthening concrete structures is when the original design strength needs to be increased. In many circumstances, such as when design plans are modified, the required strength increase could be precisely determined. Therefore, current guidelines and specifications for the design and construction of FRP systems do not explicitly address the repair of structures, as the number of FRP layers should be determined based on the level of deterioration and after using visual inspection, nondestructive testing, and potentially FE analyses.

The second repairing scheme consists of externally bonded CFRP wraps and near surface mounted CFRP reinforcement bars. Design codes such as ACI 440.1R-15: *Guide for the Design and Construction of Structural Concrete Reinforced with FRP Bars*, excludes any provisions for the analysis and design of concrete columns reinforced with FRP bars as their contribution to the strength of RC columns is negligible (ACI 440.1R-15, 2015; Choo et al., 2006b). However, longitudinal FRP reinforcements were examined herein as they could affect the performance of pier columns experiencing reasonable flexural demand resulting from lateral impact and blast loads.

The process of selecting CFRP wrap thickness and the number of CFRP rods utilized in the hybrid schemes is presented in this chapter. The modeled retrofitting schemes are illustrated in

Figure 7.1. Modeling techniques and validation results are summarized in this section for each scheme.

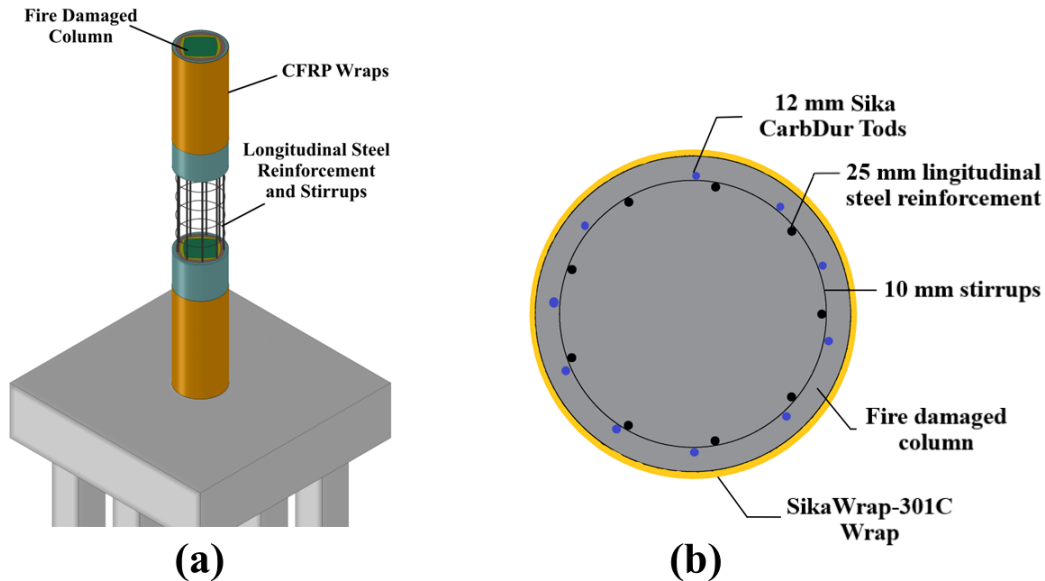


Figure 7.1 Studied retrofitting schemes: (a) Scheme 1, CFRP wrap; (b) Scheme 2, hybrid system

### 7.2.2 CFRP wrapping

LS-DYNA *Belytschko-Tsay* ( $ELFORM = 2$ ), four node, shell elements were utilized to model the CFRP wrap (Hallquist, 2014). The *Part-Composite* option in LS-DYNA was used to define the number of CFRP layers and corresponding integration points and material properties (Deleo & Feraboli, 2011; Fang et al., 2022; L. Liu et al., 2018). LS-DYNA's *Enhanced Composite Damage* (*MAT-54*) nonlinear material model was employed to simulate CFRP dynamic response (Fang et al., 2022; Mutalib & Hao, 2011; Nam et al., 2010; Wang et al., 2018). The material model accounts for tensile and compressive failure of the fiber and matrix, with failure between composite layers being simulated using the *Chang-Chang* criterion (Hallquist,

2014). CFRP material properties were obtained from manufacturer data sheets for the *SikaWrap - 301C* CFRP mat, which is commonly used in practice and was adopted previously (Mutalib & Hao, 2011; Sami, 2021). Relevant properties are provided in Table 7.1.

Table 7.1 SikaWrap -301C Material Properties

Property	Value
Mass Density (g/cm <sup>3</sup> )	1.800
Longitudinal Modulus of Elasticity (GPa)	200
Transverse Modulus of Elasticity (GPa)	9.650
In Plane Shear Modulus (GPa)	5.240
Out of Plane Shear Modulus (GPa)	5.240
Longitudinal Tensile Strength (MPa)	3850
Longitudinal Compressive Strength (MPa)	1095
Transverse Tensile Strength (MPa)	57.00
Transverse Compressive Strength (MPa)	84.40
In Plane Shear Strength (MPa)	71.00
Ultimate Tensile Strain (%)	1.910
Ultimate Compressive Strain (%)	1.175
Poisson's Ratio	0.021
Sheet Thickness (mm)	0.167

### 7.2.3 Epoxy adhesive

Modeling the epoxy that commonly used to bond CFRP to structural elements was accomplished using LS-DYNA's *Automatic Surface to Surface – Tie break* algorithm (Fang et al., 2022; Hallquist, 2014; Mutalib & Hao, 2011; Nam et al., 2010). Failure occurs if the criterion in Equation 12 is satisfied:

$$\left(\frac{|\sigma_n|}{NFLS}\right)^2 + \left(\frac{|\sigma_s|}{SFLS}\right)^2 \geq 1 \quad \text{Equation. 12}$$

where:  $\sigma_n$  and  $\sigma_s$  are the tensile normal and shear stresses; and *NFLS* and *SFLS* are the tensile normal and shear failure stresses, respectively. In accordance with previous studies, failure stresses were selected as 32 MPa for *NFLS* and 29.4 MPa for *SFLS* (Mutalib & Hao, 2011; Nam et al., 2010; Sayed-Ahmed, 2006).

#### 7.2.4 CFRP reinforcement

LS-DYNA's *Piecewise Linear Plasticity (MAT-24)* nonlinear material model in conjunction with round *Hughes-Liu*, two-node, round beam elements were used to model CFRP reinforcement for Scheme 2 (Hallquist, 2014). Research has indicated that dynamic amplification in CFRP strength from high strain rates can be neglected and, as a result, strength gains were not included (Kimura et al., 2001; Mutalib & Hao, 2011) and Cowper-Symonds strain rate parameters were set to zero. LS-DYNA's penalty-based *Lagrangian in Solid* algorithm was again used to couple CFRP bars to surrounding concrete (Hallquist 2014). CFRP bars' materials properties were again selected from *Sika CarboDur Rods* data sheets and are summarized in Table 7.2.

Table 7.2 Sika CarbDur Rods Material Properties

Property	Value
Mass Density (g/cm <sup>3</sup> )	1.600
Modulus of Elasticity (GPa)	155
Yielding Strength (MPa)	2800
Failure Strain (%)	1.800

### 7.2.5 Model development

FE models of repaired bridge columns were created following the approach presented in Section 3.9 with the studied repair schemes being incorporated using the previously discussed techniques. The segment-based, penalty-type, *Automatic Surface to Surface* algorithm was utilized to model contact between the SUT and the CFRP with static and dynamic friction coefficients set to 0.30 (Hallquist 2014). LS-DYNA's *Constrained Lagrangian in Solid command* simulated interaction between blast waves and the repaired columns. Penalty-based coupling (*CTYPE = 4*) was employed to allow for erosion of the CFRP (Hallquist, 2014).

It is of interest to note that, in practice, RC columns are commonly prepared by grooving the surface of concrete prior to installing NSM, FRP rods. According to ACI 440 provisions, the groove dimension should be at least 1.5 the diameter of FRB rod (ACI 440.2R-17, 2017). Grooves should also be properly cleaned and filled by a resin or cement mortar before installing FRP rods (Ashteyat et al., 2021). In modeling perspective, there is no need to implement this procedure as FRP rods can be installed to the required depth and coupled with the surrounding concrete using *Constrained Lagrangian in Solid command*. Since filling the grooves with resin or mortar is mainly to ensure adequate bonding between the rods and concrete, the original concrete can be maintained in the FE model if the bonding requirement is satisfied. According to Bank (2006), when hybrid systems, such as the one in the current study, are utilized to retrofit

RC columns, bonding between FRP rods and the surrounding concrete is guaranteed due to the confinement produced by the FRP wraps. Thus, disregarding surface grooves and their filling material in the proposed FE approach is justified.

### 7.3 Validation

Experimental research studying response of retrofitted RC structural elements under coupled impact and blast could not be located in the literature. Consequently, FE models were validated against separate, published, impact and blast tests. In the first test, performance of a strengthened RC pier column was examined under impact (Sha & Hao, 2015). The second test studied response of a GFRP strengthened RC panel to air blast (Razaqpur et al., 2007).

#### *7.3.1 CFRP wrapped pier column under impact*

Performance of a reduced scale, CFRP strengthened, round, RC, bridge pier column to impact was examined using a pendulum (Sha & Hao, 2015). The circular column was 78 mm in diameter and 700 mm tall and was reinforced using eight 2 mm longitudinal steel bars and 1 mm transverse steel ties spaced at 12.5 mm. A 0.13 mm thick, externally bonded, CFRP sheet wrapped the entire surface of the column. Column dead and live axial loads were represented using a 173.6 kg concrete block at the top. Material properties are provided in Table 7.3.

As shown in Figure 7.2, a pendulum arm with a 2850 mm swing radius supporting a impactor weighing 60 kg struck the column 570 mm above its 25 mm steel base plate. The column was subjected to increasing impact energy by gradually increasing the swing arc between the pendulum arm and vertical direction using  $5^\circ$  ( $\theta$ ) increments until failure occurred.

The same numerical modeling approach discussed in Chapter 3 was utilized to simulate the pendulum tests. LS-DYNA's *Rigid* material model (*MAT-20*) was used to model the impactor and concrete block to optimize computational cost (Hallquist, 2014). LS-DYNA's *Automatic*

*Surface to Surface*, penalty-based contact algorithm was again employed to simulate contacts between the impactor and the strengthened column and contact between the wrap and pier column face was modeled using the *Automatic Surface to Surface Tie Break* command. LS-DYNA's *Interface Springback* command was utilized so that stresses, strains, and permanent sets resulting from a previous impact stage would be the initial conditions for the subsequent impact. Final damage observed in the model was comparable to that from the test, with shear failure being observed at the column ends when  $\theta = 25^\circ$  (Figure 7.3). Moreover, numerical and experimental impact forces and reinforcement strains also demonstrated good agreement, as illustrated in Figure 7.4.

Table 7.3 Material properties of the pier column (Sha and Hao, 2015)

Material	Property	Value
Concrete	Compressive Strength (MPa)	28.3
Steel	Young's Modulus (GPa)	200
	Yielding Strength (MPa)	550
CFRP	Young's Modulus (GPa)	230
	Tensile Strength (MPa)	3500
Epoxy	Young's Modulus (GPa)	3800
	Tensile Strength (MPa)	30

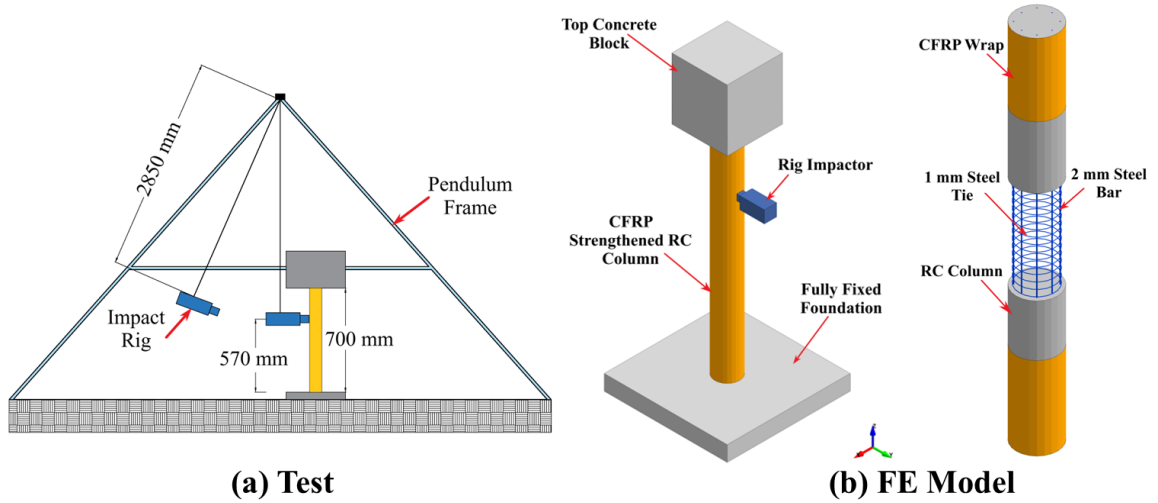


Figure 7.2 Pendulum setup and FE model (Sha and Hao 2015)

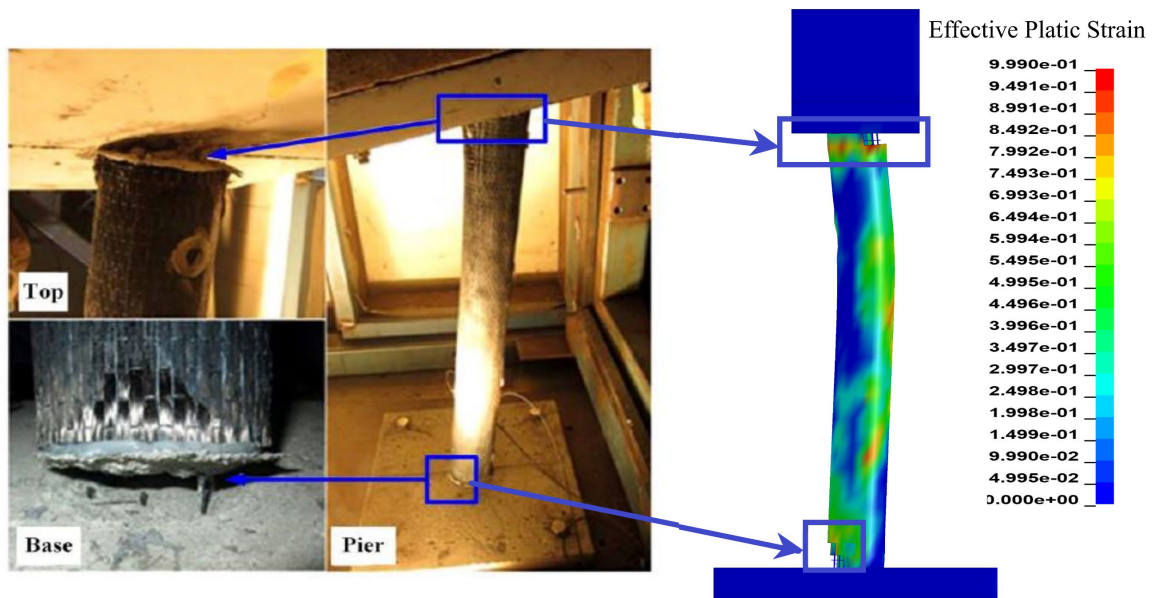
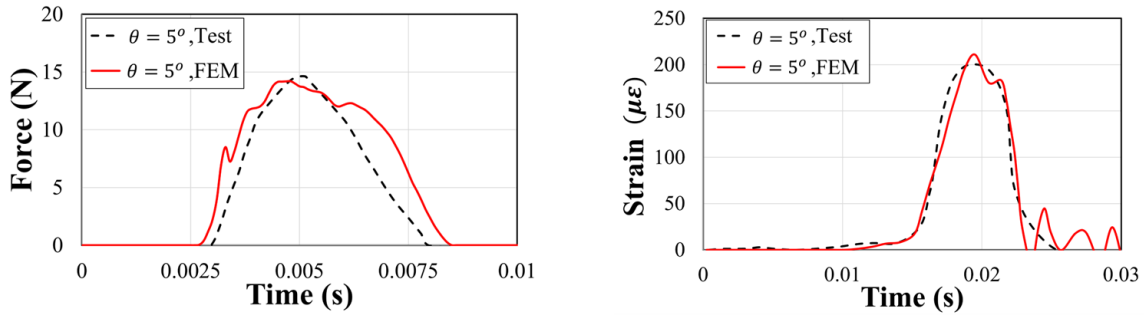
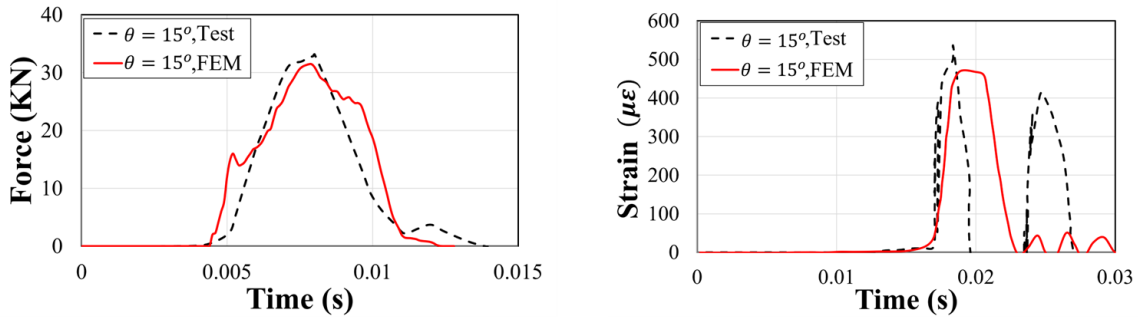


Figure 7.3 Experimental, modeled final damage states (Sha and Hao 2015)



(a) Impact angle,  $\theta = 5^\circ$



(b) Impact angle,  $\theta = 15^\circ$

Figure 7.4 Experimental, numerical impact force and reinforcement strain time histories (Sha and Hao 2015)

### 7.3.2 GFRP strengthened RC panel under blast

A blast test on an RC panel strengthened using externally bonded glass fiber reinforced polymer (GFRP) sheets was also utilized for model validation (Razaqpur et al. 2007). As shown in Figure 7.5, 000 x 1000 x 70 mm panels were subjected to a 33.4 kg ANFO explosive placed 3000 mm away from the slab face. Two 500 mm wide and 1.3 mm thick GFRP sheets were externally bonded to both faces of the panel. Material properties are provided in Table 7.4.

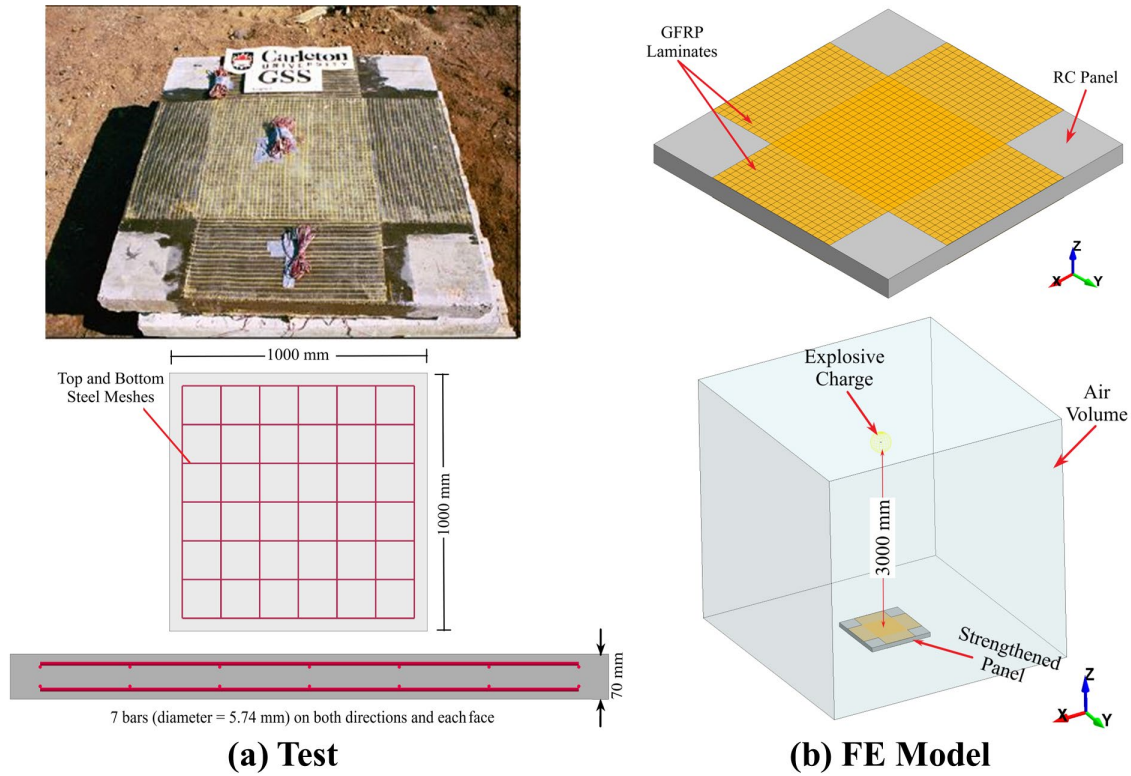


Figure 7.5 Blast test, FE model (Razaqpur et al. 2007)

Table 7.4 Material properties (Razaqpur et al. 2007)

Material	Property	Value
Concrete	Compressive Strength (MPa)	42
Steel	Young's Modulus (GPa)	200
	Yielding Strength (MPa)	480
GFRP	Young's Modulus (GPa)	27.5
	Tensile Strength (MPa)	580
Epoxy	Tensile Strength (MPa)	54

The panels and air blast were simulated using the procedure presented in this chapter and Chapter 3. Shell elements were utilized to model externally bonded GFRP laminates. LS-DYNA's

*Automatic Surface to Surface Tie Break* algorithm was again employed to model the interface between the RC panel and GFRP sheets with failure criteria defined using published epoxy tensile strengths (Hallquist, 2014).

Experimental and numerical reflected pressure and midspan displacement time histories were compared and are shown in Figure 7.6. Good agreement was demonstrated, with a discrepancy between peak displacements of approximately 10%. As discussed earlier, the first peak displacements were the focus for calibration. Similarly, positive phase pressures are of the most interest for structural design under blast loads (Sudeep & Rao, 2019) and, as shown in the figure, good agreement was again demonstrated.

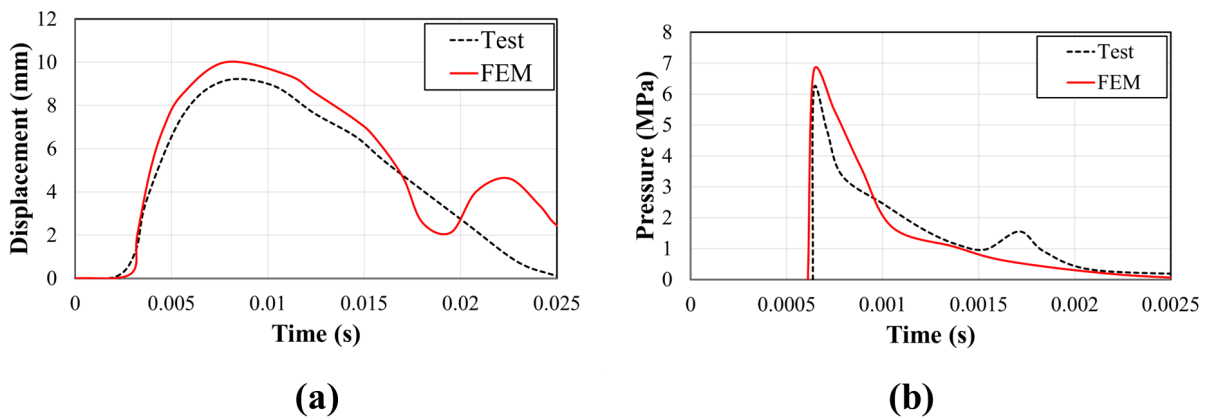


Figure 7.6 Experimental, numerical: (a) displacement time history; (b) reflected pressure time history.

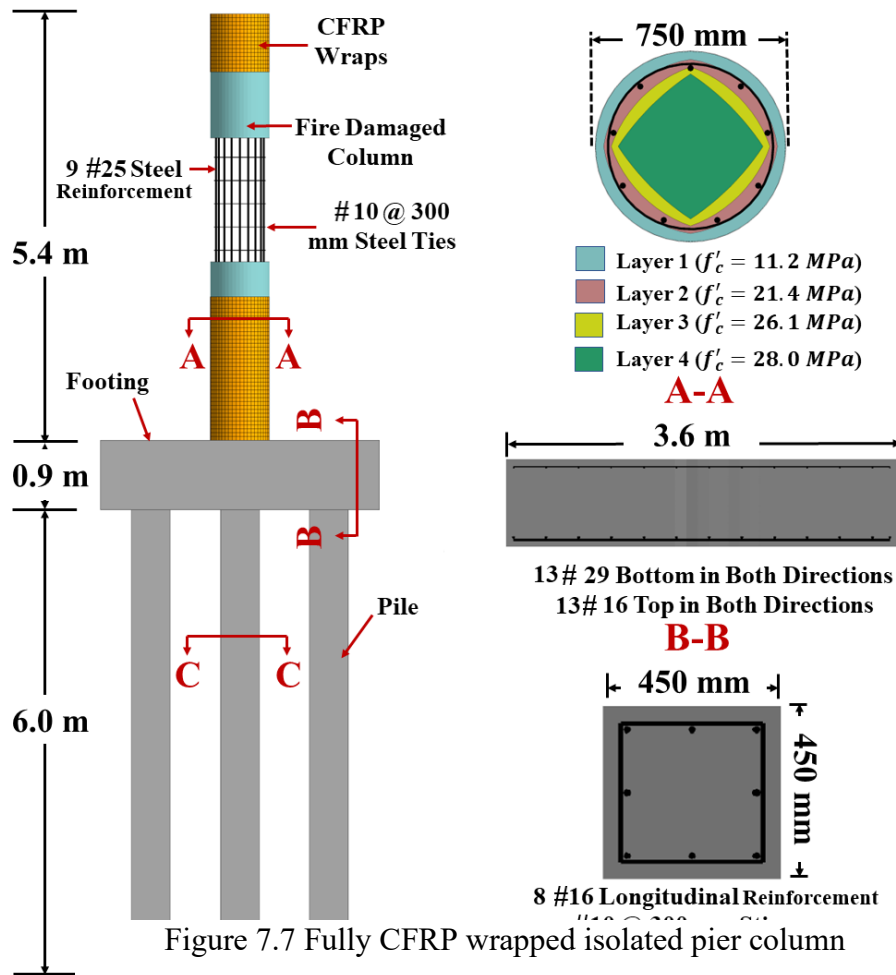
## 7.4 Numerical Studies

### 7.4.1 Fire damaged column

The effectiveness of the studied schemes was examined via the study of a 750 mm fire-damaged column under the most critical combination of fire exposure, impact velocity, and scaled

distance (i.e.,  $F90$ , 120 km/h,  $0.25 \text{ kg/m}^{1/3}$ ). Column design information can be found in Figure 7.7.

Push down analyses were carried out for all column diameters under  $F90$ . For the 750 mm diameter column, the ratio between residual and nominal capacities was 26%, which indicated that the column maintained 74% of its design capacity after 90-minute fire exposure, as shown in Figure 7.8. This ratio was used to examine the effectiveness of studied retrofit schemes with respect to capacity.



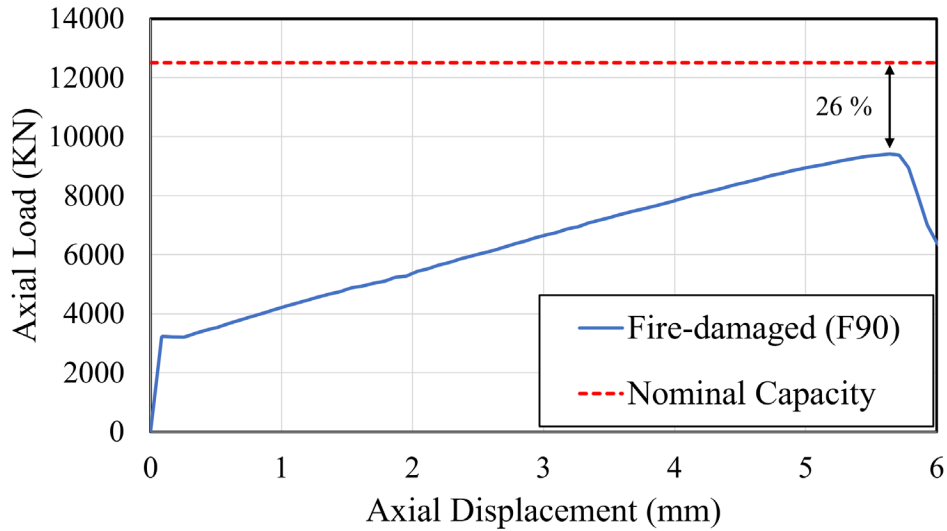


Figure 7.8 Load-axial displacement curve, 750 mm column, F90

#### 7.4.2 Retrofit design

The number of CFRP wraps used to repair fire-damaged pier columns for Scheme 1 were selected to return the columns to their design axial load capacity. A series of “push down” analyses examined the performance of four arbitrarily selected CFRP thicknesses ( $t_{FRP}$ ) of 0.5 mm (3 layers), 1 mm (6 layers), 1.5 mm (9 layers), and 2 mm (12 layers). Estimated residual capacity for each CFRP wrap thickness is illustrated in Figure 7.9. As expected, results indicated that column residual capacities increased by increasing the number of CFRP layers, but no significant increases were observed when more than 12 layers (2 mm) were used.

Similar to CFRP wrap thickness, the number of reinforcing bars is generally determined based on the extent of damage and the degree of retrofitting required. Following similar research studies and recommendations, the CFRP longitudinal reinforcement ratio was randomly selected to be between 0.15% and 1% (Chinthapalli et al. 2020; Choo, Harik, and Gesund 2006).

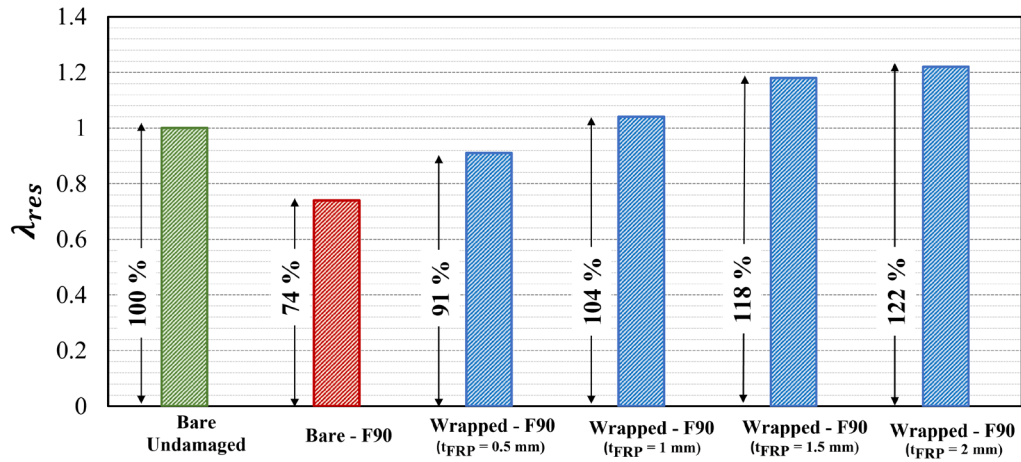


Figure 7.9 Residual axial load carrying capacity, 750 mm wrapped columns, F90

#### 7.4.3 Study matrix

As stated earlier, four CFRP thicknesses were examined for Scheme 1. Two CFRP thicknesses and four longitudinal CFRP reinforcement ratios were investigated for Scheme 2. Studied schemes and corresponding key parameters are summarized in Table 7.5. In the table, “*W*” stands for wrap, “*L*” for layer, and “*R*” reinforcement bar. For instance, *W-3L* corresponds to the first scheme where columns are wrapped with three CFRP layers. Also, *4R12-3L* designated the hybrid scheme where a combination of four CFRP bars of 12 mm diameter with three CFRP layers were used to retrofit the fire damaged column. In the same table,  $t_{FRP}$  refers to the overall thickness of the CFRP wrap and  $\rho_{FRP}$  corresponds to the CFRP reinforcement ratio.

Table 7.5 Retrofitting Schemes Cases

Retrofitting Scheme	Case Study	Nomenclature
First Scheme: CFRP Wrapping	CFRP wrapped column – 3 layers ( $t_{FRP} = 0.50 \text{ mm}$ )	W-3L
	CFRP wrapped column – 6 layers ( $t_{FRP} = 1.00 \text{ mm}$ )	W-6L
	CFRP wrapped column – 9 layers ( $t_{FRP} = 1.50 \text{ mm}$ )	W-9L
	CFRP wrapped column – 12 layers ( $t_{FRP} = 2.00 \text{ mm}$ )	W-12L
Second Scheme: Hybrid Retrofitting	Four 12 mm CFRP bars ( $\rho = 0.13\%$ ) and 1 CFRP layer ( $t_{FRP} = 0.167 \text{ mm}$ ).	4R12-1L
	Four 12 mm CFRP bars ( $\rho_{FRP} = 0.13\%$ ) and 3 CFRP layer ( $t_{FRP} = 0.50 \text{ mm}$ )	4R12-3L
	Eight 12 mm CFRP bars ( $\rho_{FRP} = 0.21\%$ ) and 3 CFRP layer ( $t_{FRP} = 0.50 \text{ mm}$ )	8R12-3L
	Twelve 12 mm CFRP bars ( $\rho_{FRP} = 0.35\%$ ) and 3 CFRP layer ( $t_{FRP} = 0.50 \text{ mm}$ )	12R12-3L
	Twelve 22 mm CFRP bars ( $\rho_{FRP} = 1.00\%$ ) and 3 CFRP layer ( $t_{FRP} = 0.50 \text{ mm}$ )	12R22-3L

## 7.5 Results

Repaired column performance was evaluated using similar criterion to earlier parametric studies: final damage states, permanent set, identified damage levels presented in 6.2, and residual capacities. Maximum kinetic energy was included in this assessment as it reflects the amount of energy absorbed by the CFRP wraps. LS-DYNA's *Material Summary (MATSUM)* command was used to obtain kinetic energies (Hallquist, 2014).

### 7.5.1 Scheme 1

Effective plastic strain contours are compared, as shown in Figure 7.10. Cracking was reduced by increasing CFRP thickness, with no significant difference being observed for CFRP thicknesses greater than 1.5 mm (9 layers). Irrespective of thickness, more extensive cracking extended into the foundation system compared to the bare columns for *F90-I-B*. It was also

observed that plastic hinges formed in  $W-3L$  and  $W-6L$  which correspond to concrete cover spalling accompanies column core cracking, reinforcement yielding, and localized buckling. This signifies that the number of CFRP layers should be further increased to enhance column performance.

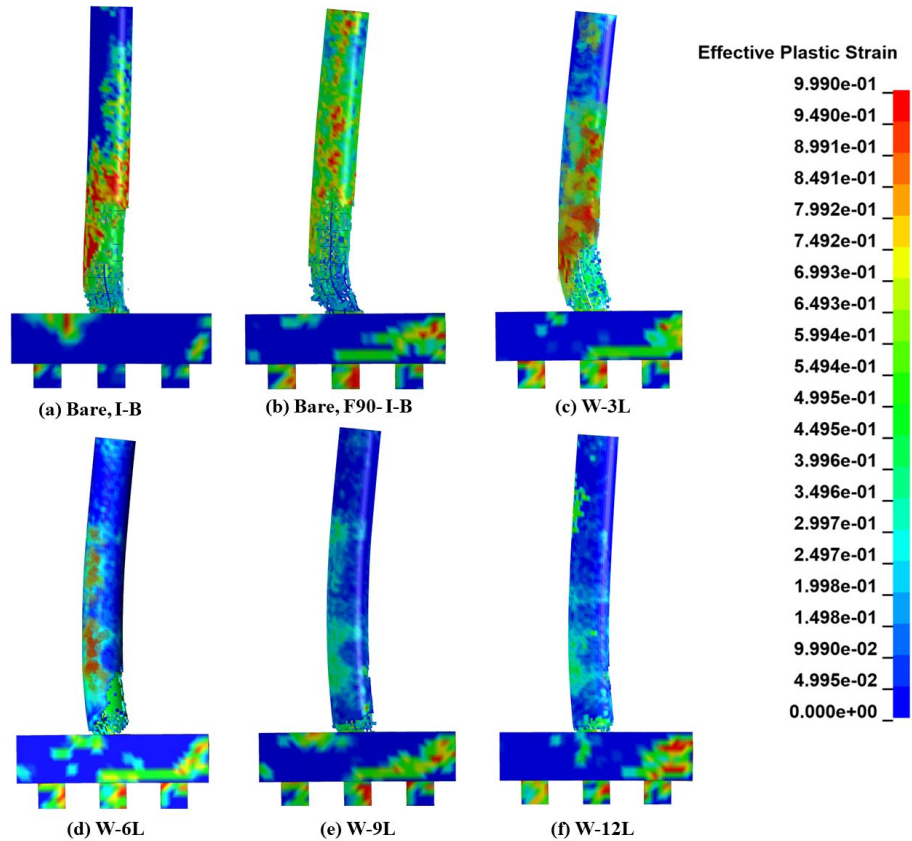


Figure 7.10 Crack propagation, bare and CFRP-wrapped columns

Figure 7.11 presents damage categories summarized in 6.2 and compares the volume of spalled concrete ( $\gamma_{CS}$ ) for bare and CFRP-wrapped columns. All columns experienced surface cracking ( $M1$ ) and concrete cover spalling ( $M2$ ). Plastic hinge formulation and reinforcement failure were observed for  $t_{FRP}$  values of 0.5 mm and 1.0 mm. The amount of eroded concrete significantly reduced when CFRP wrapping was used, with the volume of spalled concrete being

39% for  $t_{FRP}$  of 0.5 mm. Localized, minor spalling was observed for  $t_{FRP}$  of 1 mm. On the other hand, the imperceptible damage observed when 1.5 mm and 2.0 mm wraps were used indicated that the column could remain in operation with minor repairs.

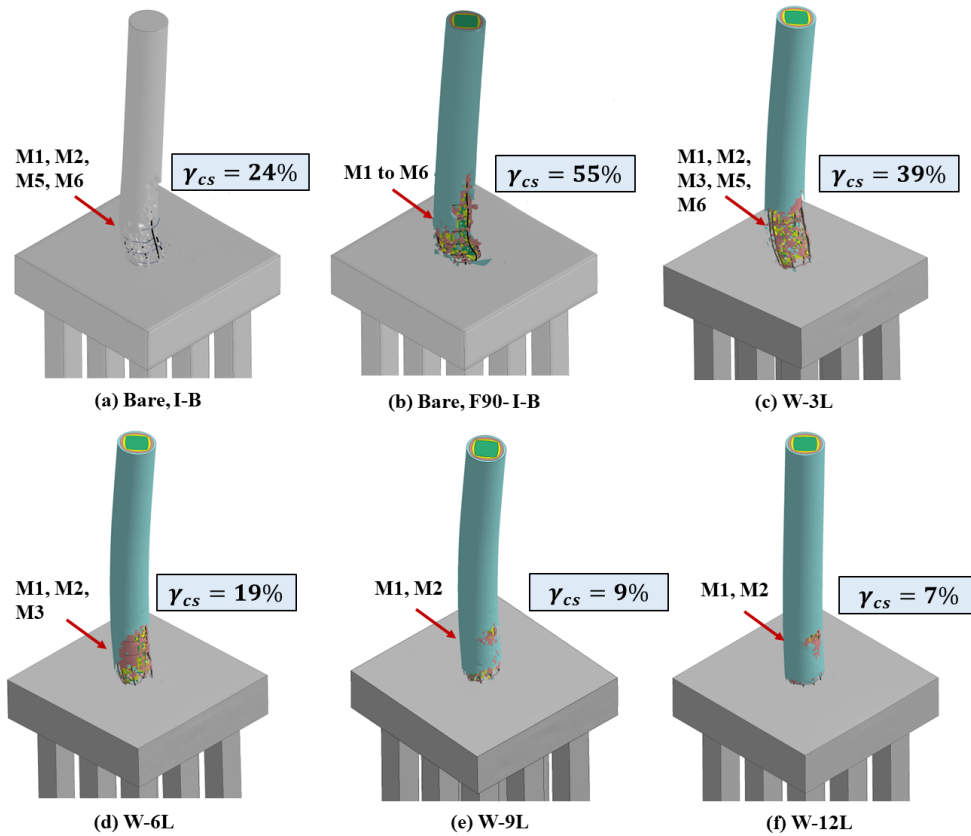
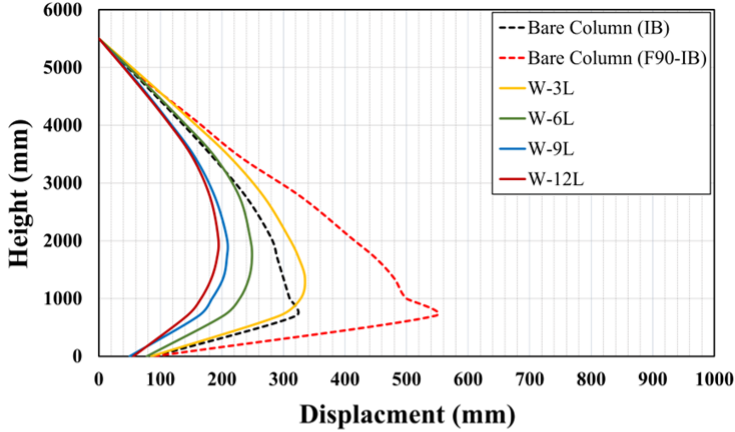


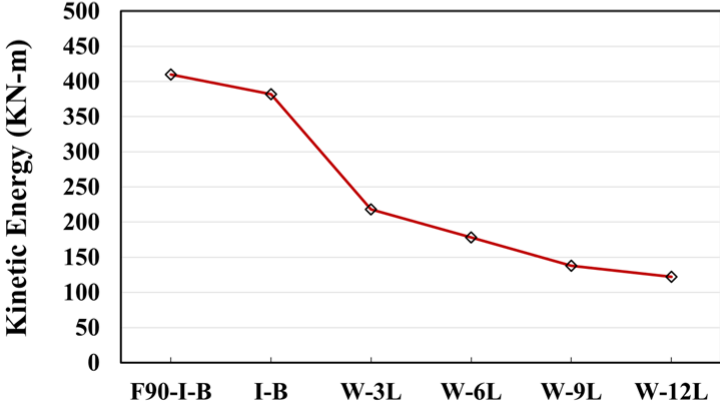
Figure 7.11 Final damage states and spalled concrete volumes, bare and CFRP-wrapped columns

Displacement variations and maximum kinetic energies are illustrated in Figure 7.12. Final lateral displacements were considerably reduced when CFRP wrap was used and increased CFRP thickness contributed to lower displacement and larger kinetic energy absorption. For instance, for a CFRP thickness of 0.5 mm peak displacements and kinetic energies were 40% and 53% less than those experienced by the based, fire-damaged column. As stated earlier, increasing

CFRP thickness from 1.5 mm to 2.0 mm did not offer much improvement. Kinetic energy reduction followed a similar pattern. More uniform displaced shapes were also observed as CFRP thickness increased. As a result, nine CFRP layers were deemed sufficient to mitigate the combined effects of impact and blast after fire exposure.



(a) Column Displacement



(b) Column Kinetic Energy

Figure 7.12 Displacements and kinetic energies, bare and CFRP-wrapped columns

In similar fashion to earlier evaluations, Figure 7.13 summarizes residual axial load carrying capacities ( $\lambda_{res}$ ) for bare and CFRP wrapped columns. Following similar patterns,  $\lambda_{res}$

appreciably increased with increased CFRP thickness until the thickness equaled 1.5 mm (nine layers).

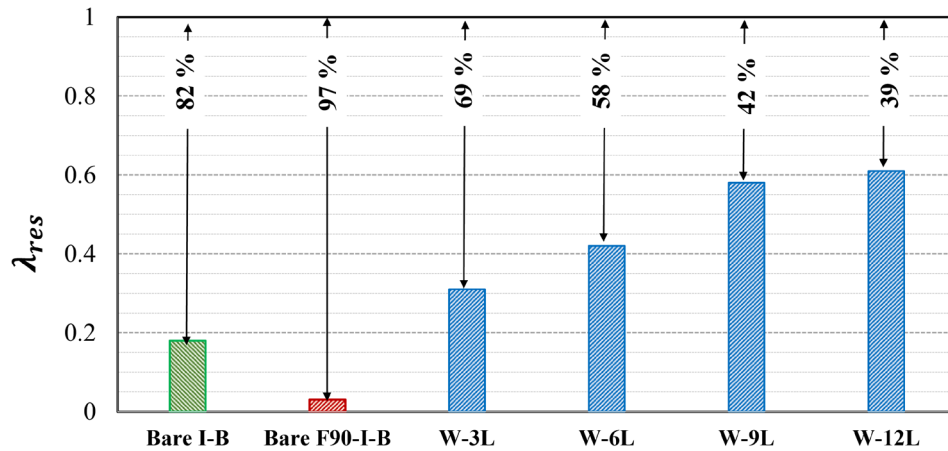


Figure 7.13 Residual axial load carrying capacities, bare and CFRP-wrapped columns

#### 7.5.1.1 Effect of partial wrapping

Additional studies were completed to investigate the effects of partial and intermittent wrapping on performance. These studies were initiated because previous studies have indicated that partially wrapping columns could be effective in mitigating column response to various demands (H. Al-Nimry et al., 2013; H. S. Al-Nimry & Ghanem, 2017; Fang, 2020). As illustrated in Figure 7.14, three cases were considered with nine CFRP layers ( $t_{FRP} = 1.5$  mm) being used for each. The first configuration wrapped the bottom half of the column height (*HH-9L*), the second wrapped the column with intermittent 1000 mm strips (*I1000-9L*), and the third wrapped the column with intermittent 500 mm strips (*I500-9L*). Performance effectiveness was examined via comparisons to fully wrapped columns (*W-9L*).

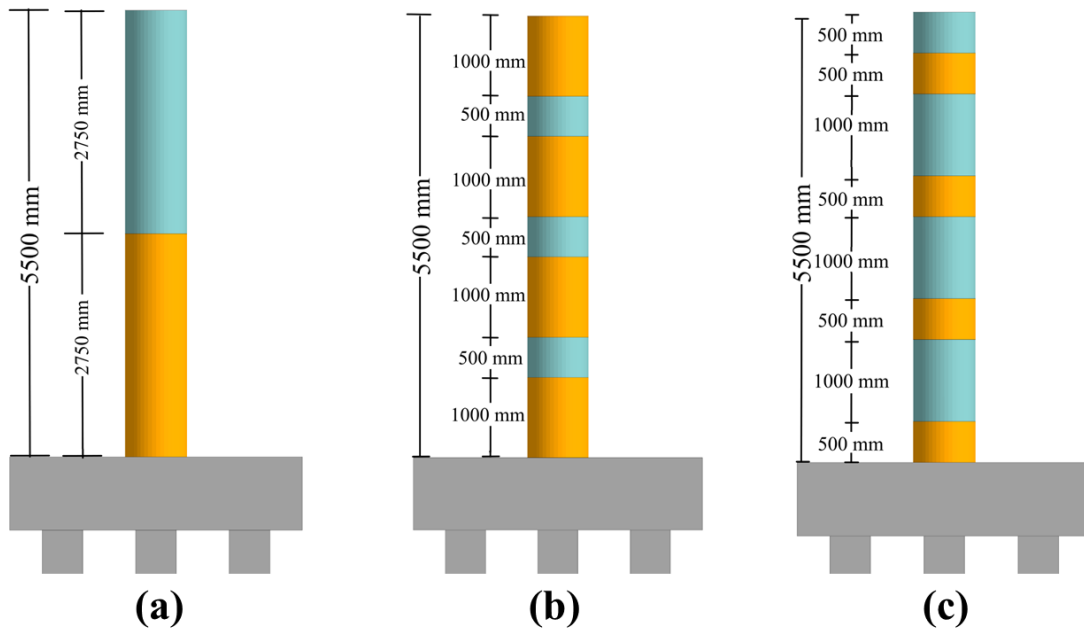


Figure 7.14 Partially CFRP wrapped columns: (a) HH-9L; (b) I1000-9L; (c) I500-9L

Effective plastic strain contours were employed to again examine crack propagation along the column height (Figure 7.15). For *HH-9L*, more flexural cracks were observed along the top half of the column. No notable difference in cracking intensity was observed for *I1000-9L*. Intense localized, cracks were observed in the impact region for *I500-9L*. Also, it was noted that cracks extended to the foundation for all cases.

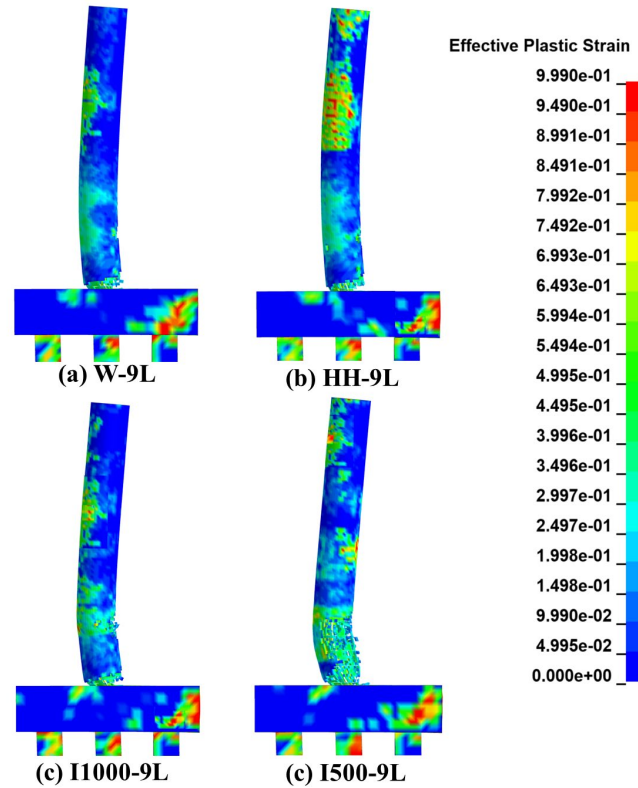


Figure 7.15 Crack propagation; fully and partially CFRP-wrapped columns

Final damage states and spalled volumes are shown in Figure 7.16. Columns *W-9L*, *HH-9L*, and *I1000-9L* sustained identical damage ( $M1$ ,  $M2$ ) and experienced comparable spalling magnitudes ( $\gamma_{cs}$ ). This indicated that wrapping columns near the impact location or utilizing intermittent wrapping would mitigate vehicle collision and air blast effects. These columns could remain in operation with minor repairs.

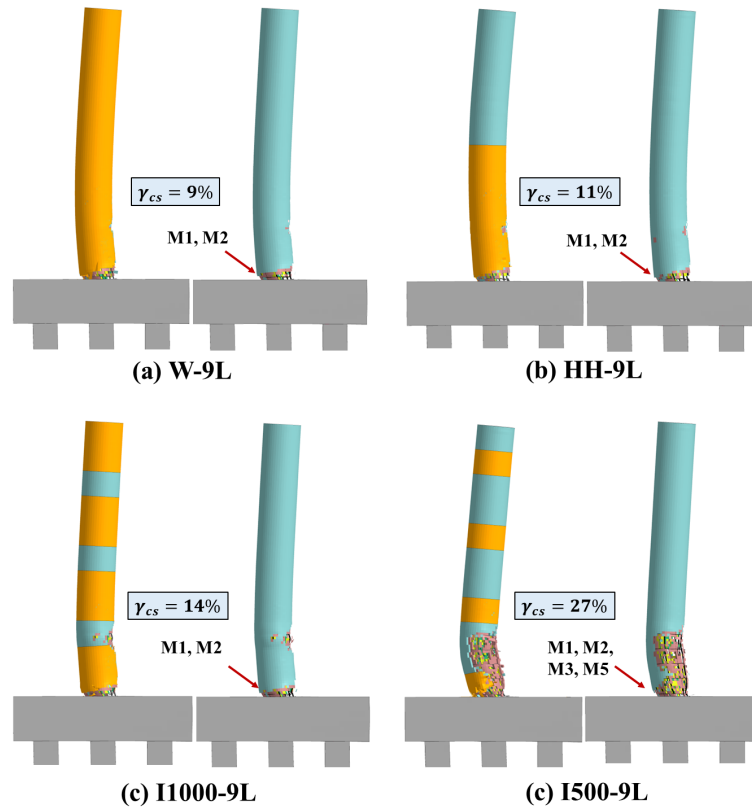
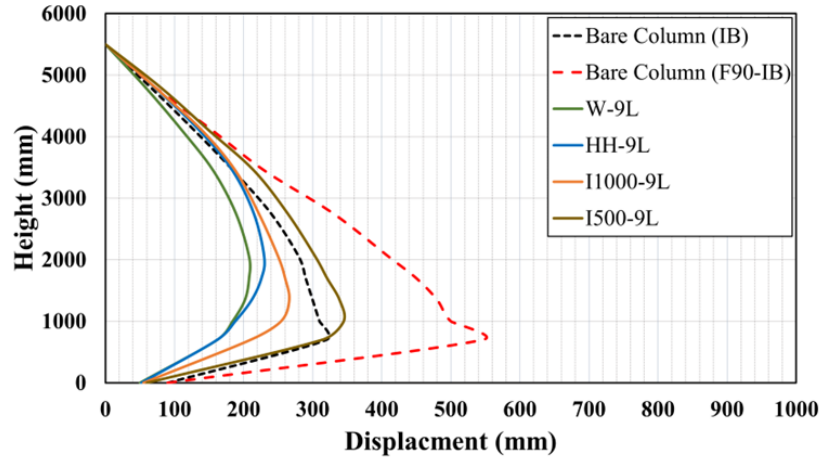
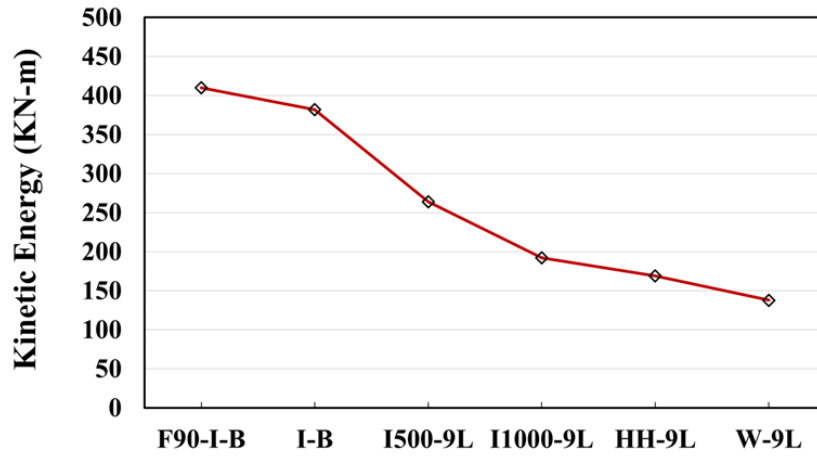


Figure 7.16 Final damage states and spalled concrete volumes; fully and partially CFRP-wrapped columns

Displacement variations and maximum kinetic energies are illustrated in Figure 7.17. Lateral displacements and kinetic energies were significantly reduced when *W-9L*, *HH-9L*, and *I1000-9L* were used. For instance, peak displacement and kinetic energy were 58% and 59% less than those experienced by the fire-damaged column when *HH-9L* was used. Similarly, peak displacement was reduced by 51% and kinetic energy by 54% when *I1000-9L* was implemented. It was also noted that the first 1000 mm of the column height has identical displacements when *W-9L* and *HH-9L* was used. *I500-9L* contributed to lower reduction in final displacement and kinetic energy, which identifies that no pronounced improvement in column performance was achieved. As a result, both *HH-9L* and *I1000-9L* were deemed sufficient to mitigate combined effects of impact and blast after fire exposure.



(a) Column Displacement



(b) Column Kinetic Energy

Figure 7.17 Displacements and kinetic energies; fully and partially CFRP-wrapped columns

In similar fashion to earlier assessment, Figure 7.18 compares residual axial load carrying capacities ( $\lambda_{res}$ ) for bare and CFRP wrapped columns. Conforming with the earlier discussion, W-9L, HH-9L, and I1000-9L showed predominant enhancement in  $\lambda_{res}$  with at least 50% of columns capacity maintained after impact and blast.

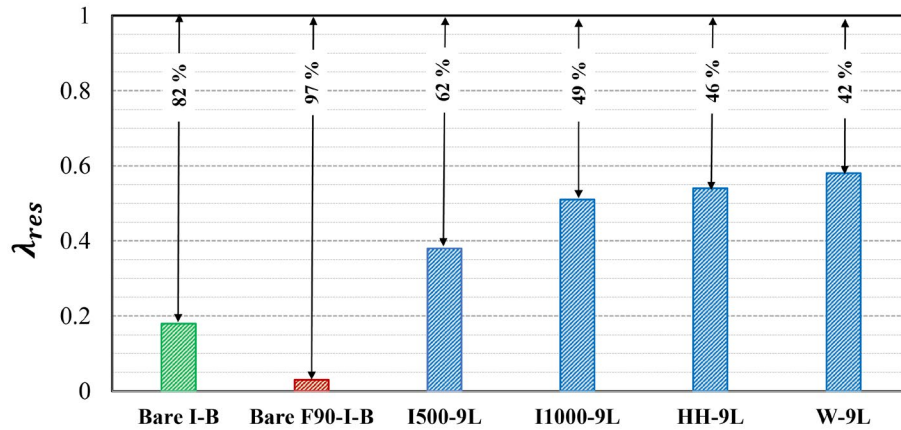


Figure 7.18 Residual axial load carrying capacities; fully and partially CFRP-wrapped columns

### 7.5.2 Scheme 2

Figure 7.19 depicts effective plastic strain and no significant performance improvement was observed for 4R12-1L, with extensive concrete cracking propagating along the column height. Increasing CFRP wrap thickness from 0.167 mm (1 wrap) to 0.50 mm (3 wraps) slightly mitigated surface cracking. Similar and less extensive cracking patterns were observed when the number of CFRP bars doubled. Noticeable shifts from mid-height flexure-shear cracking to purely flexural cracking was observed with increased CFRP reinforcement ratios for the same CFRP wrap thickness. No pronounced differences in surface cracking were observed when 12R12-3L and 12R22-3L happened.

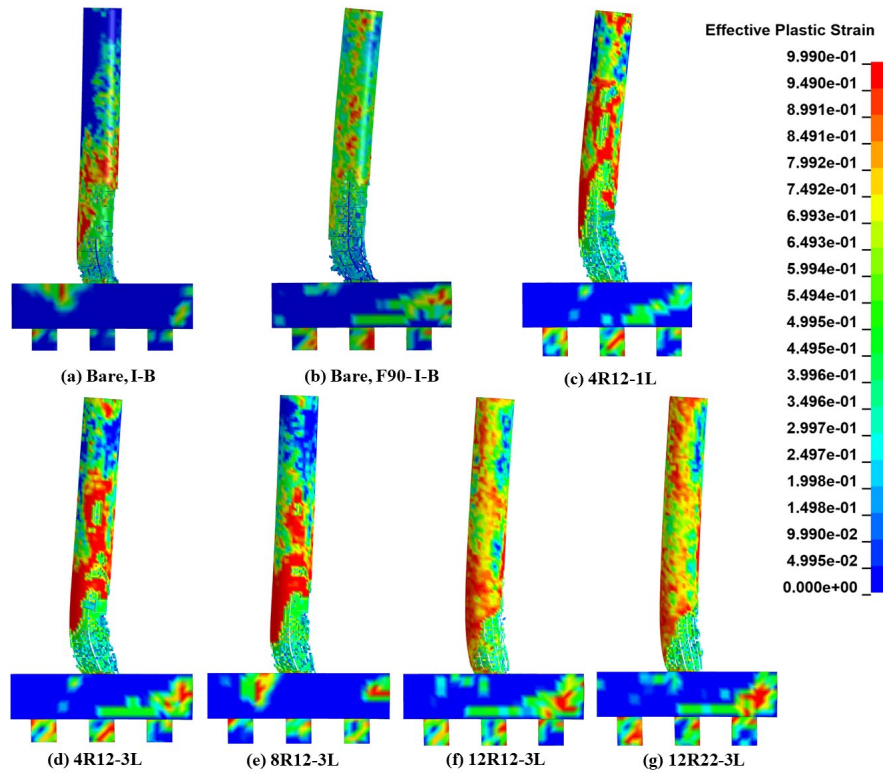


Figure 7.19 Crack propagation, bare and hybrid retrofitted columns

Figure 7.20 illustrates damage categories summarized in 6.2 and compares the volume of concrete spalled ( $\gamma_{cs}$ ), and damage categories for bare and hybrid retrofitted columns. In line with the previous observations, repaired columns experienced considerable concrete cover spalling when *4R12-1L* and *4R12-3L* were used and indistinguishable relative spalling was noticed in the remaining cases. All columns sustained similar damage levels (*M1*, *M2*, *M3*, *M5*) with concrete core breaching (*M6*) observed only in *4R12-1L*. Accordingly, all columns require extensive repairs to restore the level of operation.

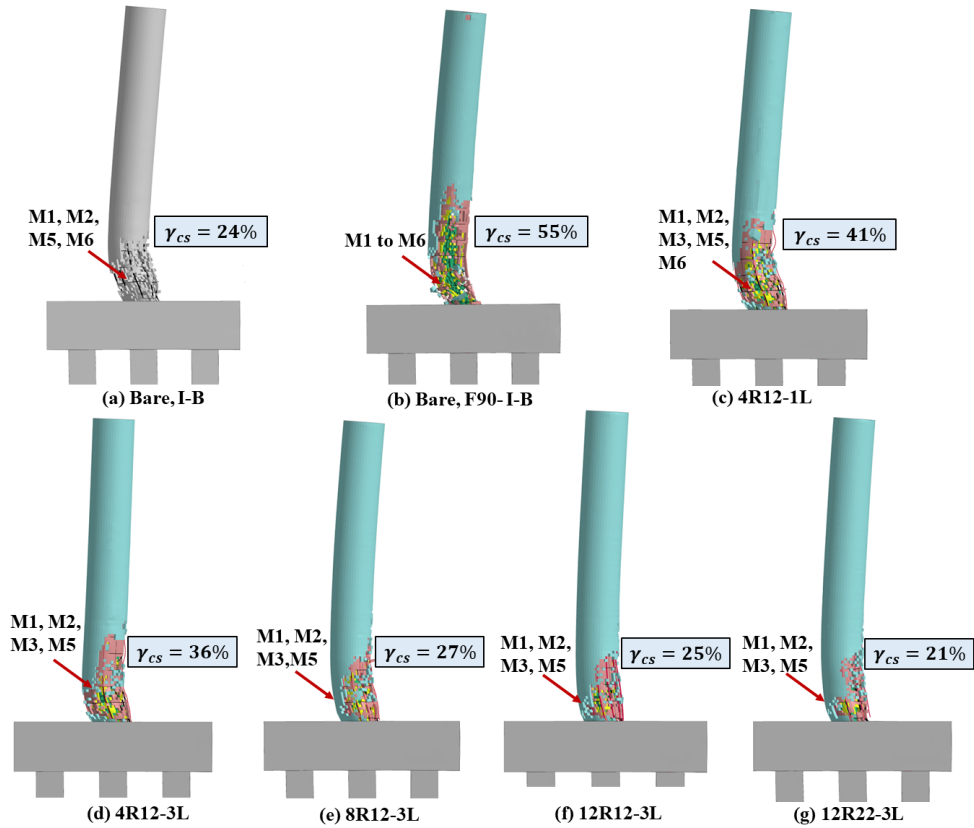
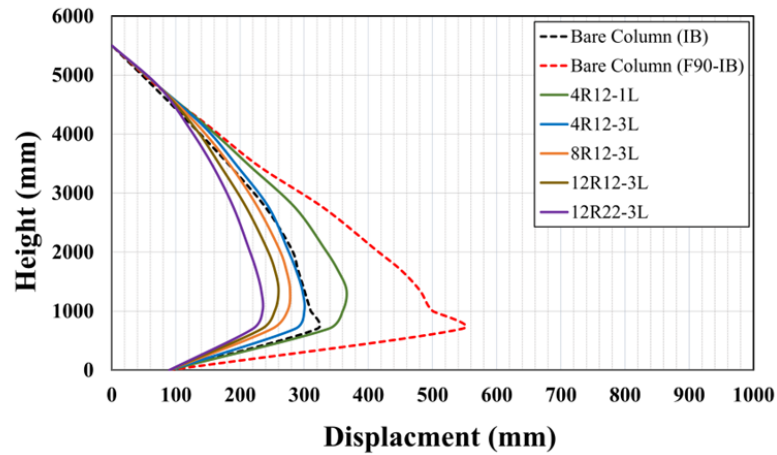


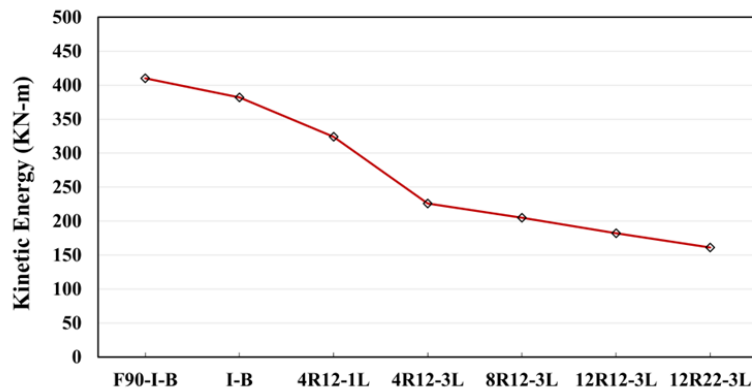
Figure 7.20 Final damage states, bare and hybrid retrofitted columns

Displacements variations and maximum kinetic energy are depicted in Figure 7.21. Final lateral displacements were considerably reduced when hybrid retrofitting was used. As expected, a more pronounced reduction in displacement and kinetic energy was observed when a 0.5 mm CFRP wrap was used. For instance, for *4R12-1L*, the peak displacements and kinetic energies were 34% and 22% less than those experienced by the bare, fire-damaged column. Column displacement and kinetic energy were reduced by 46% and 45%, respectively, for *4R12-3L* indicating that three CFRP layers are more effective than using only one. Comparable displacement and kinetic energy reductions were observed in the three remaining cases. This is due to the increased stiffness resulting from increasing the number of CFRP bars in repaired columns. This signifies that increasing the CFRP reinforcement ratio has a priceable contribution

to reducing lateral displacements and kinetic energies and has very limited effect on concrete spalling and surface cracking mitigation.



(a) Column Displacement



(b) Column Kinetic Energy

Figure 7.21 Displacements and kinetic energies, bare and hybrid retrofitted columns

Figure 7.22 illustrates residual axial load carrying capacities ( $\lambda_{res}$ ). A more pronounced improvement was observed when CFRP wrap thickness increased from 0.167 mm (one wrap) to 0.50 mm (three wraps) with no significant enhancement in residual capacity observed for increased CFRP reinforcement ratio.

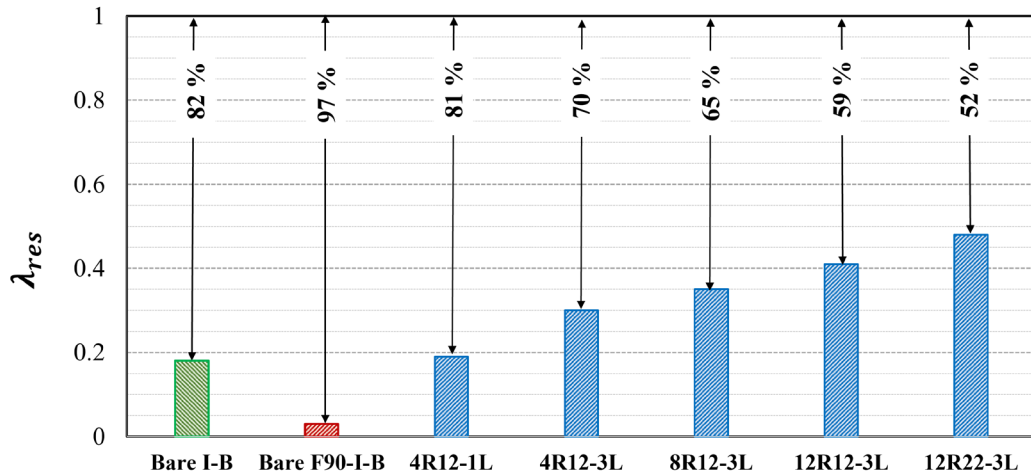


Figure 7.22 Residual axial load carrying capacities, bare and hybrid retrofitted columns

### 7.6 Effect of Bridge Column Diameter

To assess the effectiveness of previously examined retrofitting schemes more comprehensively, the performance of 1050 mm, and 1350 mm bridge column diameters were investigated in this section and compared to that of the 750 mm column. The most efficient repairing techniques were involved in this evaluation. As no pronounced change in fire-damaged column performance was observed when *W-9L* and *W-12L* were utilized, *W-9L* would be recommended as it is more economically justified. From the second retrofitting scheme, *12R22-3L* was selected as it surpassed the performance of the four other studied cases. Additionally, *HH-9L* and *I1000-9L* were utilized as they significantly mitigated the response of bridge columns under impact and blast demands.

Figure 7.23 compares concrete surface crack propagation in the three column diameters and when the four selected retrofitting schemes were utilized. For all column diameters, less significant concrete cracking was observed in *W-9L*, and considerably serious cracks occur when *12R22-3L* was used. For *HH-9L*, intensive flexural cracks were noticed in the bare portion of the

column height, while the wrapped portion sustained localized cracks comparable to those in *W-9L*. Similarly, cracks extended to the unwrapped portions of the columns in *I1000-9L* with almost the same cracks observed in the vicinity of the impact location compared to *W-9L* and *HH-9L*.

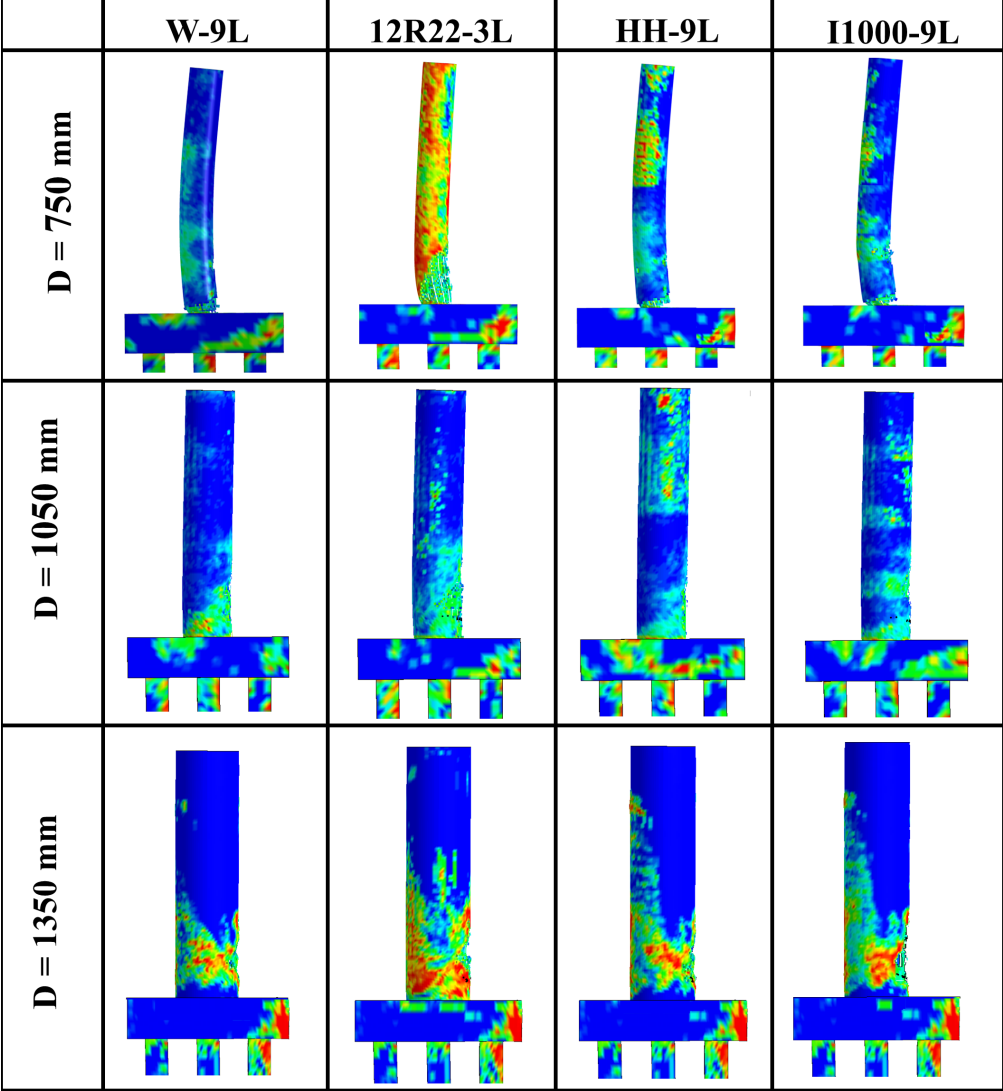


Figure 7.23 Concrete crack propagations for different retrofitting schemes and column diameters

Final damage states, relative volume of concrete cover spalling, and damage categories are illustrated in Figure 7.24. For all column diameters, columns retrofitted using *I2R22-3L* experienced larger concrete cover spalling compared to all other cases. Also, all columns sustained M1 and M2 when *W9-L*, *HH-9L*, and *I1000-9L* were utilized, which identifies that those columns could remain in operation while being repaired. However, more significant damage was observed in *I2R22-3L* including reinforcement failure (M5) in the 750 mm and 1050 mm diameter columns, and plastic hinge formulated (M3) in the 750 mm diameter column indicated that extensive repairs are required.

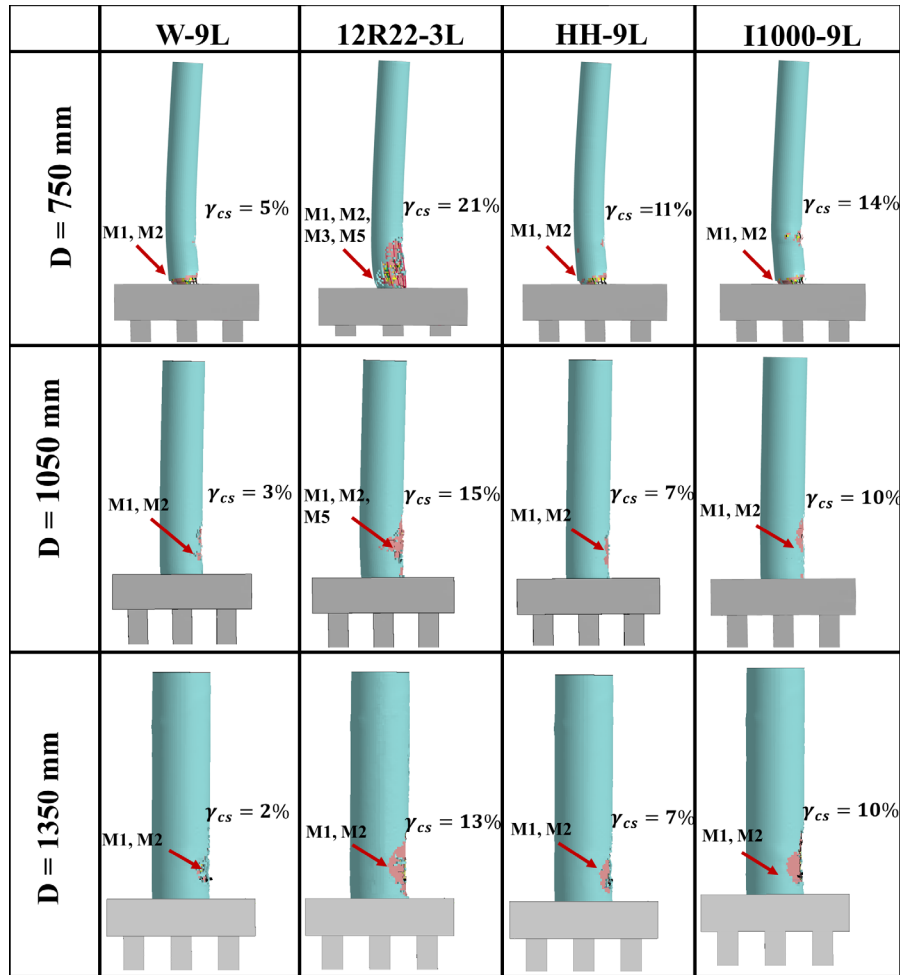


Figure 7.24 Final damage states, selected retrofitting schemes

Consistently, displacement plots shown in Figure 7.25 indicated that all repairing techniques reduced lateral displacements of the bridge columns. Unlike the 750 mm diameter column, it was noted that limited difference in peak displacements was observed when the 1050 mm and 1350 mm columns retrofitted using *W-9L* and *HH-9L*. This is because larger diameters bare columns sustained lower displacements under *F90-I-B*.

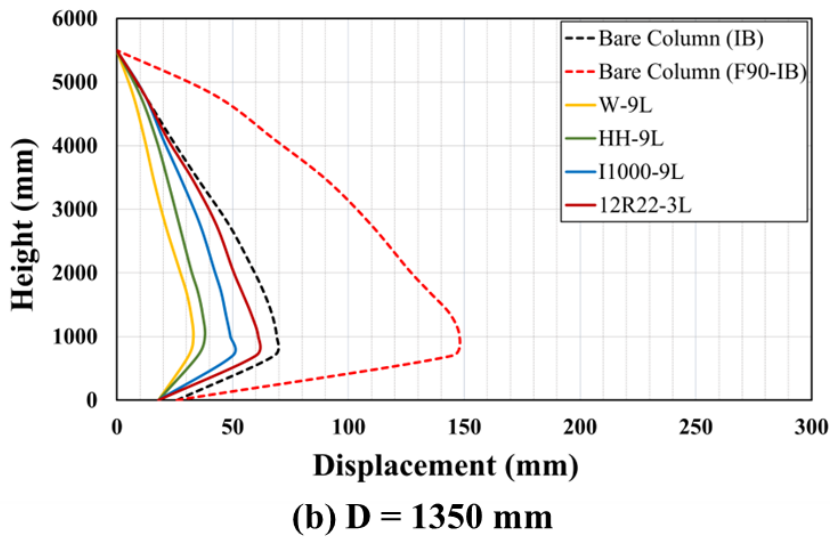
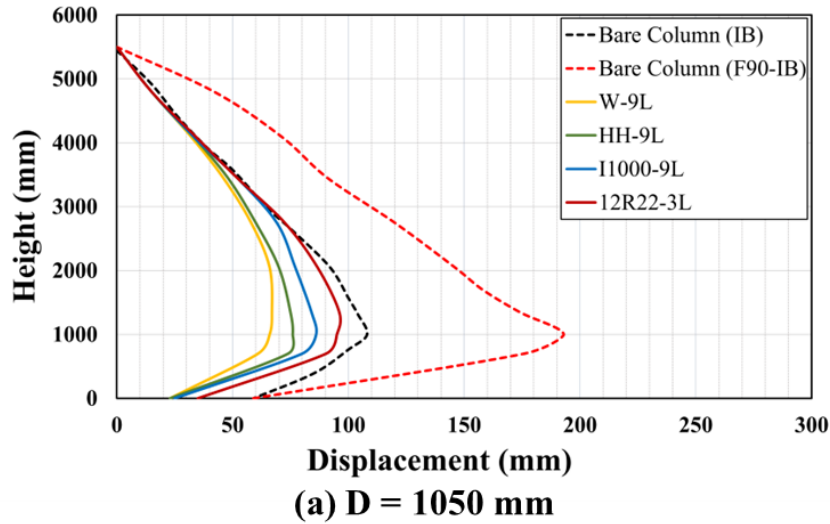


Figure 7.25 Comparison of lateral displacement in bare and retrofitted columns (a) D1050 mm; (b) D1350 mm

Figure 7.26 compares column maximum kinetic energy. As illustrated in this figure, more energy was dissipated when the full height of the column was wrapped as in *W-9L* for all column diameters. For the 1050 mm and 1350 mm diameter columns, the effectiveness of retrofitting schemes on energy dissipation was not as prominent as the 750 mm columns. On the other hand, no pronounced difference in energy dissipation was observed in *W-9L*, *HH-9L*, and *22R12-3L* in the two larger columns.

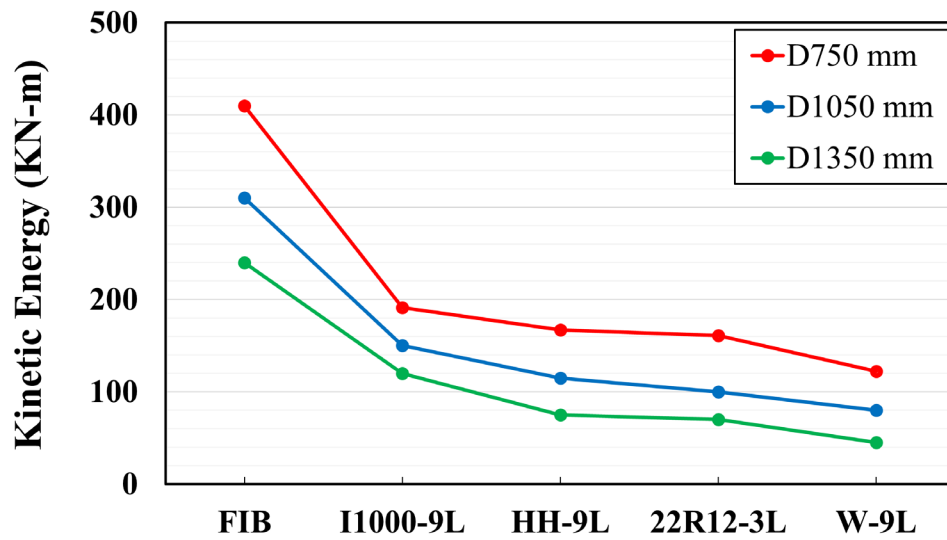


Figure 7.26 Comparison of kinetic energies in bare and retrofitted columns

Conforming with the earlier discussion, higher residual capacities were obtained when W-9L was used as it provides more efficient column confinement and shear resistance compared to the other schemes. Although significant spalling and concrete surface cracking were observed in *I2R22-3L*, columns sustained comparable residual capacities compared to *HH-9L* and *I1000-9L*. This is because the longitudinal CFRP reinforcement provided in *I2R22-3L* promoted column resistance when push down analysis was performed.

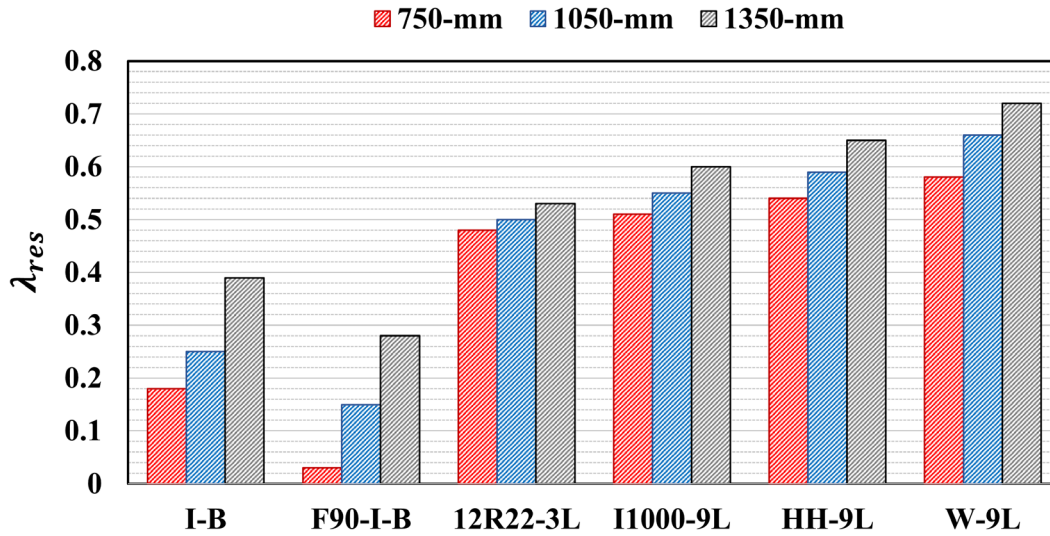


Figure 7.27 Residual axial load carrying capacity for studied column diameters and retrofitting schemes

### 7.7 Summary and Conclusions

The effectiveness of two in situ retrofitting schemes utilized to improve fire-damaged bridge pier column performance under coupled impact and blast was investigated. In the first scheme, columns were repaired using externally bonded CFRP wrap. A hybrid retrofitting technique that combined externally bonded CFRP wrap and near surface mounted (NSM) longitudinal CFRP bars was investigated in the second scheme. Parametric studies were conducted to assess the effectiveness of utilizing various CFRP wrap thicknesses and reinforcement ratios for the two retrofitting schemes. Additionally, the effects of partial and intermittent CFRP wrapping on performance were studied. A more comprehensive assessment was completed by examining the performance of two larger column diameters (i.e., 1050 mm and 1350 mm) repaired using four selected techniques that demonstrated promising damage mitigation effects. Simulation results and damage categories are summarized in Table 7.6, where

$\gamma_{CS}$  is the volume of spalled concrete,  $D_{max}$  is the maximum lateral displacement, and  $KE$  is kinetic energy.

Table 7.6 Retrofitted pier column performance summary

D (mm)	Study Case	$t_{FRP}$ (mm)	$\rho_{FRP}$ (%)	$\gamma_{CS}$ (%)	$\gamma_{res}$ (%)	$D_{max}$ (mm)	KE (N-mm)	Damage Categories
Bare	I-B	-	-	24	18	317	$3.82 \times 10^8$	M1, M2, M5, M6
	F90-I-B	-	-	55	3	547	$4.11 \times 10^8$	M1, M2, M3, M4, M5, M6
Scheme 1	W-3L	0.50	-	39	31	332	$2.18 \times 10^8$	M1, M2, M3, M5, M6
	W-6L	1.00	-	19	42	249	$1.78 \times 10^8$	M1, M2, M3
	W-9L	1.50	-	9	58	209	$1.35 \times 10^8$	M1, M2
	W-12L	2.00	-	7	61	196	$1.24 \times 10^8$	M1, M2
Partially Wrapped	HH-9L	1.50	-	11	54	230	$1.67 \times 10^8$	M1, M2
	I1000-9L	1.50	-	14	51	266	$1.91 \times 10^8$	M1, M2
	I500-9L	1.50	-	27	38	345	$2.64 \times 10^8$	M1, M2, M3, M5
Scheme 2	4R12-1L	0.167	0.13	41	19	366	$3.24 \times 10^8$	M1, M2, M3, M5, M6
	4R12-3L	0.50	0.13	36	30	299	$2.16 \times 10^8$	M1, M2, M3, M5
	8R12-3L	0.50	0.21	27	35	278	$2.05 \times 10^8$	M1, M2, M3, M5
	12R12-3L	0.50	0.36	25	41	260	$1.82 \times 10^8$	M1, M2, M3, M5
	12R22-3L	0.50	1.00	21	48	238	$1.61 \times 10^8$	M1, M2, M3, M5

Simulation results indicated that:

- 1) Using both CFRP wrap and hybrid techniques to repair fire-damaged columns considerably mitigated damage resulting from coupled vehicle collisions and the subsequent air blast.

- 2) For the same material properties, the effectiveness of each scheme varied as a function of retrofit parameters, such as CFRP wrap thickness and CFRP reinforcement ratio.
- 3) The effectiveness of the first retrofitting scheme was highly influenced by CFRP wrap thickness, with noticeable performance improvements observed for larger CFRP thicknesses, which were attributed to confined concrete increased compressive strength. No significant performance difference was noted when wrap thickness increased from 1.5 mm to 2.0 mm in *W-9L* and *W-12L*, respectively, which identified that the 1.5 mm thickness was sufficient to alleviate effects of prescribed impact and blast demands. As a result, *W-9L* is recommended as it would be more economically justified.
- 4) For the first repair scheme, all columns are assumed to remain in operation after repair except the for *W-3L*.
- 5) For the hybrid retrofitting scheme, more distinct performance improvement and damage mitigation was noticeable when thicker CFRP wraps were utilized. No pronounced concrete spalling mitigation and crack intensity reduction was noticed when the reinforcement ratio increased for the same CFRP wrap thickness.
- 6) For the same CFRP wrap thickness, increasing CFRP reinforcement ratios enhanced columns stiffness and consequently contributed to more displacement reduction and kinetic energy absorption.
- 7) For *4R12-1L* and *4R12-3L*, extensive repairs were required to restore column functionality, while columns for the three other cases could remain in operation after implementing moderate repairs.

- 8) For partially wrapped columns, displacements, kinetic energies, and concrete spalling were less than those experienced by bare, fire-damaged columns, with considerable performance improvement and damage mitigation observed for *HH-9L* and *I1000-9L*. Columns retrofitted using *I500-9L* demonstrated severe concrete spalling and significant lateral displacements, which identified this as a less effective repair scheme.
- 9) Similar to *W-9L*, *HH-9L* and *I1000-9L* required minor repairs to preserve column functionality, while extensive repairs were needed for *I500-9L* columns to remain in operation.
- 10) Performance of the 750 mm and 1050 mm column diameters was considerably improved post retrofit.

Based on observed results, for the variables that were studied, the following points should be considered when thinking about repairing a fire-damaged bridge column:

- a) CFRP wrap thickness should be a minimum of 1.5 mm to ensure column capacity is restored and to avoid extensive repairs after impact and blast.
- b) When fire-damaged column repairs are driven by the desire to reduce lateral displacements and kinetic energies, using a CFRP reinforcement ratio of 1% with at least 0.5 mm CFRP wrap is recommended to achieve the highest level of performance.
- c) Partially wrapping the bottom half of the column height could be sufficient to mitigate damage resulting from vehicle collisions coupled with air blast.
- d) Intermittent wrapping could be effective if at least the bottom 20% of the column height is wrapped, as this portion would experience considerably larger demand resulting from a vehicle collision.

## Chapter 8 Multi-Column Piers Subjected to Fire, Vehicle Collision, and Air Blast

### 8.1 Introduction

The study presented herein moves from the isolated pier column investigations completed in previous chapters to examining multi-column pier, multi-hazard performance. Piers with 1050-mm diameter columns were selected for these studies and were subjected to fire prior to impact and blast (i.e., *F-I-B*). This investigation included two, three, and four-column piers. The effectiveness with which CFRP retrofitting techniques studied in Chapter 7 mitigated structural damage was evaluated via examinations of five retrofitting schemes. Parameters used to evaluate performance included column and pier cap permanent sets, crack levels and propagation, final damage states, and spalled concrete volumes. Previously established damage levels were again utilized to quantify multi-hazard event performance. Through these comprehensive examinations, this chapter aims to provide valuable insights into the resiliency of multi-column piers and effectiveness of select retrofitting schemes on performance.

### 8.2 Finite Element Models

#### *8.2.1 Prototype RC multi-column piers*

The four-column bridge pier from an FHWA design example (Wassef et al. 2003) was again used as the base, prototype model in this chapter (Figure 3.1). As illustrated in Figure 8.1, the pier consisted of four circular RC columns spaced at 4300 mm center to center. It is worth noting that fire damage was imposed to one of these columns prior to impact and blast following the approach discussed in Section 3.9. Each column is 5400 mm high and 1050 mm in diameter. Columns are reinforced with 18 No. 25 longitudinal steel bars (1% reinforcement ratio), and No. 10 stirrups spaced at 300 mm. These columns support a 16500 mm long rectangular with 1200 mm x 1200 mm pier cap. The foundation system consists of a 900 mm thick, 3600 mm square

footing supported by eight 450 mm square piles extending 6000 mm into the soil. Pier cap and foundation system reinforcement details are provided in Figure 8.1.

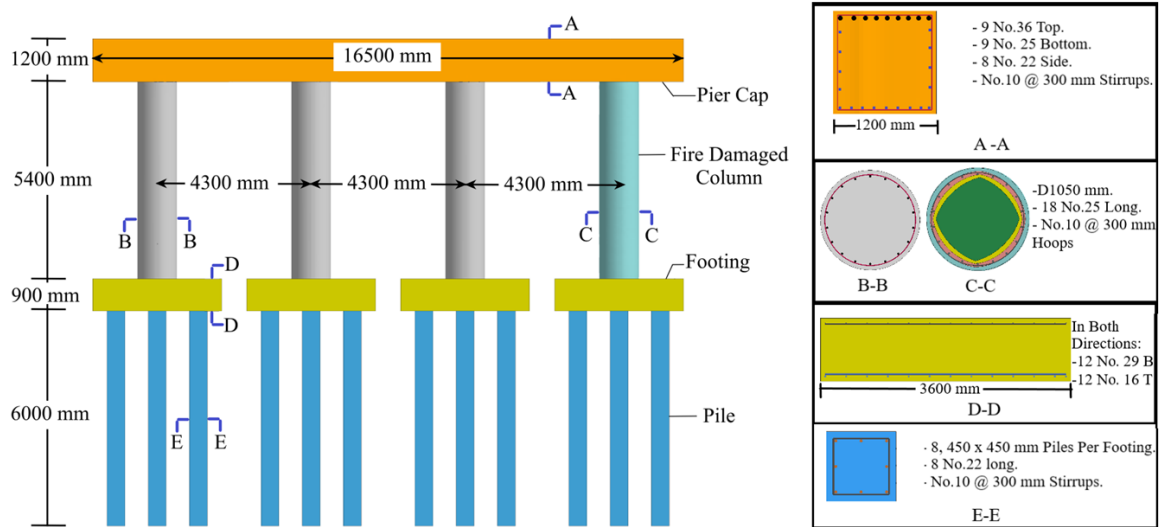
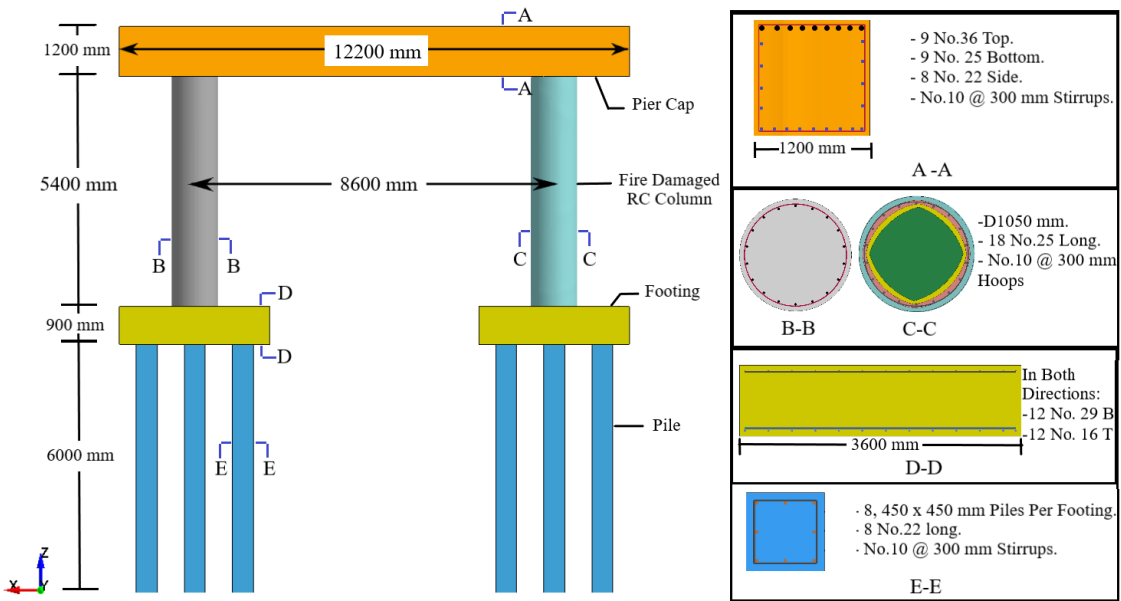
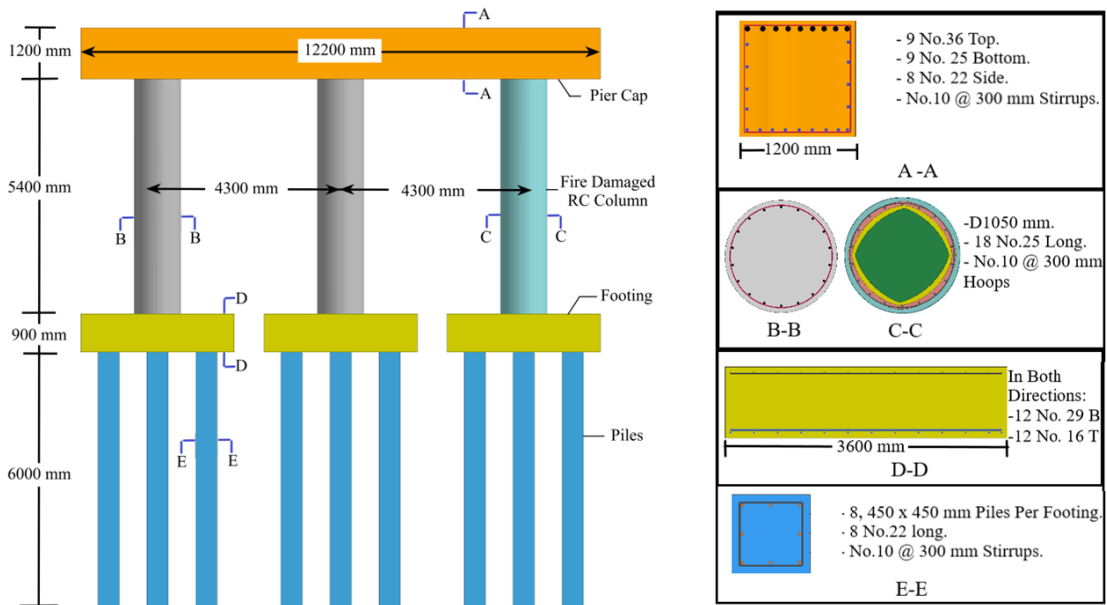


Figure 8.1 Four-column pier finite element model and geometry

Based on earlier research (Fang et al., 2023; Linzell et al., 2020), two- and three-column pier designs were developed from the four-column prototype via removal of supporting columns. While all design parameters remain the same, cap length and column spacing were reduced. Although this decision was taken to examine various bridge pier configurations, the two additional piers still meet the minimum design requirements of *AASHTO-LRFD* (AASHTO LRFD, 2020). Resulting two- and three-column pier models and dimensions are illustrated in Figure 8.2.



(a) Two-column pier



(b) Three-column pier

Figure 8.2 Two- and three-column piers finite element models and geometry

### 8.2.2 Material models

Akin to the isolated bridge pier columns, the piers, foundation systems, steel reinforcement, air, soil, and explosive used the same LS-DYNA material models presented in Section 3.6 and summarized in Table 8.1.

Table 8.1 Material Models

Material	LS-DYNA Model
Concrete	<i>Continuous Surface Cap Concrete (CSCM), MAT-159</i>
Steel Reinforcement	<i>Piecewise Linear Plasticity, MAT-024</i>
Soil	<i>FHWA Soil MAT-147</i>
Soil	<i>Null, MAT-009</i>
Explosive	<i>High Explosive Burn, MAT-008</i>

### 8.2.3 Boundary conditions

To eliminate blast wave reflections LS-DYNA's Boundary-Non-Reflecting option was on the exterior faces of the air and soil volumes. As discussed in Section 3.7, superstructure dead loads were simulated using nodal loads along the top of the cap as illustrated in Figure 8.3. The magnitude of each axial load equaled 6% of the column's nominal capacity. It is important to note that all pier columns were fixed at the base and integrated to the pier cap at the top, following the basic definitions available in AASHTO-LRFD, Section 11.2 (AASHTO LRFD, 2020). Air and soil volumes were as depicted in Figure 8.3 (Linzell et al., 2020; Reid et al., 2004).

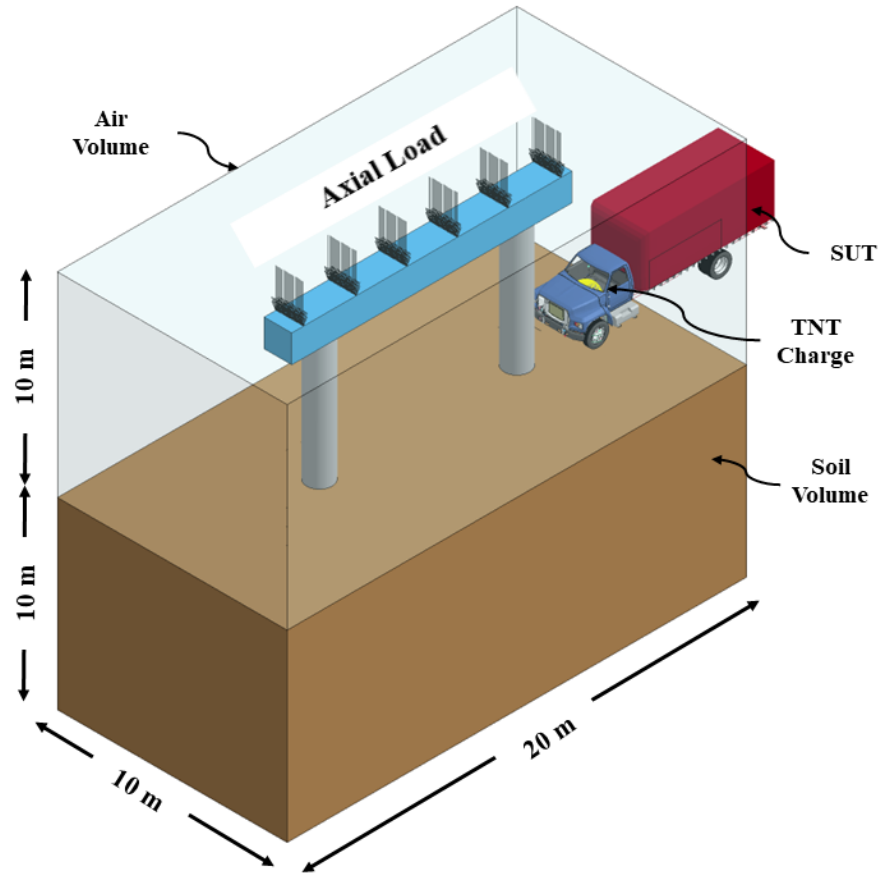


Figure 8.3 Representative two-column pier FE model depicting, air and soil volumes and impact and blast loads

### 8.3 Response of Multi-column Piers

Multi-column, performance was examined subject to the most critical combination of fire, vehicle collision, and air blast identified from previous studies. The exterior pier column, which is being impacted by the SUT, was exposed to 90-minute fire prior to impact and blast (i.e., *F90-I-B*), with the impact speed equaling 120 km/h and the scaled distance set to  $0.25 \text{ m/kg}^{1/3}$ .

Although exposing all columns to fire is more conservative, one column was exposed in this study assuming that the heat produced by fire diminishes with moving away from its source, which was initially assumed to be localized around the exterior pier column. Studies examined

the effect of increased redundancy on resiliency. Results from thermal and subsequent impact and blast analyses are presented in the following sections.

### *8.3.1 Fire response and damage propagation, F90*

Stresses resulting from a simulated 90-minute exposure are shown in Figure 8.4. Similar to results obtained for isolated columns (see Figure 5.10), exposing a single column to fire produced flexural-shear cracks over the height, matching reported test results (Chinthapalli et al., 2019). Cracks initiated at the intersection of the pier columns and caps. The two-column pier was shown to sustain more damage from fire exposure compared to the three- and four-column piers, with shear cracks developed in non-exposed column and flexural cracks initiated at mid-span of the pier cap.

Following the modeling approach presented in Section 3.9, stresses, strains, and geometric imperfections resulting from the thermal analyses stage were used as initial conditions for subsequent coupled impact and blast analyses. Maximum element temperatures were utilized to divide fire-damaged columns into layers, with each layer assigned a unique strength reduction according to Eurocode 2-1 as summarized in Table 3.8.

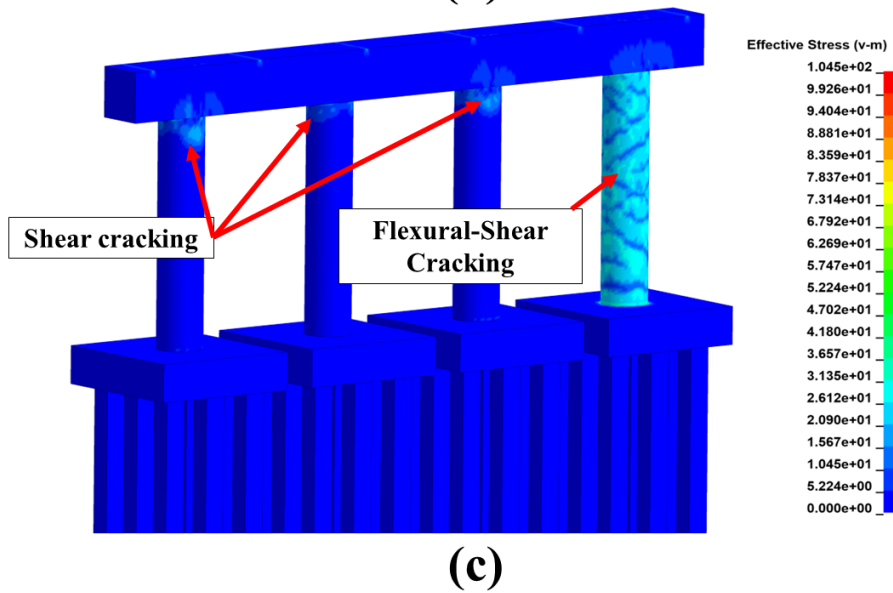
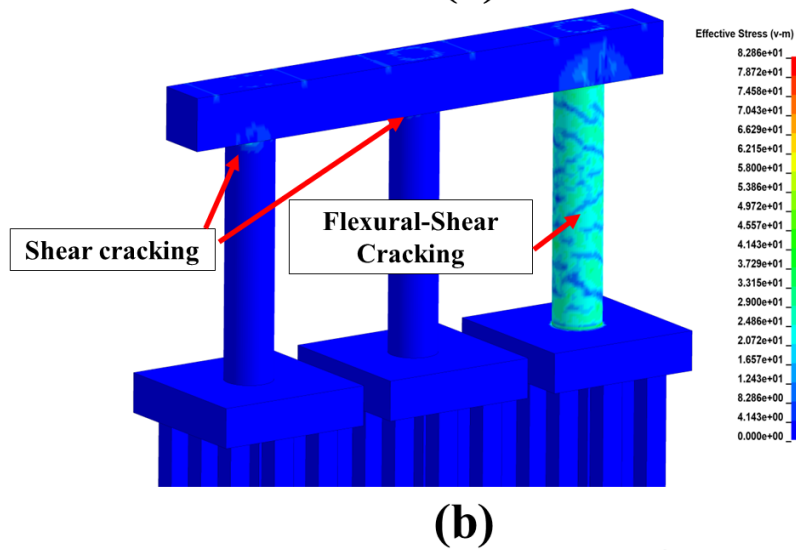
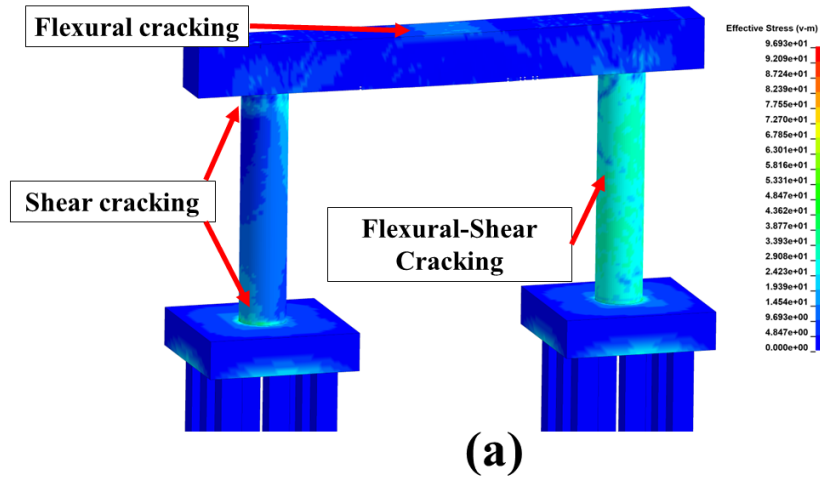


Figure 8.4 Effective thermal stress distribution and crack propagation: (a) two-column pier; (b) three-column pier; (c) four-column pier

### 8.3.2 Post-fire impact and blast response, damage propagation, F90-I-B

Figure 8.5 shows impact and blast load time histories and resulting column mid-height lateral displacement, time histories for studied piers. Vehicle impact initiated after 35 ms, with peak load occurring when the engine impacted the column at  $t = 55$  ms. The explosive detonated at  $t = 60$  ms and reached a peak pressure within 3 ms. Impact and blast forces slightly increased as the number of columns increased, not surprisingly. However, more pier columns have limited influence on distribution of impact and blast forces compared to column diameter. This observation matches findings reported in the literature (Buth et al., 2010; Gomez, 2014).

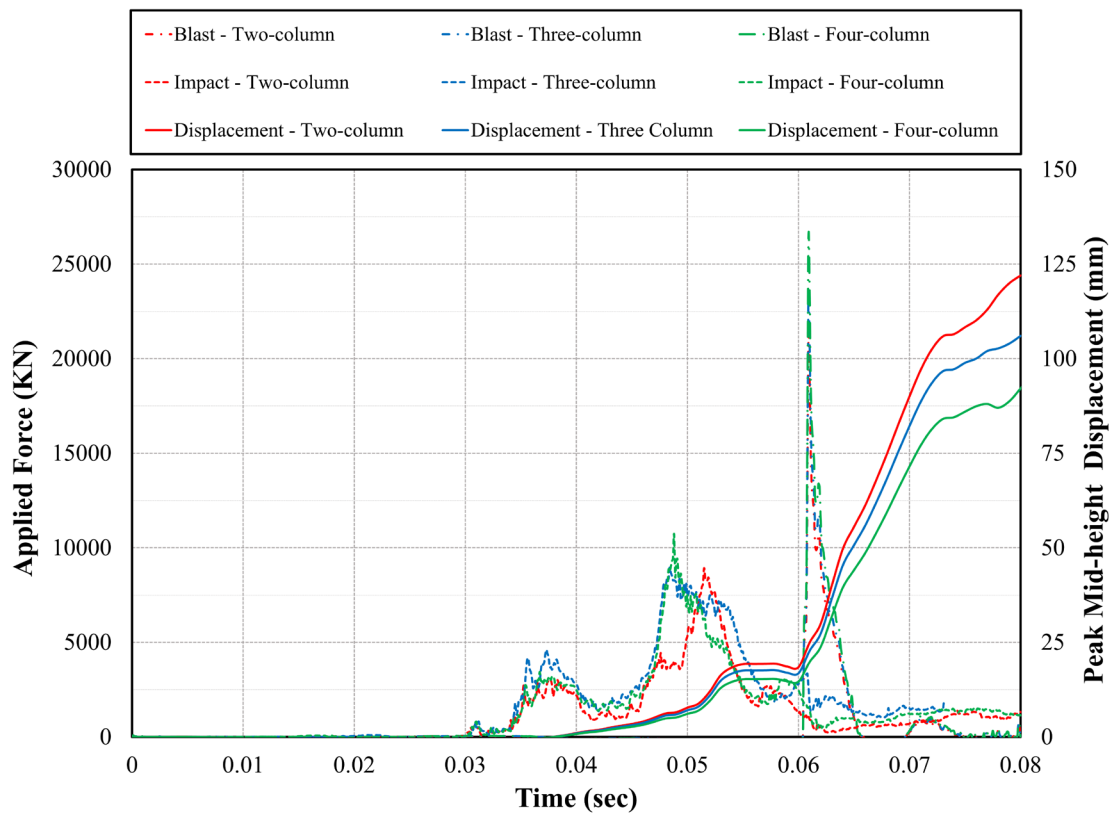


Figure 8.5 Applied load and mid-height lateral displacement time histories, all piers, F90-I-B

Table 8.2 summarizes incremental damage propagation to help identify and classify failure using designations developed in Section 6.2. The table indicates that localized cracks (M1) initiated in the impact region immediately after impact. Engine impact ( $t = 55$  ms) resulted in concrete spalling (M2) in the vicinity of impact location and cracking propagated to the non-impact region for all examined piers. Cracking also initiated in non-impacted columns and in the pier cap. Spalling was observed in the pier cap above impacted columns for the two and three column piers. Detonation initiated mid-height flexural cracking and extensive spalling in the impact region. At  $t = 70$  ms, more extensive spalling occurred, all columns sustained more cracking, and nearly all longitudinal reinforcing bars buckled in the impacted column near the region of impact. Plastic hinge formation was noted near the impact location for the two- and three-column piers. Ground shock waves generated produced cracks in the foundation. At  $t = 85$  ms, the impacted column in the two-column pier experienced shear failure (M4) at its base (M5), significant flexural cracks formed on the non-collision side, and breaching of concrete core was initiated. Shear cracks also developed at the top and bottom of the non-impacted columns and flexural cracks along their height, with cracking severity being influenced by column number.

Representative damage resulting from subjecting pier columns to *I-B* and *F90-I-B* at  $t = 55$  ms (i.e., engine impact), and at  $t = 85$  ms (i.e. blast wave propagation), for studied two-, three-, and four-column piers are presented in Figure 8.6, Figure 8.7, and Figure 8.8. Damage level classifications from Section 6.2 are also shown.

Table 8.2 Response of two-, three-, and four-column piers, F90-I-B

Time Step		t = 35 ms	t = 55 ms	t = 60 ms	t = 70 ms	t = 85 ms
Demand Progression		Initial SUT Collision	SUT Engine impact	Detonation	Blast Wave Engulfment	Blast Wave Propagation
Pier	Response					
Two-column	Damage	<ul style="list-style-type: none"> <li>Cracks initiated in impact region.</li> </ul>	<ul style="list-style-type: none"> <li>Cracks on non-impact faces;</li> <li>Cover spalling at impact location;</li> <li>Cracks in non-impacted columns;</li> <li>Cracks and spalling in pier cap.</li> </ul>	<ul style="list-style-type: none"> <li>Extensive spalling;</li> <li>Shear cracks at the base;</li> <li>Mid-height flexural cracks;</li> <li>Non-impacted column cracking.</li> </ul>	<ul style="list-style-type: none"> <li>Extensive concrete spalling;</li> <li>Plastic hinge development in the impact location.</li> <li>Foundation cracking.</li> </ul>	<ul style="list-style-type: none"> <li>Shear failure at the base;</li> <li>Concrete core breach in the location of impact;</li> <li>Sever cracking in pier and non-impacted column.</li> </ul>
	Reinforcement	Normal	Two reinforcement bars yielded at base	Four bars buckled ( $\gamma_{br} = 22.2\%$ )	Six bars buckled ( $\gamma_{br} = 33.3\%$ )	Three bars and five stirrups fractured.
	Displacement	0	19.4	23.2	93.2	119
Three-column	Damage	<ul style="list-style-type: none"> <li>Cracks in the impact region.</li> </ul>	<ul style="list-style-type: none"> <li>Cracks on non-impact faces;</li> <li>Spalling at impact location;</li> <li>Cracks in non-impacted columns;</li> <li>Cracks and spalling in pier cap.</li> </ul>	<ul style="list-style-type: none"> <li>Shear cracks at base of impacted column;</li> <li>Mid-height flexural cracks.</li> <li>Non-impacted columns cracking.</li> </ul>	<ul style="list-style-type: none"> <li>Cracks along height of impacted column;</li> <li>Concrete spalled in impact region;</li> <li>Plastic hinge development in the impact location</li> <li>Foundation cracking.</li> </ul>	<ul style="list-style-type: none"> <li>Shear cracks in non-impacted columns;</li> <li>Extensive cracks in pier cap.</li> </ul>
	Reinforcement	Normal	Two bars yielded at base	Two bars buckled ( $\gamma_{br} = 11.1\%$ )	Four bars buckled ( $\gamma_{br} = 22.22\%$ )	Two bars and three hoops fractured.
	Displacement	0	17.1	20.2	80.3	106
Four-column	Damage	<ul style="list-style-type: none"> <li>Cracks in impact region.</li> </ul>	<ul style="list-style-type: none"> <li>Cracks in impact and non-impact faces.</li> </ul>	<ul style="list-style-type: none"> <li>Shear cracks at base of impacted column;</li> <li>Mid-height flexural cracks</li> </ul>	<ul style="list-style-type: none"> <li>Cracks along height of impacted column;</li> <li>Concrete spalled in impact region.</li> </ul>	<ul style="list-style-type: none"> <li>Cracking in non-impacted columns;</li> <li>Plastic hinge development in the impact location.</li> </ul>
	Reinforcement	Normal	Normal	Three bars yielded	One bar buckled ( $\gamma_{br} = 5.55\%$ )	Two hoops fractured; two bars buckled ( $\gamma_{br} = 11.1\%$ )
	Displacement	0	13.3	16.4	61.5	88.7

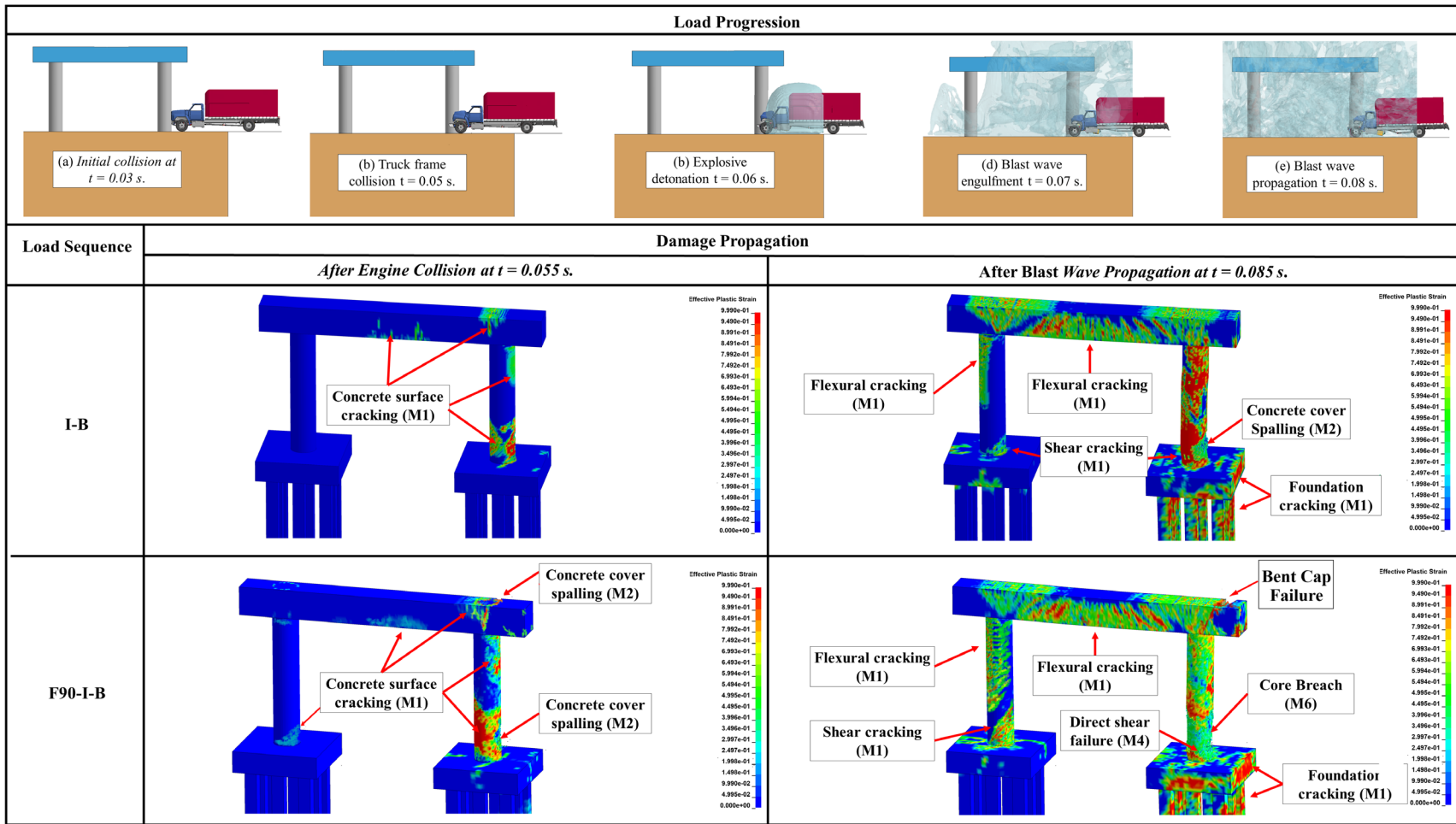


Figure 8.6 Two-column pier: impact and blast load propagation; damage propagation, I-B and F90-I-B

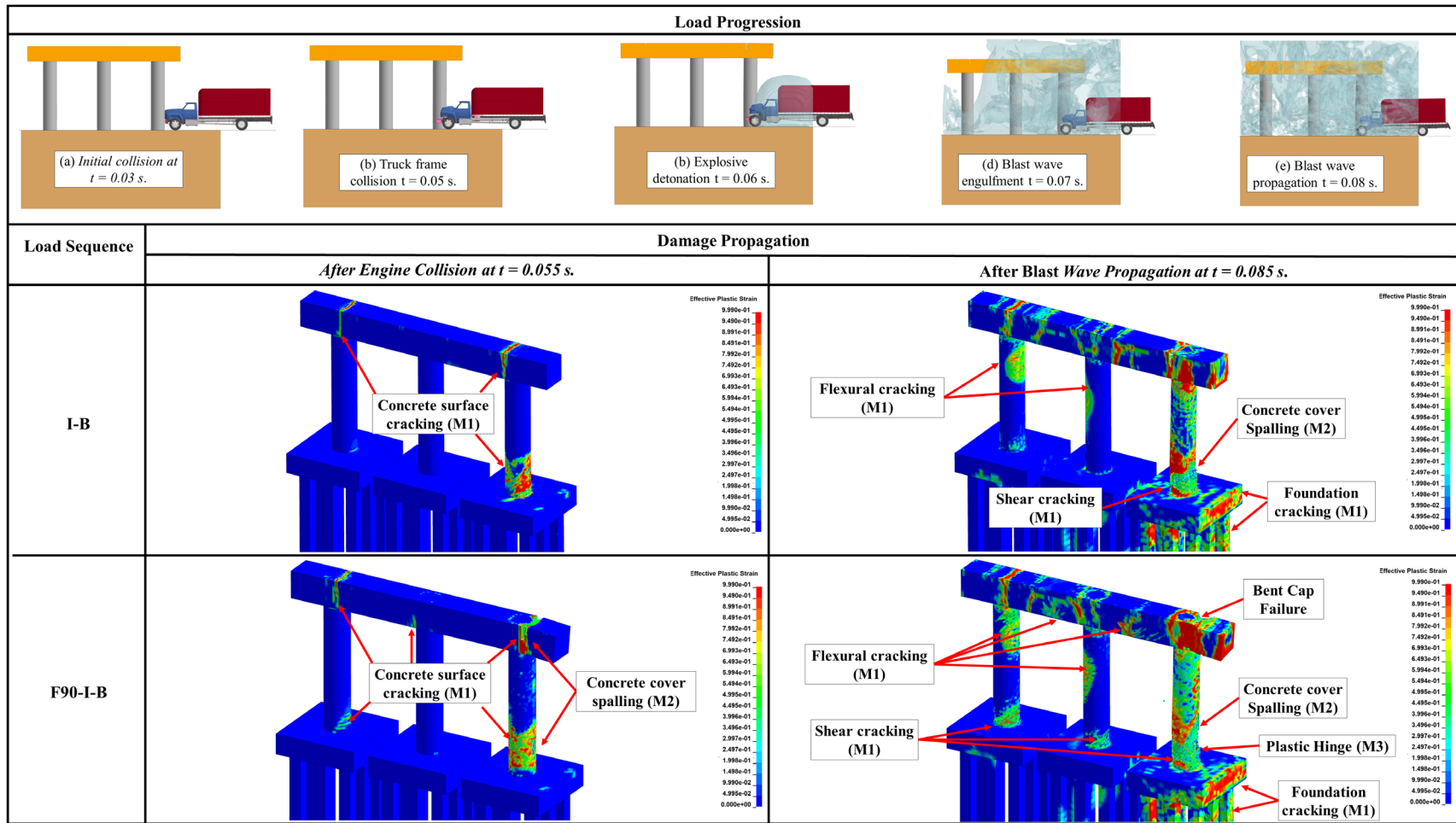


Figure 8.7 Three-column pier: impact and blast load propagation; damage propagation, I-B and F90-I-B

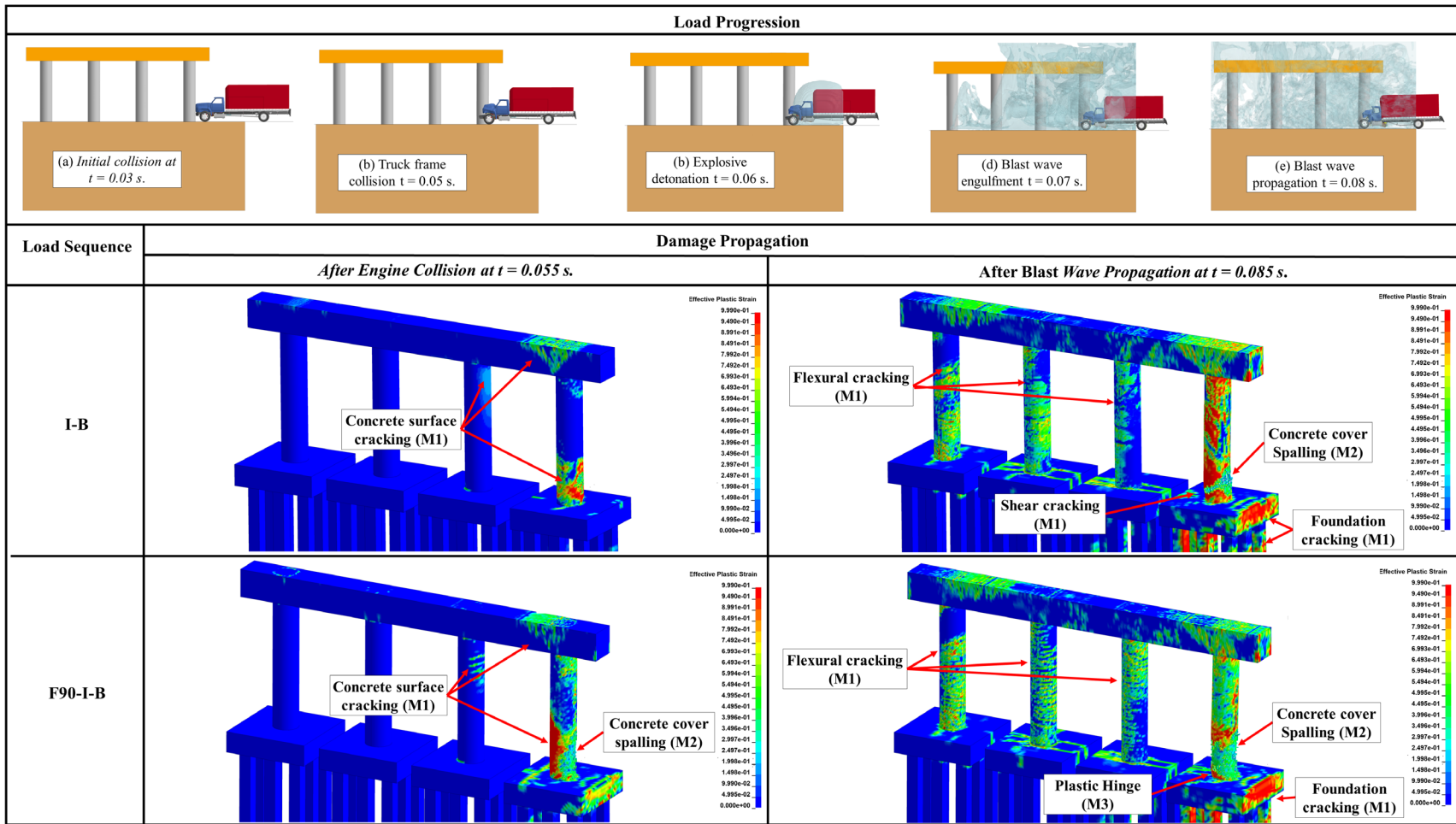


Figure 8.8 Four-column pier: impact and blast load propagation; damage propagation, I-B and F90-I-B

### 8.3.3 Final damage states, permanent sets, deflections

Figure 8.9 depicts pier final damage states, where the volume of spalled concrete ( $\gamma_{cs}$ ) was estimated using LS-DYNA eroded volume time histories. Damage states resulting subject to *F90-I-B* were compared to those for *I-B* loading. As expected, exposing columns to fire prior to impact and blast reduced the concrete considerably reduced concrete strength and produced more significant spalling. Buckled reinforcement was observed for all cases (Table 8.2), with more severe buckling occurring in the two-column pier. Spalling propagated to the non-impact side of the impacted column for cases that involved fire exposure. Significant spalling was observed in the pier cap and at the top end of the impacted column for the two- and three-column piers.

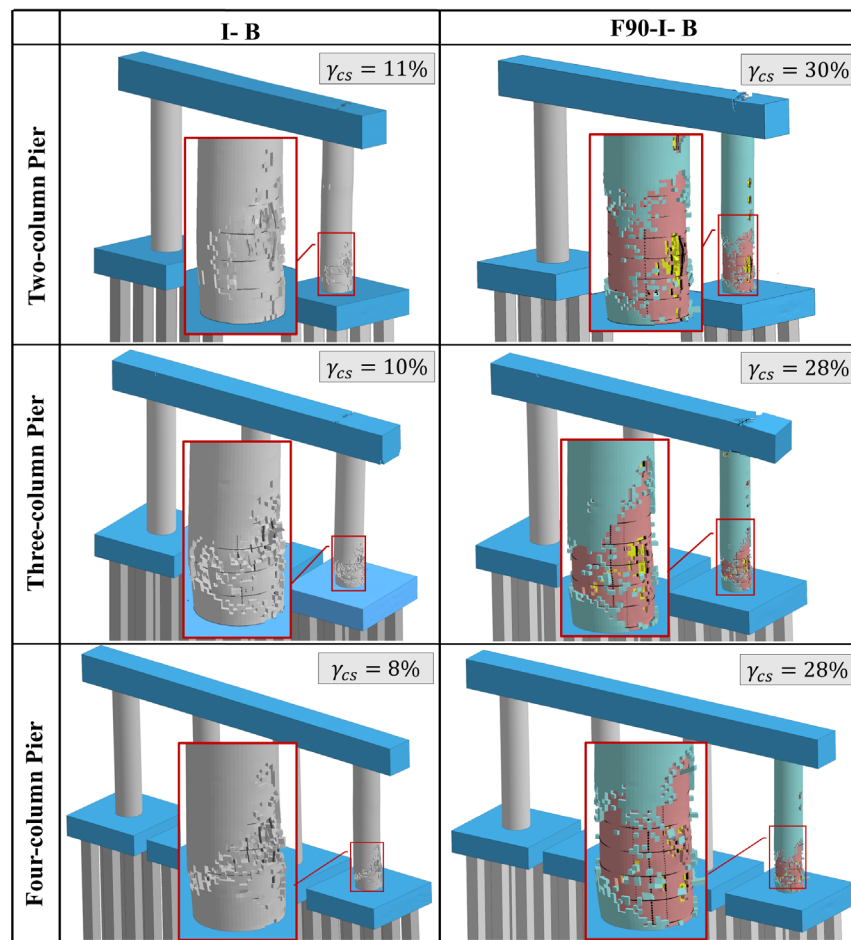


Figure 8.9 Final damage states for studied piers under I-B and F90-I-B

Impacted column permanent sets are shown in Figure 8.10. It was noted that the peak permanent sets were recorded near the impact location and gradually decreased along the height. Larger permanent sets were observed along the height of the impacted column for the two-column pier. It can also be seen that the top end of the impacted column in the two-column pier experienced the largest lateral displacements.

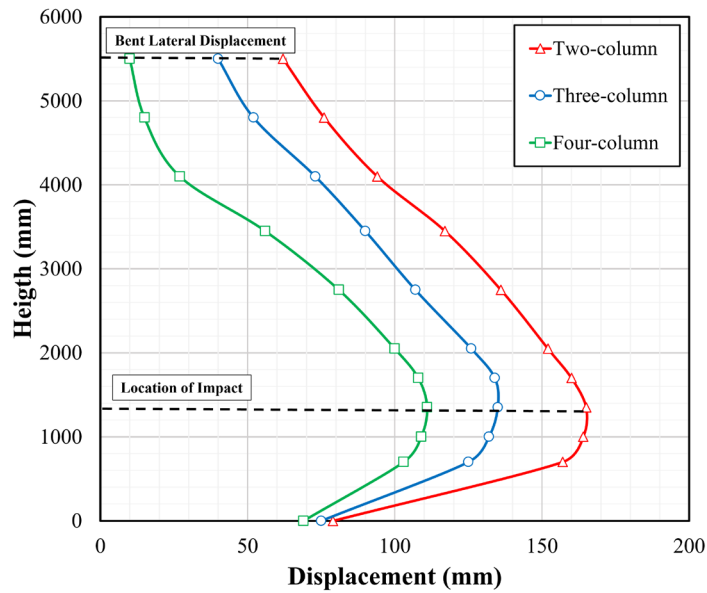


Figure 8.10 Permanent sets of impacted columns in two-, three-, and four-column pier

Deflection of pier caps under *I-B* and *F90-I-B* is shown in Figure 8.11. This figure demonstrated that, compared to *I-B*, there was no considerable variation in pier deflections above non-impact columns for all piers under *F90-I-B*. However, a clear discrepancy in pier deflection was evident above the impacted column, emphasizing potential failure in pier cap in that location. Again, the number of pier columns that support pier cap highly influenced its deflection, since deflection increased when the number of columns in a pier decreased.

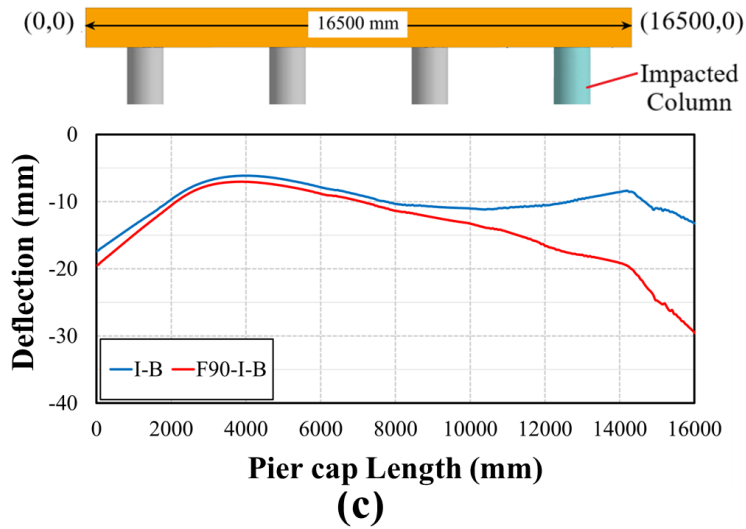
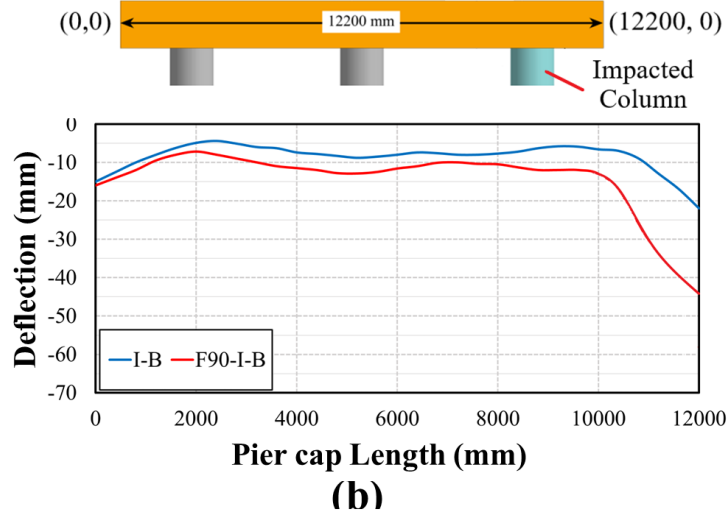
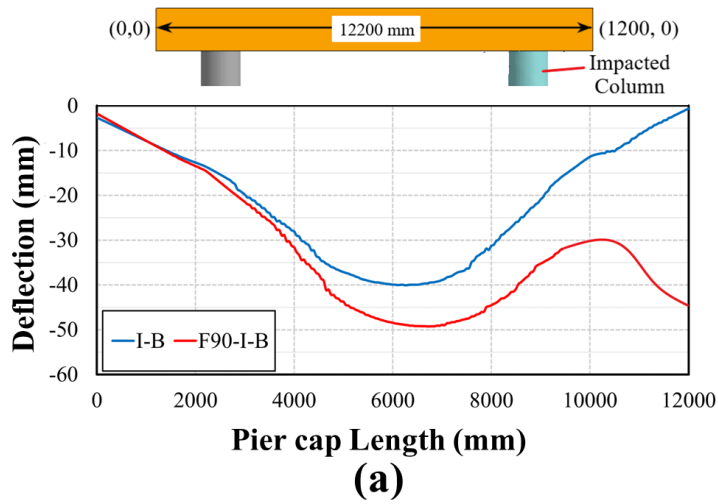


Figure 8.11 Pier cap deflection: (a) two-column pier (b) three-column pier (c) four-column pier

Results indicate that the four-column pier could potentially remain in service while being repaired as most of the concrete spalling occurred near the impact location, no spalling was observed in the pier cap, and limited buckled reinforcement was evident. Extensive repairs would be required to restore the two and three-column piers to their design capacity levels, necessitating bridge closure.

#### 8.4 Multi-column Pier CFRP Retrofitting, F-I-B

Studies of the effectiveness of two CFRP retrofitting schemes examined in Chapter 7 for multi-column piers was examined. As two-column piers were shown to be more vulnerable to examined multi-hazards, they were examined for all retrofitting studies. Selected repair schemes were employed for fire-damaged columns prior to vehicular collision and air blast. In the first scheme, the fire-damaged column was retrofitted using four different externally bonded CFRP wrapping configurations: the entire column, half of the column height, the bottom third of the column height, and intermittently along the height. A hybrid technique combining externally bonded CFRP wrap with near surface mounted (NSM) longitudinal FRP reinforcement was also examined. Modeling approaches and material models matched those described in Chapter 7. Repaired column impact and blast performance was compared to unrepaired fire-damaged columns and to intact columns subject to impact and blast.

##### *8.4.1 Retrofitting scheme details*

Based on findings from Chapter 7, nine CFRP layers having a total thickness of 1.5 mm were used for the four studied configurations. Three CFRP layers with a total thickness of 0.50 mm and 18 longitudinal CFRP bars were used for the second scheme. Studied schemes are illustrated in Figure 8.12, where “*W*” stands for wrap, “*L*” for layer, “*HH*” corresponds to half height, “*TH*” refers to one third height, “*I*” designated intermittent wrapping, and “*R*”

reinforcement. For example, *W-9L* represents columns wrapped solely using nine CFRP layers while *18R25-3L* represents a hybrid scheme where a combination of 25 mm diameter 18 CFRP bars and three CFRP layers were used.

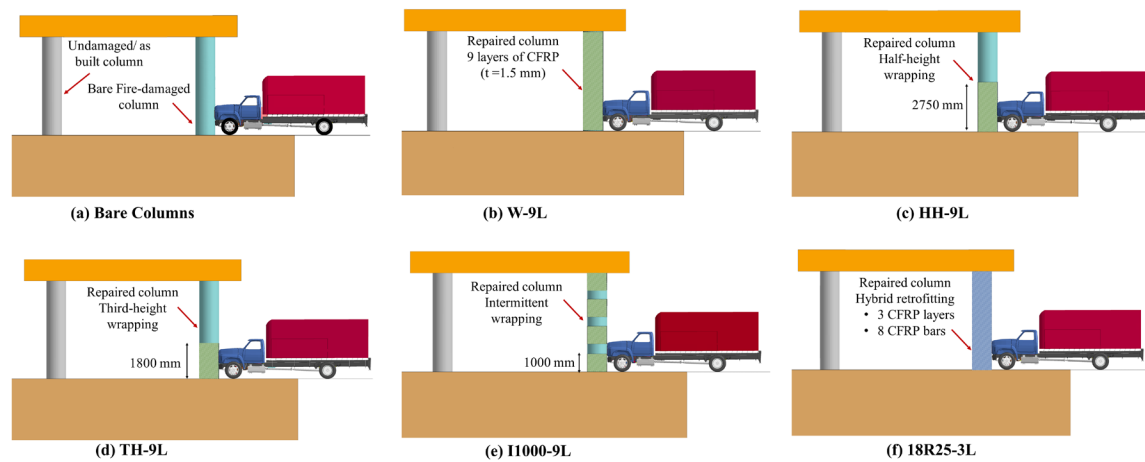


Figure 8.12 Studied retrofitting schemes

#### 8.4.2 Response, damage propagation, permanent sets

Effective plastic strains were compared to assess performance as shown in Figure 8.13. Results indicated that, when compared to non-retrofitted columns, CFRP retrofitting significantly mitigated damage and crack propagation. Irrespective of the retrofitting scheme, a similar performance was observed with flexural cracking propagated along the height of the impacted columns and shear cracks at their bases. Results also indicated that plastic hinges formed at the bottom of columns retrofitted using *HH-9L*, *TH-9L*, and *I1000-9L*. As a result, it was determined that, for the cases that were studied, wrapping the entire height of fire-damaged columns was more effective at mitigating damage resulting from impact and blast given the reduced cracking and concrete spalling. On the other hand, the intensity of flexural and shear cracking observed along the height of the column repaired using *18R25-3L* demonstrates the hybrid retrofitting has

limited influence on damage mitigation under impact and blast compared to all previous schemes.

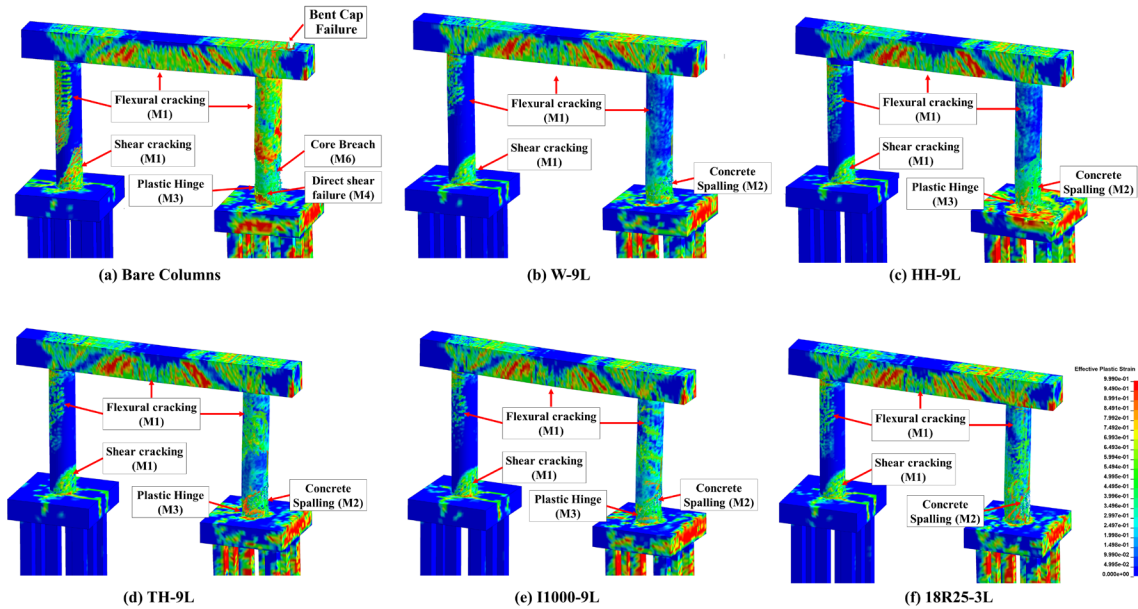


Figure 8.13 Crack propagation, bare and retrofitted columns

Final damage states and relative spalling volumes are shown in Figure 8.14. Columns retrofitted using *18R25-3L* experienced more spalling compared to other studied cases. Given that most spalling was localized to the impact region and limited reinforcement buckling was observed, it is believed that minor repairs will be needed to restore serviceability of all the investigated schemes. It is certainly recognized that inspectors would need to evaluate deterioration levels post impact/blast using visual inspection, nondestructive testing, and analyses in accordance with *AASHTO Manual for Condition Evaluation and LRF of Highway Bridges* and FHWA regulations to determine if repairs are feasible (AASHTO, 2003; FHWA, 1995; Tapan & Aboutaha, 2008).

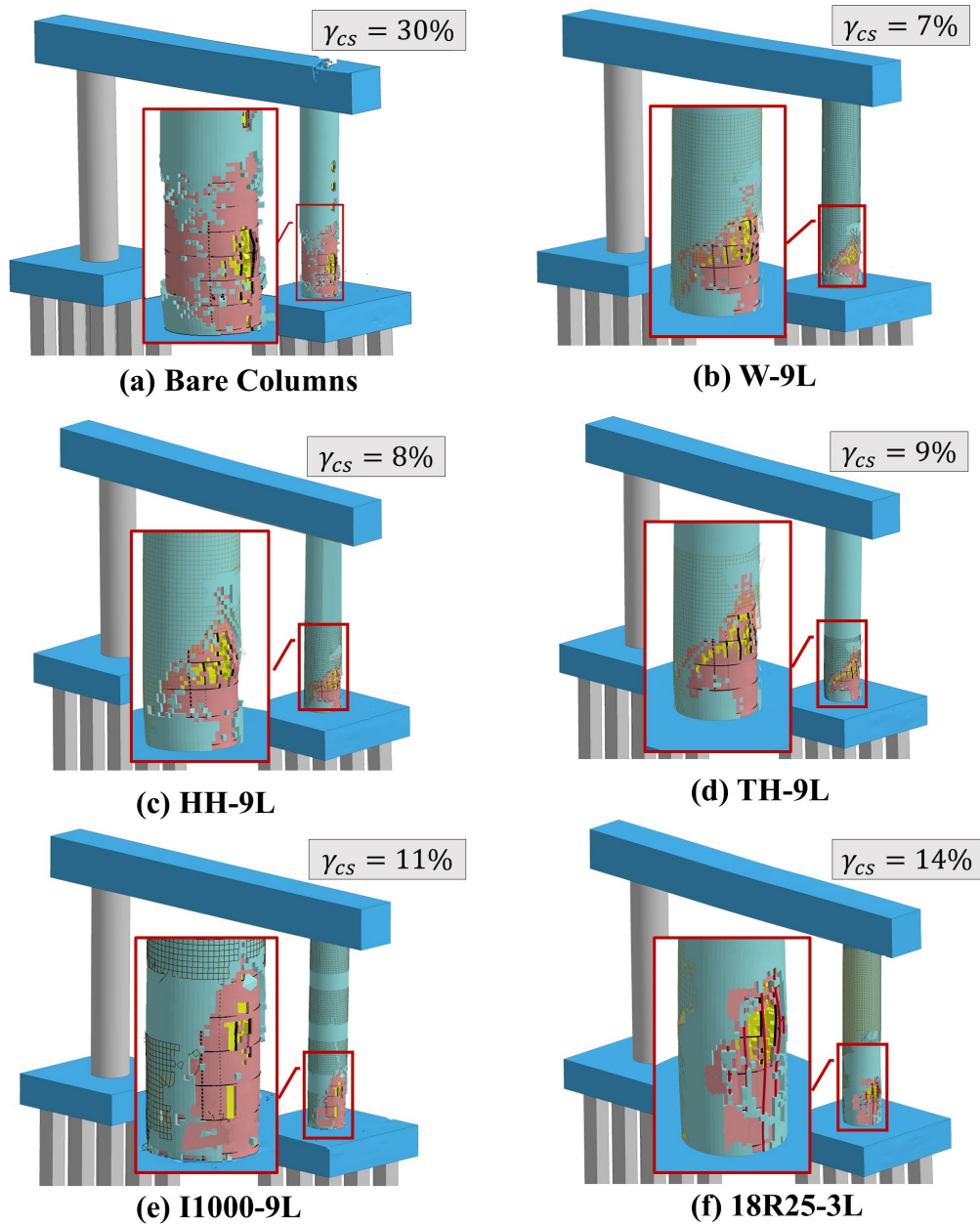


Figure 8.14 Final damage states and spalled concrete volumes, bare and retrofitted columns

Figure 8.15 depicts the permanent sets of impacted column and pier deflections for bare and retrofitted piers. Results indicate that all techniques significantly reduced lateral displacements. It was evident that limited difference in peak displacements was observed for columns retrofitted using *HH-9L* and *TH-9L*. This finding underscores the effectiveness of

wrapping the bottom third of pier columns and offers a more economically justified option for practitioners seeking to mitigate damage. However, it is important to note that while the hybrid retrofitting technique contributed to an appreciable reduction in lateral displacements, its effectiveness at reducing spalling and cracking was limited. As a result, implementing the studied hybrid retrofitting technique may not be advisable due to associated cost.

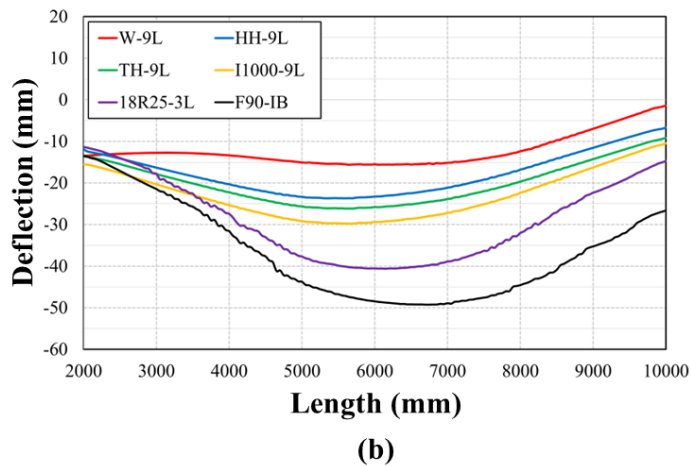
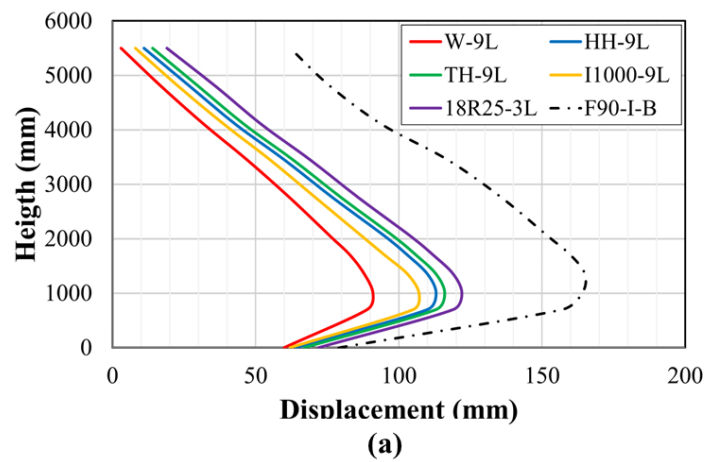


Figure 8.15 Permanent sets: (a) column lateral displacement (b) pier cap deflection

## 8.5 Summary and Conclusions

In this chapter, response and damage experienced by multi-column piers under the most critical combination of fire, impact, and blast (i.e., *F90-I-B*) identified previously. This investigation encompassed two-, three-, and four-column piers whose designs were selected from or loosely based on the FHWA design example and, in certain cases, matched multi-column piers examined previously (Linzell et al., 2020; Wassef et al., 2003). The effectiveness of two proposed CFRP retrofitting schemes for mitigating structural response and damage was further explored. Performance was assessed using damage parameters from previous chapters and included: permanent set, cracking levels, developed damage categories, final damage states, and spanned concrete volumes.

Findings indicated that:

1. The two-column pier was more vulnerable to fire exposure than the three- and four-column piers, with shear cracks developed in the non-impacted column and at interfaces between the columns and cap and flexural cracks at mid-span of the pier cap.
2. Exposing concrete to elevated temperatures prior to impact and blast resulted in more pronounced damage.
3. No considerable change in pier deflection above non-impact columns was observed for *F90-I-B* in comparison to *I-B*. Two- and three-column piers exhibited clear pier deflection discrepancies, which were evident above the impacted column, emphasizing potential pier cap failure in that location.
4. Extensive repairs are required to restore two and three-column piers to their design capacities, necessitating bridge closure.

5. The four-column pier could potentially remain in service while being repaired as most spalling occurred near the impact location and limited reinforcement buckling was observed.
6. Damage was significantly mitigated when CFRP retrofitting was used. Irrespective of scheme, retrofitted piers largely performed similarly with flexural cracking along the height of impacted columns, shear cracks at their bases, and concrete spalling in the impact region.
7. CRFP wrap along the entire height of the fire-damaged columns was more effective at mitigating damage resulting from impact and blast compared to the cases that involved partial and intermittent wrapping. However, resulting concrete spalling and lateral displacement indicated that wrapping the bottom third of the columns could be potentially used as an economically feasible option.
8. The studied hybrid retrofit technique, which involved CFRP wrap and near surface mounted CFRP longitudinal reinforcement, was less effective at mitigating damage than retrofits that increase wrap thickness. As a result, the studied hybrid technique is not recommended.

## Chapter 9 Full Bridge Performance under Fire, Impact, and Air Blast

### 9.1 Introduction

Performance investigations were further extended to examine the behavior of a full-scale bridge system under SUT impact, air blast, and fire. An existing, two-span, steel-concrete composite bridge in Sidney, NE was examined under four loading scenarios involving: (i) vehicle impact (ii) air blast (iii) coupled impact and blast and (v) post-fire impact and blast (i.e., *F90-I-B*). Bridge plans were obtained from the Nebraska Department of Transportation (NDOT). The selected prototype bridge was analyzed under these multi-hazards to provide more insight into resiliency, damage levels, and collapse vulnerability when inherent redundancy provided by a bridge system is considered. Previously identified damage parameters including crack propagation levels, final damage states, spalled concrete volumes, and categorized damage levels were utilized to quantify bridge performance. The effectiveness of an innovative and cost-effective retrofitting approach that utilizes soil infill between pier columns to potentially harden substructure units against extreme demands was also investigated.

### 9.2 Prototype Bridge Model

As indicated earlier, an existing two-span, grade separation bridge located over I-80 in Sidney, NE was considered, and design plans were obtained from NDOT. The bridge consists of two simple spans with a total length of 56000 mm and a 13400 mm width and carries two lanes of traffic. The superstructure consists of a 200 mm thick reinforced concrete (RC) slab structurally connected to five 1270 mm deep steel plate girders with their centers spaced 3000 mm. The bridge is supported by abutments and a single, three-column pier. The pier has 1000 mm diameter and 5000 mm clear height RC circular columns, and a 13500 mm long, rectangular pier cap. Each column is supported by a 2400 mm x 2400 mm x 1350 mm square spread footing.

Each footing is, in turn, supported by eight RC 250 mm square piles that are 6000 mm long.

General geometric information is found in Figure 9.1 through Figure 9.4.

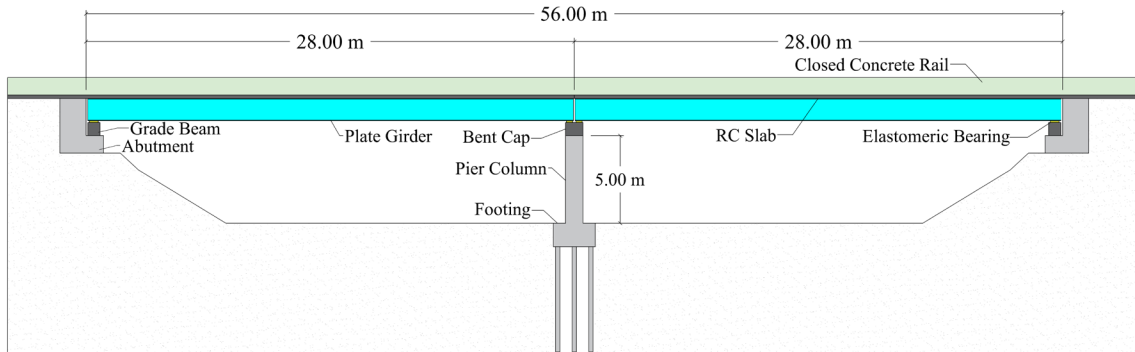


Figure 9.1 Bridge elevation

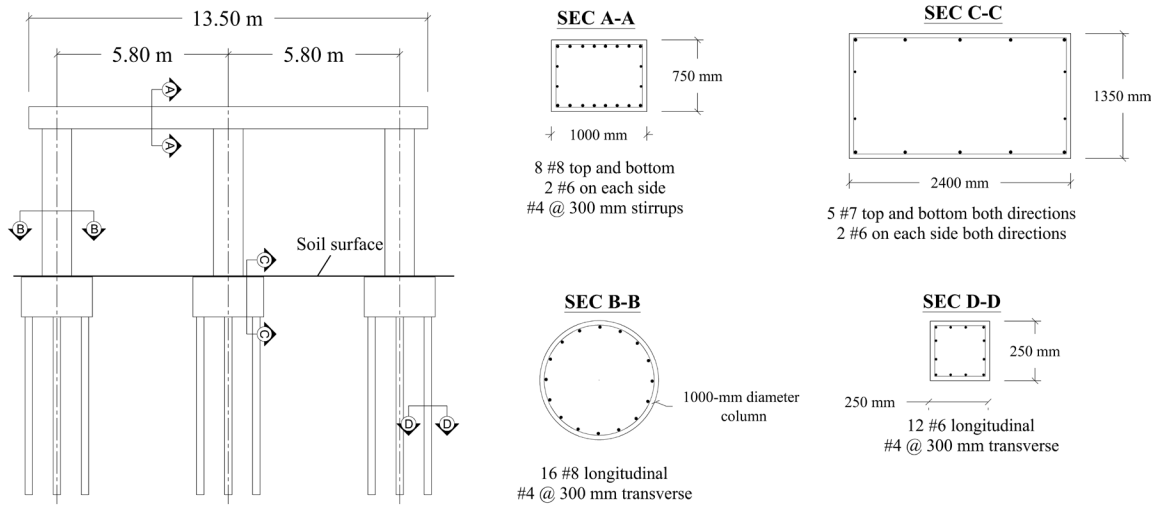


Figure 9.2 Pier elevation and details

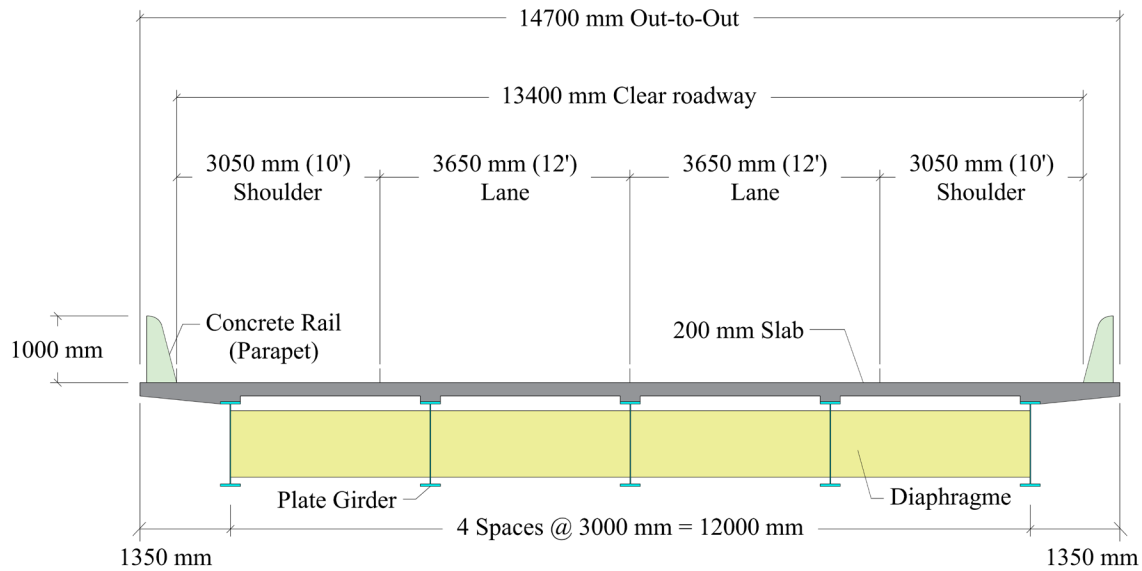


Figure 9.3 Superstructure cross section

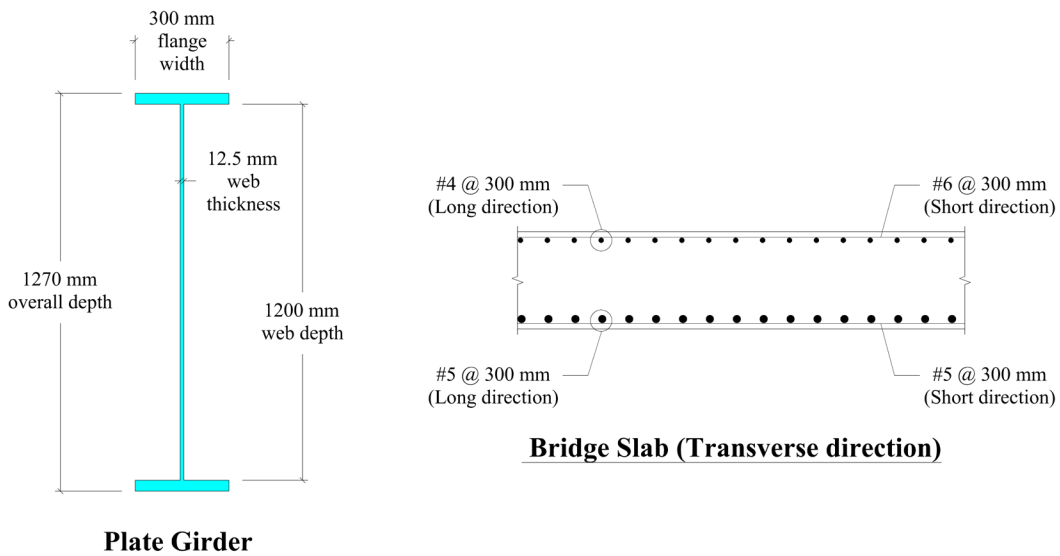


Figure 9.4 Superstructure details

### 9.3 Finite Element Modeling

A detailed description of the finite element model is provided in the following sections. Information related to model development, selected constitutive models, model coupling and boundary conditions, and load types and their application to the model is provided.

### 9.3.1 Element formulation and material models

A three-dimensional FE model of the bridge was developed in LS-DYNA. Constant stress hexahedral solid elements were utilized to model the slab, pier, elastomeric bearings, abutments, grade beams, and foundation system. Even though shell elements are frequently used to model steel girders and diaphragms to optimize computational cost, solid elements were utilized in the current study as they could better capture localized deformations and stress concentration and better mimic composite action, performance aspects that could become critical to track under studied extreme demands (Alos-Moya et al., 2014). To mitigate zero energy deformation modes, which represented strain-free element distortion, Type 5 ( $IHQ=5$ ) hourglass control with an hourglass coefficient ( $QM$ ) of 0.1 was employed (Fang et al., 2021b; Murray, 2007). Steel reinforcement was modeled using Hughes- Liu beam elements. Concrete and steel material models matched those presented in Chapter 3. While the *Continuous Surface Cap* material model was utilized to model bridge abutments in the first modeling attempt, LS-DYNA's *RIGID* material model ( $MAT-20$ ) was eventually used given the negligible impact of the abutments on the overall bridge performance and to minimize computational cost (Hallquist, 2014). As no details about bridge bearings were provided, elastomeric bearings, which are extensively used in current bridge practice in the US, were used in this research (Yi et al., 2014a). Elastomeric bearings with a 0.5 m length, 0.25 m width, and 0.15 m thickness were selected in accordance with previous research studies (Yi et al., 2014a). As recommended in the literature, LS-DYNA's viscoelastic material model ( $MAT-006$ ) was selected to define the bearing behavior (Lin et al., 2020; Yi et al., 2014a). Selected concrete, steel, and elastomeric bearing properties are summarized in Table 9.1.

Table 9.1 Material properties of the bridge overpass

Member	Material Model	Parameter	Magnitude
Steel Girder	Piecewise Linear Plasticity (MAT-24)	Mass density (kg/m <sup>3</sup> )	7850
		Yield strength (MPa)	250
		Young's modulus (GPa)	200
		Tangent modulus (MPa)	1500
		Poisson's ratio	0.30
		Failure strain (%)	0.20
		Strain rate parameter C	40
		Strain rate parameter P	5
Slab, columns, pier cap, footings, and piles	Continuous surface cap (MAT-159)	Mass density (kg/m <sup>3</sup> )	2380
		Unconfined compressive strength (MPa)	28
		Maximum aggregate diameter (mm)	19
		Element erosion parameter	1.10
Abutments and grade beams	Rigid (MAT-20)	Mass density (kg/m <sup>3</sup> )	7850
		Young's modulus (GPa)	200
		Poisson's ratio	0.30
Steel reinforcement	Piecewise Linear Plasticity (MAT-24)	Mass density (kg/m <sup>3</sup> )	7850
		Yield strength (MPa)	415
		Young's Modulus (GPa)	200
		Tangent Modulus (MPa)	2000
		Poisson's ratio	0.30
		Failure strain (%)	0.15
		Strain rate parameter C	40
		Strain rate parameter P	5
Elastomeric bearings	Viscoelastic (MAT-006)	Mass density (kg/m <sup>3</sup> )	2300
		Bulk modulus (MPa)	2000
		Shear modulus (MPa)	1.00

In a similar fashion to completed isolated column and multi-column pier studies, LS-DYNA's *Multi-Material Arbitrary Lagrangian Eulerian (MM-ALE)* approach was implemented to model the soil, air, and explosive, with material models matching those presented in Section

3.6 (Alomari & Linzell, 2022, 2024; Hallquist, 2014). After several trials, soil and air volumes were proportioned so that realistic soil-structure interaction was achieved, potential reflected blast wave disturbances through the soil domain was eliminated, and to ensure realistic representation of blast wave propagation around the bridge system (Reid et al., 2004). The detailed finite element developed in LS-DYNA is depicted in Figure 9.5. More detail on information presented in the figure is provided in the following sections.

### 9.3.2 Model coupling, contact, and boundary conditions

All RC structural elements and steel reinforcement were coupled using LS-DYNA's *Lagrangian in Solid* option (Hallquist, 2014). The same coupling method was utilized to define interaction between the bridge and ALE domains (i.e., air, soil, and explosive). Following previous studies, the *Automatic Surface to Surface* option was used to model contact between the bridge and SUT (Hallquist, 2014; Murray, 2007; Reese et al., 2014). Computational instabilities resulting from blast wave propagation were addressed by employing LS-DYNA's *Boundary Non-Reflecting* command at surfaces defining air and soil domains (Hallquist, 2014). The nodes shared with the footing at the column base were merged to achieve full fixation. Given that a rigid material model was utilized to model the abutments, LS-DYNA's *CMO* option, which stands for center of mass constraint option and defines the corresponding coordinates system, was employed to constrain displacements and rotations in all directions. To effectively simulate composite action between bridge the slab and supporting girders, shared interface nodes were merged as recommended in literature (Lin et al., 2020). The *Automatic Surface to Surface* option was again used to define contact between the elastomeric bearings and adjacent structural elements (i.e., pier cap, girders).

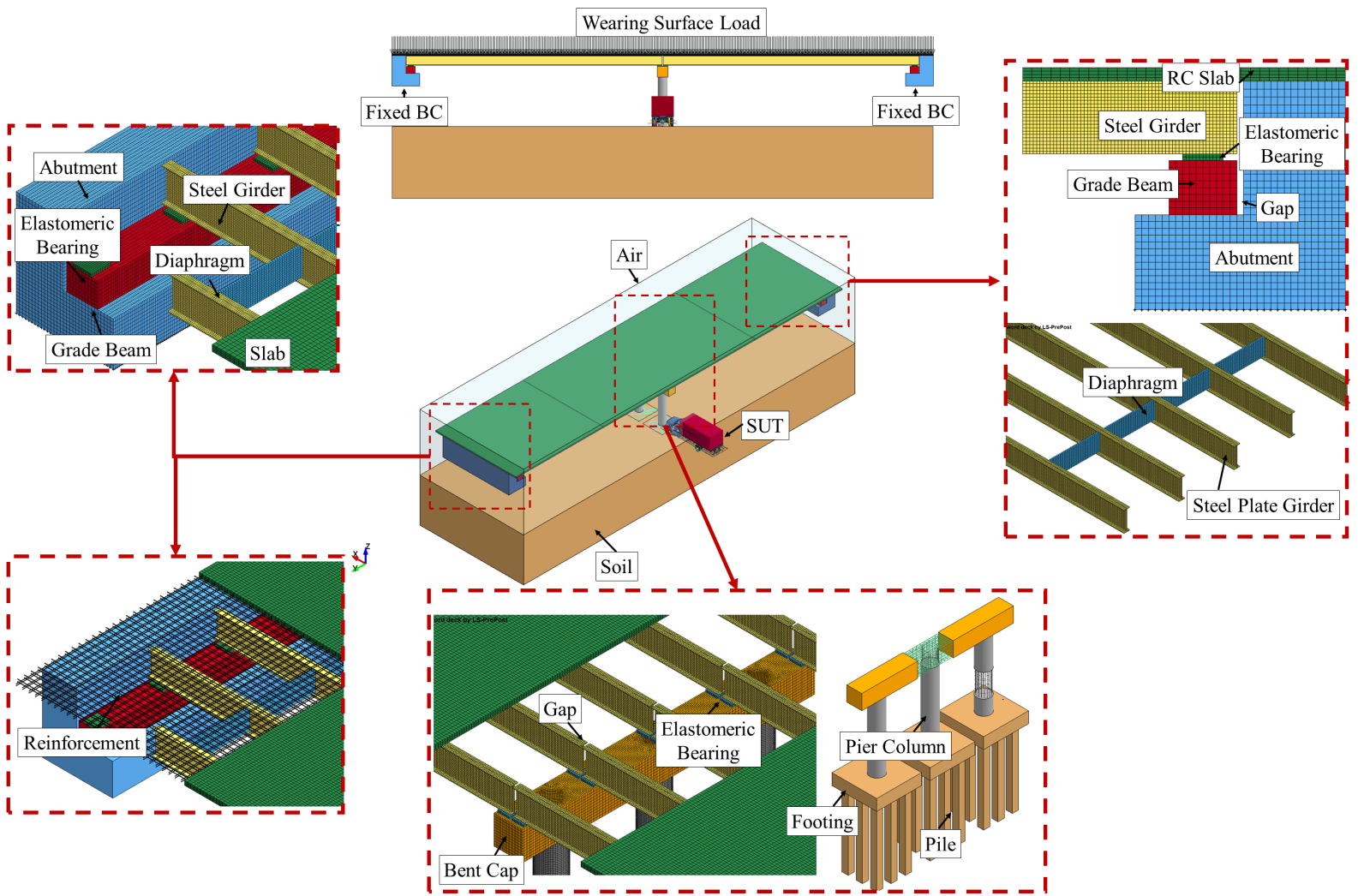


Figure 9.5 Bridge FE model

### 9.3.3 Load application

For all analysis stages, LS-DYNA's *LOAD-BODY-Z* option was used to activate gravity loads and applied loads were gradually increased over time to avoid undesirable dynamic effects (Hallquist, 2014). A future wearing surface was considered, with the load corresponding to a 50-mm (2 in) thick wearing surface having a unit weight of 2242 kg/m<sup>3</sup> (140 lb/ft<sup>3</sup>), according to *AASHTO-LRFD* (2020). The load was distributed to the slab using the *LOAD-NODE-SET* keyword.

As indicated earlier, bridge performance was examined under individual impact and blast loads, coupled impact and blast, and coupled impact and blast after fire exposure. As *F90-I-B* had the most adversely affected isolated column performance and was identified to be the worst-case scenario of the three studied demands, it was conservatively employed to study post-fire impact and blast performance of the bridge system. Vehicle collision was again simulated using the Ford F800 single unit truck (SUT) model. An impact speed of 120 km/h was selected, which corresponded to conventional maximum rural highway speed limits in the U.S. Furthermore, the current study used the previously selected scaled distance of  $Z = 0.25 \text{ m/kg}^{1/3}$ . Like analyses completed on isolated columns and multi-column piers, the developed multi-step modeling approach was utilized to couple heat transfer and thermal analyses prior to any explicit structural analyses. The two-step modeling technique combined (1) implicit, quasi-static, heat transfer analyses using ISO-834 standard fire curves (ISO, 1999) with (2) explicit analyses simulating collision and blast with prescribed speed and scaled distance. This process is illustrated in Figure 9.6. As recommended by several research studies, fire analyses encompassed exposing portions of the pier cap, deck slab, and steel girders to fire prior to impact and blast, (Alos-Moya et al., 2014; Nahid, 2015; Timilsina et al., 2021; X. Wu et al., 2020).

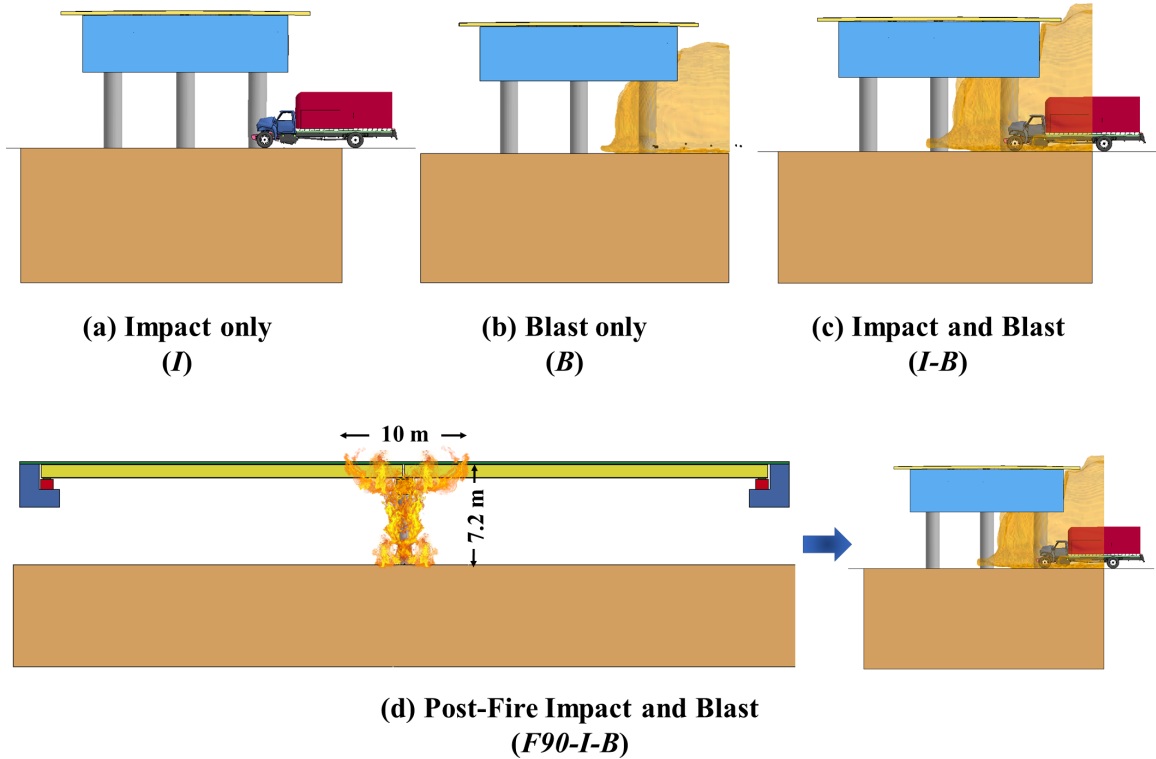


Figure 9.6 Studied loading sequences

#### 9.4 FE Model Validation

In addition to validation work presented in Chapter 4, the bridge model was validated by comparing simulated deflections to those obtained from the fundamental beam theory. The accuracy of the middle girder deflection predictions under self-weight and slab and wearing surface dead loads was simplistically investigated by comparing simulated deflections to those computed using closed form solutions based on the double integration method. Representative sections of the middle girder and effective slab width used in hand calculations are depicted in Figure 9.7. The analytical procedure used to calculate girder's deflection is summarized as follows:

1. Effective span length:

As specified in *AASHTO-LRFD*, Section 6.7.1 (2020), effective span length should be taken as the distance between centers of bearings or other supports. For the selected bridge system, effective span length ( $L_{eff}$ ) is 28.00 m.

2. Calculate the effective slab width:

As specified in *AASHTO-LRFD*, Article 6.10.1.1.1e (2020), the effective flange width should be taken as the least of : (1) one quarter of the effective span length; (2) twelve times the average slab thickness, plus the greater of the web thickness or one half the width of the top flange of the girder; and (3) the average spacing between adjacent girders. Hence, effective slab width ( $b_{eff}$ ) is 2.55 m.

3. Compute the transformed moment of inertia ( $I_{tr}$ ):

Given concrete and steel material properties, the modular ratio ( $n$ ), which is the ratio between steel and concrete moduli of elasticity, is conservatively rounded to 8.0. Then, section properties were used to estimate the cross-sectional areas and the moments of inertia for the slab, the girder, and the haunch. The location of neutral axis of the transformed section ( $Y_{tr}$ ) is 0.3805 m. Parallel axis theory was then employed to calculate the transformed moment of inertia as  $0.02086 m^4$ .

4. Calculate the total dead load ( $DL$ ):

The dead load that is acting on this section is divided into its own weight ( $W_{own}$ ), and the superimposed load of the wearing surface ( $W_s$ ). Based on the material properties listed in Table 9.1, the own weight of the composite section is 15.02 kN/m. On the other hand, the weight corresponding to a 50 mm-thick wearing surface is 2.80 kN/m. Thus, the total dead load equated to 17.82 kN/m.

5. Calculate the maximum mid-span deflection ( $\Delta_{DL}$ ):

Deflection caused by the dead load only can be calculated as follows:

$$\Delta_{DL} = \frac{5 * DL * L_{eff}^4}{384 * E_s * I_{tr}} = \frac{(5)(17.82)(28000^4)}{(384)(200000)(2.086 \times 10^{10})} = 34.18 \text{ mm}$$

Simulated and calculated middle girder deflections are compared in Figure 9.8 and demonstrated reasonable agreement, with simulated deflections lower than those calculated using fundamental principles. Differences can be attributed to the assumptions made in hand calculations, such as neglecting steel reinforcement in slab and diaphragm, and other factors including out-of-plane load shearing.

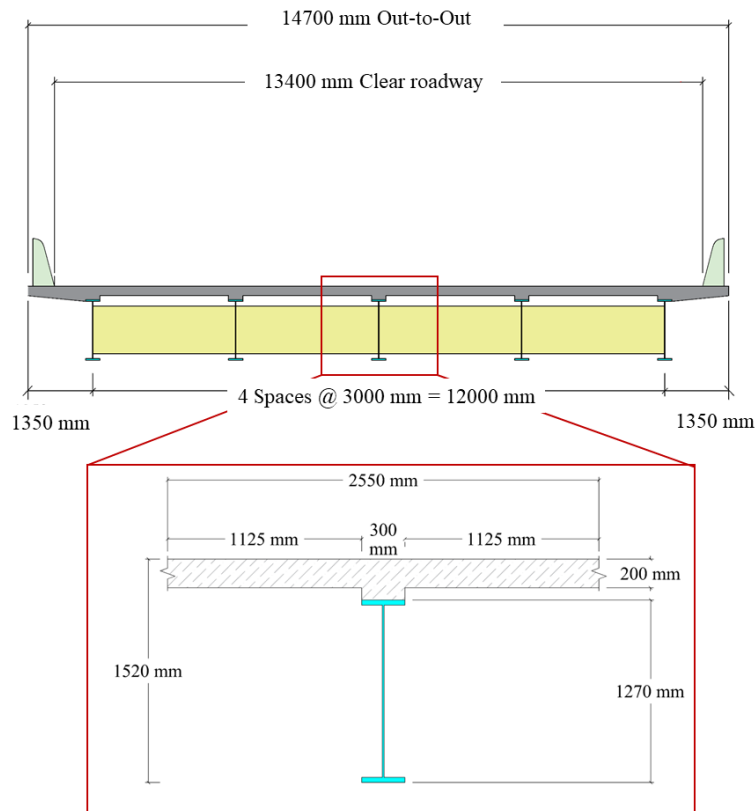


Figure 9.7 Effective Width

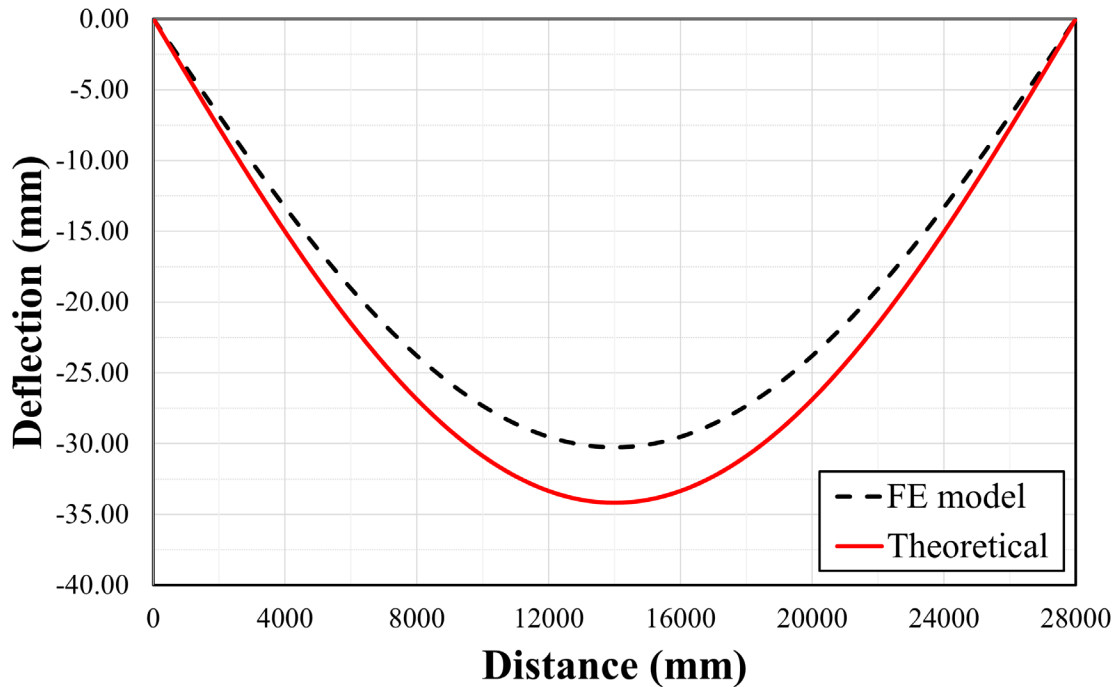


Figure 9.8 Deflections in the middle bridge girder

### 9.5 Bridge System Response to Fire, Impact, and Blast

Qualitative comparisons between damage propagation, final damage states, and spalled concrete volumes were completed for the four studied demand scenarios to assess bridge performance. Simulation results and performance evaluations are summarized in the following sections.

#### *9.5.1 Vehicle collision (I)*

This scenario subjected a pier column to a SUT impact at 120 km/h. Figure 9.9 depicts resulting damage propagation. The superstructure sustained minor damage with concrete surface cracking in the slab and no yielding observed in the girders. The exterior girder, above the impacted column experienced more flexural demand. The pier sustained extensive cracking in the vicinity of the impact. The column also exhibited extensive spalling accompanied and

reinforcement failure in the non-impact side. Shear failure was also observed at the top of the impacted column. The final damage state and relative volume of spalled concrete ( $\gamma_{cs}$ ) are illustrated in Figure 9.10. No spalling was observed in the superstructure and spalling in the pier was limited to the impacted column. Given the limited spalling and damage localization to the impacted column, it is believed that extensive repair or replacement to the damaged pier column are needed.

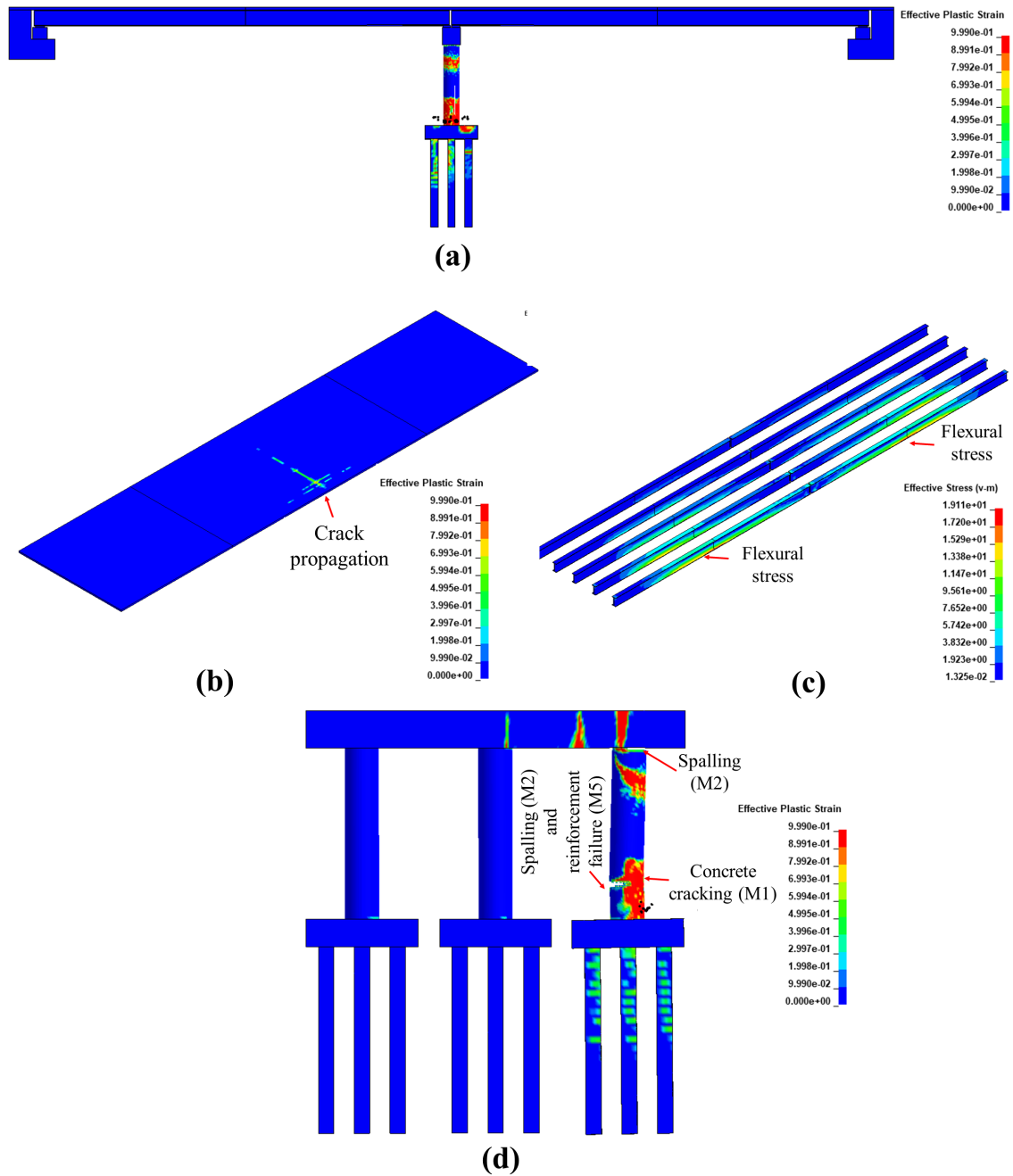


Figure 9.9 Damage propagation under SUT collision: (a) full bridge (b) slab (c) girders (d) pier

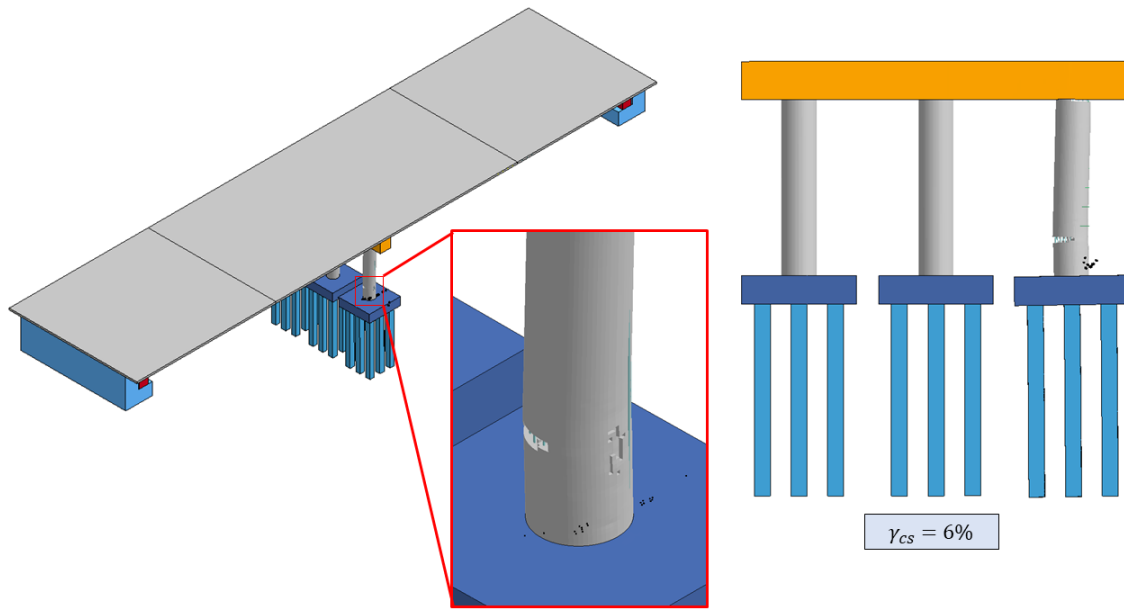


Figure 9.10 Final damage state of bridge and pier, SUT collision

### 9.5.2 Air blast (B)

The second loading scenario examined bridge performance under air blast at a scaled distance of  $Z = 0.25 \text{ m/kg}^{1/3}$ . Figure 9.11 represents damage propagation on the bridge and its main structural elements. Unlike the bridge under vehicle collision, bridge superstructure sustained severe damage with concrete surface cracking propagated along the entire bridge slab and concrete spalling observed above the pier. Girder flexural stresses did not approach first yield. Extensive cracking propagated along the impacted pier column with the non-impacted columns sustained minor flexural and shear cracking. The impacted column also exhibited extensive mid-height concrete spalling with two fractured longitudinal reinforcement bars. The final damage state and the relative volume of spalled concrete ( $\gamma_{CS}$ ) are depicted in Figure 9.12. This figure highlights the vulnerability of this bridge system to air blast compared to vehicle collision for the examined impact speed and blast load intensity, with significant spalling

observed in both the deck and pier. As a result, substantial repairs are anticipated to be required to restore bridge strength and serviceability. Temporarily closing the bridge while performing these repairs appears to be necessary.

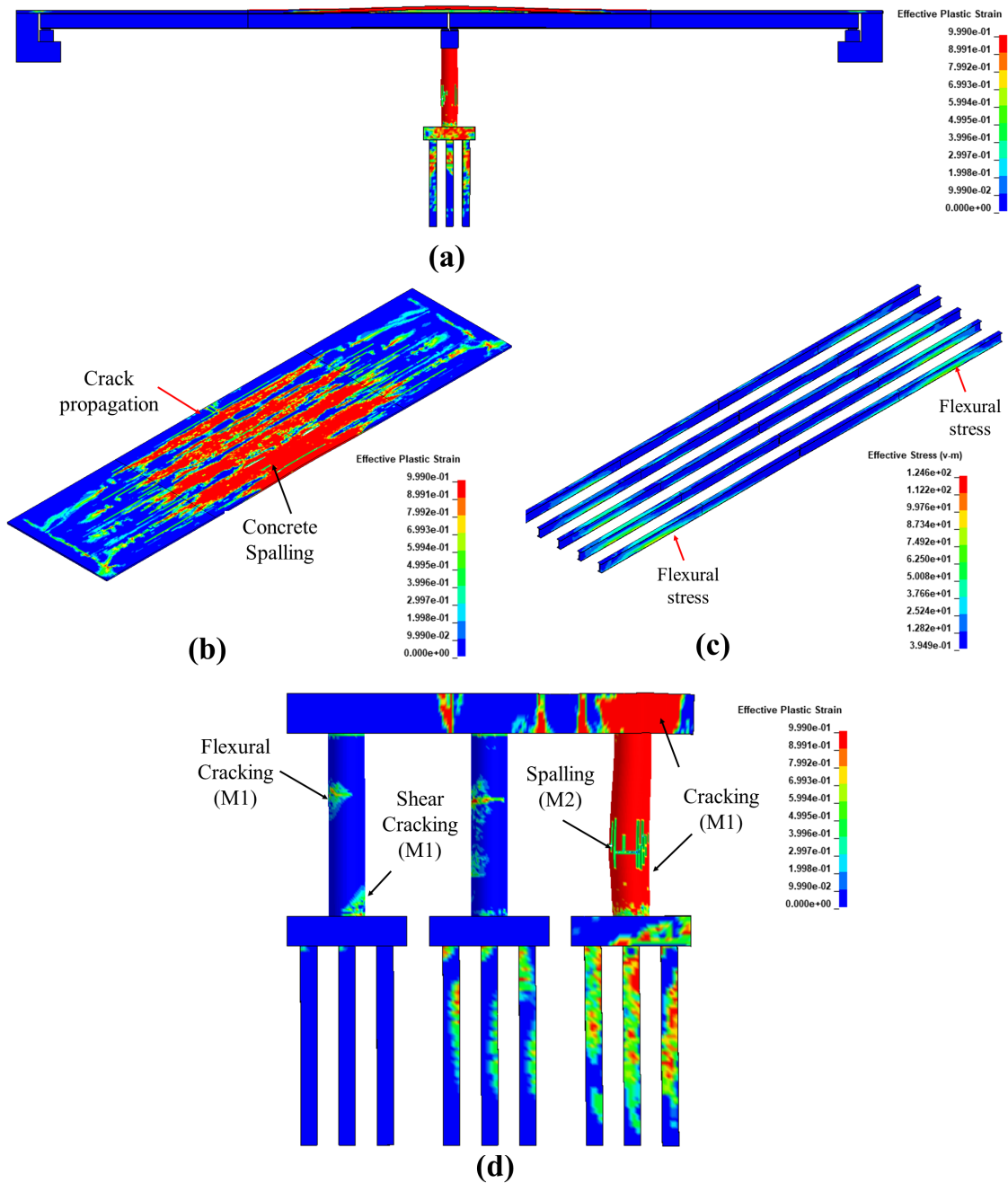


Figure 9.11 Damage propagation under air blast: (a) full bridge (b) slab (c) girders (d) pier

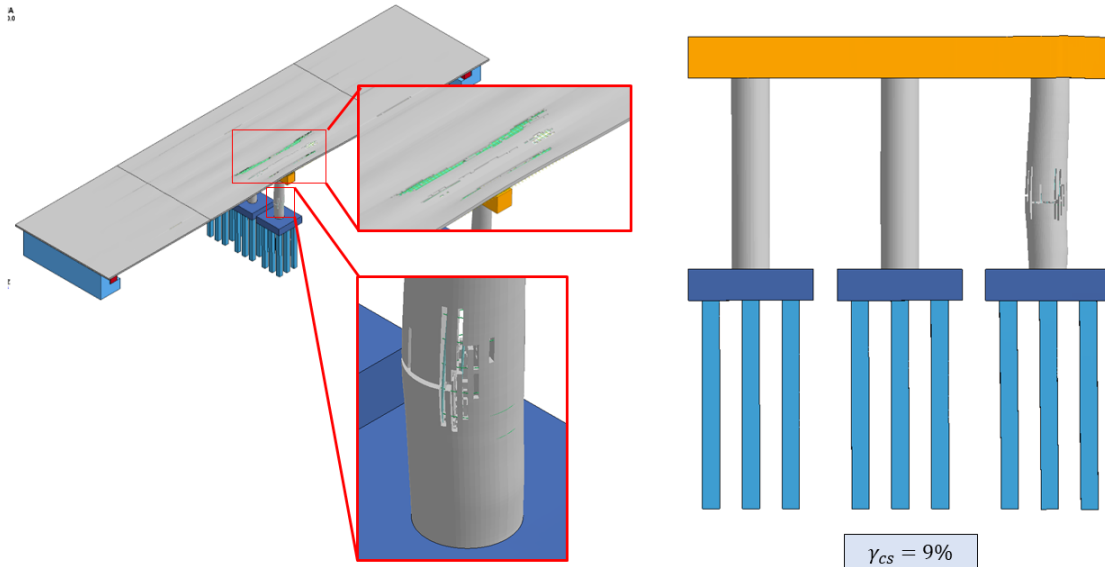


Figure 9.12 Final damage state of bridge and pier, air blast

### 9.5.3 Coupled vehicle collision and air blast (I-B)

Bridge performance was investigated under the combined effects of vehicle collision and a subsequent air blast. A single unit truck moving at 120 km/h collided with one pier column, then an explosion at a scaled distance of  $Z = 0.25 \text{ m/kg}^{1/3}$  occurred. Damage caused by these two extreme demands is depicted in Figure 9.13. As expected, it is evident that the coupled impact and blast resulted in more significant damage compared to the loading scenarios examined earlier. In particular, this figure indicated that the bridge slab sustained widespread and significant concrete surface cracking with potential for the slab overhang to collapse. All girders exhibited what appeared to be lateral torsional buckling, with flange local buckling noted in the edge girder located above the impacted column. Moreover, the figure also demonstrated that the impacted pier column experienced severe surface cracking, with direct shear failure observed near the location of impact. Non-impacted columns sustained shear cracking at their top and bottom ends. Reinforcement fracturing and separation between the middle pier column and pier

cap and supporting foundation was noted which indicated that the column failed due to shear. This failure pattern matched reported experimental results for a reduced scale RC pier column tested under lateral impact (Pham et al., 2018). Damage extent of the bridge system and the multi-column pier is illustrated in Figure 9.14. This figure further clarifies the observations discussed earlier and underscores the vulnerability of this bridge system to the combined effects of vehicle impact and air blast. The figure demonstrates the anticipated collapse of the bridge deck overhang and the direct shear failure observed in the impacted column. While potential collapse is not evident in Figure 9.14, pier column failure and extensive damage in the bridge superstructure—including concrete spalling, reinforcement fracturing, and failure of steel girders—strongly denotes the impending collapse. More comprehensive research is certainly needed to validate this presumption. Given resulting damage and failure of the bridge system, significant repairs or complete replacement of severely damaged elements would be advised.

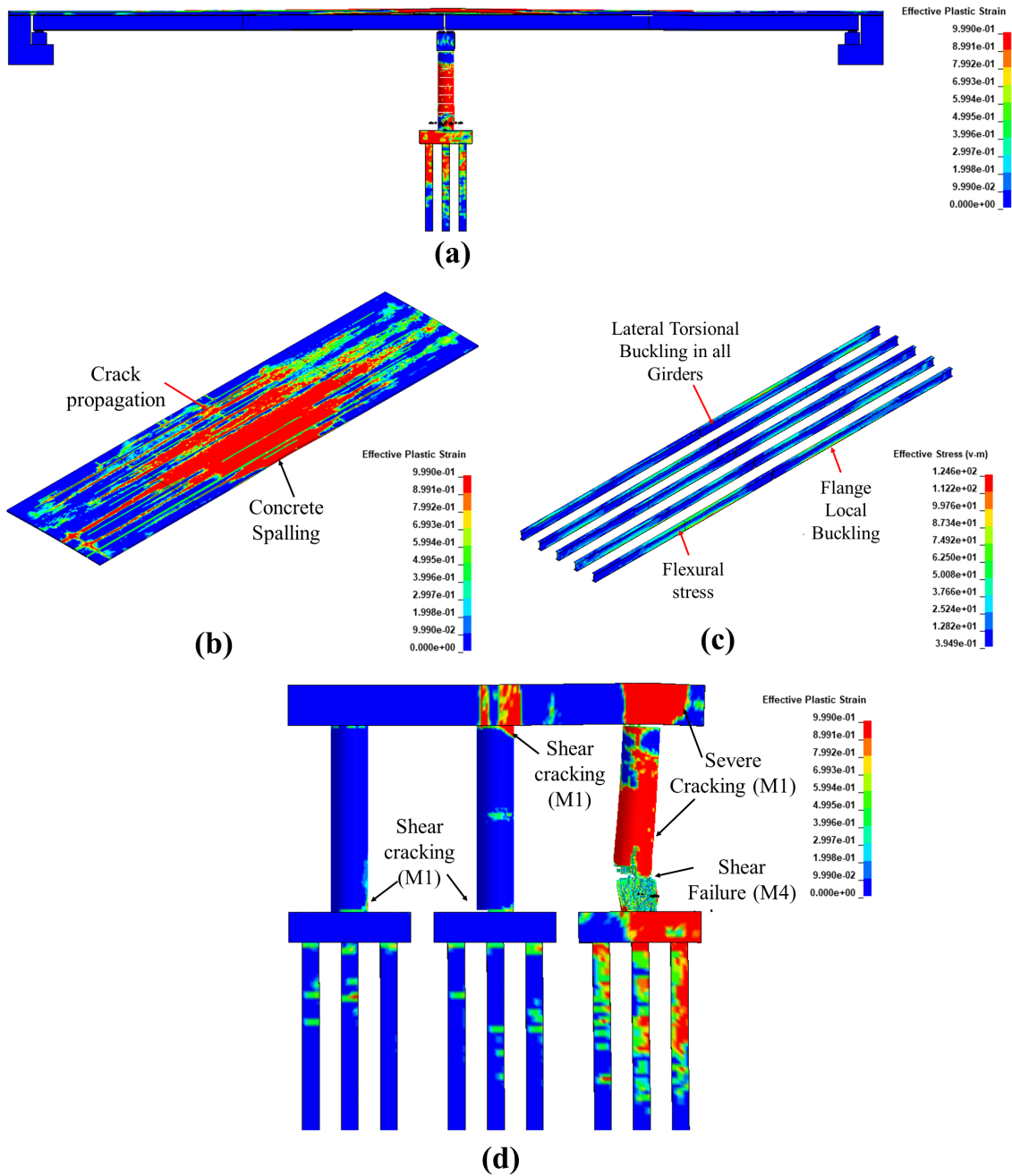


Figure 9.13 Damage propagation under I-B: (a) full bridge (b) slab (c) girders (d) pier

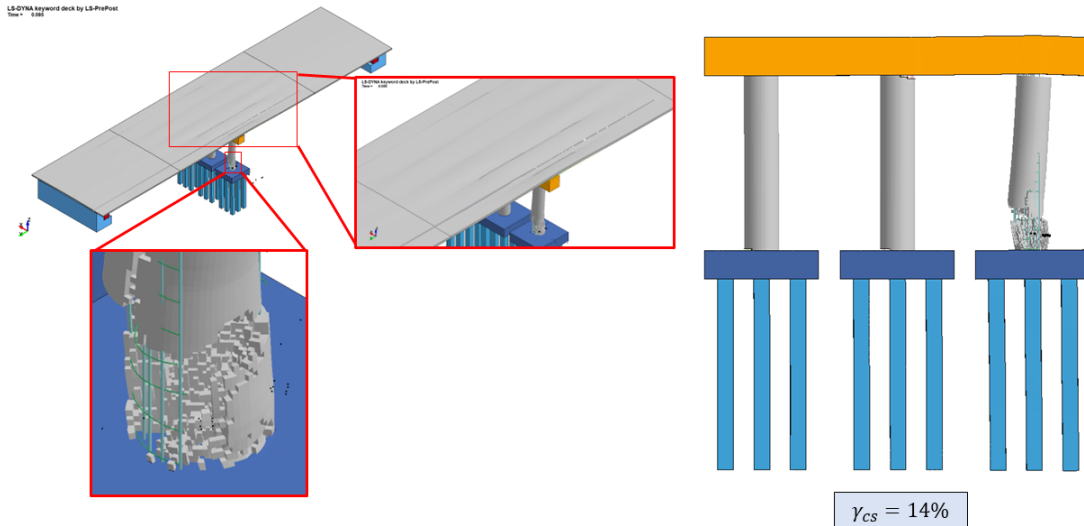


Figure 9.14 Final damage state of bridge and pier, I-B

#### 9.5.4 Fire, vehicle collision, and air blast (F90-I-B)

Performance of the selected bridge system was examined under coupled vehicle impact and air blast after fire exposure. Bridge performance was investigated subject to *F90-I-B*, which corresponds to exposing a selected region of the bridge to 90-minute fire prior to impact and blast, the most severe fire exposure case that was studied. In similar to previous studies completed herein, temperature variation over time was defined following the ISO-834 standard fire curve (ISO, 1999). Structural elements exposed to fire are depicted in Figure 9.15.

Three-dimensional transient heat transfer analyses of the bridge were initially performed to integrate fire effects into subsequent impact and blast analyses. Following the developed and validated multi-step modeling approach, resulting degradation and physical damage resulting from fire exposure were considered to be the initial conditions for subsequent impact and blast analyses as presented in Section 3.9.

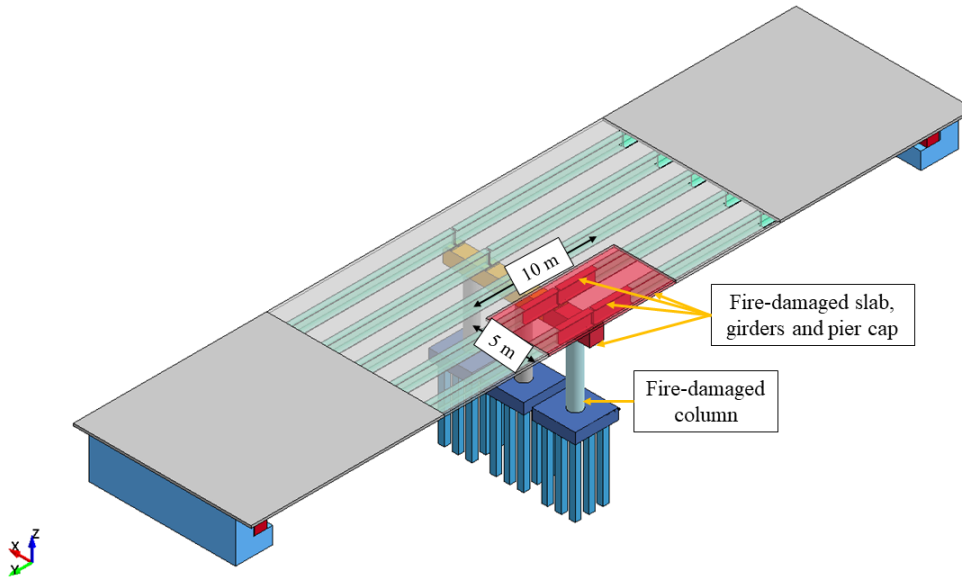


Figure 9.15 Fire damaged structural elements, F90

Resulting thermal stress distributions caused by the fire exposure are shown in Figure 9.16. The girders sustained uniform flexural stresses in both spans and flexural stresses were developed at the pier cap location in the deck slab. The distribution of thermal stresses in the fire-damaged column indicated that flexural-shear cracks were initiated along its height, which mimics reported test results (Chinthapalli et al., 2019). It was also observed that shear cracks developed at the top of the non-exposed columns.

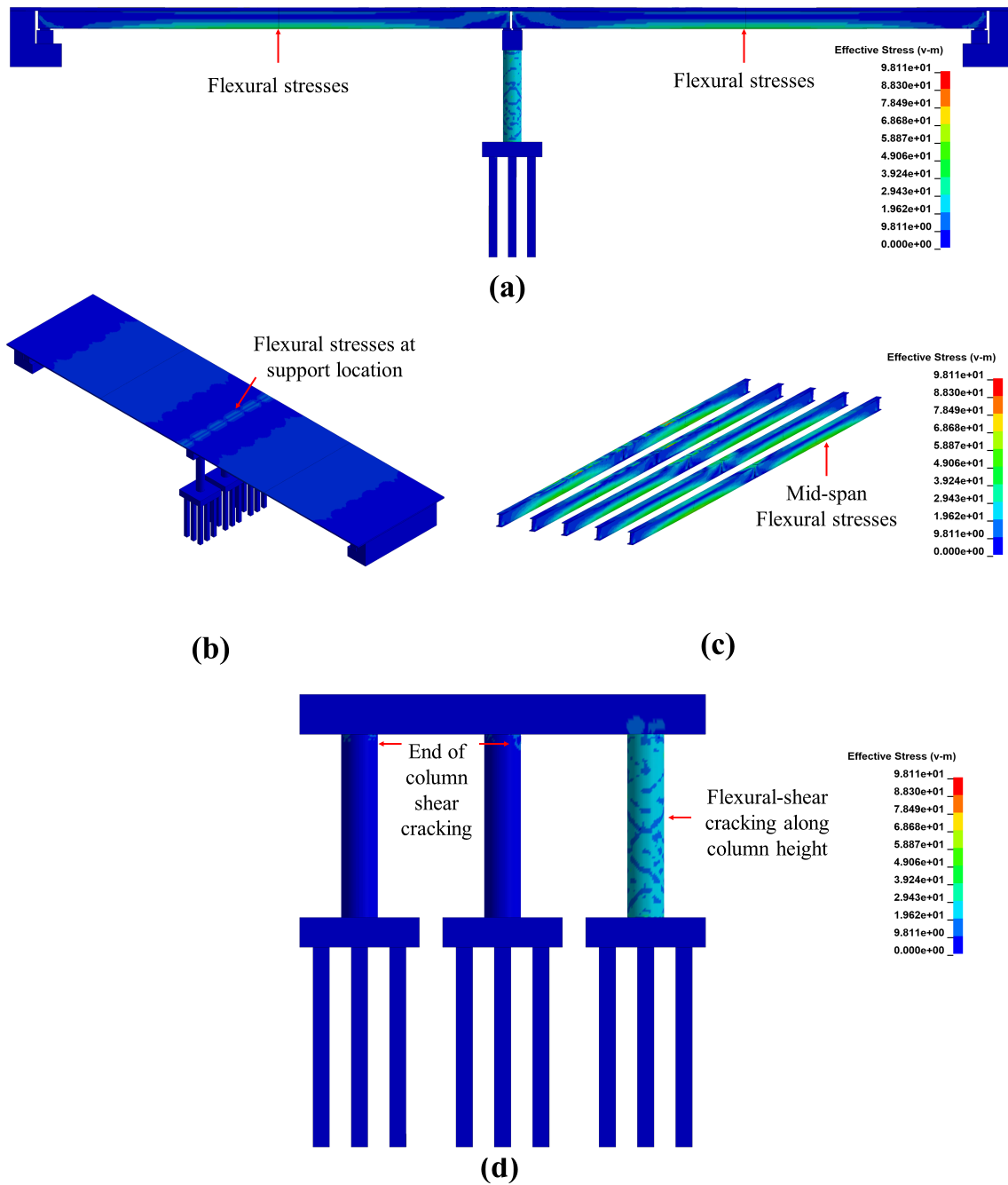


Figure 9.16 Thermal stress distribution, F90: (a) bridge (b) slab (c) girders and (d) pier

The LS-DYNA's explicit solver was utilized for the second analysis stage. In this stage, the fire-damaged pier column was subjected to a SUT impact with a velocity of 120 km/h and an explosion with a scaled distance of  $0.25 \text{ m/kg}^{1/3}$ . Cumulative damage produced by the fire,

vehicle collision, and blast is illustrated in Figure 9.17. Unsurprisingly, this loading scenario, which integrated the effects of fire into impact and blast analysis, resulted in more pronounced damage compared to the other studied loading scenarios. Specifically, Figure 9.17 indicated that the bridge slab sustained severe damage with widespread concrete surface cracking initiated and substantial spalling in the fire damaged portion of the slab. Extensive reinforcement fracturing was observed above the impacted column and in the vicinity of the fire damaged slab. It was also noted that both slab overhangs potentially collapsed. All bridge girders were observed to experience lateral torsional buckling and flange local buckling, and plastic bending. Failure modes observed in the steel girders are illustrated in Figure 9.18. The figure also demonstrates that the impacted pier column experienced severe surface cracking, with direct shear failure and complete column core breaching observed near the location of impact. Non-impacted columns sustained shear cracking at their top and bottom ends and mid-height flexural cracking. Despite limited deformation of the non-impacted columns, separation between these columns and pier cap and supporting foundation was noted and accompanied with longitudinal reinforcement fracturing, which identified that these columns failed due to shear. Again, this failure pattern matched reported experimental results when a reduced scale RC pier column was tested under lateral impact (Pham et al., 2018).

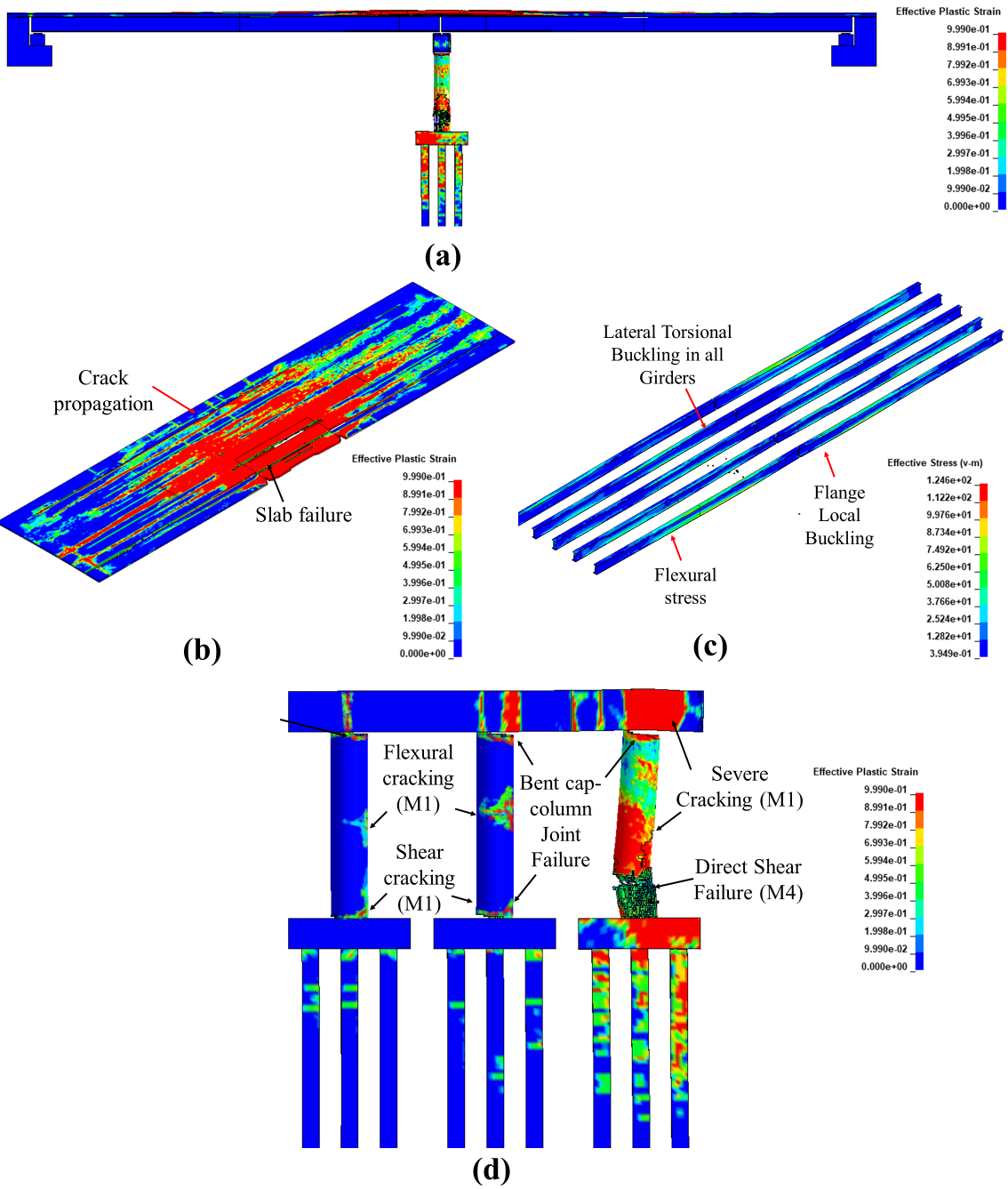


Figure 9.17 Damage propagation under F90-I-B: (a) full bridge (b) slab (c) girders (d) pier

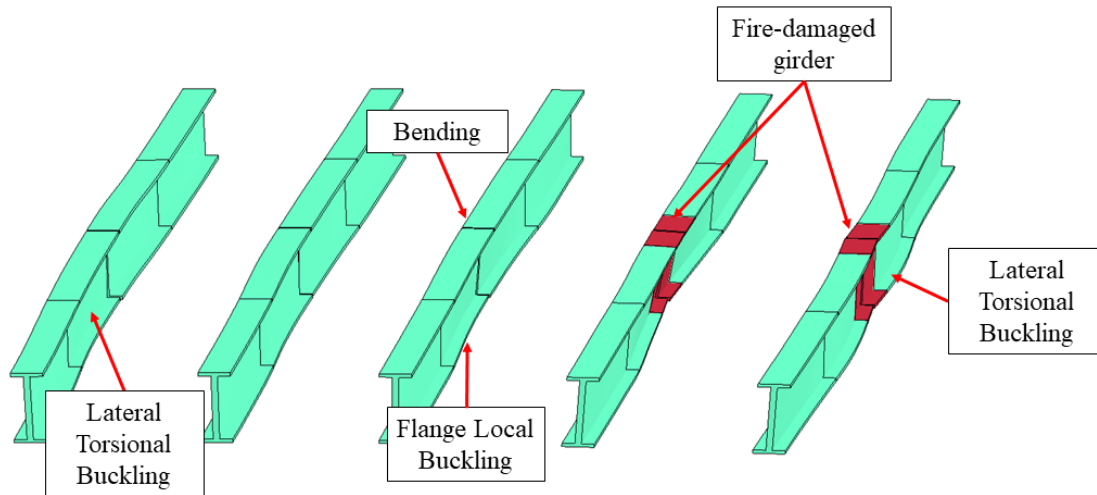


Figure 9.18 Failure modes of bridge girders

The final damage state in the bridge system is illustrated Figure 9.19. This figure clearly demonstrates that when the bridge was exposed to fire prior to impact and blast, partial or complete collapse appears unavoidable. Simulation results indicated that the bridge experienced another unique failure mode; complete separation between the steel girders and the elastomeric bearings above the pier cap, with a separation height of 37 mm, as shown in Figure 9.20. This failure pattern mimics reported test results and indicates that severe bending and permanent set occurred in the bridge deck and supporting steel girders (Lin et al., 2020). According to the Lin et al. (2020), although relatively rare, this separation can occur if the bridge superstructure is overloaded and demonstrates failure in bridge bearings. This observation is evident as significant bending in both the right and left spans was observed above the pier location. Complete replacement of the entire bridge or significant portion of the structure is highly recommended.

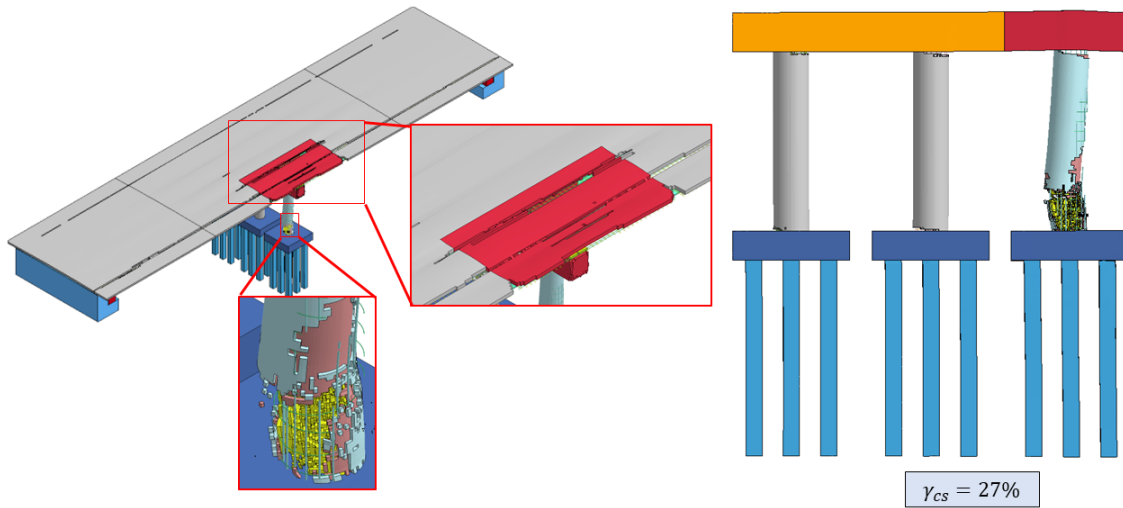


Figure 9.19 Final damage state of bridge and pier, F90-I-B

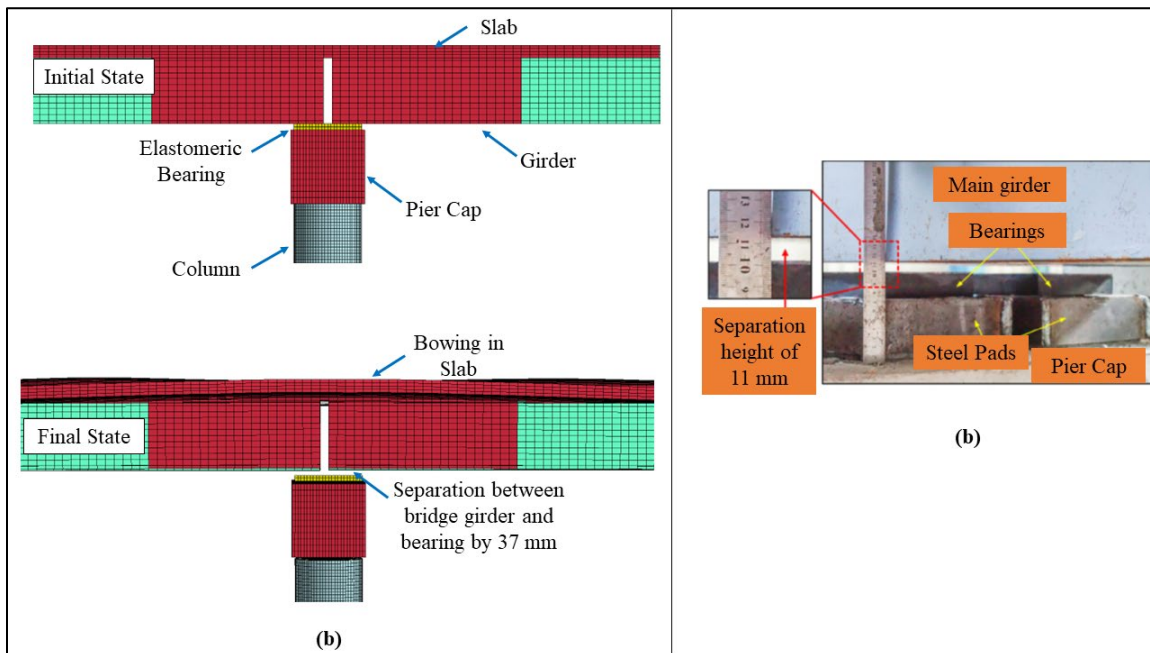


Figure 9.20 Separation between the bridge girders and the elastomeric bearings (Lin et al., 2020)

## 9.6 Resiliency Enhancement using Soil Infill

An additional retrofitting option was examined using the entire bridge model with the use of soil infill between the pier columns. The effectiveness with which this cost-effective protection and strengthening technique mitigated damage resulting from coupled vehicle collision and air blast was numerically investigated. A case was examined to lay the groundwork for future investigations. To further evaluate the performance of the proposed protection technique, two-reduced scale bogie crash tests were conducted at Midwest Roadside Safety Facility (MwRSF) at UNL. More details on the numerical and experimental examinations are provided in the following sections.

### *9.6.1 FE model development*

The proposed strengthening scheme is illustrated in Figure 9.21. Two soil volumes were placed between the pier columns. To ensure soil stability in LS-DYNAS, sacrificial, 50-mm thick, plain concrete panels were included in the model. The height of soil volumes was set to half the height of the column (i.e., 2500 mm), as previous results indicated this location typically sustained more extensive damage. The width of each soil volume was set to 1000 mm, which is equivalent to pier column diameters.

*FHWA-Soil (MAT-147)* was used to represent the ALE soil domain and was again selected to model the soil infill. To ensure realistic representation of soil performance under impact and blast events, the damage level parameter (*DALEV*) and maximum principle failure strain (*EPSMAX*) were set to 0.99 and 0.80, respectively, to ensure that highly-distorted soil elements would be deleted based on published literature (Lewis, 2004; Reid et al., 2004). To model the sacrificial concrete panels, LS-DYNA's *Continuous-Surface-Cap (MAT-159)* material model was again used with an unconfined set to 18 MPa (Hallquist, 2014). As recommended in

previous studies, the *Automatic Surface to Surface* algorithm was used to model contact between the soil and pier columns, with static and dynamic coefficients set to 0.50 (Hallquist, 2014; Murray, 2004; Reese et al., 2014).

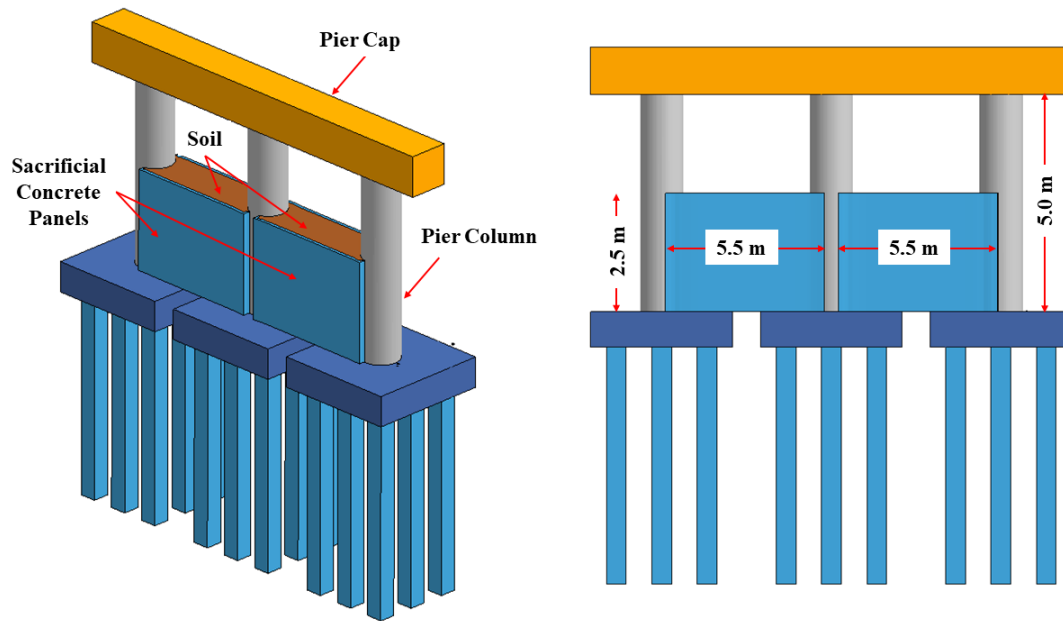


Figure 9.21 Proposed retrofitting scheme

### 9.6.2 Simulation results

Performance of the retrofitted pier was evaluated using similar criterion to earlier sections in this chapter. Results were compared to those obtained from analyzing the non-strengthened bridge system under vehicle impact and air blast presented in Section 9.5.3.

Figure 9.22 compares damage propagation in retrofitted and original bridge systems. This figure clearly illustrates the effectiveness of the proposed infill scheme for mitigating damage to the main structural elements. Though the bridge deck sustained widespread concrete surface cracking for both cases, cracking intensity at the end quarter slab was reduced with the soil infill. While the figure signifies that the slab in the original bridge is vulnerable to collapse, the

retrofitted bridge slab sustained only localized spalling. Lower flexural demand was also imposed at the girders located above the impacted column, with flange local buckling being observed. As discussed earlier, the original impacted pier column experienced severe surface cracking and shear failure, and non-impacted columns sustained shear cracking at their ends. Reinforcement fracturing and separation between the middle pier column and pier cap and supporting foundation were also noted, further supporting the premise that this column also failed due to shear. Use of soil infill resulted in fewer cracks in the pier columns with localized spalling in the impacted column being observed.

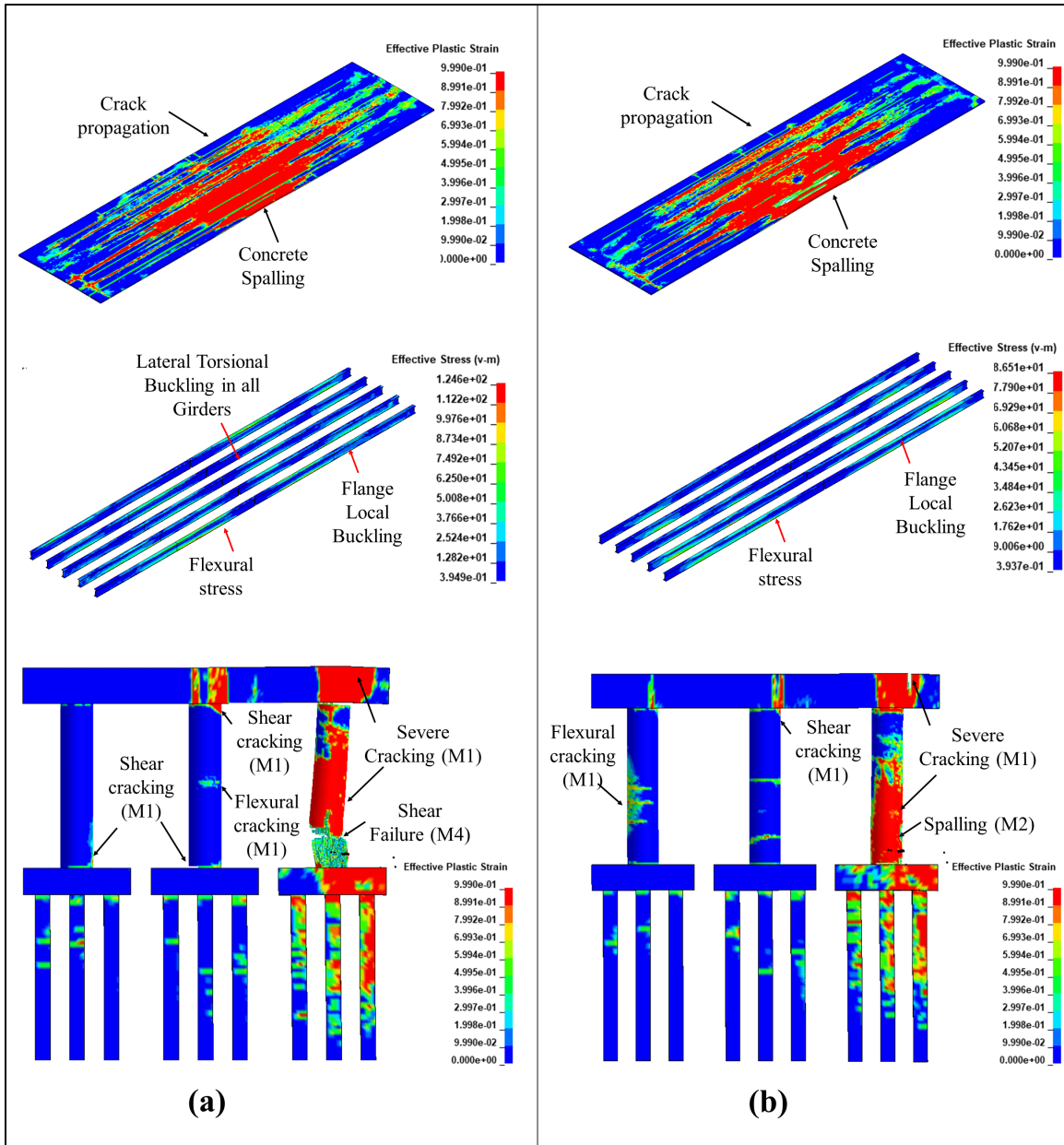


Figure 9.22 Damage propagation under I-B: (a) original pier (b) retrofitted pier

Figure 9.23 further illustrates damage sustained by the bridge system for the retrofitted and original systems. The figure underscores the vulnerability of the original bridge system to the combined effects of vehicle impact and air blast. It also further demonstrated potential benefits from the retrofit given damage localization observed in the slab and pier columns. These results

show that the retrofitted system could potentially remain in service, while minor repairs were performed.

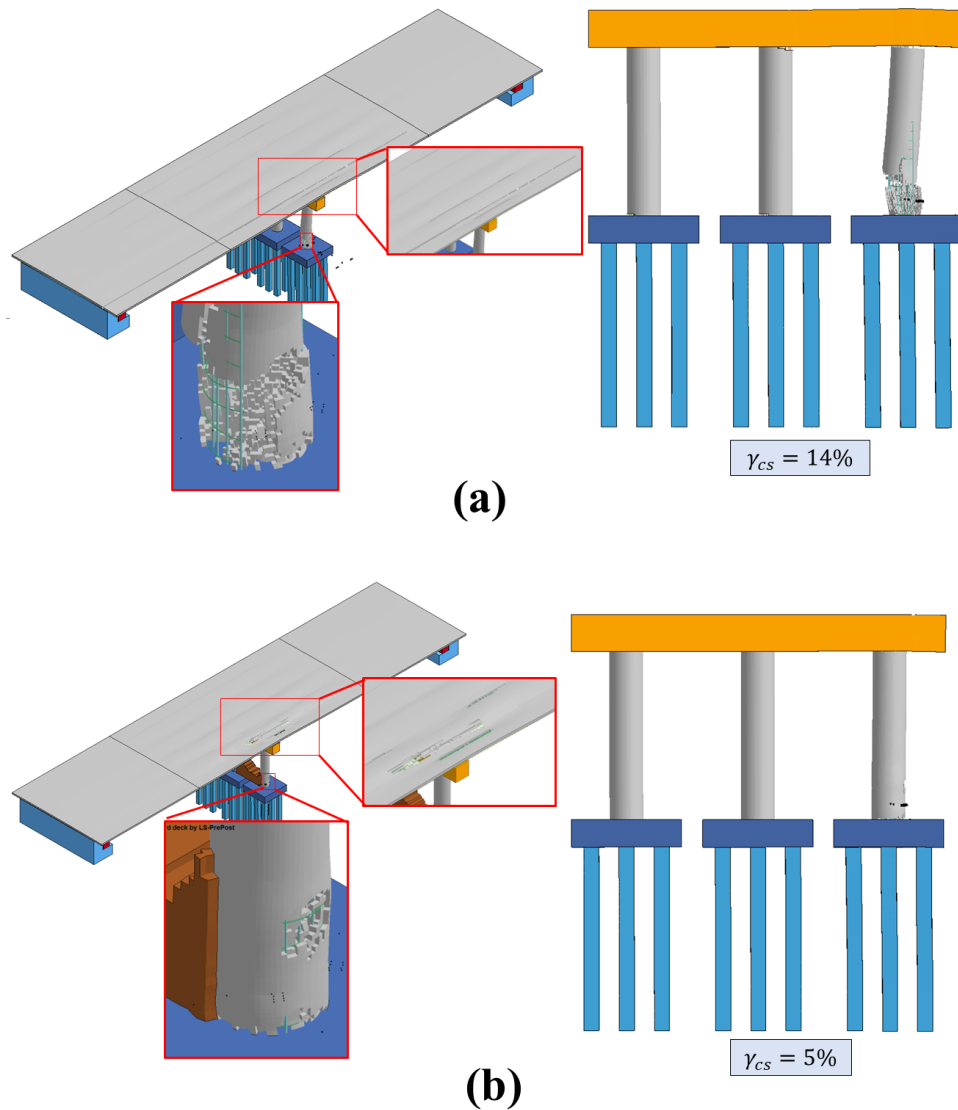


Figure 9.23 Final damage state of bridge and pier, I-B: (a) original pier (b) retrofitted pier

### 9.6.3 Bogie Crash Tests

Based on results from the models, two reduced-scale impact tests (MATC-1 and MATC-2) were conducted to evaluate performance of unprotected and soil-protected reduced scale,

representative bridge piers. Subsequent air blasts were not included in the physical tests. The goal of these tests was to establish the level of load sharing that would occur between an impacted “column” and a non-impacted “column.” MATC-1 did not have soil infill between the columns while MATC-2 included an uncompacted MASH soil infill (MASH, 2016). Tests were performed at UNL’s Midwest Roadside Safety Facility (MwRSF) using a 2,145 lb. bogie. Test specimens and the testing system were designed with the aid of LS-DYNA models using similar techniques to the models summarized in the previous section.

The layout of these test systems and further details on system design are provided in Appendix A. Each system included a steel impact panel representing the impacted “column”, consisting of three W6x25 Grade 50 steel beams welded to two 0.5-inch-thick ASTM A572 steel plates. An identical steel panel was used to simulate the non-impacted “column.” To reiterate, the focus of these tests was to establish if soil uncompacted, contained, soil infill could produce, and load sharing between the “columns”. To contain the soil, two steel side panels were employed. These side panels were supported by 36-inch-high portable concrete barriers to attempt to replicate complete infill restraint. The constructed test systems are further illustrated in Figure 9.24 and Figure 9.25.

As stated earlier, for MATC-1, the system was impacted without soil infill while MATC-2 utilized a similar impact scenario with soil infill between the panels. Bogie impact speeds were 26.2 mph for MATC-1 and 29.07 mph for MATC-2. Despite the speed discrepancy, displacement time histories indicate that soil infill significantly reduced both dynamic and permanent deflections for the impacted “column”, with peak dynamic displacement decreasing by 28.2% for MATC-2, even with energy introduced into the system due to the higher impact speed. These preliminary tests appear to warrant additional studies examining the efficacy of

utilizing soil infill as an inexpensive option to improve pier column resiliency to vehicle impact and blast. Resulting displacement and force time histories are provided in the appendix.



Figure 9.24 MATC-1 Bogie test



Figure 9.25 MATC-2 Bogie Test

9.7 Summary and Conclusions

Studies of the performance of isolated pier columns and multi-column piers subject to SUT impact, air blast, and fire. A three-dimensional FE model of an existing, two-span, steel-concrete composite bridge in Sidney, NE, using plans obtained from the Nebraska Department of

Transportation (NDOT), was modeled in LS-DYNA and its accuracy was validated against hand calculations. Performance of the modeled bridge was examined subject to four multi-hazard scenarios: (i) vehicle impact, (ii) air blast, (iii) coupled impact and blast, and (iv) post-fire impact and blast (i.e., *F90-I-B*). Results were utilized to evaluate bridge resiliency and to provide insights on susceptibility to partial or complete collapse. Previously identified damage parameters including crack propagation, final damage states, volume of spalled concrete, and established damage levels to quantify bridge performance. The effectiveness with which an innovative and cost-effective retrofitting approach improved bridge resiliency against the studied extreme demands, one that utilized soil infill between pier columns, was also investigated.

Conclusions from this study include:

1. For the studied impact speed, scaled distance, and fire exposure, damage in bridge encompassed:
  - Shear and flexural crack propagation in the slab, pier, and foundation system;
  - Concrete cover spalling and longitudinal reinforcement fracturing slab and pier;
  - Lateral torsional buckling, local flange buckling, and plastic bending in steel girders;
  - Direct shear failure coupled with reinforcement fracture at pier column bases;
  - Concrete core breaching in the impacted column; and
  - Potential bridge collapse.
2. While vehicle collision into a single pier column produced localized and potentially repairable damage, exposure to an air blast adjacent to that column produced more pronounced damage that may require full or partial bridge closure.
3. As expected, simulation results demonstrated that the I-B loading scenario produced more extensive damage, with the collapse of deck overhang anticipated and direct shear failure

observed in the impacted column. Reinforcement fracturing and separation between the middle column and its pier cap and foundation was noted, also indicating shear failure. As a result, bridge closure and significant repairs or complete replacement of the damaged structural elements were anticipated.

4. Complete collapse of the bridge superstructure was observed to be unavoidable with exposure to multi-hazard scenario F90-I-B. Bridge girders experienced permanent sets caused by lateral-torsional buckling and vertical bending. All pier columns were also observed to have failed. Replacement of a significant portion of the bridge or complete replacement would be anticipated.
5. The proposed low-cost retrofitting technique, one that utilized soil infill between support columns, was shown to effectively mitigate structural damage and improve bridge resiliency under combined effects of impact and air blast. As a result, more research is justified to further study the influence of various design and analysis parameters on performance.

## Chapter 10 Advanced Analysis of Intact, Fire-Damaged, and CFRP Retrofitted Bridge Pier Columns under Vehicle Collisions: Empirical Equivalent Static Force Equation and Framework

### 10.1 Introduction

As highlighted by multiple catastrophic incidents, bridge pier columns are vulnerable to vehicle collisions that may cause extensive damage and could lead to collapse. Investigating the resiliency of these structural components and establishing comprehensive analysis and design guidelines is needed to mitigate costly repairs, lengthy closures and, most importantly, injury and loss of life. One widely adopted approach that has been implemented in bridge design guidelines involves utilizing an Equivalent Static Force (ESF) method. ESFs are used to conservatively represent the transverse loads resulting from vehicle collisions into bridge columns. However, concern has been raised about the accuracy of this simplified method and prompting the need for a more precise and reliable approach.

A series of numerical simulations were conducted to investigate the behavior of intact, fire-damaged, and CFRP retrofitted isolated reinforced concrete (RC) bridge columns of varying size subjected to vehicle collisions with the intent of examining the effects of nine parameters on performance of bridge columns. Studied parameters included: column diameter, column height, unconfined compressive strength, steel reinforcement ratio, fire duration, CFRP wrap thickness, wrapping configuration, vehicle mass, and vehicle speed. For each studied scenario, a Peak Twenty-five Milli-second Moving Average (PTMSA) was employed to estimate the corresponding ESF, as recommended in previous research (Abdelkarim & ElGawady, 2017; AuYeung & Alipour, 2016; El-Tawil et al., 2005). Resulting ESFs were then utilized to assess effectiveness of the current Equivalent Static Force (ESF) approach available in the *American Association of State Highway and Transportation Officials (AASHTO) Load and Resistance Factor Design (LRFD) Bridge Design Specification*, Article 2.3.2.2 and Section 3.6.5.1, for

analyzing and helping design bridge columns under vehicle collision (AASHTO LRFD, 2020). Multivariate nonlinear regression analyses were used to derive an empirically-based, simplified equation to determine the ESF. This equation established a correlation between equivalent force and kinetic energy, column axial capacity, and column height. To facilitate realistic implementation of the derived equation, an ESF assessment framework was also devised.

## 10.2 Background

Incidents involving catastrophic vehicle collisions with bridge pier columns are limited in number but can have a massive impact. Several research studies and surveys have indicated that vehicle collisions are one of the main causes of bridge failures in the U.S. A survey conducted by Lee et al. that examined 1062 U.S bridge failures between 1980 and 2012 revealed that the majority were caused by floods and vehicle collisions (Lee et al., 2013). Harik et al. investigated major causes of bridge failures in the United States between 1951 and 1988 and showed that vehicle collisions were the leading cause of bridge failures during that period (Harik et al., 1990). Additional research carried out by Wardhana and Hadipriono examined causes of 503 bridge failures in the U.S between 1989 to 2000 (Wardhana & Hadipriono, 2003) and showed that floods, scouring, and vehicle collisions were leading causes of bridge failures, with about 12% of bridges failing due to collisions.

Given their close proximity to traffic and, oftentimes, improper employment of protective systems, bridge pier columns are especially vulnerable to vehicle collisions. The consequences of these destructive events not only impose significant economic burdens, but most importantly, jeopardize human lives. As the cost associated with protecting these support units is substantially high, it is imperative to utilize proper analysis and design methods so that they could, if desired, withstand collisions (S. Roy et al., 2021).

In relation to available design provisions, vehicle collision is addressed in pier column design by introducing an equivalent transverse static load applied at a prescribed distance from the column base. According to the 9<sup>th</sup> edition of *AASHTO LRFD* Article 2.3.2.2 and Section 3.6.5.1, RC pier columns should be designed for an equivalent static force (ESF) of 600 Kips (2,670 kN) located 5 ft (1.52 m) above the ground, with the force applied at an angle between 0 and 15 degrees with respect to the pavement edge (AASHTO LRFD, 2020). This equivalent static force was identified based on full-scale tests of 910 mm diameter rigid columns impacted by a 36,300 kg tractor-trailer moving at 80.5 km/h (Buth et al., 2010, 2011). While the current *AASHTO-LRFD* code adopts a constant static force approach for designing bridge columns under vehicle impacts, it ignores other variables that play a crucial role in determining the actual impact force. These variables can include external factors, such as vehicle speed and mass, and internal design variables (Auyeung et al., 2019). Consequently, several research studies have indicated that more research is required to assess the recommended ESF as it may underestimate or overestimate impact energy in certain circumstances (Buth et al., 2010, 2011; El-Tawil et al., 2005; Gomez & Alipour, 2014; S. Roy et al., 2021).

While Peak Dynamic Forces (PDF) can be easily extracted from experimental tests or finite element analysis, estimating corresponding ESFs, which is required to design bridge columns under impact and to assess current design codes requirements, can be challenging. To address concerns related to the accuracy and feasibility of the *AASHTO-LRFD* approach, researchers have adopted alternative methods to determine ESF. One such alternative is the Equal Energy method recommended by *Eurocode-1 — Part 1-7: General actions—Accidental actions*, which is frequently used to design barriers and similar protection systems (European Committee for Standardization: Eurocode 1, 2006). In this method, force is correlated to impact

speed ( $V_o$ ), vehicle equivalent stiffness ( $K$ ), and vehicle mass ( $M$ ) as shown in Equation 13.

While this method offers a simplified alternative for estimating ESF, its applicability remains limited and uncertain as it does not account for any potential inertial effects on structural response (Auyeung et al., 2019; T. Roy & Matsagar, 2021).

$$ESF = V_o \sqrt{K \cdot M}, \quad \text{Equation. 13}$$

Another alternative approach, also from *Eurocode-1: Part 1-1* (E. 1991-1-1 Eurocode 1, 2002), is frequently used to estimate ESF. ESF is expressed as a function of vehicle kinetic energy ( $KE$ ), and vehicle ( $\delta_c$ ) and column deformations ( $\delta_d$ ), as presented in Equation 14. It has been demonstrated by several researchers that this equation tends to underestimate ESF, particularly in collisions that involve heavy trucks (Abdelkarim & ElGawady, 2017; El-Tawil et al., 2005).

$$ESF = \frac{KE}{(\delta_c + \delta_d)}, \quad \text{Equation. 14}$$

Abdelkarim and ElGawady proposed another approach for estimating ESF using the peak of the 25-ms dynamic impact force time history moving average (PTMSA) (Abdelkarim & ElGawady, 2017). This approach was utilized to derive a simplified equation that predicts ESF given imposed kinetic energy ( $KE$ ) as shown in Equation. 15. This equation neglects structural parameters that could certainly influence calculated impact forces, such as column size, reinforcement levels, and material properties (T. Roy & Matsagar, 2021).

$$ESF = 46\sqrt{KE},$$

Equation. 15

As all cited investigations and proposed equations ignored several variables that could influence impact force, it appears there is a need to develop a generalized, simple equation to accurately predict ESF over a wide range of demand and performance scenarios. Research presented herein focused on developing this equation and comparing recommended values and their performance to the *AASHTO-LRFD* bridge design specifications ESF value over a range of scenarios. Particularly, the study examined: (i) intact columns under impact; (ii) columns that survive fire and retain adequate structural integrity prior to impact; and (iii) compromised columns retrofitted using the CFRP wrap prior to impact.

Previously validated LS-DYNA three-dimensional finite element models of circular Reinforced Concrete (RC) isolated bridge columns exposed or not exposed to fire and subject to vehicle collisions were employed to conduct a series of numerical simulations. Equivalent static forces were evaluated using a parametric study that involves design parameters including concrete compressive strength, longitudinal reinforcement ratio, column diameter, and column height. In addition, vehicle velocity and mass, fire exposure, and influence of the aforementioned retrofitting scheme were also incorporated into the study.

An empirically based equation that established correlation between equivalent static force and identified dominant variables (imposed kinetic energy, column axial capacity and height) was developed and validated. To facilitate realistic implementation of the derived equation, an ESF assessment framework was also proposed.

### 10.3 Finite Element Model

The previously developed and validated three-dimensional FE model of an isolated, round, RC bridge pier column, its foundation system, and surrounding soil was used as the base line model to perform all impact analyses. This system was initially obtained from an FHWA design example, as depicted in Figure 10.1 (Wassef et al., 2003). Soil volume dimensions were selected based on previous studies (Reid et al., 2004) to ensure that realistic soil-structure interaction was achieved. The modeling approach matched that presented in Chapter 3.

### 10.4 Parametric Study

A parametric study that examined the effects of concrete compressive strength, longitudinal reinforcement, column diameter and height, vehicle velocity and mass, fire exposure, and retrofitting scheme on equivalent static force levels was performed. Results of this study were utilized to develop a simplified and empirically based equation that predicts ESF over a wide range of vehicle collision scenarios.

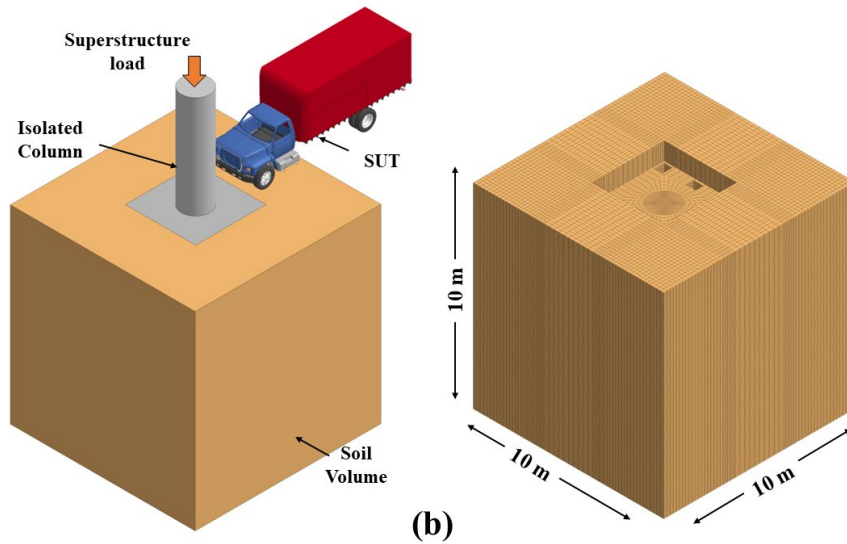
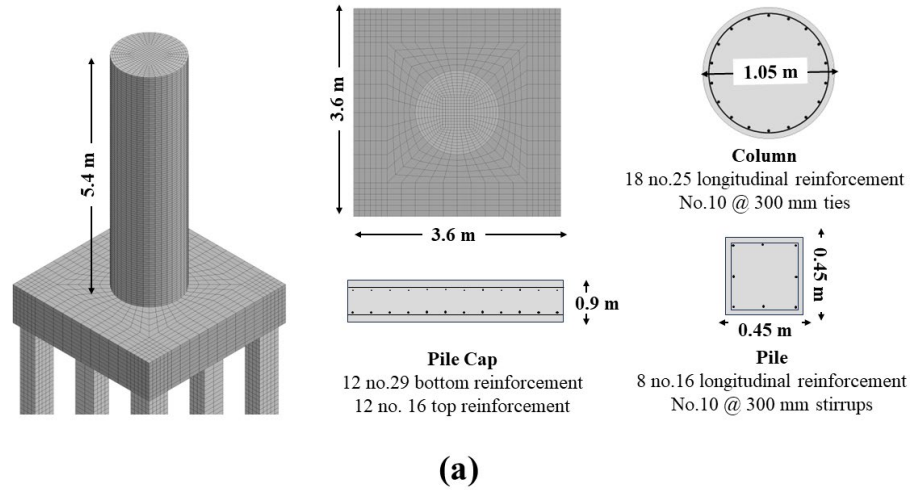


Figure 10.1 Finite Element Model: (a) structural system and (b) full domain and soil volume

#### 10.4.1 Study matrix

Numerical simulations were completed using LS-DYNA to comprehensively investigate bridge column performance and to estimate resulting impact forces. Studied parameters and associated nomenclatures are summarized in Table 10.1. In this table the sources from which these parameters were selected are provided. Following this table, FE models of these vehicles

are illustrated in Figure 10.2. Table 10.2 summarizes investigated cases. Sixty-one cases, labeled  $C_0$  to  $C_{60}$ , were examined.

Table 10.1 Selected study parameters

Parameter	Value	Source	Parameter	Value	Source
Column Diameter ( <i>D</i> ) (mm)	1050	Wassef et al., 2003	Wrap thickness ( $t_{FRP}$ ) (mm)	0.5	As presented in Chapter 7
	750	Williamson, 2010		1.0	
	1350	Abdelkarim & ElGawady 2017.		1.5	
	1500			2.0	
	1800				
Column Height ( <i>H</i> ) (mm)	4000	Abdelkarim & ElGawady 2017	Wrapping configuration	Full-height	H. Al-Nimry et al., 2013  H. S. Al-Nimry & Ghanem, 2017
	5400			Half-height	
	7000	Fang et al., 2021c		Third-height	
	9000			Intermittent	
Unconfined Compressive Strength ( $f'_c$ ) (MPa)	28	Abdelkarim & ElGawady 2017	Vehicle mass ( <i>M</i> ) (ton)	8.175 (SUT)	Mohen et al., 2007
	34.5			1.997 (Ram)	
	48.3	Fang et al., 2021a		0.893 (Yaris)	
	56				
Steel Reinforcement Ratio ( $\rho$ ) (%)	1	AASHTO LRFD, 2020	Vehicle speed ( <i>V</i> ) (km/h)	65	Fang et al., 2021c
	2			100	
	3			120	
	4				
Fire Duration ( <i>FD</i> ) (minute)	60	W. Chen et al., 2016b			
	90	Garlock et al., 2012			
	120	Guo et al., 2017			
	180	Zhai et al., 2016			

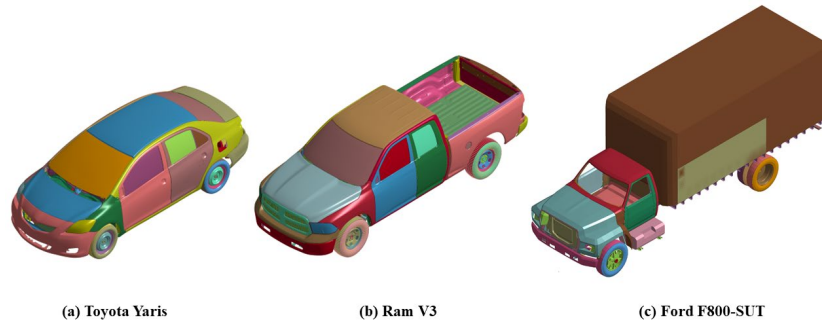


Figure 10.2 Vehicle FE models

### 10.5 Parametric Study Results

Following the same approach utilized for earlier investigations, column performance was assessed based on levels of: (i) crack propagation, (ii) volume of spalled concrete ( $\gamma_{cs}$ ), (iii) the amount of buckled longitudinal reinforcement ( $\gamma_{br}$ ), (iv) residual axial load carrying capacity ( $\gamma_{res}$ ), and (v) previously established damage levels ( $M_1 - M_6$ ). The effects of selected parameters on column performance are investigated in the following sections.

#### *10.5.1 Effect of column diameter ( $D$ )*

Column diameters of 750 mm, 1050 mm, 1350 mm, 1500 mm, and 1800 mm were considered. Representative results for cases  $C_0$  to  $C_4$ , which refer to intact columns being impacted by SUT at 120 km/h, are depicted in Figure 10.3. This figure illustrates the effects of increasing column diameter on crack levels and propagation, damage levels, concrete spalling volumes, reinforcement behavior, and residual axial capacities. As expected, larger diameter columns sustained less damage and had larger residual capacities. It was also observed that the 750-mm column core was breached. Results also indicated that moderate repairs might be needed to restore the 1050-mm column to its original design capacity. The 1350-mm and 1500-mm diameter columns behaved similarly and experienced localized damage at the impact

location. It is believed that minor repairs would be required to restore capacity. The 1800-mm diameter column performed well and was assumed to continue operation while being repaired.

Table 10.2 Study cases

Case	D (mm)	H (mm)	$f'_c$ (MPa)	$\rho$ (%)	FD (min)	$t_{CFRP}$ (mm)	Conf	M (ton)	V (km/h)
$C_0$	750	5.4	28	1	0	0	NA	8.175	120
$C_1$	1050	5.4	28	1	0	0	NA	8.175	120
$C_2$	1350	5.4	28	1	0	0	NA	8.175	120
$C_3$	1500	5.4	28	1	0	0	NA	8.175	120
$C_4$	1800	5.4	28	1	0	0	NA	8.175	120
$C_5$	750	5.4	28	1	90	0	NA	8.175	120
$C_6$	1050	5.4	28	1	90	0	NA	8.175	120
$C_7$	1350	5.4	28	1	90	0	NA	8.175	120
$C_8$	1500	5.4	28	1	90	0	NA	8.175	120
$C_9$	1800	5.4	28	1	90	0	NA	8.175	120
$C_{10}$	750	5.4	28	1	90	1.5	W9L	8.175	120
$C_{11}$	1050	5.4	28	1	90	1.5	W9L	8.175	120
$C_{12}$	1350	5.4	28	1	90	1.5	W9L	8.175	120
$C_{13}$	1500	5.4	28	1	90	1.5	W9L	8.175	120
$C_{14}$	1800	5.4	28	1	90	1.5	W9L	8.175	120
$C_{15}$	1050	5.4	28	1	90	0.5	W3L	8.175	120
$C_{16}$	1050	5.4	28	1	90	1.0	W6L	8.175	120
$C_{17}$	1050	5.4	28	1	90	2.0	W12L	8.175	120
$C_{18}$	1050	5.4	28	1	90	1.5	HH9L	8.175	120
$C_{19}$	1050	5.4	28	1	90	1.5	TH9L	8.175	120
$C_{20}$	1050	5.4	28	1	90	1.5	I1000-9L	8.175	120
$C_{21}$	1050	5.4	28	1	0	0	NA	8.175	65
$C_{22}$	1050	5.4	28	1	0	0	NA	8.175	100
$C_{23}$	1050	5.4	28	1	90	1.5	W9L	8.175	65
$C_{24}$	1050	5.4	28	1	90	1.5	W9L	8.175	100
$C_{25}$	1050	5.4	28	1	60	0	NA	8.175	120
$C_{26}$	1050	5.4	28	1	120	0	NA	8.175	120
$C_{27}$	1050	5.4	28	1	180	0	NA	8.175	120
$C_{28}$	1050	5.4	28	1	60	1.5	W9L	8.175	120
$C_{29}$	1050	5.4	28	1	120	1.5	W9L	8.175	120
$C_{30}$	1050	5.4	28	1	180	1.5	W9L	8.175	120
$C_{31}$	1050	4.0	28	1	0	0	NA	8.175	120
$C_{32}$	1050	7.0	28	1	0	0	NA	8.175	120
$C_{33}$	1050	9.0	28	1	0	0	NA	8.175	120

Case	D (mm)	H (mm)	$f'_c$ (MPa)	$\rho$ (%)	FD (min)	$t_{CFRP}$ (mm)	Conf	M (ton)	V (km/h)
C <sub>34</sub>	1050	4.0	28	1	90	1.5	W9L	8.175	120
C <sub>35</sub>	1050	7.0	28	1	90	1.5	W9L	8.175	120
C <sub>36</sub>	1050	9.0	28	1	90	1.5	W9L	8.175	120
C <sub>37</sub>	1050	5.4	28	1	0	0	NA	1.997	65
C <sub>38</sub>	1050	5.4	28	1	0	0	NA	1.997	100
C <sub>39</sub>	1050	5.4	28	1	0	0	NA	1.997	120
C <sub>40</sub>	1050	5.4	28	1	90	1.5	W9L	1.997	65
C <sub>41</sub>	1050	5.4	28	1	90	1.5	W9L	1.997	100
C <sub>42</sub>	1050	5.4	28	1	90	1.5	W9L	1.997	120
C <sub>43</sub>	1050	5.4	28	1	0	0	NA	0.893	65
C <sub>44</sub>	1050	5.4	28	1	0	0	NA	0.893	100
C <sub>45</sub>	1050	5.4	28	1	0	0	NA	0.893	120
C <sub>46</sub>	1050	5.4	28	1	90	1.5	W9L	0.893	65
C <sub>47</sub>	1050	5.4	28	1	90	1.5	W9L	0.893	100
C <sub>48</sub>	1050	5.4	28	1	90	1.5	W9L	0.893	120
C <sub>49</sub>	1050	5.4	34.5	1	0	0	NA	8.175	120
C <sub>50</sub>	1050	5.4	48.3	1	0	0	NA	8.175	120
C <sub>51</sub>	1050	5.4	56	1	0	0	NA	8.175	120
C <sub>52</sub>	1050	5.4	34.5	1	90	1.5	W9L	8.175	120
C <sub>53</sub>	1050	5.4	48.3	1	90	1.5	W9L	8.175	120
C <sub>54</sub>	1050	5.4	56	1	90	1.5	W9L	8.175	120
C <sub>55</sub>	1050	5.4	28	2	0	0	NA	8.175	120
C <sub>56</sub>	1050	5.4	28	3	0	0	NA	8.175	120
C <sub>57</sub>	1050	5.4	28	4	0	0	NA	8.175	120
C <sub>58</sub>	1050	5.4	28	2	90	1.5	W9L	8.175	120
C <sub>59</sub>	1050	5.4	28	3	90	1.5	W9L	8.175	120
C <sub>60</sub>	1050	5.4	28	4	90	1.5	W9L	8.175	120

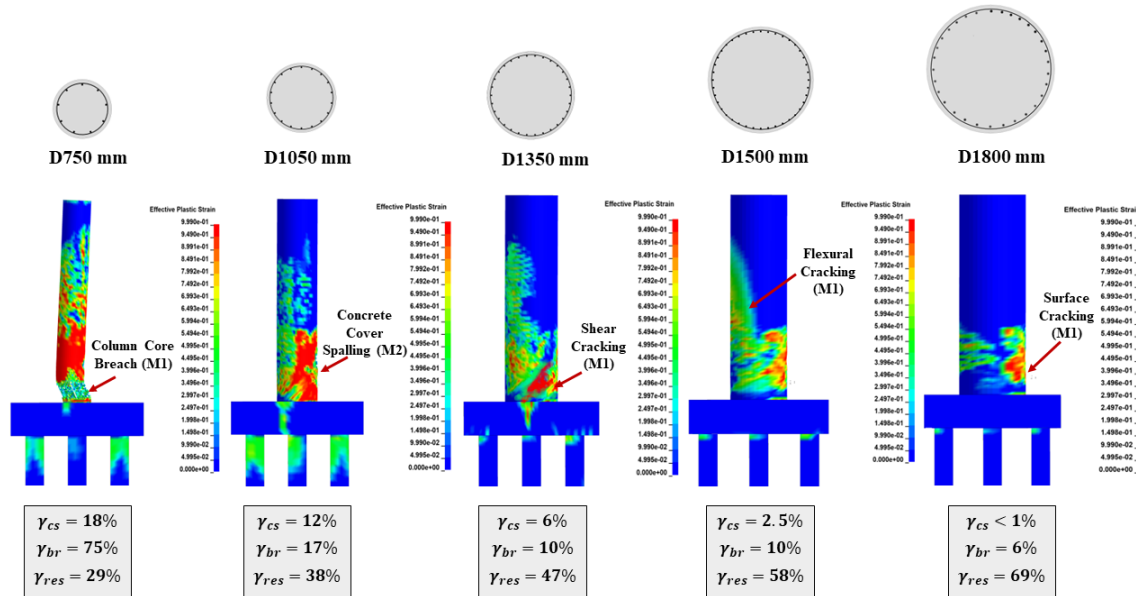


Figure 10.3 Effect of column diameter on impact performance

### 10.5.2 Effect of column height ( $H$ )

As indicated earlier and presented in Table 10.2, columns with heights of 4000 mm, 5400 mm, 7000 mm, and 9000 mm were examined under vehicle impact. In this context, representative response, and damage propagation of columns in cases  $C_1$ , and  $C_{31} - C_{33}$ , which represent the 1050-mm diameter columns with the aforementioned heights subjected to SUT impact at 120 km/h, are depicted in Figure 10.4. This figure demonstrates that columns in these cases largely performed similarly, with more cracking observed for shorter columns as they tend to absorb more impact energy due to their relatively high flexural stiffness. Despite having the greatest relative volume of spalled concrete, the 4000-mm column had higher residual axial capacity than the other columns as more slender columns experienced second order effects that further reduced capacity.

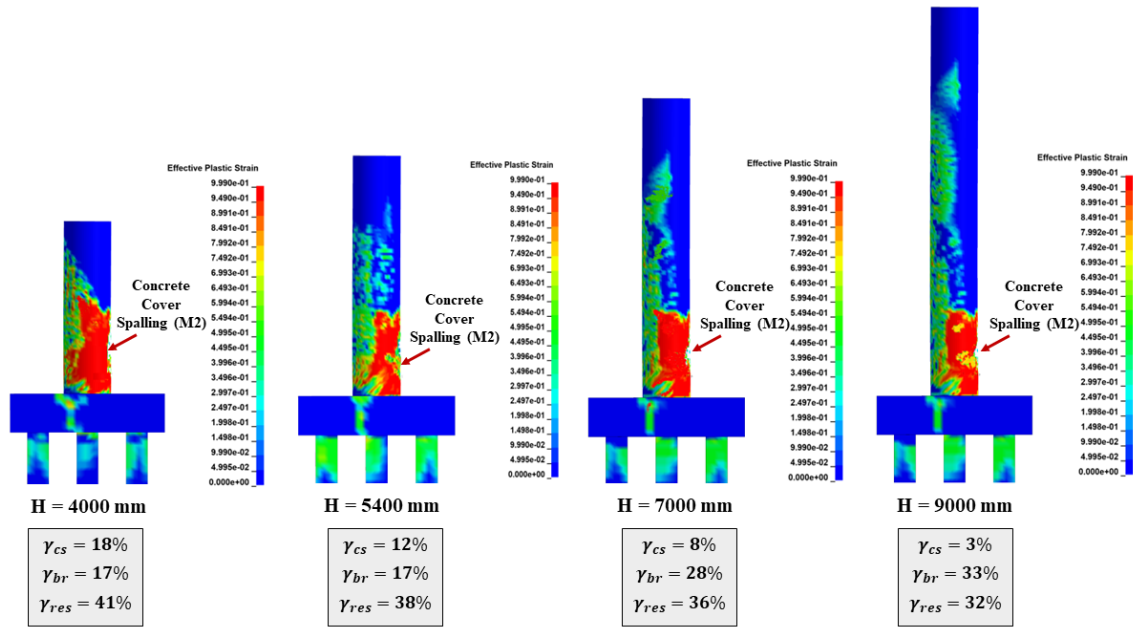


Figure 10.4 Effect of column height on impact performance

### 10.5.3 Effect of unconfined compressive strength ( $f'_c$ )

Four unconfined compressive strengths ( $f'_c$ ) were examined, with strengths ranging between 28 MPa and 56 MPa. Resultant damage and performance indicators of cases  $C_1$ , and  $C_{49} - C_{51}$ , which correspond to the 1050-mm diameter columns with various strengths impacted by the SUT moving at 120 km/h, are illustrated in Figure 10.5. This figure indicates that increasing the  $f'_c$  of columns has a very limited effect on crack propagation and concrete spalling. Furthermore, it was noted that the number of buckled reinforcements was the same in all the studied cases. However, it was observed that increasing  $f'_c$  has a pronounced effect on columns' residual axial load carrying capacity. Given the similar deformation and sustained column damage, columns with a larger  $f'_c$  value sustained larger axial loads during the push down analysis. This finding can be further justified in accordance with Equation. 11, where the nominal capacity is directly proportional to  $f'_c$ .

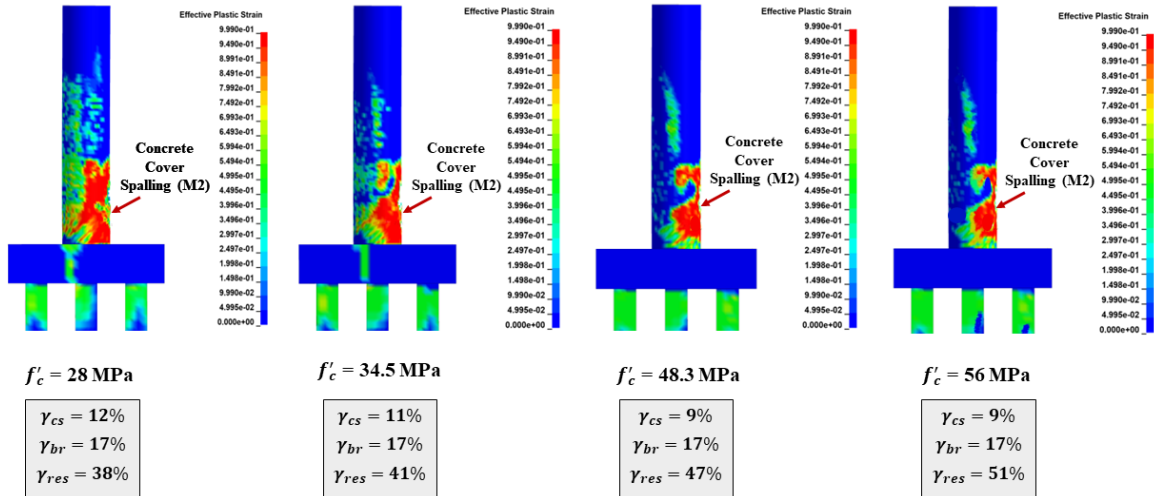


Figure 10.5 Effect of unconfined compressive strength on impact performance

#### 10.5.4 Effect of longitudinal steel reinforcement ratio ( $\rho$ )

As indicated earlier, four longitudinal steel reinforcement ratios of 1%, 2%, 3%, and 4% were selected in accordance with common practices widely used in the U.S and used in the present study. Accordingly, cases  $C_1$ , and  $C_{55} - C_{57}$ , which refer to the intact, 1050-mm diameter columns with various reinforcement ratios under SUT impact, are depicted in Figure 10.6. Similar to what was discussed in the previous section, it was found that varying steel reinforcement have a limited impact on the damage propagation and the volume of spalled concrete. It was shown that limited flexural demand was placed on columns with 3% and 4% steel ratios, with only two longitudinal reinforcement bars buckled near the impact location. Due to the increased flexural stiffness, columns with larger reinforcement better resisted the imposed impact load and sustained acceptable residual axial capacities.

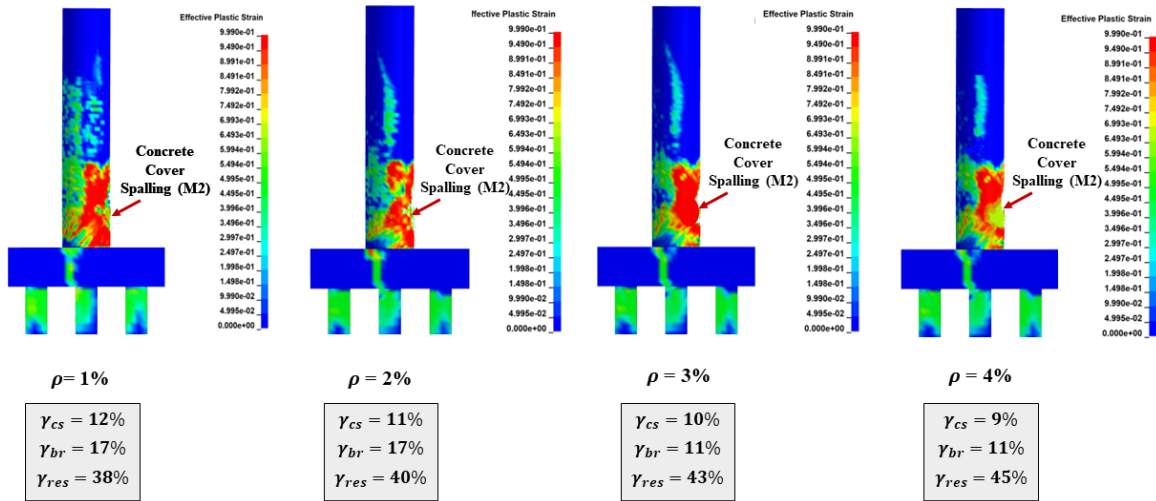


Figure 10.6 Effect of longitudinal steel reinforcement ratio on impact performance

### 10.5.5 Effect of fire exposure and fire duration (FD)

The entire column periphery was subjected to 60, 90, 120, and 180-minute fire exposures, with variation of temperature over time defined in accordance with the ISO-834 standard fire curve (ISO, 1999). Figure 10.7 compares damage propagation and final damage states of columns for the 90-minute exposure (i.e.,  $F90$ ). Intact columns in cases  $C_0 - C_3$  are presented and compared to fire damaged columns in cases  $C_5 - C_8$ . As expected, the effect of exposing bridge columns to fire prior to vehicle impact is evident, with fire exposed columns experiencing more severe damage. It was also observed that, for the same fire duration, larger column diameters better resisted impact load and sustained acceptable structural integrity and residual capacity. The effect of fire duration on column performance is depicted in Figure 10.8. Case  $C_5$ , where the 1050-mm column was exposed to a 90-minute fire, was compared to cases  $C_{25}$ ,  $C_{26}$ , and  $C_{27}$ , where the same column was exposed to 60, 120, and 180-minute fire, respectively. The figure clearly shows that increased fire duration exposure affects column performance, with more critical damage observed in 120 and 180-minute fire durations. In these two cases, columns

were vulnerable to impact with more than 50% of longitudinal reinforcements buckled and column core breach initiated.

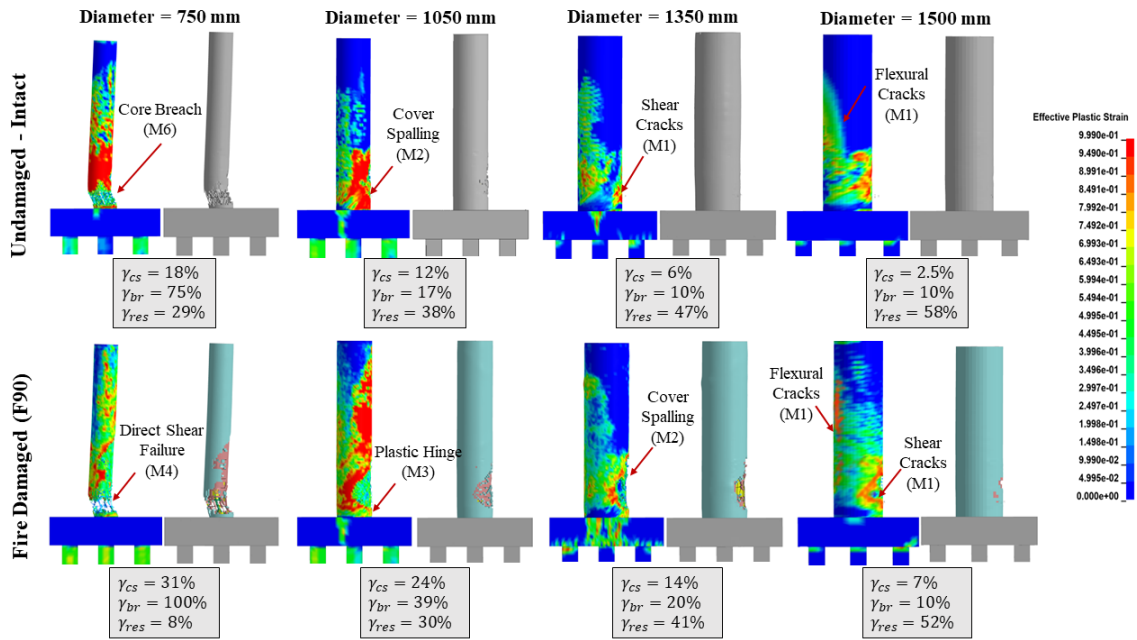


Figure 10.7 Effect of ISO-834 fire exposure on impact performance

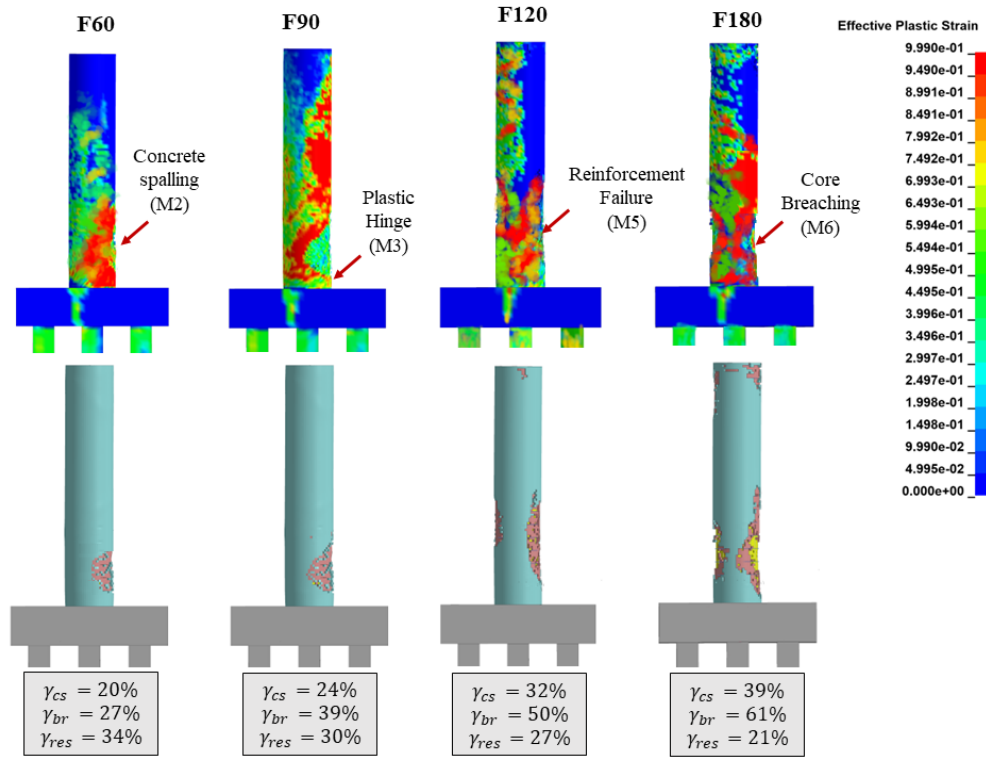


Figure 10.8 Effect of fire exposure duration on impact performance

### 10.5.6 Effect of CFRP wrap thickness ( $t_{CFRP}$ )

Following research outlined in Chapter 7, the effectiveness with which externally bonded CFRP could restore column design axial load carrying capacities was examined. Four CFRP thicknesses were selected: 0.5 mm (3 layers), 1 mm (6 layers), 1.5 mm (9 layers), and 2 mm (12 layers). Figure 10.9 compares the performance of 1050-mm diameter CFRP retrofitted columns to bare intact and fire-damaged columns after SUT collision (cases  $C_1$ ,  $C_6$ ,  $C_{11}$ , and  $C_{15} - C_{17}$ ). As shown in this figure, compared to the bare fire-damaged column, the volume of spalled concrete significantly reduced when CFRP wrapping was used. Furthermore, increasing CFRP thickness from 1.5 mm to 2.0 mm did not offer much improvement.

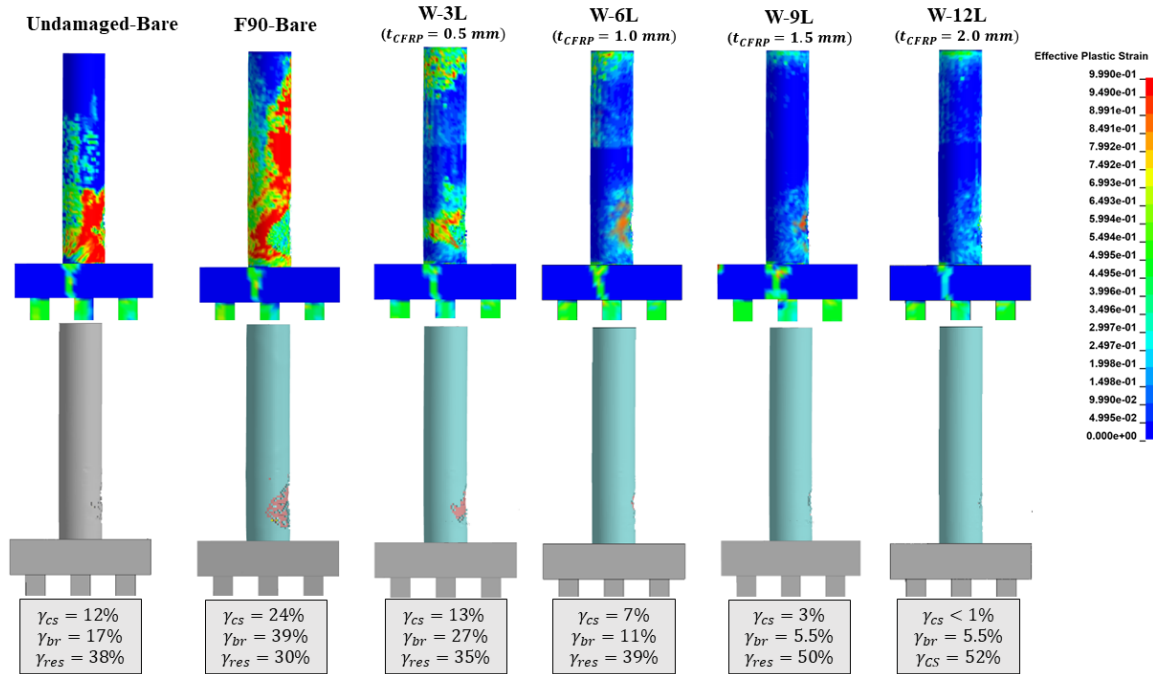


Figure 10.9 Effect of CFRP wrap thickness on impact performance

### 10.5.7 Effect of CFRP wrapping configuration (Conf)

In addition to wrapping the entire column height, the current study investigated the effects of partial and intermittent wrapping on performance. Three wrapping configurations were considered using nine CFRP layers ( $t_{CFRP} = 1.5 \text{ mm}$ ): half of the column height (*HH-9L*), the bottom two-thirds of the column height, and intermittent wrapping using 1000 mm strips (*II1000-9L*). These wrapping configurations are illustrated in Figure 10.10.

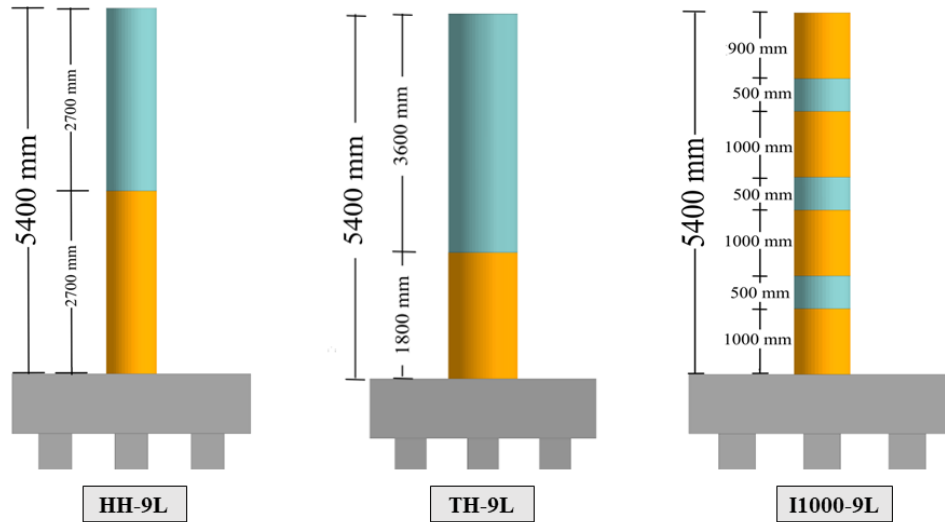


Figure 10.10 CFRP partial wrapping configurations

Figure 10.11 demonstrates the effects of partial and intermittent wrapping on fire-damaged column performance under vehicle collision. In this figure, cases  $C_1$ ,  $C_6$ ,  $C_{11}$ , and  $C_{18}$  –  $C_{20}$ , which correspond to intact, fired-damaged, fully and partially wrapped, 1050-mm diameter columns when subjected to SUT impact, are compared. It was noted that all three configurations effectively mitigated the resulting damage and improved residual capacity compared to bare fire-damaged columns. It was also observed that columns in *HH-9L* and *TH-9L* sustained identical damage and largely performed similarly. While slightly more concrete spalling occurred in *I1000-9L*, it was shown that this retrofitting configuration was deemed more efficient in mitigating reinforcement buckling and enhancing post-impact residual capacity.

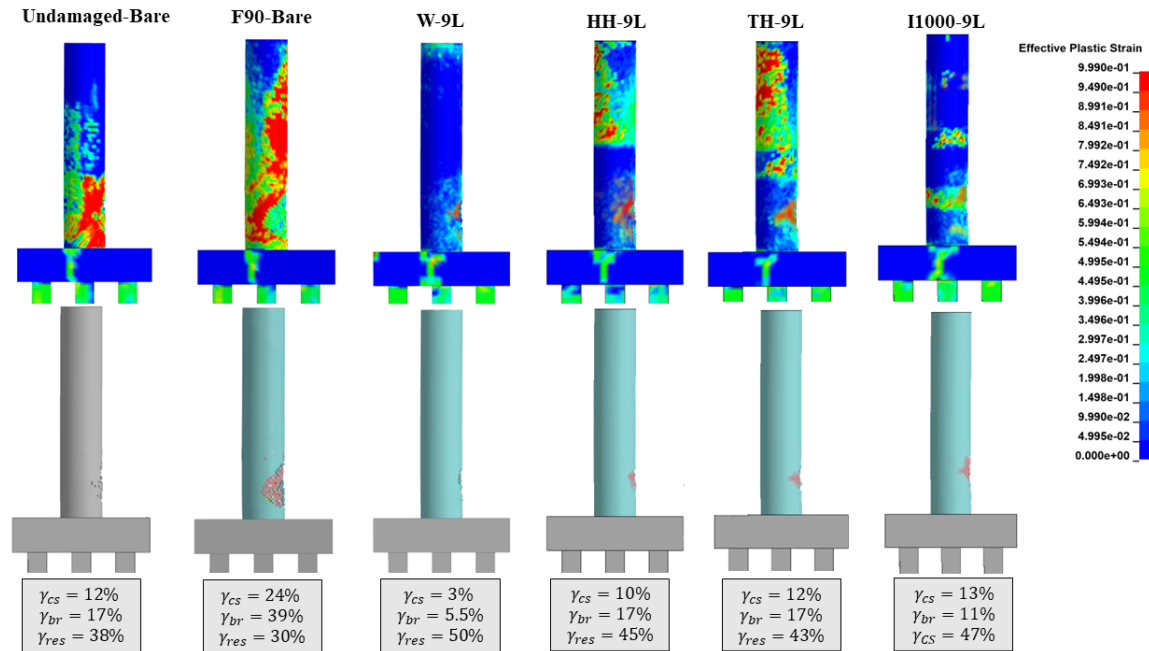


Figure 10.11 Effect of CFRP wrapping configuration on impact performance

### 10.5.8 Effect of vehicle mass ( $M$ )

To examine the effect of vehicle mass on column performance, three types of vehicles were selected: an 8.175-ton Ford F800 Single Unit Truck (SUT), a 1.997-ton Dodge Ram, and a 0.893-ton Toyota Yaris. Figure 10.12 illustrates the effect of varying mass on column impact performance. In this figure, cases  $C_1$ ,  $C_{39}$ , and  $C_{46}$ , where the selected vehicles impacted the bridge column with a 120 km/h, are presented. Compared to other investigated parameters, vehicle mass was shown to more prominently affect column performance. As expected, damage induced by smaller vehicles is considerably less than that caused by larger vehicles.

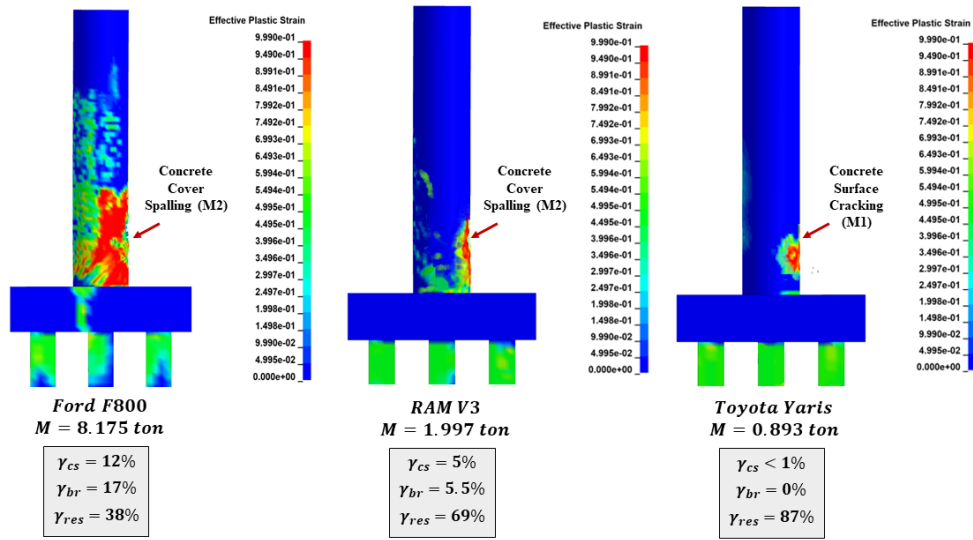


Figure 10.12 Effect of vehicle mass on impact performance

### 10.5.9 Effect of impact speed ( $V$ )

Three impact speeds were examined: 65 km/h (40 mph), 100 km/h (60 mph), and 120 km/h (75 mph). Results from cases  $C_1$ ,  $C_{21}$ , and  $C_{22}$  are shown in Figure 10.13. Like what was discussed in the previous section, impact speed also has a more pronounced effect on column performance than other examined parameters. It is evident that increasing the speed of impact resulted in more significant damage.

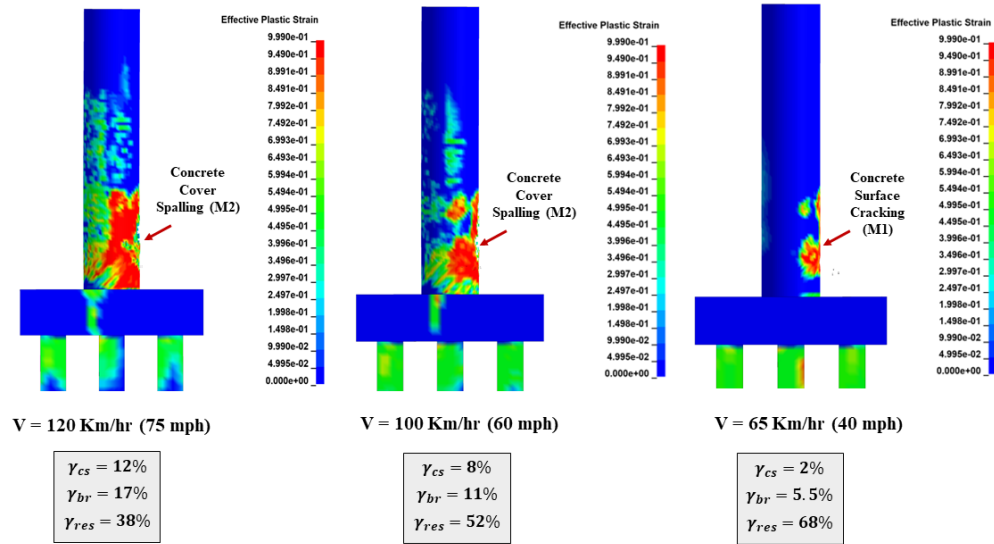


Figure 10.13 Effect of vehicle speed on impact performance

## 10.6 Impact Force Estimation and ESF assessment

As indicated earlier, the maximum contact force computed during a simulated or an actual vehicle impact event is referred to as the Peak Dynamic Force (PDF). As this force usually acts over a very short time duration, much shorter than a bridge's fundamental period, engineers traditionally do not consider the PDF when analyzing or designing for vehicle collisions (El-Tawil et al., 2005). Alternatively, engineers adopt an ESF as it has been stated to be conservatively representative of design demand (Chopra, 2007). ESF corresponds to a static force that produces displacement equal to that produced by a vehicle at the point of impact (Abdelkarim & ElGawady, 2017; El-Tawil et al., 2005). Accordingly, the 9<sup>th</sup> edition of *AASHTO LRFD* mandated dramatically increasing the historical ESF of 1780 kN (400 Kips) to an ESF of 2670 kN (600 Kips) for the analysis and design of RC pier columns under vehicle impact (2020). This dramatic increase spurred many follow-up research studies (Abdelkarim & ElGawady, 2017; AuYeung & Alipour, 2016; El-Tawil et al., 2005; S. Roy et al., 2021).

As stated earlier, PTMSA has been frequently used by researchers to accurately estimate impact force from a vehicle collision (Abdelkarim & ElGawady, 2017; El-Tawil et al., 2005; S. Roy et al., 2021), and this method was employed for ESF estimation. PDF's that corresponded to all examined collision scenarios were extracted from parametric study FE models and MATLAB was employed to perform signal processing utilizing PTMSA. ESFs were then identified as the peak force from filtered impact force time history. Representative PDFs and the corresponding ESFs for cases  $C_0 - C_4$  are depicted in Figure 10.14.

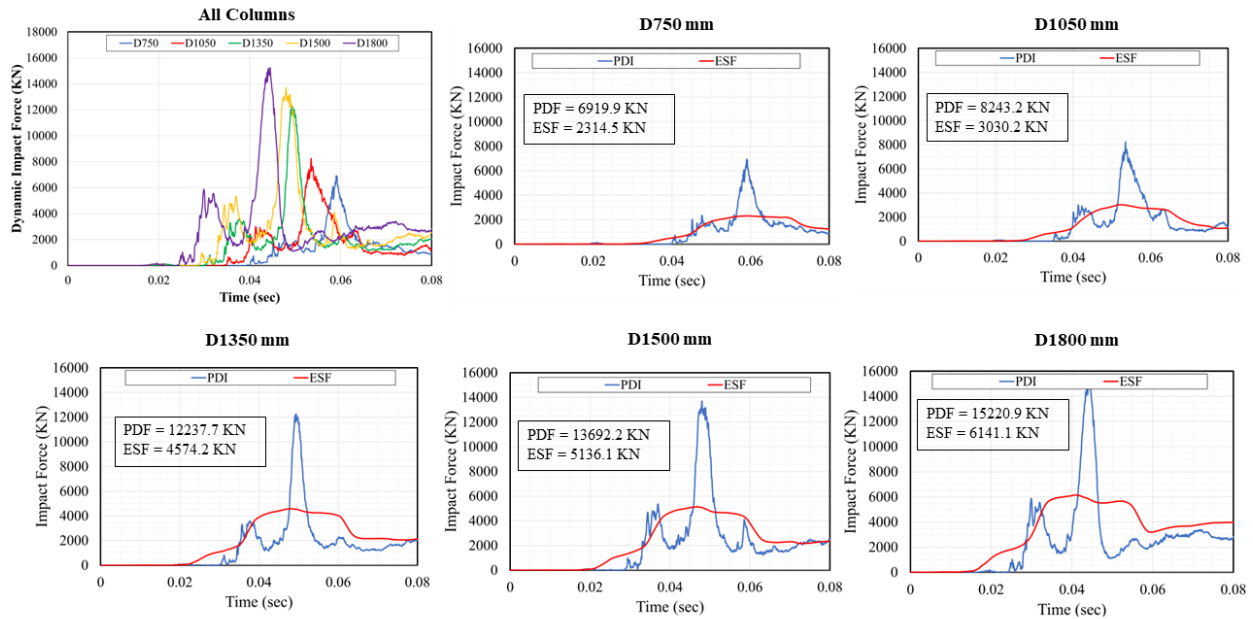


Figure 10.14 Representative PDFs and their corresponding ESFs; Cases  $C_0 - C_4$

Comparisons of resulting PTMSA based ESFs to the AASHTO ESF were achieved using nondimensional ratios normalized as summarized in Table 10.3, and magnitudes are graphically shown in Figure 10.15. Note that the figure also depicts the current AASHTO ESF value.

Table 10.3 Normalized ESFs, all studied cases

Case No.	Normalized ESF	Case No.	Normalized ESF	Case No.	Normalized ESF
C <sub>0</sub>	0.87	C <sub>21</sub>	0.64	C <sub>42</sub>	0.51
C <sub>1</sub>	1.13	C <sub>22</sub>	0.74	C <sub>43</sub>	0.19
C <sub>2</sub>	1.70	C <sub>23</sub>	0.70	C <sub>44</sub>	0.26
C <sub>3</sub>	1.80	C <sub>24</sub>	0.82	C <sub>45</sub>	0.30
C <sub>4</sub>	2.30	C <sub>25</sub>	1.12	C <sub>46</sub>	0.22
C <sub>5</sub>	0.79	C <sub>26</sub>	0.70	C <sub>47</sub>	0.27
C <sub>6</sub>	0.95	C <sub>27</sub>	0.64	C <sub>48</sub>	0.33
C <sub>7</sub>	1.53	C <sub>28</sub>	1.21	C <sub>49</sub>	1.01
C <sub>8</sub>	1.58	C <sub>29</sub>	0.78	C <sub>50</sub>	1.04
C <sub>9</sub>	2.17	C <sub>30</sub>	0.74	C <sub>51</sub>	1.07
C <sub>10</sub>	0.93	C <sub>31</sub>	1.45	C <sub>52</sub>	1.06
C <sub>11</sub>	1.17	C <sub>32</sub>	0.79	C <sub>53</sub>	1.10
C <sub>12</sub>	1.74	C <sub>33</sub>	0.70	C <sub>54</sub>	1.13
C <sub>13</sub>	1.84	C <sub>34</sub>	1.50	C <sub>55</sub>	1.01
C <sub>14</sub>	2.36	C <sub>35</sub>	0.86	C <sub>56</sub>	1.12
C <sub>15</sub>	0.94	C <sub>36</sub>	0.75	C <sub>57</sub>	1.13
C <sub>16</sub>	0.98	C <sub>37</sub>	0.33	C <sub>58</sub>	1.09
C <sub>17</sub>	1.17	C <sub>38</sub>	0.38	C <sub>59</sub>	1.16
C <sub>18</sub>	1.00	C <sub>39</sub>	0.42	C <sub>60</sub>	1.21
C <sub>19</sub>	0.98	C <sub>40</sub>	0.36		
C <sub>20</sub>	1.01	C <sub>41</sub>	0.43		

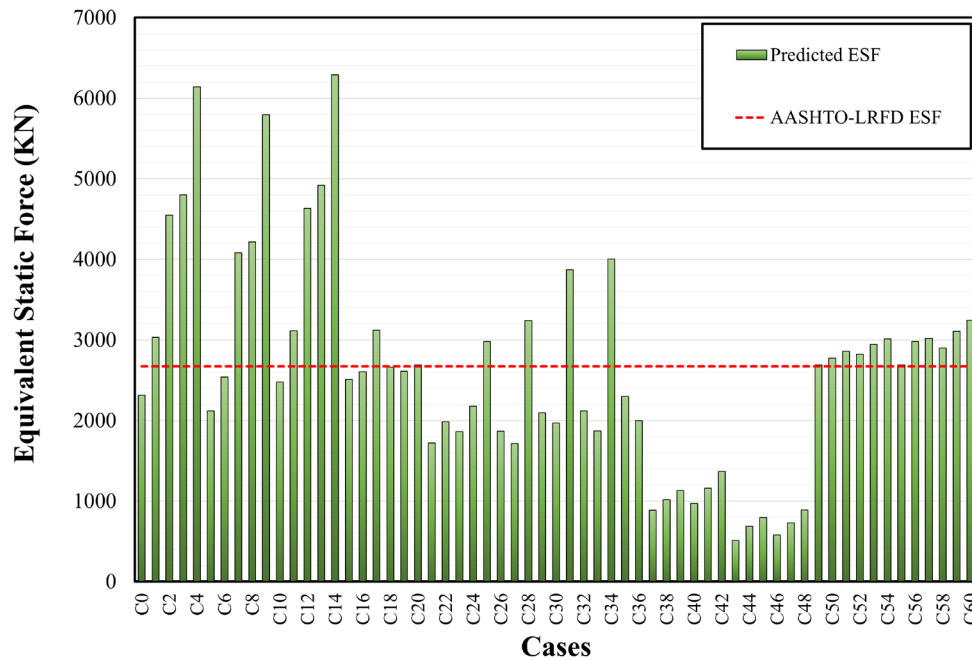


Figure 10.15 Predicted ESFs, all studied cases

General observations on the PDF and ESF are summarized as following:

1. For the parameters studied and the modeling approach used, vehicle speed and mass most significantly influenced impact forces.
2. *AASHTO-LRFD* underestimated ESF for 41% of the studied cases. These results envelope collisions by the Ford F800 SUT at 120 km/h for:
  - Intact columns with diameters greater than 750 mm.
  - Fire-damaged columns with diameters greater than 1050 mm and fire exposures of more than 60 minutes.
  - 1050-mm diameter and larger fully-wrapped columns with  $t_{CFRP}$  greater than or equal to 1.5 mm.
  - 1050-mm diameter and larger intact and CFRP wrapped columns shorter than 5.4 m.
  - 1050-mm diameter and larger intact and CFRP wrapped columns with  $f'_c$  greater than 34.5 MPa.
  - 1050-mm diameter and larger intact and CFRP wrapped columns with  $\rho$  greater than 2%.
3. *AASHTO-LRFD* was shown to conservatively predict ESFs for collisions involving the light Toyota Yaris and medium Dodge Ram vehicles for:
  - Speeds less than 120 km/h.
  - Columns with diameters smaller than 1050 mm and heights greater than 5.4 m.
  - Bare fire-damaged columns, columns with  $f'_c$  smaller than or equal to 34.5 MPa.

- Columns with reinforcement ratios less than or equal to 2%.
- Fully-wrapped columns with  $t_{CFRP}$  less than 1.5 mm, and partially wrapped columns.

In summary, AASHTO ESF was found to be either higher or lower than what was estimated using the FE model depending mainly on the kinetic energy resulting from the impact event, and other factors associated with column design or residual capacities. These discrepancies offer an opportunity for improvement in AASHTO ESF and underscore the need for more accurate and realistic representation that may better simulate a wide range of demands and subsequent design and retrofit decisions.

### 10.7 Proposed ESF Equation, Derivation and Validation

As demonstrated by several researchers and further identified by results presented in the previous section, the current 600 Kips (2,670 kN) ESF recommended by *AASHTO-LRFD* could underestimate or overestimate actual impact forces over a wide range of collision scenarios (Buth et al., 2010, 2011; El-Tawil et al., 2005; Gomez & Alipour, 2014; S. Roy et al., 2021). This is because this constant force completely ignores essential variables that characterize actual impact forces including vehicle speed and mass, column design and geometry and initial conditions. In this section, a simple, empirically-based, ESF equation is developed and validated.

#### *10.7.1 ESF equation development*

Results presented earlier revealed that ESF is sensitive to multiple examined parameters, with certain external factors (i.e., vehicle mass and speed) and design variables (i.e., diameter, height, concrete strength, steel reinforcement levels) having the most influence. It was also recognized that initial conditions (i.e., previous fire exposure) and retrofit techniques (i.e., CRFP wrap) could also influence ESF.

Consequently, an ESF equation that attempted to incorporate prevailing parameters was empirically developed. Variables initially included in the equation were:

1. Column axial load capacity ( $P_r$ ) as a function of concrete compressive strength ( $f'_c$ ), column diameter ( $D$ ), steel reinforcement ratio ( $\rho$ ), fire exposure, and lateral confinement by CFRP wrap.
2. Column height ( $H$ ).
3. Kinetic Energy ( $KE$ ) which reflects vehicle mass and speed.

A multi-variate, nonlinear regression was performed using IBM-SPSS Statistics 25 to establish correlation between estimated ESFs and the variables listed above and is shown in Equation. 16. The regressed relationship is also illustrated in Figure 10.16. As shown in this figure, the proposed equation showed agreement with FE results across the range of studied demand and design variables, with an  $R^2$  of 0.863. To further visualize errors between the regressed equation and FE results, +/- 15% upper and lower bounding curves are also arbitrarily provided in the figure.

$$ESF = 0.018 \sqrt{\frac{P_r \cdot KE}{H}} \quad \text{Equation. 16}$$

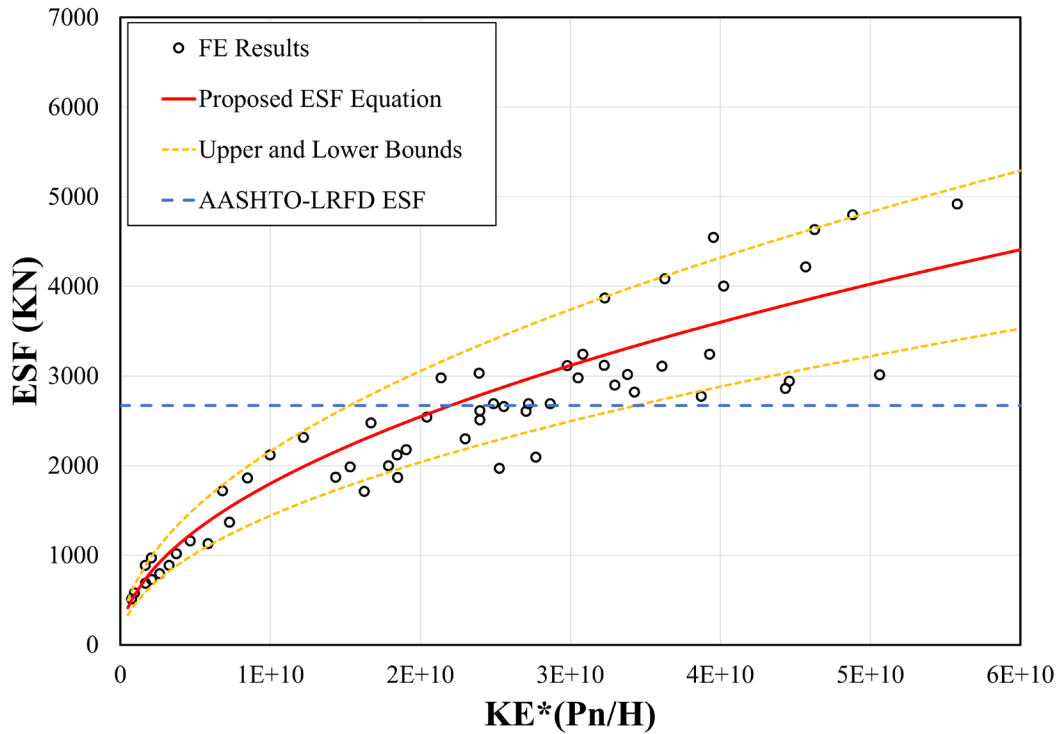


Figure 10.16 Developed ESF equation, FE model comparison

### 10.7.2 ESF equation validation

Equation. 16 was validated by comparing calculated ESFs to those obtained from published studies that examined RC columns subjected to vehicular collisions (Abdelkarim & ElGawady, 2017; Gomez, 2014) and from modeling twelve additional columns subject to collisions. Table 10.4 summarizes columns and collision conditions utilized for validation. Comparisons between ESFs from Equation. 16, the published studies, and 12 developed models are illustrated in Table 10.4. As illustrated in this figure, good agreement was obtained over the range of validation column models. In particular, statistical metrics that included a coefficient of determination ( $R^2$ ) of 0.81, a Coefficient of Variation (CV) of 5.1%, and a Normalized Root Mean Square Error (N-

RMSE) of 7.4%, signify the accuracy and reliability of the proposed predictive equation across a diverse range of collision scenarios.

Table 10.4 Summary of FE models used in validation

Case	D (mm)	H (mm)	$f'_c$ (MPa)	$\rho$ (%)	FD (min)	$t_{CFRP}$ (mm)	Conf	M (ton)	V (km/h)
<b>Developed FE Models</b>									
$C_{V1}$	1350	4.5	36	1	0	0	NA	8.175	105
$C_{V2}$	1350	4.5	36	1	60	0	NA	8.175	90
$C_{V3}$	1350	4.5	36	1	75	0.667	W4L	1.998	105
$C_{V4}$	1350	4.5	36	1	100	0.833	W5L	1.998	90
$C_{V5}$	750	4.5	36	1	0	0	NA	8.175	105
$C_{V6}$	750	4.5	36	1	60	0	NA	8.175	90
$C_{V7}$	750	4.5	36	1	75	0.667	W4L	1.998	105
$C_{V8}$	750	4.5	36	1	100	0.833	W6L	1.998	90
$C_{V9}$	1500	4.5	36	1	0	0	NA	8.175	105
$C_{V10}$	1500	4.5	36	1	60	0	NA	8.175	90
$C_{V11}$	1500	4.5	36	1	75	0.667	W4L	1.998	105
$C_{V12}$	1500	4.5	36	1	100	0.833	W5L	1.998	90
<b>Abdelkarim and ElGawady, 2017</b>									
$C_{V13}$	1500	7.5	34.5	1	0	0	NA	8.00	80
$C_{V14}$	1500	7.5	34.5	1	0	0	NA	8.00	80
$C_{V15}$	1500	7.5	34.5	3	0	0	NA	8.00	80
$C_{V16}$	1500	3.75	34.5	1	0	0	NA	8.00	80
$C_{V17}$	1500	7.5	34.5	2	0	0	NA	8.00	80
$C_{V18}$	1500	7.5	34.5	1	0	0	NA	8.00	112
$C_{V19}$	1500	7.5	34.5	1	0	0	NA	8.00	65
$C_{V20}$	1500	7.5	34.5	1	0	0	NA	2.00	80
<b>Gomez, 2014</b>									
$C_{V21}$	1200	5.0	29	1	0	0	NA	8.063	55
$C_{V22}$	1200	5.0	30.2	1	0	0	NA	8.063	55
$C_{V23}$	1200	5.0	34.9	1	0	0	NA	8.063	55
$C_{V24}$	1200	5.0	29	1	0	0	NA	8.063	80
$C_{V25}$	1200	5.0	30.2	1	0	0	NA	8.063	80
$C_{V26}$	1200	5.0	34.9	1	0	0	NA	8.063	80

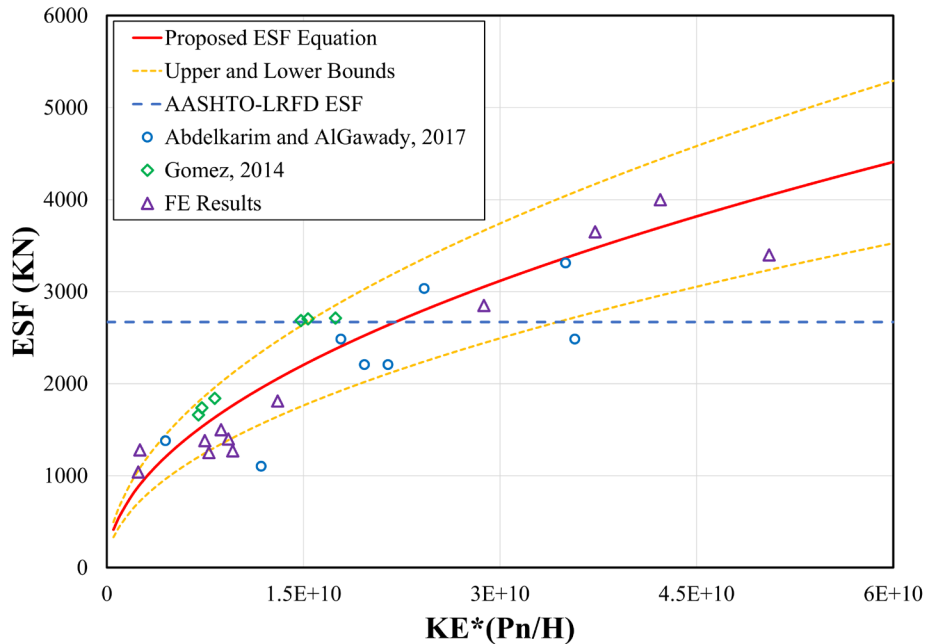


Figure 10.17 Developed ESF equation, FE results, published study results

### 10.8 ESF assessment framework

In conjunction with development of Equation. 16, a calculation framework was developed. The developed equation and the complementary framework enable bridge owners and practitioners to better estimate demands from varying impact energies, which can, in turn, be used to better design or retrofit columns needing strengthened. The framework is shown in Figure 10.18. Note that exposure and FRP strengthening are addressed prior to ESF determination.

As illustrated in this figure, the framework is divided into four subsequent stages. The first stage applies only if columns survive a fire and maintain adequate structural integrity prior to vehicle collision and include indirect post-fire assessments. The second stage encompasses estimations of intact, fire-damaged, and CFRP wrapped column capacities. A detailed procedure for these estimations is provided in the next section. Then, anticipated design speeds and vehicle

masses are to be used to calculate the  $KE$ . For existing bridges,  $KE$  is identified based on highway speed limit and traffic data, where vehicle types that use this specific roadway can be specified. Ultimately, the final stage incorporates all previously completed calculations to estimate the ESF. While this equation can be used for design purposes, it would also provide valuable insights on how susceptible existing pier columns are to vehicle collisions.

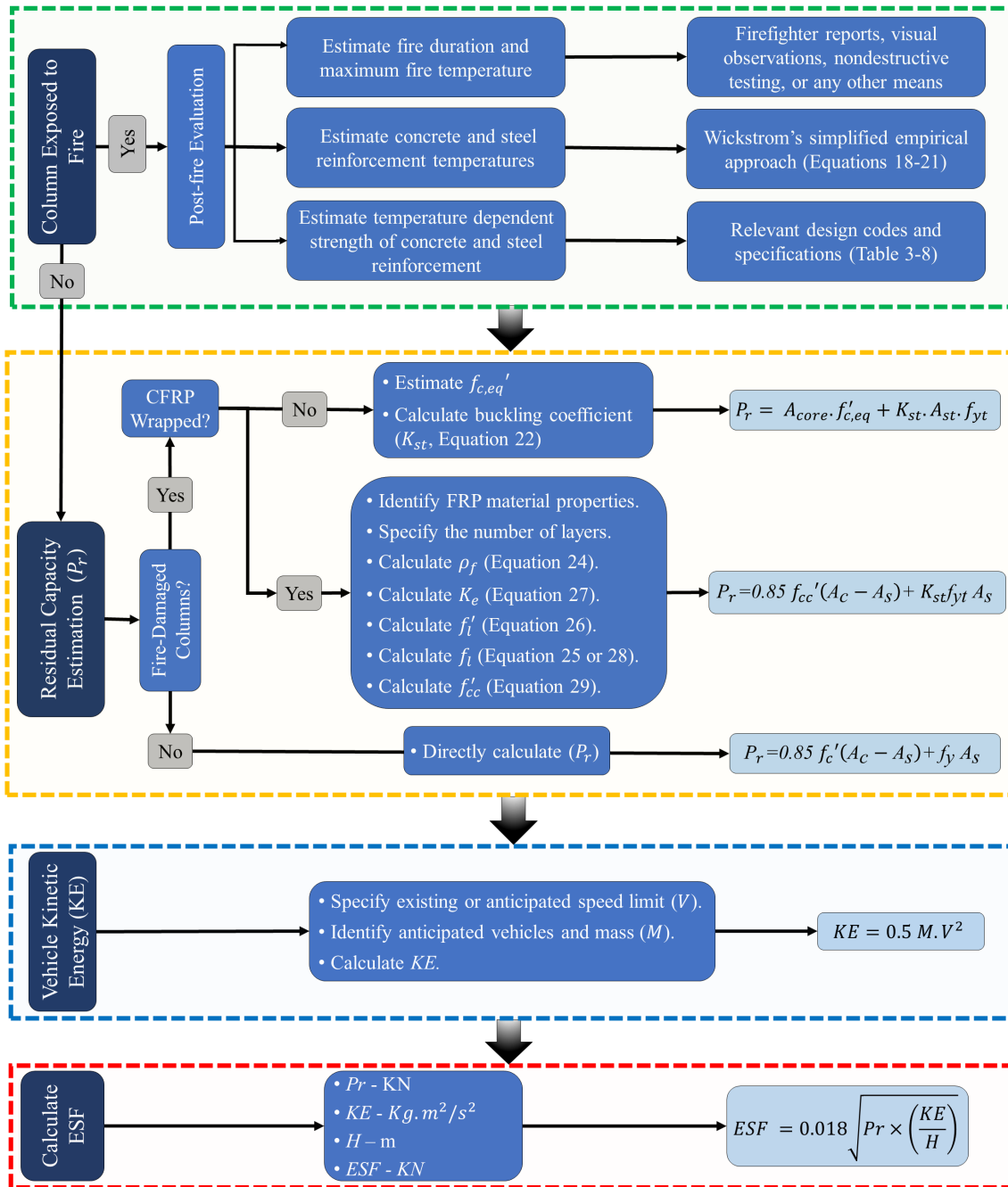


Figure 10.18 Proposed ESF Framework

### 10.9 Axial Load Capacity Calculation

While  $KE$  and  $H$  from Equation 16 can be found, estimating a column’s residual capacity can be challenging. As a result, a step-by-step guide that estimates residual capacity for intact,

fire-damaged, or CFRP retrofitted columns was developed. Capacity of intact (undamaged) RC columns.

#### 10.9.1 Capacity of intact (undamaged) RC columns

Nominal capacity of RC columns can be calculated in accordance with AASHTO-LRFD bridge design code as shown in Equation. 17 below:

$$P_r = 0.85 f'_c (A_c - A_s) + f_y A_s \quad \text{Equation. 17}$$

where  $P_r$  is the nominal axial load carrying capacity;  $f'_c$  is the unconfined concrete compressive strength;  $A_c$  is the cross-sectional area; and  $f_y$  and  $A_s$  are the yielding strength and cross-sectional area of longitudinal steel reinforcement, respectively.

#### 10.9.2 Capacity of bare fire-damaged RC columns

Unlike intact columns, estimating the capacity of fire-damaged RC columns requires a more extensive and thorough procedure. Post-fire assessment is imperative to accurately estimate this capacity. Therefore, the points listed below summarize the essential steps needed to determine the capacity of fire-damaged columns:

- 1) Estimation of maximum fire temperature and fire duration:

This can be reported by firefighters, determined via visual observations of concrete color, and other methods including non-destructive testing (V. K. R. Kodur et al., 2013).

- 2) Estimation of maximum temperature in steel reinforcement ( $T_r$ ):

Wickstorm's method is frequently used by researchers to determine the temperature of steel reinforcement (V. K. R. Kodur et al., 2013; Wickström, 1986). In this method, the temperature of steel reinforcement ( $T_r$ ) can be estimated as follows:

$$T_r = [\eta_w(\eta_x + \eta_y - 2\eta_x\eta_y) + \eta_x\eta_y]T_f \quad \text{Equation. 18}$$

$$\eta_w = 1 - 0.0616t_h^{-0.88} \quad \text{Equation. 19}$$

$$\eta_x = 0.18 \ln \left[ \frac{t_h}{x^2} \right] - 0.81 \quad \text{Equation. 20}$$

$$\eta_y = 0.18 \ln \left[ \frac{t_h}{y^2} \right] - 0.81 \quad \text{Equation. 21}$$

where  $T_f$  is fire temperature,  $t_h$  is the time of interest in hour, and  $x$  and  $y$  are the coordinates of reinforcement bar measured from the exposed surface. After estimating steel temperatures, reinforcement bars should be assigned a unique reduced yielding strength ( $f_{yt}$ ) determined in accordance with *Eurocode 2: Part 1-2* or any other relevant specifications (Eurocode 2, 2004).

### 3) Estimation of equivalent unconfined compressive strength of concrete ( $f'_{cequ}$ ):

In addition to non-destructive testing, two alternative approaches can be employed to determine the reduced strength of concrete after being exposed to fire. The first method defines a core region of concrete column as the region that experienced a temperature less than  $500^\circ C$ . The method assumes that this region maintains full design strength. A detailed procedure to locate the core region can be found elsewhere (V. K. R. Kodur et al., 2013; Wickström, 1986). Another simplified approach proposed by Chen et al. (2016) can be also employed. In this approach, equivalent compressive strength can be

determined based on maximum recorded temperature during a fire event. Based on post-fire assessment and non-destructive testing, weighted average of compressive strengths measured at certain distances from exposed surfaces can be utilized to determine the reduced compressive strength. It is worth noting that in all approaches, compressive strength reduction factors can be determined in accordance with *Eurocode 2: Part 1-2* (2004) or any other applicable provisions.

4) Calculation of steel buckling coefficient ( $K_{st}$ ):

In many circumstances, exposing RC columns to fire causes concrete cover to spall. In such cases, longitudinal steel reinforcement may experience local buckling due to the loss of lateral confinement provided by concrete. To accommodate for the effect of this local buckling on a column's capacity, a buckling coefficient ( $K_{st}$ ) should be calculated. As proposed by Jiang et al. (2007), this coefficient can be calculated as follows:

$$K_{st} = \left(1.136 - 111.6 \frac{e}{s}\right) \left(0.972 + 0.004 \frac{s}{d_s} - 0.003 \left(\frac{s}{d_s}\right)^2\right) \quad \text{Equation. 22}$$

where  $e$  is the lateral bending of steel reinforcement bar,  $s$  is the spacing between transverse reinforcements, and  $d_s$  is the diameter of the steel bar.

5) Estimation of residual capacity of fire-damaged columns ( $P_r$ ):

Once all the previous parameters are estimated, residual capacity of the fire-damaged column can be calculated as:

$$P_r = 0.85 f'_{cequ}(A_c - A_s) + K_{st} f_{yt} A_s$$

Equation.  
23

### 10.9.3 Capacity of CFRP wrapped RC columns

One major advantage of using externally bonded FRP wraps to retrofit RC columns is increasing confinement. As confining concrete apparently increases its compressive strength, FRP wrapping is frequently used to enhance column ductility and shear and axial load capacities (Bank, 2006). Apparent increase in unconfined compressive strength due to confinement pressure ( $f_l$ ) is referred to a concrete confined compressive strength ( $f_{cc}'$ ). According to ACI 440.2-R17: *Guide for the Design and Construction of Externally Bonded FRP Systems for Strengthening Concrete Structures* (2017),  $f_{cc}'$  is directly proportional to the overall thickness of CFRP wrap ( $t_{CFRP}$ ). The following procedure is proposed to estimate the axial load carrying capacity of CFRP wrapped RC columns:

- 1) Identify the material properties of CFRP laminates that will be used to retrofit the RC columns.
- 2) Specify the number of CFRP layers ( $n$ ) and the corresponding thickness ( $t_{CFRP}$ ).  
Typically, this number is not explicitly driven by the desire to increase element strength, but rather, it is compelled by the extent of damage and susceptibility of the structural element to be repaired (Bank, 2006).
- 3) Determine the CFRP reinforcement ratio ( $\rho_f$ ):

In accordance with Lawrence Bank design book (2006),  $\rho_f$  is expressed as:

$$\rho_f = \frac{A_f}{A_c} = \frac{\pi D t_{CFRP}}{\pi D^2 / 4} = \frac{4 t_{CFRP}}{D}$$

Equation.  
24

4) Calculate the lateral confinement pressure ( $f_l$ ):

For fully wrapped columns,  $f_l$  can be calculated according to ACI 440.2R-17:11-3 (2017) as reproduced below:

$$f_l = \frac{k_a \rho_f E_f \varepsilon_{fe}}{2} \quad \text{Equation. 25}$$

Where  $k_a$  is the shape efficiency factor ( $k_a = 1$  for circular columns),  $E_f$  is the modulus of elasticity of FRP composites, and  $\varepsilon_{fe}$  is the effective strain in FRP wraps expressed as  $\varepsilon_{fe} = 0.004 < 0.75 \varepsilon_{fu}$ ,  $\varepsilon_{fu} = 0.85 \varepsilon_{ft}$ .

For partially or intermittently wrapped columns,  $f_l$  can be calculated as given in Equations 25 - 27. This formula was initially proposed by Saadamanesh et al. (1994) and frequently used to evaluate the effectiveness of partial wrapping.

$$f_l' = \frac{2f_{us}A_{fs}}{d_s s} \quad \text{Equation. 26}$$

$$K_e = \frac{\left(1 - \frac{s'}{2d_s}\right)^2}{1 - \rho_{cc}} \quad \text{Equation. 27}$$

$$f_l = K_e * f_l' \quad \text{Equation. 28}$$

Where  $k_e$  is the confining pressure efficiency factor,  $\rho_{cc}$  is the steel reinforcement ratio,  $d_s$  is the diameter of the column,  $s'$  is the spacing between FRP straps if intermittent wrapping is used,  $s$  is the width of strap,  $A_{fs}$  is the cross sectional area of the FRP strap, and  $f_{us}$  is the ultimate tensile strength of the FRP strap.

- 5) Calculate the confined compressive strength of concrete ( $f'_{cc}$ ):

According to ACI 440.2R-17: 11-2 (2017), the confined compressive strength  $f'_{cc}$  is given by Equation 28. It is worth noting that in the case of fire-damaged columns,  $f'_c$  should be replaced by  $f'_{cequ}$ .

$$f'_{cc} = f'_c \left( 2.25 \sqrt{1 + 7.9 \frac{f_l}{f'_c}} - 2 \frac{f_l}{f'_c} - 1.25 \right) \quad \text{Equation. 29}$$

- 6) Estimate axial load carrying capacity of CFRP wrapped columns ( $P_r$ ):

Utilizing Equation. 23 and based on ACI 440.2R-17: 12-1 (2017), the capacity of CFRP wrapped columns can be expressed as follows:

$$P_r = 0.85 f'_{cc} (A_c - A_s) + K_{st} f_{yt} A_s \quad \text{Equation. 30}$$

### 10.10 Summary and Conclusions

The effectiveness with which the constant Equivalent Static Force (ESF) values recommended by the *AASHTO-LRFD* bridge design specifications, 600 Kip (2670 KN), represented modeled impact loads was assessed over a range of parameters and a new, empirically based ESF equation was proposed. A Peak Twenty-five Millisecond Moving Average (PTMSA) was employed to estimate ESF for each studied scenario and results were used to estimate ESF for a wide range of vehicle collision scenarios. Equation 16 was obtained and its accuracy examined by comparing calculated ESFs to those obtained from published

studies that examined RC columns subjected to vehicular collisions (Abdelkarim & ElGawady, 2017; Gomez, 2014) and from modeling additional columns under vehicle collisions. Results showed that the proposed equation is reliable and can accurately predict ESFs over a diverse range of collision scenarios. To help with utilization of this equation, an implementation framework was also developed as shown in Figure 10.18.

## Chapter 11 Conclusions and Future Work

### 11.1 Summary

Bridges and their supporting piers, located adjacent to roads passing beneath the bridge and often inadequately protected, are highly susceptible to multi-hazards triggered by vehicle collisions and other correlated and cascading extreme events such as fires and explosions. Recent catastrophic events underscored substantial consequences of the combined effects of these hazards. However, these events are often treated as *Low-Probability – High-Consequence* bridge events. There has subsequently been a lack of research (Giuliani et al., 2012) and bridge design codes do not address these events assuming that. As a result, the performance of bridges and bridge structural components under these combined extreme events remain largely unknown. The goals of this research study were to comprehensively explore performance of substructure units subject to the aforementioned multi-hazards and determine if effective retrofitting schemes could be developed and deployed in lieu of replacement for certain situations.

LS-DYNA three-dimensional finite elements models were used to simulate the behavior of prototype isolated, round, reinforced concrete columns and multi-column piers and an existing bridge in Sidney, NE under coupled vehicle collision and air blast before or after fire. The models included all relevant sub- and superstructure elements, foundations, and surrounding soil and air domains. The research built upon previous studies by integrating fire exposure effects, necessitating development and validation of a unique, multi-step modeling approach that involved uncoupled implicit heat transfer analyses and explicit structural analyses involving impact and blast (Linzell et al., 2020).

Developed FE models were used to complete a number of parametric studies that investigated performance of structural systems over a wide range of design parameters and demand conditions. They were also used to study the feasibility of two in-situ retrofitting

schemes involving CRFP wrap and reinforcement. An empirically based, simplified, equivalent static force equation was also developed using the analytical tools.

## 11.2 Conclusions

Major research findings are summarized in the following sections.

### *11.2.1 Isolated bridge columns*

- Irrespective of loading sequence, damage of bridge columns during a fire-impact-blast event encompassed: (a) shear and flexural surface cracking (M1), (b) concrete cover spalling (M2), (c) plastic hinge formulation (M3), (d) direct shear failure (M4), (e) reinforcement fracturing (M5), and (f) column core breaching (M6). These categorized damage levels are summarized in Table 11.1, with column core breach and direct shear failure produced failure.

Table 11.1 Damage states and corresponding damage categories

Damage State	Superficial	Plastic Hinge	Extensive	Failure
Damage Level	M1 and M2	M1 to M3	M1 to M5	M1 to M6

- Fire prior to impact and blast was found to be a more critical load sequence for the 1050 mm and 1350 mm columns; however, observed damage indicated that, except for the 1050 mm columns under *F90-I-B* and *H90-I-B*, the 1050 mm and 1350 mm columns maintained structural integrity and were deemed repairable for the studied demand scenarios.
- Although all 750 mm diameter columns experienced similar failure modes (i.e., core breach and shear failure) for both load sequences, more pronounced damage, larger

displacements, and lower residual capacities were observed for post impact and blast fire exposures (i.e., I-B-F). Therefore, fire applied after impact and blast was assumed to be the worst-case scenario and indicated that the supported bridge could be susceptible to collapse and, if collapse did not occur, the columns would need to be replaced.

- Table 11.2 summarizes damage levels and performance parameters for all the cases that involved fire happening after impact and blast. As expected, exposing concrete to elevated temperatures prior to impact and blast resulted in more pronounced damage compared to cases in which the studied columns were subjected to impact and blast only, with longer fire durations contributed to more significant damage.
- As indicated in Table 11.2, for any given loading sequence and fire exposure duration, no major variation in residual capacities and displacements for similar column diameters that had half their periphery exposed to fire when compared to those whose entire surface area was exposed. This implies that centroid shifts towards the nonexposed surface of the columns, caused by nonuniform fire exposures, may have produced second order effects that further reduced capacities. This finding could be beneficial in many practical applications where protective tools and retrofit techniques are implemented.

Table 11.2 Isolated columns, post-fire impact and blast performance summary

<b>D (mm)</b>	<b>Load Scenario</b>	<b><math>\gamma_{cs}</math> (%)</b>	<b><math>\gamma_{br}</math> (%)</b>	<b><math>\gamma_{res}</math> (%)</b>	<b><math>\gamma_{sh}</math></b>	<b><math>D_{max}</math></b>	<b>Damage Categories</b>
750	I-B	22	89	18	1.06	317	M1, M2, M5, M6
	H60-I-B	31	100	10	1.38	353	M1, M2, M3, M4, M5, M6
	F60-I-B	34	100	9	1.39	391	M1, M2, M3, M4, M5, M6
	H90-I-B	36	100	5	1.40	478	M1, M2, M3, M4, M5, M6
	F90-I-B	41	100	3	1.41	547	M1, M2, M3, M4, M5, M6
1050	I-B	12	17	25	0.70	106	M1, M2
	H60-I-B	19	27.8	21	0.81	122	M1, M2, M3
	F60-I-B	22	27.8	17	0.83	136	M1, M2, M3, M5
	H90-I-B	26	27.8	16	0.85	165	M1, M2, M3, M5
	F90-I-B	36	33.3	14	0.89	189	M1, M2, M3, M5
1350	I-B	8	10	39	0.60	68	M1, M2
	H60-I-B	14	20	34	0.62	85	M1, M2, M5
	F60-I-B	17	20	32	0.65	94	M1, M2, M5
	H90-I-B	21	20	29	0.67	129	M1, M2, M3, M5
	F90-I-B	24	23	28	0.71	147	M1, M2, M3, M5

- Based on performance assessments and damage parameters employed for this research, columns having diameters of at least 1350 mm are recommended to avoid potential collapse under the studied multi-hazards, as they maintained acceptable structural integrity and were deemed repairable.

### 11.2.2 Multi-column piers

- As expected, the two-column pier was more vulnerable to fire exposure compared to the three- and four-column piers, with shear cracks developed in the non-impacted column and at the interfaces between the columns and cap, and flexural cracks at the mid-span of the pier cap.
- Damage parameters that included permanent sets, final damage states, volume of spalled concrete, and failure patterns demonstrated that two and three-column piers are more vulnerable to the imposed extreme demands compared to the four-column piers.
- No considerable change in pier deflection above non-impact columns was observed for *F90-I-B* in comparison to *I-B*. Two and three-column piers exhibited clear pier deflection discrepancies which were evident above the impacted column, emphasizing potential pier cap failure in that location.
- Extensive repairs are required to restore two and three-column piers to their design capacities, necessitating bridge closure.
- The four-column pier could potentially remain in service while being repaired as most spalling occurred near the impact location and limited reinforcement buckling was observed.

### 11.2.3 Full bridge system

- For a given impact speed, blast scaled distance, and fire exposure condition, damage in bridge encompassed:
  - a. Shear and flexural crack propagation in the slab, pier, and foundation system;
  - b. Concrete cover spalling and longitudinal reinforcement fracturing slab and pier;

- c. Lateral torsional buckling, local flange buckling, and plastic bending in steel girders;
  - d. Direct shear failure coupled with reinforcement fracture at pier column bases;
  - e. Concrete core breaching in the impacted column; and
  - f. Potential bridge collapse.
- While vehicle collision into a single pier column produced localized and potentially repairable damage, exposure to an air blast adjacent to that column produced more pronounced damage that may require full or partial bridge closure.
  - As expected, simulation results demonstrated that *I-B* loading scenarios produced more extensive damage, with the collapse of deck overhang anticipated and direct shear failure observed in the impacted column. Reinforcement fracturing and separation between the middle column and its pier cap and foundation was noted, also indicating shear failure. As a result, bridge closure and significant repairs or complete replacement of the damaged structural elements were anticipated.
  - Complete collapse of the bridge superstructure was observed to be unavoidable with exposure to multi-hazard scenario F90-I-B. Bridge girders experienced permanent sets caused by lateral-torsional buckling and vertical bending. All pier columns were also observed to have failed. Replacement of a significant portion of the bridge or complete replacement would be anticipated.
  - The proposed low-cost retrofitting technique, one that utilized soil infill between support columns, was shown to effectively mitigate structural damage and improve bridge resiliency under the combined effects of impact and air blast. As a result, more

research is justified to further study the influence of various design and analysis parameters on performance.

#### *11.2.4 Retrofitting schemes*

Performance and selected response parameters of isolated columns and columns in multi-column piers retrofitted using the most effective schemes under *F90-I-B* are summarized in Table 11.3. It is worth noting that the presented displacements, kinetic energies, and residual capacities are relative to those obtained from the baseline, fire-damaged, bare columns under impact and blast.

Table 11.3 Performance of CFRP retrofitted columns, F90-I-B

Column Diameter (mm)	750 mm			1050 mm			1350 mm		
	W-9L	HH-9L	12R22-3L	W-9L	HH-9L	12R22-3L	W-9L	HH-9L	12R22-3L
Column Damage	Minor	Moderate	Severe	Minor	Minor	Moderate	Minor	Minor	Minor
Column Displacement	Decreased 62%	Decreased 58%	Decreased 56%	Decreased 65%	Decreased 61%	Decreased 52%	Decreased 75%	Decreased 73%	Decreased 67%
Kinetic Energy	Decreased 64%	Decreased 61%	Decreased 59%	Decreased 73%	Decreased 64%	Decreased 67%	Decreased 71%	Decreased 68%	Decreased 68%
Residual Capacity	Increased 55%	Increased 43%	Increased 45%	Increased 51%	Increased 42%	Increased 35%	Increased 44%	Increased 32%	Increased 25%
Spalled Concrete	Decreased 48%	Decreased 44%	Decreased 34%	Decreased 33%	Decreased 29%	Decreased 21%	Decreased 22%	Decreased 17%	Decreased 13%
Recommendations	<ul style="list-style-type: none"> <li>Full or half height CFRP wrapping with 1.5 mm total thickness.</li> </ul>			<ul style="list-style-type: none"> <li>Full or half height CFRP wrapping with 1.5 mm total thickness.</li> <li>Hybrid repair with at least 1% reinforcement ratio and 0.5 mm wrap thickness.</li> </ul>			<ul style="list-style-type: none"> <li>Full or half height CFRP wrapping with 1.5 mm total thickness.</li> <li>Hybrid repair with at least 1% reinforcement ratio and 0.5 mm wrap thickness.</li> </ul>		

Other major findings are:

- When CFRP wrapping was implemented, no significant performance difference was noted when wrap thickness increased from 1.5 mm to 2.0 mm for *W-9L* and *W-12L*, respectively, which indicated that the 1.5 mm thickness was sufficient to alleviate effects of prescribed impact and blast demands. As a result, *W-9L* was recommended. It was also noted that by using this retrofitting scheme, all columns were assumed to remain in operational after repair except for *W-3L*.
- For the hybrid retrofitting scheme, more distinct performance improvement and damage mitigation was noticeable when thicker CFRP wraps were utilized. No pronounced concrete spalling mitigation and crack intensity reduction was noticed when reinforcement ratio increased for the same CFRP wrap thickness.
- Partially wrapping columns with HH-9L and I1000-9L as deemed an efficient and cost-effective option to mitigate displacements, kinetic energies, and concrete spalling resulting from impact and blast.
- For multi-column piers, investigations of proposed retrofitting schemes demonstrated that:
  1. CRFP wrap along the entire height of the fire-damaged columns was more effective at mitigating damage resulting from impact and blast compared to the cases that involved partial and intermittent wrapping. However, resulting concrete spalling and lateral displacement indicated that wrapping the bottom third of the columns could be potentially used as an economically feasible option.

2. Increasing the wrap thickness has a more predominant effect on damage mitigation compared to using near surface mounted CFRP longitudinal reinforcements.
3. Incorporating hybrid retrofitting techniques may not be advisable due to its associated cost, challenging practical implementation, and limited impact on concrete spalling and surface cracking.

#### *11.2.5 ESF predictive equation and advised assessment framework*

The effectiveness with which the constant Equivalent Static Force (ESF) values recommended by the *AASHTO-LRFD* bridge design specifications, 600 Kip (2670 KN), represented modeled impact loads was assessed over a range of parameters and a new, empirically based ESF equation was proposed. A Peak Twenty-five Millisecond Moving Average (PTMSA) was employed to estimate ESF for each studied scenario and results were used to estimate ESF for a wide range of vehicle collision scenarios investigated. Equation 16 was obtained, and its accuracy examined by comparing calculated ESFs to those obtained from published studies that examined RC columns subjected to vehicular collisions (Abdelkarim & ElGawady, 2017; Gomez, 2014) and from modeling additional columns under vehicle collisions. Results showed that the proposed equation is reliable and can accurately predict ESFs over a diverse range of collision scenarios. To help with utilization of this equation, an implementation framework was also developed as shown in Figure 10.18. Major findings of this study are:

- For the parameters that were studied and modeling approach that was used, vehicle speed and mass most significantly influenced impact forces.
- *AASHTO-LRFD* underestimated ESF for 41% of the studied cases. These results envelope collisions by the Ford F800 SUT at 120 km/h for:

- Intact columns with diameters greater than 750 mm.
  - Fire-damaged columns with diameters greater than 1050 mm and fire exposures of more than 60 minutes.
  - 1050-mm diameter and larger fully wrapped columns with  $t_{CFRP}$  greater than or equal to 1.5 mm.
  - 1050-mm diameter and larger intact and CFRP wrapped columns shorter than 5.4 m.
  - 1050-mm diameter and larger intact and CFRP wrapped columns with  $f'_c$  greater than 34.5 MPa.
  - 1050-mm diameter and larger intact and CFRP wrapped columns with  $\rho$  greater than 2%.
- *AASHTO-LRFD* was shown to conservatively predicts ESFs for collisions involving the light Toyota Yaris and medium Dodge Ram vehicles for:
    - Speeds less than 120 km/h.
    - Columns with diameters smaller than 1050 mm and heights greater than 5.4 m.
    - Bare fire-damaged columns, columns with  $f'_c$  smaller than or equal to 34.5 MPa.
    - Columns with reinforcement ratios less than or equal to 2%.
    - Fully wrapped columns with  $t_{CFRP}$  less than 1.5 mm, and partially wrapped columns.

- When columns are exposed to fire prior to impact, AASHTO-LRFD was found to be non-conservative under the same impact energy stated above for all columns larger than 1050 mm and fire durations shorter than 90 minutes.
- Results demonstrated that 1050 mm diameter columns are susceptible for shear failure under heavy vehicle impact. This finding is noteworthy given that the current AASHTO-LRFD specifications identified vulnerability to impact only for 750 mm diameter columns.

### 11.3 Recommendations for Future Work

Looking forward, future research could be directed towards innovative protection techniques, recommended design and analysis provisions, and advanced assessment tools and predictive models. In this context, potential future research areas could include:

#### 1. Short-term, expanded investigations

- To comprehensively explore the response of bridge columns to wide range of vehicle collisions, fires, and air blasts, it is imperative to conduct full-scale experimental tests encompassing diverse loading scenarios.
- Conducting experimental testing of concrete, steel, and FRP materials under the combined effects of extreme temperatures and high loading rate scenarios.
- A more in-depth study to examine the effects of various bridge and column configurations on the fire-collision-blast resistance needs to be considered.
- Considering the infrequent occurrence of combined fire, vehicle collision, and air blast, it is essential to employ reliability analysis methodologies. By assessing and quantifying uncertainties related to material behavior and structural response, reliability analysis enhances the robustness of bridge pier designs, ensuring their

resilience against extreme events and contributing significantly to the overall safety and stability of critical infrastructure.

- Conducting a more realistic fire analysis by utilizing specialized software and existing data derived from past bridge fire incidents.
- The previous points could be eventually utilized in revising bridge design codes to incorporate the effects of fire and multi-hazards in their design and analysis provisions. By updating the codes to encompass these aspects, engineers and designers can ensure the structural integrity of bridges under a wide range of extreme conditions, to ensure public safety and maintain infrastructure integrity.
- Exploring the potential applications and further refinement of the developed predictive Equivalent Static Force (ESF) model stands as a promising avenue for future research.

## 2. Long-term, innovative research areas

- Expanding the study to include more comprehensive analyses that integrate the effects of fire, vehicle impact, and air blast in a seamless manner. This could involve integrated computational fluid dynamics and machine learning algorithms.
- Exploring advanced materials, such as ultra-high-strength and high-performance concrete, self-healing concrete, and fiber-reinforced concrete, that could enhance the resilience of bridge systems under multi-hazards is highly recommended.
- Utilizing real-time structural health monitoring and reliability analysis would offer a continuous and comprehensive assessment of structural performance under multi-hazard events. This can involve advanced sensing technologies and data harvesting techniques.

- Incorporating innovative protective devices into bridge design strategies represents a critical area for future exploration. These advanced technologies, ranging from impact-absorbing materials to intelligent sensor systems, have the potential to significantly enhance bridge resilience.

## References

- AASHTO. (2003). *Manual for condition evaluation and load and resistance factor rating (LRFR) of highway bridges*. American Association of State Highway and Transportation Officials, Washington DC.
- AASHTO. (2020). *AASHTO LRFD Bridge Design Specifications, 9th Edition*. AASHTO.
- AASHTO LRFD. (2020). *Bridge Design Specifications, 9th edition*. American Association of State Highway and Transportation Officials (AASHTO), Washington, DC.
- Abdelkarim, O. I., & ElGawady, M. A. (2017). Performance of bridge piers under vehicle collision. *Engineering Structures*, *140*, 337–352.
- ACI 440.1R-15. (2015). *Guide for the Design and Construction of Structural Concrete Reinforced with FRP Bars*. ACI.
- ACI 440.2R-17. (2017). *Guide for the Design and Construction of Externally Bonded FRP Systems for Strengthening Concrete Structures*. ACI.
- Agrawal, A. K., Liu, G. Y., & Alampalli, S. (2013). Effects of truck impacts on bridge piers. *Advanced Materials Research*, *639*, 13–25.
- Al-Kamaki, Y. S., Al-Mahaidi, R., & Bennetts, I. (2015). Experimental and numerical study of the behaviour of heat-damaged RC circular columns confined with CFRP fabric. *Composite Structures*, *133*, 679–690.
- Al-Nimry, H., Haddad, R., Afram, S., & Abdel-Halim, M. (2013). Effectiveness of advanced composites in repairing heat-damaged RC columns. *Materials and Structures*, *46*(11), 1843–1860.
- Al-Nimry, H. S., & Ghanem, A. M. (2017). FRP confinement of heat-damaged circular RC columns. *International Journal of Concrete Structures and Materials*, *11*(1), 115–133.
- Alomari, Q. A., & Linzell, D. G. (2022). Bridge pier column multi-hazard response—fire, impact and blast. In *Bridge Safety, Maintenance, Management, Life-Cycle, Resilience and Sustainability* (pp. 2276–2284). CRC Press.
- Alomari, Q. A., & Linzell, D. G. (2024). Reinforced Concrete Bridge Column Multihazard Performance: A Computational Tool to Assess Response to Vehicle Impact, Air Blast, and Fire. *Journal of Performance of Constructed Facilities*, *38*(1), 04023061.
- Alos-Moya, J., Paya-Zaforteza, I., Garlock, M. E. M., Loma-Ossorio, E., Schiffner, D., & Hospitaler, A. (2014). Analysis of a bridge failure due to fire using computational fluid dynamics and finite element models. *Engineering Structures*, *68*, 96–110.
- ASCE, A. S. of C. E. (1992). *ASCE, Structural Fire Protection*. ASCE Committee on Fire Protection, Structural Division.

- Ashteyat, A. M., Obaidat, Y. T., Al-Btoush, A. Y., & Hanandeh, S. (2021). Experimental and numerical study of strengthening and repairing heat-damaged RC circular column using hybrid system of CFRP. *Case Studies in Construction Materials*, 15, e00742.
- ASTM, E. (2007). 119, Standard Test Methods for Fire Tests of Building Construction and Materials. *1995 Annual Book of ASTM Standards*, 4, 436.
- AuYeung, S., & Alipour, A. (2016). Evaluation of AASHTO suggested design values for reinforced concrete bridge piers under vehicle collisions. *Transportation Research Record*, 2592(1), 1–8.
- Auyeung, S., Alipour, A., & Saini, D. (2019). Performance-based design of bridge piers under vehicle collision. *Engineering Structures*, 191, 752–765.
- Bank, L. C. (2006). *Composites for construction: Structural design with FRP materials*. John Wiley & Sons.
- Bao, X., & Li, B. (2010). Residual strength of blast damaged reinforced concrete columns. *International Journal of Impact Engineering*, 37(3), 295–308.  
<https://doi.org/10.1016/j.ijimpeng.2009.04.003>
- Baylot, J. T., Bullock, B., Slawson, T. R., & Woodson, S. C. (2005). Blast response of lightly attached concrete masonry unit walls. *Journal of Structural Engineering*, 131(8), 1186–1193.
- Buchanan, A. H., & Abu, A. K. (2017). *Structural design for fire safety*. John Wiley & Sons.
- Bulwa, D., & Fimrite, P. (2007). Tanker fire destroys part of MacArthur maze. *San Francisco Chronicle*, 29.
- Buth, C. E., Brackin, M. S., Williams, W. F., & Fry, G. T. (2011). *Collision loads on bridge piers: Phase 2, report of guidelines for designing bridge piers and abutments for vehicle collisions*. Texas Transportation Institute.
- Buth, C. E., Williams, W. F., Brackin, M. S., Lord, D., Geedipally, S. R., & Abu-Odeh, A. Y. (2010). *Analysis of large truck collisions with bridge piers: Phase 1, report of guidelines for designing bridge piers and abutments for vehicle collisions*. Texas Transportation Institute.
- Cardone, J. (2023, June). Birmingham’s ‘Malfunction Junction’ is no stranger to emergency bridge repairs. *CBS News*.
- Carrigan, C. E., & Ray, M. H. (2017). *Assessment of the MASH Heavy Vehicle Weights for Field Relevancy*.
- Castellano, A. J., Caltagirone, J. P., Sock, F. E., & Dobbs, N. (1982). *Structures to Resist the Effects of Accidental Explosions (TM 5-1300, NAVFAC P-397, AFM 88-22). Revision of*

- Chen, L., Fang, Q., Jiang, X., Ruan, Z., & Hong, J. (2015). Combined effects of high temperature and high strain rate on normal weight concrete. *International Journal of Impact Engineering*, 86, 40–56.
- Chen, W., Guo, Z., Zhang, T., Zou, H., & Gu, J. (2016). Near-field blast test on reactive powder concrete-filled steel tubular columns after exposure to fire. *International Journal of Protective Structures*, 7(2), 193–212.
- Chen, W., Pan, J., Guo, Z., & Zou, H. (2019). Damage evaluations of fire-damaged RPC-FST columns under blast loading. *Thin-Walled Structures*, 134, 319–332.
- Chen, W., Zhou, Z., Zou, H., & Guo, Z. (2018). Predictions of residual carrying-capacities for fire and near-field blast-damaged reactive powder concrete-filled steel tube columns. *International Journal of Protective Structures*, 9(4), 525–553.
- Chinthapalli, H. K., Chellapandian, M., Agarwal, A., & Prakash, S. S. (2019). *EMERGENCY REPAIR OF SEVERELY DAMAGED REINFORCED CONCRETE COLUMN UNDER FIRE: AN EXPERIMENTAL STUDY*.
- Chinthapalli, H. K., Chellapandian, M., Agarwal, A., & Prakash, S. S. (2020). Effectiveness of hybrid fibre-reinforced polymer retrofitting on behaviour of fire damaged RC columns under axial compression. *Engineering Structures*, 211, 110458.
- Chiple, M. (2003). *Reference Manual to Mitigate Potential Terrorist Attacks Against Buildings: Providing Protection to People and Building*. Federal Emergency Management Agency.
- Choi, S.-J., Lee, S.-W., & Kim, J.-H. J. (2017). Impact or blast induced fire simulation of bi-directional PSC panel considering concrete confinement and spalling effect. *Engineering Structures*, 149, 113–130.
- Choo, C. C., Harik, I. E., & Gesund, H. (2006a). Minimum reinforcement ratio for fiber-reinforced polymer reinforced concrete rectangular columns. *ACI Structural Journal*, 103(3), 460.
- Choo, C. C., Harik, I. E., & Gesund, H. (2006b). Strength of rectangular concrete columns reinforced with fiber-reinforced polymer bars. *ACI Materials Journal*, 103(3), 452.
- Chopra, A. K. (2007). *Dynamics of structures*. Pearson Education India.
- Chung, P., Wolfe, R. W., Ostrom, T., & Hida, S. (2008). Accelerated bridge construction applications in California—A lessons learned report. *USA: California Department of Transportation (CALTRANS)*.

- Coughlin, A. M., Musselman, E. S., Schokker, A. J., & Linzell, D. G. (2010). Behavior of portable fiber reinforced concrete vehicle barriers subject to blasts from contact charges. *International Journal of Impact Engineering*, 37(5), 521–529.
- Cowper, G. R., & Symonds, P. S. (1957). *Strain-hardening and strain-rate effects in the impact loading of cantilever beams*. Brown Univ Providence Ri.
- Day, J. (2009). *Guidelines for ale modelling in ls-dyna*. Technical report, Livermore Software Technology Corporation.
- de Borst, R., & Peeters, P. P. (1989). Analysis of concrete structures under thermal loading. *Computer Methods in Applied Mechanics and Engineering*, 77(3), 293–310.
- Deleo, F. R., & Feraboli, P. (2011). *Crashworthiness energy absorption of carbon fiber composites: Experiment and simulation* [PhD Thesis]. University of Washington.
- Department of Defense. (2008). *Structures to resist the effects of accidental explosions*. Washington, DC: Unified Facilities Criteria.
- Ding, Y., Wang, M., Li, Z.-X., & Hao, H. (2013). Damage evaluation of the steel tubular column subjected to explosion and post-explosion fire condition. *Engineering Structures*, 55, 44–55.
- Echevarria, A., Zaghi, A. E., Chiarito, V., Christenson, R., & Woodson, S. (2016). Experimental Comparison of the Performance and Residual Capacity of CFFT and RC Bridge Columns Subjected to Blasts. *Journal of Bridge Engineering*, 21(1), 04015026. [https://doi.org/10.1061/\(ASCE\)BE.1943-5592.0000762](https://doi.org/10.1061/(ASCE)BE.1943-5592.0000762)
- El-Tawil, S., Severino, E., & Fonseca, P. (2005). Vehicle collision with bridge piers. *Journal of Bridge Engineering*, 10(3), 345–353.
- Eurocode 1, E. 1991-1-1. (2002). *Eurocode 1: Actions on Structures. Part 1-1: General Actions-Densities, Self-Weight, Imposed Loads for Buildings*.
- Eurocode 1, (European Committee for Standardization). (2006). *Eurocode 1: Actions on structures—Part 1-7: General actions—Accidental actions*.
- Eurocode 2. (2004). *Eurocode 2: Design of concrete structures—Part 1-2: General rules—Structural fire design*. CEN Brussels.
- Eurocode 3. (2007). *Eurocode 3: Design of Steel Structures-Part 1-2: General Rules-Structural Fire Design*. London: European Committee for Standardisation.
- Fang, C. (2020). *Structural Resilience and Hardening of Bridge Piers and Pier Columns Against Vehicle Collision and Blast Loads*. The University of Nebraska-Lincoln.
- Fang, C., Alomari, Q. A., & Linzell, D. G. (2023, May). ASSESSMENT OF BRIDGE PIER RESPONSE TO FIRE, VEHICLEIMPACT, AND AIR BLAST. *International*

*Conference on Protective Structures (ICPS 2023)*. International Conference on Protective Structures (ICPS 2023), Auburn University, USA.

- Fang, C., Linzell, D. G., Yosef, T. Y., & Rasmussen, J. D. (2022). Numerical Modeling and Performance Assessment of Bridge Column Strengthened by FRP and Polyurea under Combined Collision and Blast Loading. *Journal of Composites for Construction*, 26(2), 04022002.
- Fang, C., Yosef, T. Y., Linzell, D. G., & Rasmussen, J. D. (2021a). Computational modeling and dynamic response of highway bridge columns subjected to combined vehicle collision and air blast. *Engineering Failure Analysis*, 125, 105389.
- Fang, C., Yosef, T. Y., Linzell, D. G., & Rasmussen, J. D. (2021b). Computational modeling and dynamic response of highway bridge columns subjected to combined vehicle collision and air blast. *Engineering Failure Analysis*, 125, 105389.
- Fang, C., Yosef, T. Y., Linzell, D. G., & Rasmussen, J. D. (2021c). Residual axial capacity estimates for bridge columns subjected to combined vehicle collision and air blast. *Journal of Bridge Engineering*, 26(7), 04021035.
- FHWA, F. H. (1995). Recording and coding guide for the structure inventory and appraisal of the nation's bridges. In *Rep. No. FHWA-PD-96-001*. US Dept. of Transportation Washington, DC.
- Fletcher, I., Welch, S., Torero, J., Carvel, R., & Usmani, A. (2007). Behaviour of concrete structures in fire. *Thermal Science*, 11(2), 37–52. <https://doi.org/10.2298/TSCI0702037F>
- Fujikura, S., Bruneau, M., & Lopez-Garcia, D. (2008). Experimental Investigation of Multihazard Resistant Bridge Piers Having Concrete-Filled Steel Tube under Blast Loading. *Journal of Bridge Engineering*, 13(6), 586–594. [https://doi.org/10.1061/\(ASCE\)1084-0702\(2008\)13:6\(586\)](https://doi.org/10.1061/(ASCE)1084-0702(2008)13:6(586))
- Garlock, M., Paya-Zaforteza, I., Kodur, V., & Gu, L. (2012). Fire hazard in bridges: Review, assessment and repair strategies. *Engineering Structures*, 35, 89–98.
- Giuliani, L., Crosti, C., & Gentili, F. (2012). Vulnerability of bridges to fire. *Proceedings of the 6th International Conference on Bridge Maintenance, Safety and Management*, 8–12.
- Gomez, N. L. (2014). *Performance of circular reinforced concrete bridge piers subjected to vehicular collisions*.
- Gomez, N. L., & Alipour, A. (2014). Study of circular reinforced concrete bridge piers subjected to vehicular collisions. *Structures Congress 2014*, 577–587.
- Grote, D. L., Park, S. W., & Zhou, M. (2001). Dynamic behavior of concrete at high strain rates and pressures: I. experimental characterization. *International Journal of Impact Engineering*, 25(9), 869–886.

- Guo, Z., Chen, W., Zhang, Y., & Zou, H. (2017). Post fire blast-resistances of RPC-FST columns using improved Grigorian model. *International Journal of Impact Engineering*, 107, 80–95.
- Guthrie, D., Goodwill, V., & Hicks, M. (2009). Tanker fire shuts down I-75, collapses Nine Mile bridge. *The Detroit News*.
- Hallquist, J. O. (2014). LS-DYNA® keyword user's manual: Volumes I, II, and III LSDYNA R7. 1. *Livermore Software Technology Corporation, Livermore (LSTC), Livermore, California, 1265*.
- Harik, I. E., Shaaban, A. M., Gesund, H., Valli, G. Y. S., & Wang, S. T. (1990). United States bridge failures, 1951–1988. *Journal of Performance of Constructed Facilities*, 4(4), 272–277.
- Hollaway, L. C., & Teng, J.-G. (2008). *Strengthening and rehabilitation of civil infrastructures using fibre-reinforced polymer (FRP) composites*. Elsevier.
- Hurley, M. J., Gottuk, D. T., Hall Jr, J. R., Harada, K., Kuligowski, E. D., Puchovsky, M., Watts Jr, J. M., & WIECZOREK, C. J. (2015). *SFPE handbook of fire protection engineering*. Springer.
- Islam, M. T., & Singh, E. A. (2019). Study of behavior of RCC beam under impact loading and effect of hourglass energy by finite element analysis using ANSYS. *IJERT*, 8(07), 2278–0181.
- ISO, I. (1999). 834: Fire resistance tests-elements of building construction. *International Organization for Standardization, Geneva, Switzerland*.
- Jiang, F. C., Zhu, C. M., & Xue, J. S. (2007). Nonlinear analysis of load-carrying capacity for bar buckling based on arc-length method. *Build Sci*, 23(11), 9–12.
- Jin, L., Bai, J., Zhang, R., Li, L., & Du, X. (2021). Effect of elevated temperature on the low-velocity impact performances of reinforced concrete slabs. *International Journal of Impact Engineering*, 149, 103797. <https://doi.org/10.1016/j.ijimpeng.2020.103797>
- Kadhom, B. (2016). *Blast performance of reinforced concrete columns protected by FRP laminates* [PhD Thesis]. Université d'Ottawa/University of Ottawa.
- Kakogiannis, D., Pascualena, F., Reymen, B., Pyl, L., Ndambi, J. M., Segers, E., Lecompte, D., Vantomme, J., & Krauthammer, T. (2013). Blast performance of reinforced concrete hollow core slabs in combination with fire: Numerical and experimental assessment. *Fire Safety Journal*, 57, 69–82.
- Khalik, W., & Kodur, V. (2012). High Temperature Mechanical Properties of High-Strength Fly Ash Concrete with and without Fibers. *ACI Materials Journal*, 109(6).

- Khoury, G. A. (2000). Effect of fire on concrete and concrete structures. *Progress in Structural Engineering and Materials*, 2(4), 429–447.
- Kim, J. H., Kim, C. K., Islam, M. S., Park, S. I., & Paik, J. K. (2013). A study on methods for fire load application with passive fire protection effects. *Ocean Engineering*, 70, 177–187.
- Kimura, H., Itabashi, M., & Kawata, K. (2001). Mechanical characterization of unidirectional CFRP thin strip and CFRP cables under quasi-static and dynamic tension. *Advanced Composite Materials*, 10(2–3), 177–187.
- Kodur, V. (2014). Properties of Concrete at Elevated Temperatures. *ISRN Civil Engineering*, 2014, 1–15. <https://doi.org/10.1155/2014/468510>
- Kodur, V., & Bhatt, B. (2016). Strategies for mitigating fire hazard in tunnel structures. *The 6th International Workshop on Structural Life Management of Power Structures. Daejeon: KEPCO-RI*.
- Kodur, V., Gu, L., & Garlock, M. E. M. (2010). Review and assessment of fire hazard in bridges. *Transportation Research Record*, 2172(1), 23–29.
- Kodur, V., Hibner, D., & Agrawal, A. (2017). Residual response of reinforced concrete columns exposed to design fires. *Procedia Engineering*, 210, 574–581.
- Kodur, V. K. R., Garlock, M., & Iwankiw, N. (2012). Structures in fire: State-of-the-art, research and training needs. *Fire Technology*, 48(4), 825–839.
- Kodur, V. K. R., Raut, N. K., Mao, X. Y., & Khaliq, W. (2013). Simplified approach for evaluating residual strength of fire-exposed reinforced concrete columns. *Materials and Structures*, 46, 2059–2075.
- Kodur, V., & Naser, M. Z. (2021). Fire hazard in transportation infrastructure: Review, assessment, and mitigation strategies. *Frontiers of Structural and Civil Engineering*, 15(1), 46–60.
- Koneshwaran, S., Thambiratnam, D. P., & Gallage, C. (2015). Blast response of segmented bored tunnel using coupled SPH–FE method. *Structures*, 2, 58–71.
- Kwaśniewski, L., Ali, F., & Balcerzak, M. (2013). Coupled structural-thermal calculations for restrained steel columns in fire. *Journal of Structural Fire Engineering*.
- Lee, G. C., Mohan, S. B., Huang, C., & Fard, B. N. (2013). *Technical Report MCEER-13-008: A Study of US Bridge Failures (1980-2012)*. University at Buffalo (SUNY).
- Lewis, B. A. (2004). *Manual for LS-DYNA soil material model 147*. United States. Federal Highway Administration.

- Li, X., Zhang, R., Jin, L., & Du, X. (2021). Numerical analysis of axial compressive behavior of RC short columns subjected to non-uniform fire: A meso-scale study. *E3S Web of Conferences*, 272, 02028.
- Li, Y. Z., & Ingason, H. (2010). Maximum ceiling temperature in a tunnel fire. *SP Report*, 51.
- Li, Z.-X., Zhang, X., Shi, Y., Wu, C., & Li, J. (2021). Finite element modeling of FRP retrofitted RC column against blast loading. *Composite Structures*, 263, 113727.
- Lie, T. T., & Erwin, R. J. (1993). Method to calculate the fire resistance of reinforced concrete columns with rectangular cross section. *ACI Structural Journal*, 90(1), 52–60.
- Lie, T.T. & Denham, E.M.A. (1993). Factors affecting the fire resistance of circular hollow steel columns filled with barereinforced concrete. *NRC-CNRC Internal Report, No.651*.
- Lin, Y., Zong, Z., Bi, K., Hao, H., Lin, J., & Chen, Y. (2020). Experimental and numerical studies of the seismic behavior of a steel-concrete composite rigid-frame bridge subjected to the surface rupture at a thrust fault. *Engineering Structures*, 205, 110105.
- Linzell, D. G., Fang, C., & Alomari, Q. A. (2020). *Protecting Critical Civil Infrastructure Against Impact from Commercial Vehicles—Phase II*. Mid-America Transportation Center, UNL.
- Liu, G. (2012). *Behavior of bridge piers during vehicular impacts* [PhD Thesis]. City University of New York.
- Liu, L., Feng, H., Tang, H., & Guan, Z. (2018). Impact resistance of Nomex honeycomb sandwich structures with thin fibre reinforced polymer facesheets. *Journal of Sandwich Structures & Materials*, 20(5), 531–552.
- Lu, W., Mäkeläinen, P., Outinen, J., & Ma, Z. (2012). *Investigation of Behavior of Cold-formed Steel Sheeting Systems in Fire Using Finite Element Modeling*.
- Ma, Z., Havula, J., & Heinisuo, M. (2019). Structural fire analysis of simple steel structures by using LS-DYNA explicit solver. *Rakenteiden Mekaniikka*, 52(1), 1–22.
- Maghiar, M., Jackson, M., & Maldonado, G. (2017). *Warning systems evaluation for overhead clearance detection*. Georgia Southern University.
- Malvar, L. J. (1998). Review of static and dynamic properties of steel reinforcing bars. *Materials Journal*, 95(5), 609–616.
- Malvar, L. J., & Crawford, J. E. (1998). *Dynamic increase factors for concrete*. Naval Facilities Engineering Service Center Port hueneme CA.
- Mazars, J. (1987). Description of the behaviour of composite concretes under complex loadings through continuum damage mechanics. *American Society of Mechanical Engineers*, 135–139.

- Meng, F.-Q., Zhu, M.-C., Clifton, G. C., Ukanwa, K. U., & Lim, J. B. (2020). Performance of square steel-reinforced concrete-filled steel tubular columns subject to non-uniform fire. *Journal of Constructional Steel Research*, 166, 105909.
- Michael, W., William, W., & Brian, L. (2013). Fire risks for highway bridges: A statistical investigation. *Structures Congress 2013: Bridging Your Passion with Your Profession- Proceedings of the 2013 Structures Congress*, 744–757.
- Miele, C. R., Plaxico, C. A., Kennedy, J. C., Simunovic, S., & Zisi, N. (2005). Heavy vehicle infrastructure asset interaction and collision. *National Transportation Research Center, Knoxville, TN*.
- Moftah, M. (2008). *Numerical modelling and performance of reinforced concrete members under fire condition* [PhD Thesis]. School of Graduate and Postdoctoral Studies, University of Western Ontario.
- Mohan, P., Marzougui, D., & Kan, C. D. (2007). Validation of a single unit truck model for roadside hardware impact. *International Journal of Vehicle Systems Modelling and Testing*, 2(1), 1–15.
- Murray, Y. D. (2007). *Users manual for LS-DYNA concrete material model 159*. U.S. Department of Transportation.
- Murray, Y. D. (2004). Theory and evaluation of concrete material model 159. *8th International LS-DYNA Users Conference*.
- Murray, Y. D., Abu-Odeh, A. Y., & Bligh, R. P. (2007). *Evaluation of LS-DYNA concrete material model 159*. United States. Federal Highway Administration. Office of Research  
....
- Muszynski, L. C., & Purcell, M. R. (2003). Use of composite reinforcement to strengthen concrete and air-entrained concrete masonry walls against air blast. *Journal of Composites for Construction*, 7(2), 98–108.
- Mutalib, A. A., & Hao, H. (2011). Numerical analysis of FRP-composite-strengthened RC panels with anchorages against blast loads. *Journal of Performance of Constructed Facilities*, 25(5), 360–372.
- Nahid, M. N. (2015). *Computational study of highway bridges structural response exposed to a large fire exposure* [PhD Thesis]. Virginia Tech.
- Nam, J.-W., Kim, H.-J., Kim, S.-B., Yi, N.-H., & Kim, J.-H. J. (2010). Numerical evaluation of the retrofit effectiveness for GFRP retrofitted concrete slab subjected to blast pressure. *Composite Structures*, 92(5), 1212–1222.
- Naser, M. Z., & Kodur, V. K. R. (2015). A probabilistic assessment for classification of bridges against fire hazard. *Fire Safety Journal*, 76, 65–73.

- NFPA. (2017). *NFPA 502: Standard for road tunnels, bridges, and other limited access highways*. National Fire Protection Association Quincy, MA.
- O'Hare, E. V. (2011). *Computational assessment of steel-jacketed bridge pier column performance under blast loads*.
- Ožbolt, J., Ruta, D., & Irhan, B. (2019). Numerical study of reinforced concrete slabs under extreme loading conditions: Impact and fire. *IOP Conference Series: Materials Science and Engineering*, 615, 012012. <https://doi.org/10.1088/1757-899X/615/1/012012>
- Pahlaviani, A. G., Rousta, A. M., & Beiranvand, P. (2020). Investigation of the effect of impact load on concrete-filled steel tube columns under fire. *Frattura Ed Integrità Strutturale*, 14(54), 317–324.
- Peris-Sayol, G., Paya-Zaforteza, I., Alós-Moya, J., & Hospitaler, A. (2015). Analysis of the influence of geometric, modeling and environmental parameters on the fire response of steel bridges subjected to realistic fire scenarios. *Computers & Structures*, 158, 333–345.
- Peris-Sayol, G., Paya-Zaforteza, I., Balasch-Parisi, S., & Alós-Moya, J. (2017). Detailed analysis of the causes of bridge fires and their associated damage levels. *Journal of Performance of Constructed Facilities*, 31(3), 04016108.
- Petrini, F., Gkoumas, K., Rossi, C., & Bontempi, F. (2020). Multi-hazard assessment of bridges in case of hazard chain: State of play and application to vehicle-pier collision followed by fire. *Frontiers in Built Environment*, 6, 580854.
- Pham, T. M., & Hao, H. (2016). Impact behavior of FRP-strengthened RC beams without stirrups. *Journal of Composites for Construction*, 20(4), 04016011.
- Pham, T. M., Zhang, X., Elchalakani, M., Karrech, A., Hao, H., & Ryan, A. (2018). Dynamic response of rubberized concrete columns with and without FRP confinement subjected to lateral impact. *Construction and Building Materials*, 186, 207–218.
- Qin, D., Gao, P., Aslam, F., Sufian, M., & Alabduljabbar, H. (2021). A comprehensive review on fire damage assessment of reinforced concrete structures. *Case Studies in Construction Materials*, e00843.
- Quiel, S. E., Yokoyama, T., Bregman, L. S., Mueller, K. A., & Marjanishvili, S. M. (2015). A streamlined framework for calculating the response of steel-supported bridges to open-air tanker truck fires. *Fire Safety Journal*, 73, 63–75.
- Rackauskaite, E., Flint, G., Maani, A., Temple, A., & Kotsovinos, P. (2019). *Use of LS-DYNA for Structural Fire Engineering*. 8.
- Rackauskaite, E., Kotsovinos, P., & Rein, G. (2017). Model parameter sensitivity and benchmarking of the explicit dynamic solver of LS-DYNA for structural analysis in case of fire. *Fire Safety Journal*, 90, 123–138. <https://doi.org/10.1016/j.firesaf.2017.03.002>

- Raut, N., & Kodur, V. (2012). Behavior of circular reinforced concrete columns under fire conditions. *Journal of Structural Fire Engineering*.
- Razaqpur, A. G., Tolba, A., & Contestabile, E. (2007). Blast loading response of reinforced concrete panels reinforced with externally bonded GFRP laminates. *Composites Part B: Engineering*, 38(5–6), 535–546.
- Reese, L., Qiu, T., Linzell, D., O'hare, E., & Rado, Z. (2014). Field tests and numerical modeling of vehicle impacts on a boulder embedded in compacted fill. *International Journal of Protective Structures*, 5(4), 435–451.
- Reid, J. D., Coon, B. A., Lewis, B. A., Sutherland, S. H., & Murray, Y. D. (2004). *Evaluation of LS-DYNA soil material model 147*. United States. Federal Highway Administration.
- Ross, C. A., Purcell, M. R., & Jerome, E. L. (1997). Blast response of concrete beams and slabs externally reinforced with fiber reinforced plastics (FRP). *Building to Last*, 673–677.
- Roy, S., Unobe, I., & Sorensen, A. D. (2021). Vehicle-Impact Damage of Reinforced Concrete Bridge Piers: A State-of-the Art Review. *Journal of Performance of Constructed Facilities*, 35(5), 03121001.
- Roy, T., & Matsagar, V. (2021). Multi-hazard analysis and design of structures: Status and research trends. *Structure and Infrastructure Engineering*, 1–30.
- Ruan, Z., Chen, L., & Fang, Q. (2015). Numerical investigation into dynamic responses of RC columns subjected for fire and blast. *Journal of Loss Prevention in the Process Industries*, 34, 10–21.
- Ruta, D. (2018a). *Numerical and experimental study of concrete structures exposed to impact and fire*.
- Ruta, D. (2018b). *Numerical and experimental study of concrete structures exposed to impact and fire*.
- Saadatmanesh, H., Ehsani, M. R., & Li, M.-W. (1994). Strength and ductility of concrete columns externally reinforced with fiber composite straps. *Structural Journal*, 91(4), 434–447.
- Saetta, A., Scotta, R., & Vitaliani, R. (1995). Stress analysis of concrete structures subjected to variable thermal loads. *Journal of Structural Engineering*, 121(3), 446–457.
- Sami, A. (2021). 3. Effectiveness of External CFRP Wrapping on the Structural Behavior of Damaged FRP-RC Spiral Columns. *1ST INTERNATIONAL CONFERENCE ON RECENT ADVANCES IN CIVIL AND EARTHQUAKE ENGINEERING (ICCEE-2021)–OCT 08, 2021*, 8.

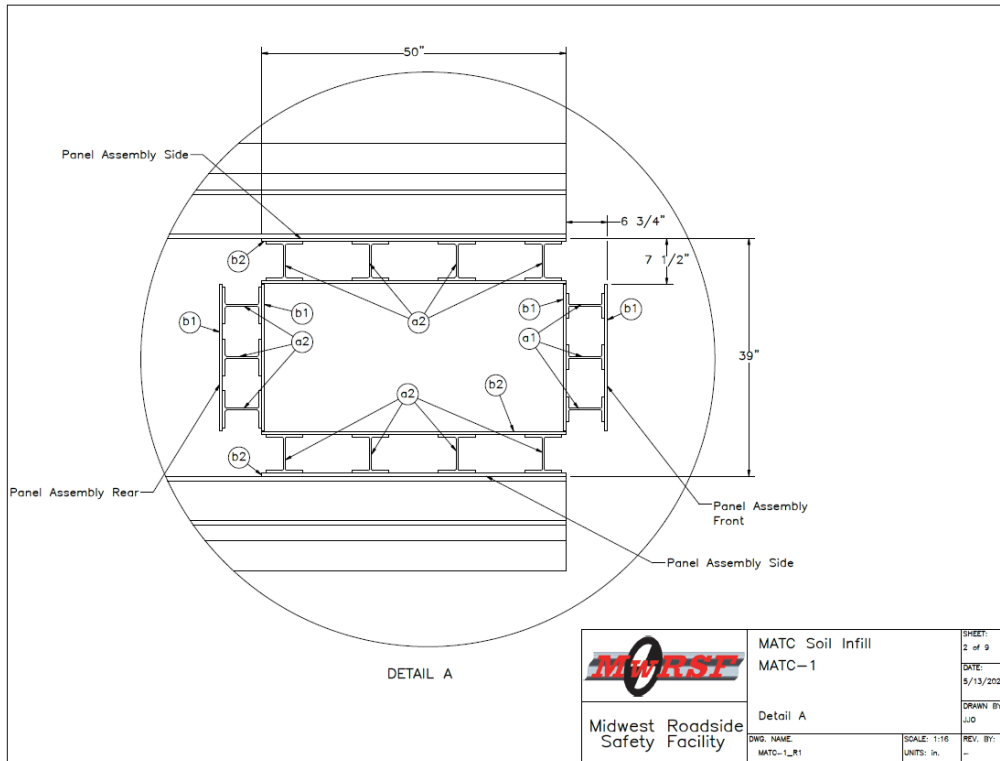
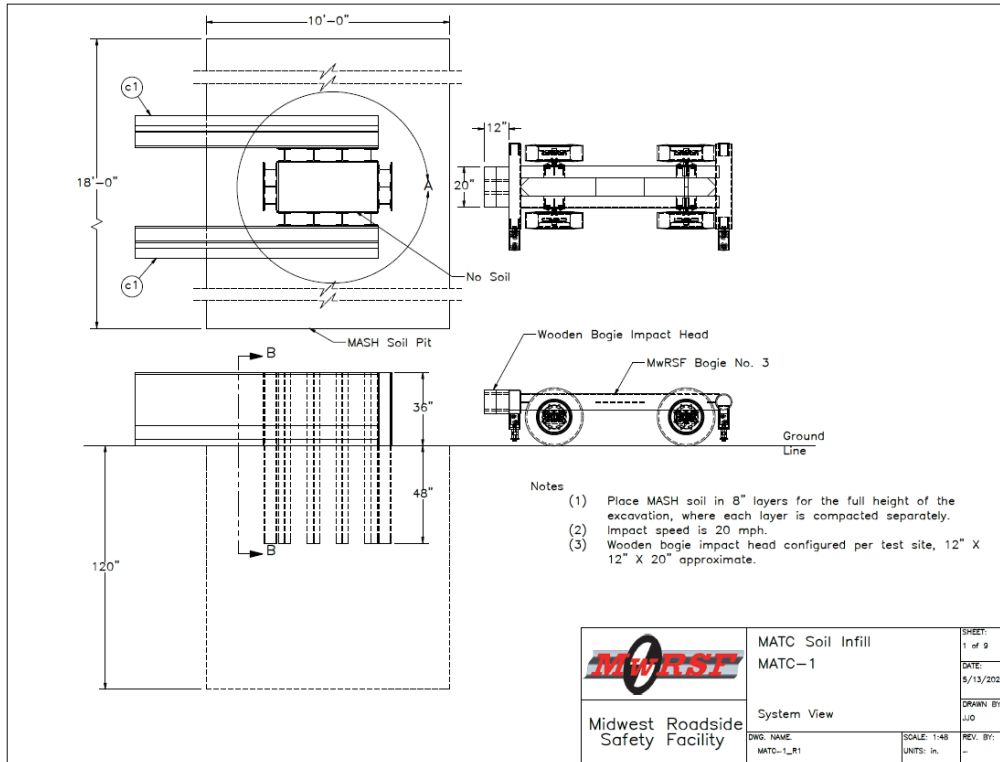
- Sayed-Ahmed, E. Y. (2006). Numerical investigation into strengthening steel I-section beams using CFRP strips. *Structures Congress 2006: Structural Engineering and Public Safety*, 1–8.
- Šelešovský, J., & Krupka, M. (2007). The using of LS-DYNA for the simulation of heat transfer in explosives. *Journal of Computer-Aided Materials Design*, 14(2), 317–325. <https://doi.org/10.1007/s10820-007-9046-0>
- Sha, Y., & Hao, H. (2015). Laboratory tests and numerical simulations of CFRP strengthened RC pier subjected to barge impact load. *International Journal of Structural Stability and Dynamics*, 15(02), 1450037.
- Shapiro, A. B. (2005). Heat transfer in LS-DYNA. *5th European LS-DYNA Users Conference New Applications and Developments*.
- Sharma, H., Gardoni, P., & Hurlbauss, S. (2015). Performance-based probabilistic capacity models and fragility estimates for RC columns subject to vehicle collision. *Computer-Aided Civil and Infrastructure Engineering*, 30(7), 555–569.
- Sharma, H., Hurlbauss, S., & Gardoni, P. (2012). Performance-based response evaluation of reinforced concrete columns subject to vehicle impact. *International Journal of Impact Engineering*, 43, 52–62.
- Stochino, F., & Tattoni, S. (2013). Exceptional Actions: Blast Loads on Reinforced Concrete Structures. *Proceedings of CIAS (Cornell International Affairs Society) Conference*.
- Su, H., Xu, J., & Ren, W. (2014). Experimental study on the dynamic compressive mechanical properties of concrete at elevated temperature. *Materials & Design (1980-2015)*, 56, 579–588.
- Sudeep, K., & Rao, V. N. (2019). *Structures to Resist the Effects of the Accidental Explosions*.
- Surech, K., & Regalla, S. P. (2014). Effect of time scaling and mass scaling in numerical simulation of incremental forming. *Applied Mechanics and Materials*, 612, 105–110.
- Tang, E. K. C., & Hao, H. (2010). Numerical simulation of a cable-stayed bridge response to blast loads, Part I: Model development and response calculations. *Engineering Structures*, 32(10), 3180–3192. <https://doi.org/10.1016/j.engstruct.2010.06.007>
- Tapan, M., & Aboutaha, R. S. (2008). Strength evaluation of deteriorated RC bridge columns. *Journal of Bridge Engineering*, 13(3), 226–236.
- Tebor, C., & Sottile, Z. (2023, June 11). Section of major I-95 highway in Philadelphia that collapsed after tanker truck caught fire underneath could take months to repair, officials say. *CNN*.
- Tilloy, A., Malamud, B. D., Winter, H., & Joly-Laugel, A. (2019). A review of quantification methodologies for multi-hazard interrelationships. *Earth-Science Reviews*, 196, 102881.

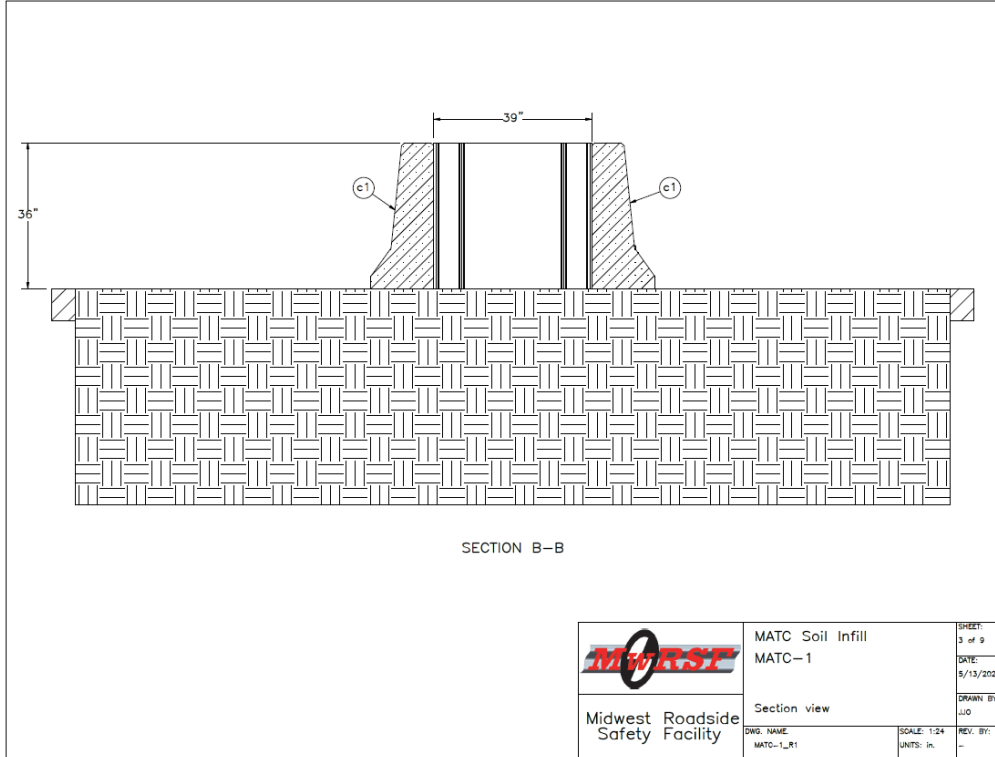
- Timilsina, S., Yazdani, N., & Beneberu, E. (2021). Post-fire analysis and numerical modeling of a fire-damaged concrete bridge. *Engineering Structures*, 244, 112764.
- Ulm, F.-J., Coussy, O., & Bažant, Z. P. (1999). The “Chunnel” fire. I: Chemoplastic softening in rapidly heated concrete. *Journal of Engineering Mechanics*, 125(3), 272–282.
- U.S Department of Transportation. (2013). *Single-Unit Straight Trucks in Traffic Crashes*. NHTSA’s National Center for Statistics and Analysis.
- Wang, W., Wu, C., & Li, J. (2018). Numerical simulation of hybrid FRP-concrete-steel double-skin tubular columns under close-range blast loading. *Journal of Composites for Construction*, 22(5), 04018036.
- Wardhana, K., & Hadipriono, F. C. (2003). Analysis of recent bridge failures in the United States. *Journal of Performance of Constructed Facilities*, 17(3), 144–150.
- Wassef, W. G., Smith, C., Clancy, C. M., & Smith, M. J. (2003). *Comprehensive Design Example for Prestressed Concrete (PSC) Girder Superstructure Bridge with Commentary (in SI Units)*. United States. Federal Highway Administration.
- Wehbe, N. I., Qin, X., Tigges, B., Shen, Z., & Boudaqa, A. (2017). *Evaluation and Mitigation of Vehicle Impact Hazard for Overpasses*. South Dakota State University.
- Wickström, U. (1986). *A very simple method for estimating temperature in fire exposed concrete structures*.
- Williams, G. D. (2009). *Analysis and response mechanisms of blast-loaded reinforced concrete columns* [PhD Thesis].
- Williamson, E. B. (2010). *Blast-resistant highway bridges: Design and detailing guidelines* (Vol. 645). Transportation Research Board.
- Williamson, E. B., Bayrak, O., Davis, C., & Williams, G. D. (2011). Performance of Bridge Columns Subjected to Blast Loads. I: Experimental Program. *Journal of Bridge Engineering*, 16(6), 693–702. [https://doi.org/10.1061/\(ASCE\)BE.1943-5592.0000220](https://doi.org/10.1061/(ASCE)BE.1943-5592.0000220)
- Winget, D. G. (2003). *Design of critical bridges for security against terrorist attacks* [PhD Thesis]. University of Texas at Austin.
- Woodworth, M. A. (2013). *Fire hazard assessment for highway bridges with thermal mechanical modeling* [PhD Thesis]. Virginia Polytechnic Institute and State University.
- Wright, W., Lattimer, B., Woodworth, M., Nahid, M., & Sotelino, E. (2013). Highway bridge fire hazard assessment draft final report. *Virginia Polytechnic Institute and State University, Blacksburg, Va.*

- Wu, K.-C., Li, B., & Tsai, K.-C. (2011). Residual axial compression capacity of localized blast-damaged RC columns. *International Journal of Impact Engineering*, 38(1), 29–40. <https://doi.org/10.1016/j.ijimpeng.2010.09.002>
- Wu, X., Huang, T., Au, F. T. K., & Li, J. (2020). A localized fire model for predicting the surface temperature of box girder bridges subjected to tanker truck fire. *Fire Technology*, 56(5), 2059–2087.
- Xu, J. J., Demartino, C., Shan, B., Heo, Y. A., & Xiao, Y. (2020). Experimental investigation on performance of cantilever CFRP-wrapped circular RC columns under lateral low-velocity impact. *Composite Structures*, 242, 112143.
- Yang, H., Han, L.-H., & Wang, Y.-C. (2008). Effects of heating and loading histories on post-fire cooling behaviour of concrete-filled steel tubular columns. *Journal of Constructional Steel Research*, 64(5), 556–570.
- Yang, H., Liu, F., & Gardner, L. (2013). Performance of concrete-filled RHS columns exposed to fire on 3 sides. *Engineering Structures*, 56, 1986–2004.
- Yang, H., Liu, F., Zhang, S., & Lv, X. (2013). Experimental investigation of concrete-filled square hollow section columns subjected to non-uniform exposure. *Engineering Structures*, 48, 292–312.
- Yaqub, M., & Bailey, C. G. (2011). Repair of fire damaged circular reinforced concrete columns with FRP composites. *Construction and Building Materials*, 25(1), 359–370.
- Yi, Z., Agrawal, A. K., Ettouney, M., & Alampalli, S. (2014a). Blast load effects on highway bridges. I: Modeling and blast load effects. *Journal of Bridge Engineering*, 19(4), 04013023.
- Yi, Z., Agrawal, A. K., Ettouney, M., & Alampalli, S. (2014b). Blast load effects on highway bridges. II: Failure modes and multihazard correlations. *Journal of Bridge Engineering*, 19(4), 04013024.
- Zhai, C., Chen, L., Xiang, H., & Fang, Q. (2016). Experimental and numerical investigation into RC beams subjected to blast after exposure to fire. *International Journal of Impact Engineering*, 97, 29–45.

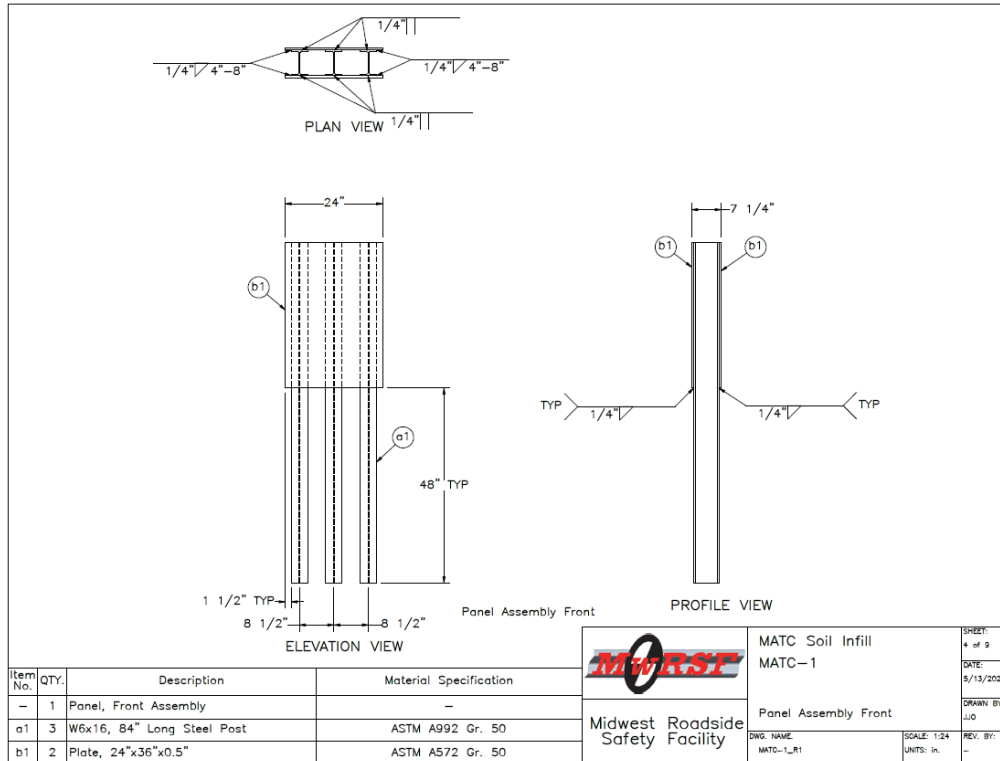
# Appendix A

System designs and test plans are provided in Figures



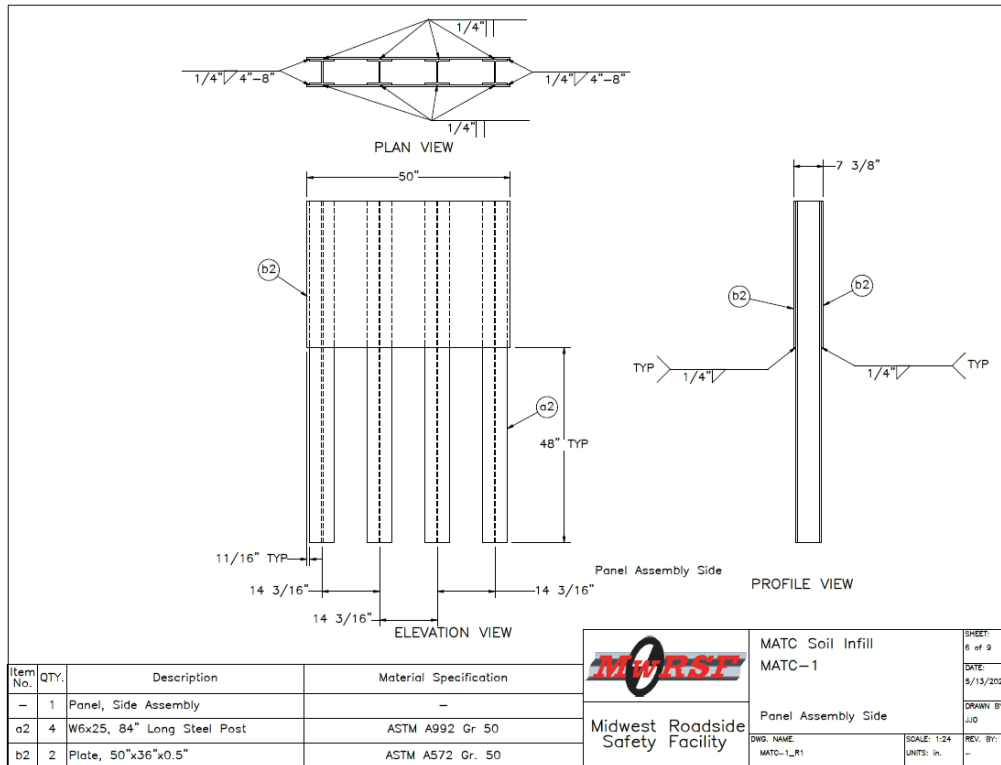
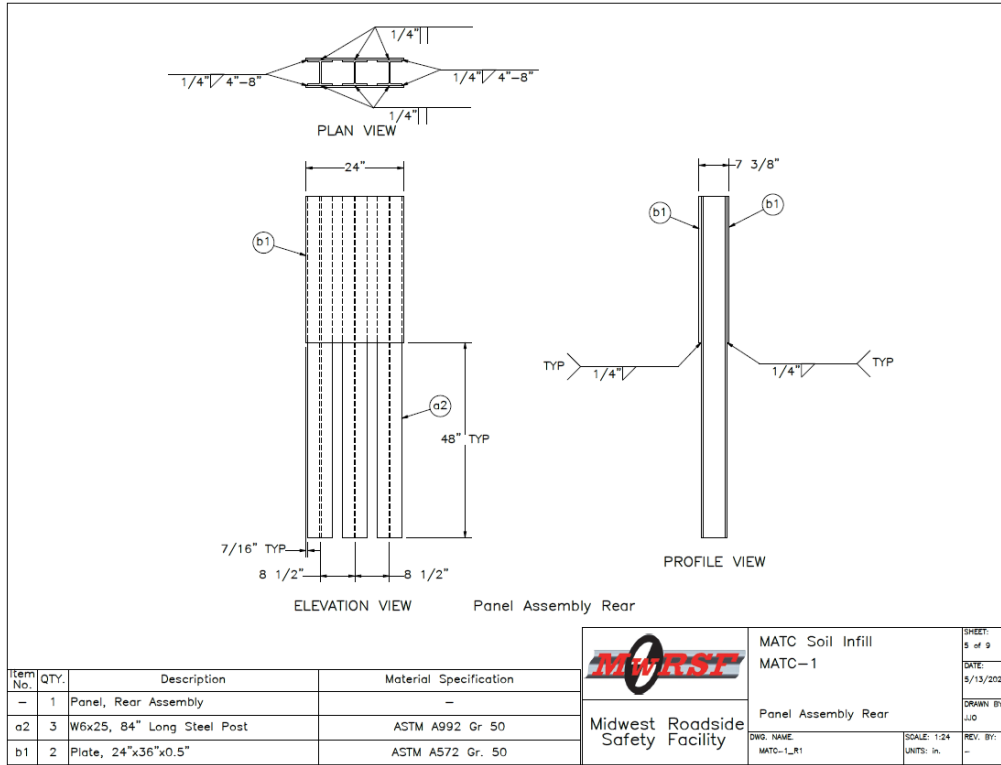


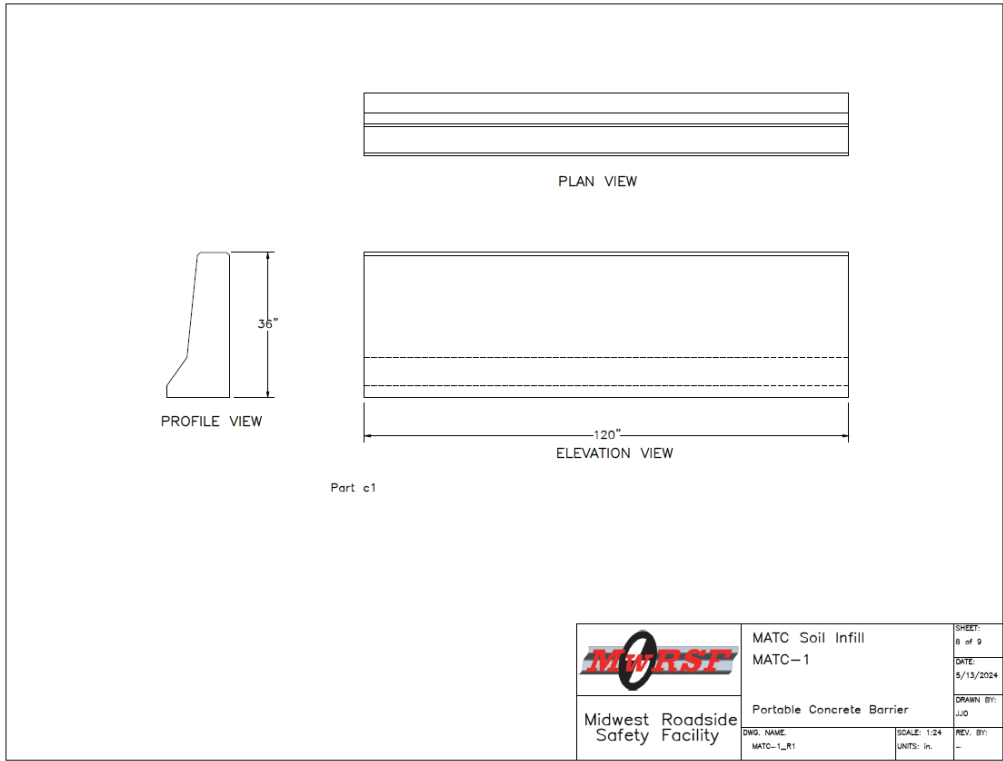
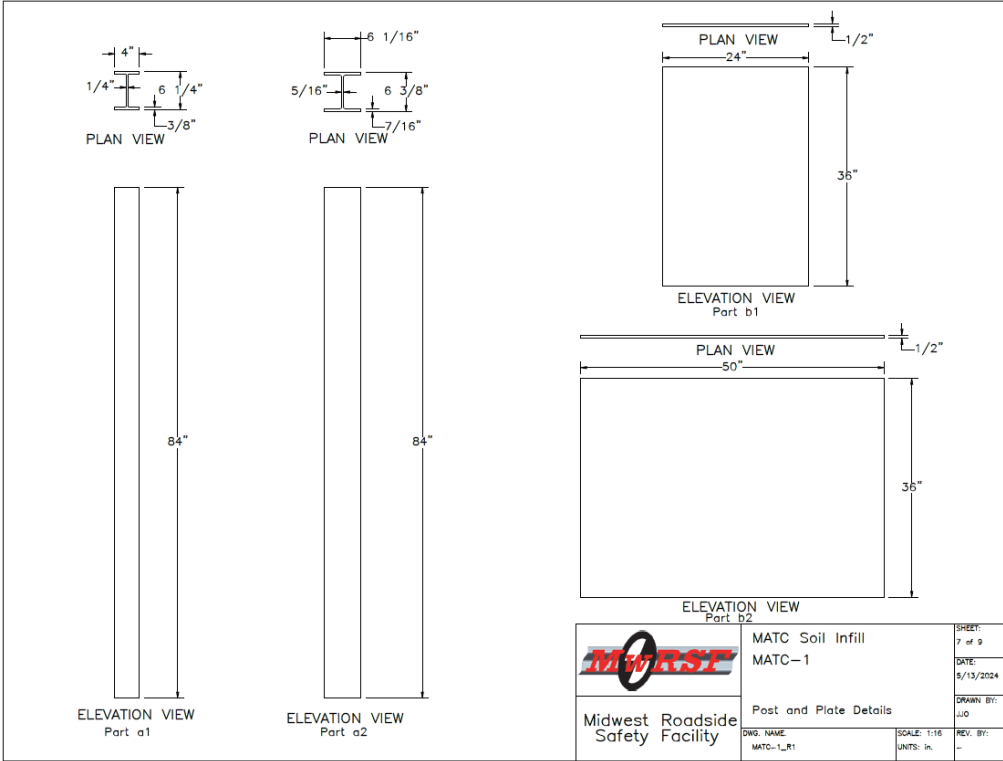
	MATC Soil Infill MATC-1	SHEET: 3 of 9
	Section view	DATE: 5/13/2024
Midwest Roadside Safety Facility	DWG. NAME: MATC-1_R1	DRAWN BY: JJO
	SCALE: 1:24 UNITS: in.	REV. BY: -



	MATC Soil Infill MATC-1	SHEET: 4 of 9
	Panel Assembly Front	DATE: 5/13/2024
Midwest Roadside Safety Facility	DWG. NAME: MATC-1_R1	DRAWN BY: JJO
	SCALE: 1:24 UNITS: in.	REV. BY: -

Item No.	QTY.	Description	Material Specification
-	1	Panel, Front Assembly	-
a1	3	W6x16, 84" Long Steel Post	ASTM A992 Gr. 50
b1	2	Plate, 24"x36"x0.5"	ASTM A572 Gr. 50





Item No.	QTY.	Description	Material Specification
a1	3	W6x16, 84" Long Steel Post	ASTM A992 Gr. 50
a2	11	W6x25, 84" Long Steel Post	ASTM A992 Gr. 50
b1	4	Plate, 24"x36"x0.5"	ASTM A572 Gr. 50
b2	4	Plate, 50"x36"x0.5"	ASTM A572 Gr. 50
c1	2	PCB	Concrete
d1	1	MASH Soil	MASH Soil

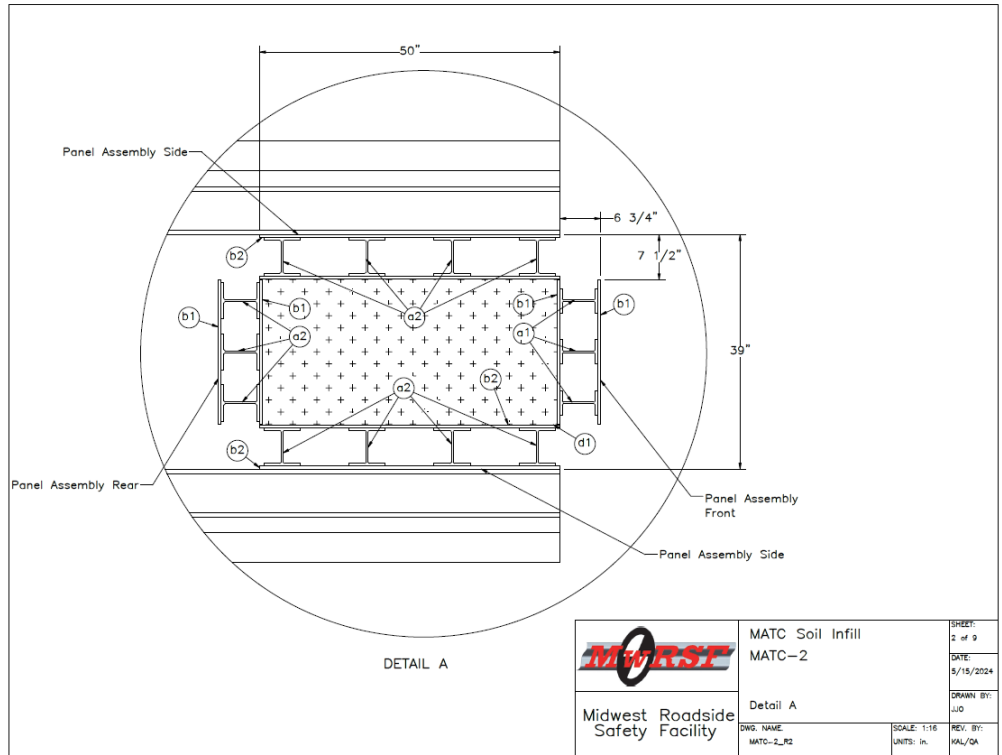
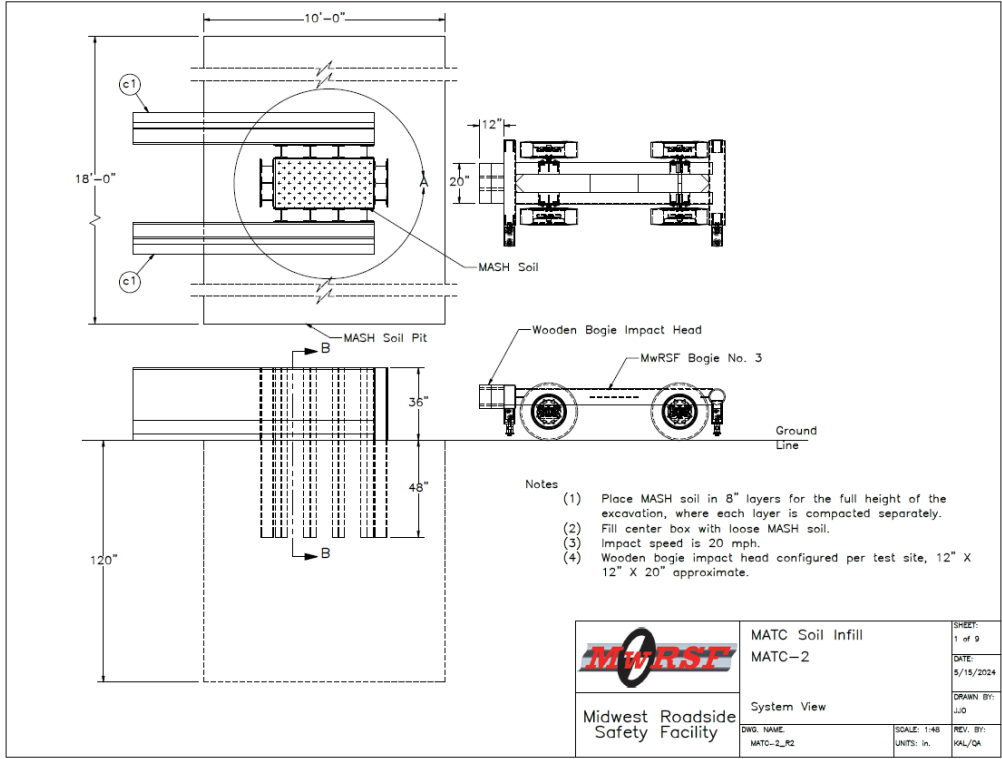
 Midwest Roadside Safety Facility	MATC Soil Infill MATC-1	SHEET: 9 of 9
	Bill of material	DATE: 5/13/2024
DWSL NAME: MATC-1_R1	SCALE: 1:128 UNITS: in.	DRAWN BY: JJO REV. BY:

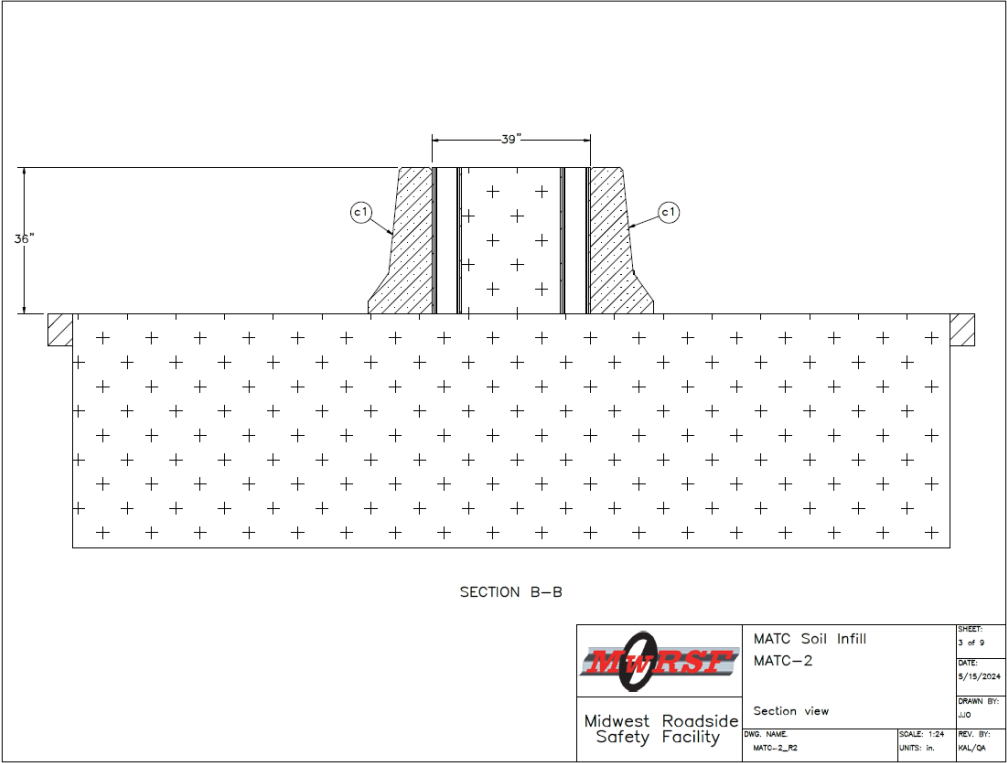




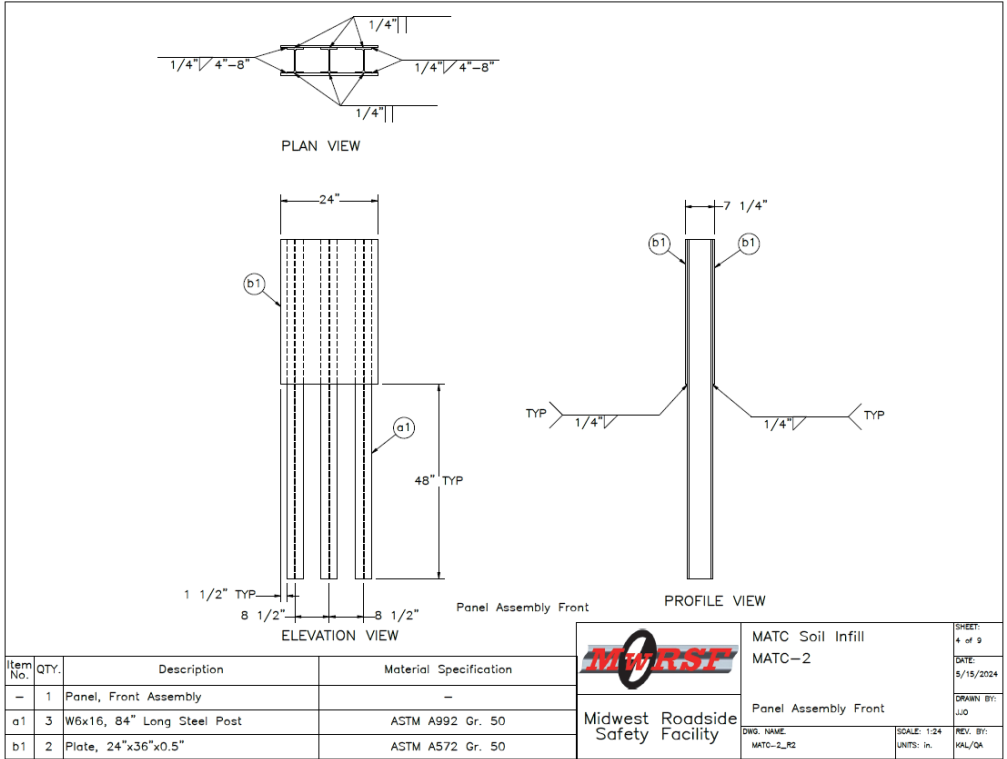






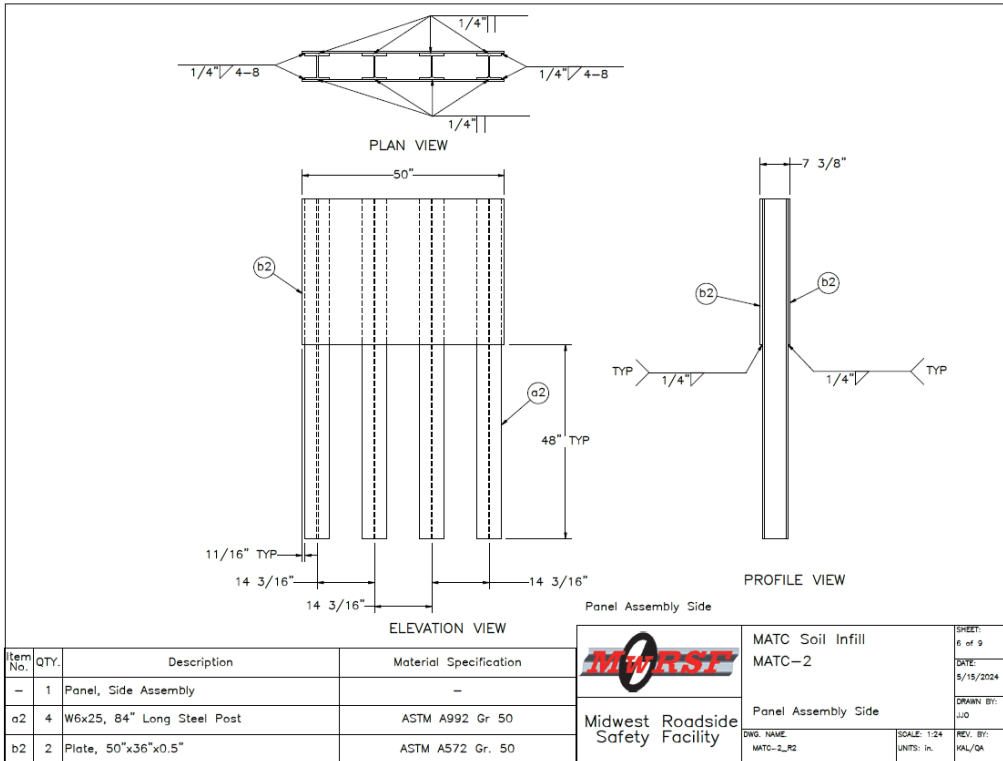
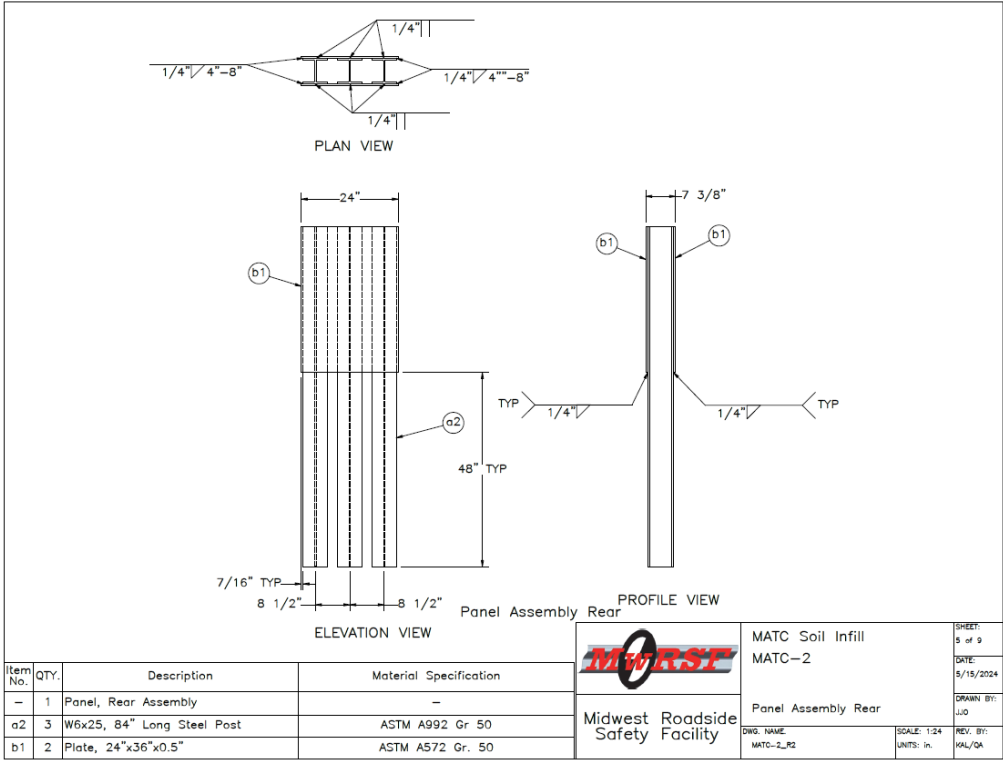


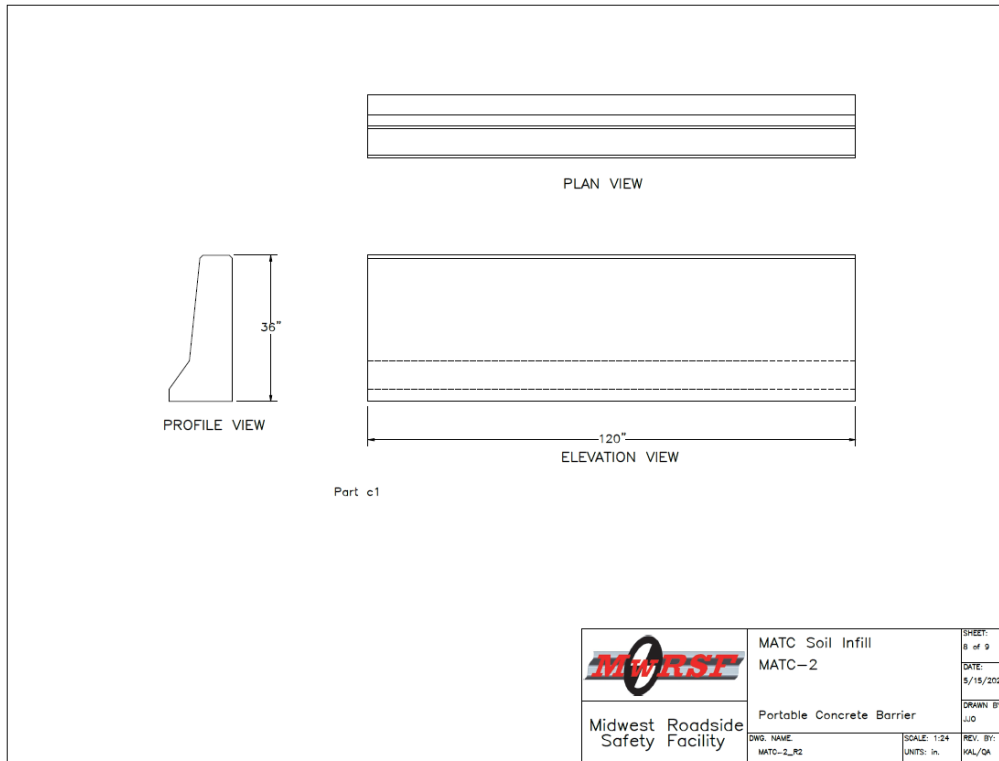
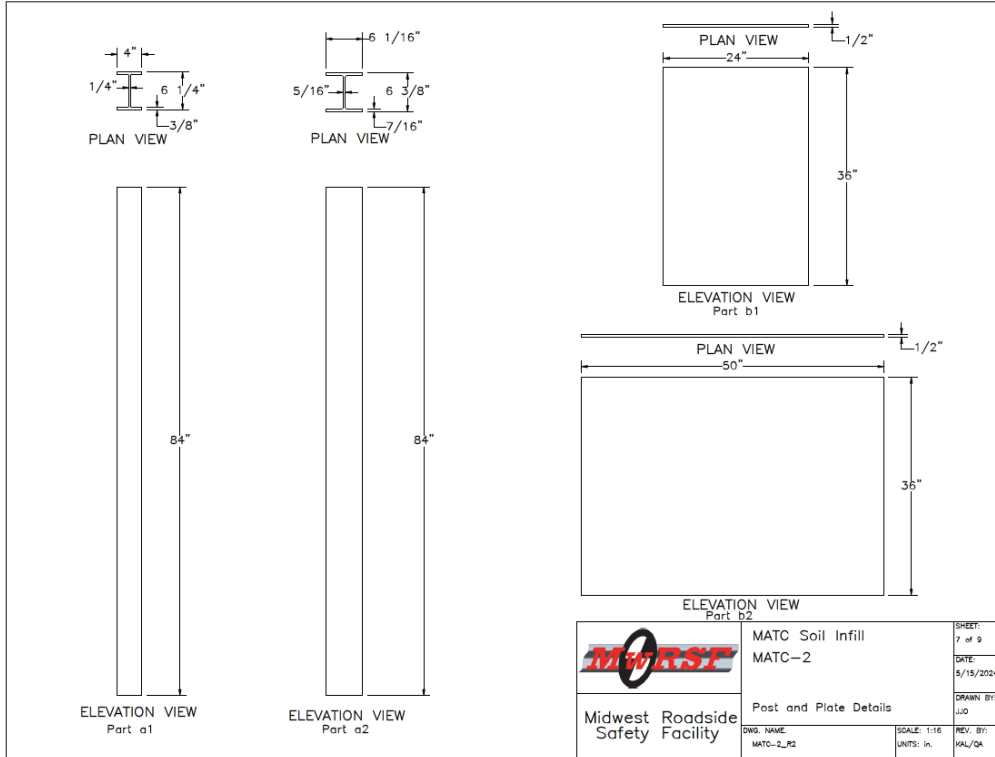
 Midwest Roadside Safety Facility	MATC Soil Infill MATC-2	SHEET: 3 of 9
	Section view	DATE: 5/15/2024
	DWG. NAME: MATC-2_R2	DRAWN BY: JJO
	SCALE: 1:24 UNITS: In.	REV. BY: KAL/GA



Item No.	QTY.	Description	Material Specification
-	1	Panel, Front Assembly	-
a1	3	W6x16, 84" Long Steel Post	ASTM A992 Gr. 50
b1	2	Plate, 24"x36"x0.5"	ASTM A572 Gr. 50

 Midwest Roadside Safety Facility	MATC Soil Infill MATC-2	SHEET: 4 of 9
	Panel Assembly Front	DATE: 5/15/2024
	DWG. NAME: MATC-2_R2	DRAWN BY: JJO
	SCALE: 1:24 UNITS: In.	REV. BY: KAL/GA





Item No.	QTY.	Description	Material Specification
a1	3	W6x16, 84" Long Steel Post	ASTM A992 Gr. 50
a2	11	W6x25, 84" Long Steel Post	ASTM A992 Gr. 50
b1	4	Plate, 24"x36"x0.5"	ASTM A572 Gr. 50
b2	4	Plate, 50"x36"x0.5"	ASTM A572 Gr. 50
c1	2	PCB	Concrete
d1	1	MASH Soil	MASH Soil

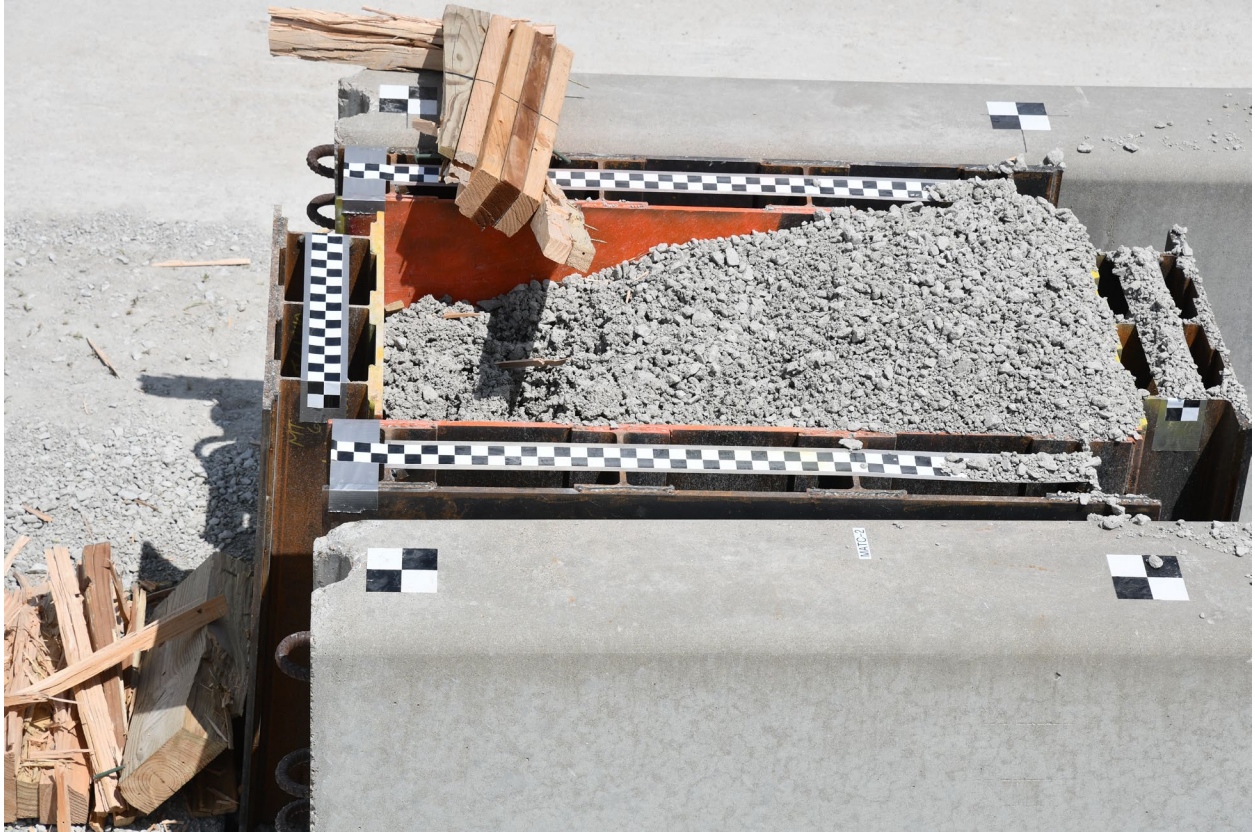
  

	MATC Soil Infill	SHEET: 9 of 9
	MATC-2	DATE: 5/15/2024
Midwest Roadside Safety Facility	Bill of material	DRAWN BY: JJO
	DWG. NAME: MATC-2_R2	SCALE: 1:120 UNITS: in.
		REV. BY: KAL/QA

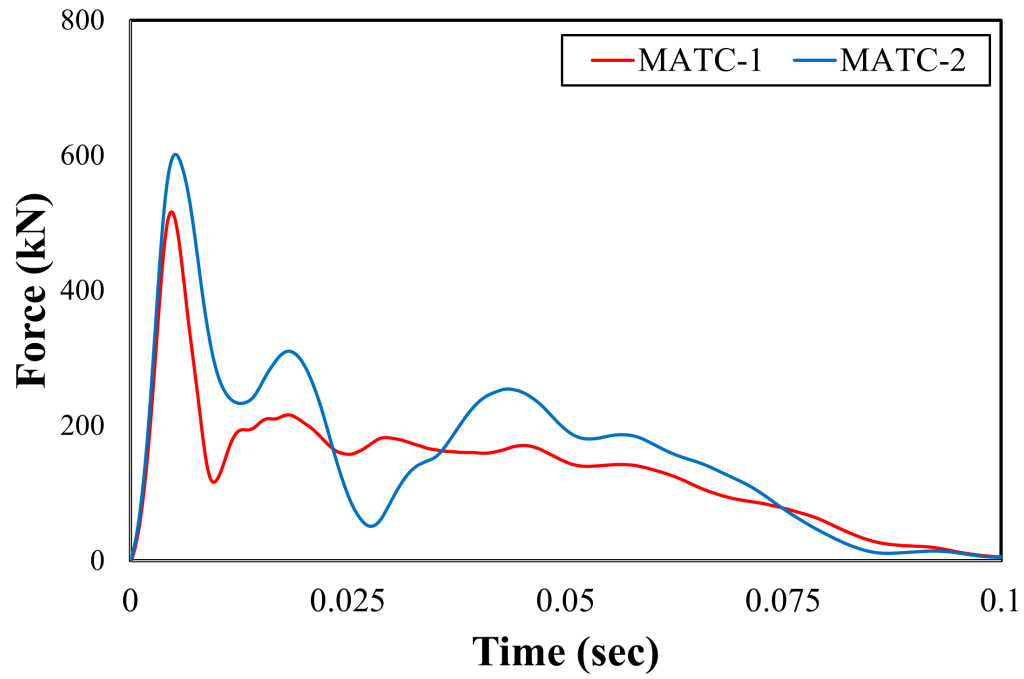








### Impact Force Time Histories



### Front Panel Displacement Time Histories

